

1982

Two-dimensional, intratidal model study of salinity intrusion structure and motion in partially-mixed estuaries (Virginia)

Carl F. Cerco

College of William and Mary - Virginia Institute of Marine Science

Follow this and additional works at: <https://scholarworks.wm.edu/etd>



Part of the [Oceanography Commons](#)

Recommended Citation

Cerco, Carl F., "Two-dimensional, intratidal model study of salinity intrusion structure and motion in partially-mixed estuaries (Virginia)" (1982). *Dissertations, Theses, and Masters Projects*. Paper 1539616604.

<https://dx.doi.org/doi:10.25773/v5-snv5-am80>

This Dissertation is brought to you for free and open access by the Theses, Dissertations, & Master Projects at W&M ScholarWorks. It has been accepted for inclusion in Dissertations, Theses, and Masters Projects by an authorized administrator of W&M ScholarWorks. For more information, please contact scholarworks@wm.edu.

INFORMATION TO USERS

This reproduction was made from a copy of a document sent to us for microfilming. While the most advanced technology has been used to photograph and reproduce this document, the quality of the reproduction is heavily dependent upon the quality of the material submitted.

The following explanation of techniques is provided to help clarify markings or notations which may appear on this reproduction.

1. The sign or "target" for pages apparently lacking from the document photographed is "Missing Page(s)". If it was possible to obtain the missing page(s) or section, they are spliced into the film along with adjacent pages. This may have necessitated cutting through an image and duplicating adjacent pages to assure complete continuity.
2. When an image on the film is obliterated with a round black mark, it is an indication of either blurred copy because of movement during exposure, duplicate copy, or copyrighted materials that should not have been filmed. For blurred pages, a good image of the page can be found in the adjacent frame. If copyrighted materials were deleted, a target note will appear listing the pages in the adjacent frame.
3. When a map, drawing or chart, etc., is part of the material being photographed, a definite method of "sectioning" the material has been followed. It is customary to begin filming at the upper left hand corner of a large sheet and to continue from left to right in equal sections with small overlaps. If necessary, sectioning is continued again—beginning below the first row and continuing on until complete.
4. For illustrations that cannot be satisfactorily reproduced by xerographic means, photographic prints can be purchased at additional cost and inserted into your xerographic copy. These prints are available upon request from the Dissertations Customer Services Department.
5. Some pages in any document may have indistinct print. In all cases the best available copy has been filmed.

**University
Microfilms
International**

300 N. Zeeb Road
Ann Arbor, MI 48106

8229790

Cerco, Carl Francis

TWO-DIMENSIONAL, INTRATIDAL MODEL STUDY OF SALINITY INTRUSION
STRUCTURE AND MOTION IN PARTIALLY-MIXED ESTUARIES

The College of William and Mary in Virginia

Ph.D. 1982

**University
Microfilms
International** 300 N. Zeeb Road, Ann Arbor, MI 48106



PLEASE NOTE:

In all cases this material has been filmed in the best possible way from the available copy. Problems encountered with this document have been identified here with a check mark .

1. Glossy photographs or pages _____
2. Colored illustrations, paper or print _____
3. Photographs with dark background _____
4. Illustrations are poor copy _____
5. Pages with black marks, not original copy _____
6. Print shows through as there is text on both sides of page _____
7. Indistinct, broken or small print on several pages _____
8. Print exceeds margin requirements _____
9. Tightly bound copy with print lost in spine _____
10. Computer printout pages with indistinct print _____
11. Page(s) 213 lacking when material received, and not available from school or author.
12. Page(s) _____ seem to be missing in numbering only as text follows.
13. Two pages numbered _____. Text follows.
14. Curling and wrinkled pages _____
15. Other _____

**University
Microfilms
International**

TWO-DIMENSIONAL, INTRATIDAL MODEL STUDY OF SALINITY
INTRUSION STRUCTURE AND MOTION IN PARTIALLY-MIXED ESTUARIES

A Dissertation

Presented to

The Faculty of the School of Marine Science
The College of William and Mary in Virginia

In Partial Fulfillment

Of the Requirements for the Degree of
Doctor of Philosophy

by


Carl F. Cerco

1982

APPROVAL SHEET

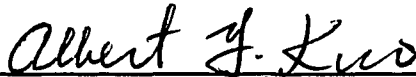
This dissertation is submitted in partial fulfillment of
the requirements for the degree of

Doctor of Philosophy



Carl F. Cerco

Approved, July 1982



Albert Y. Kuo, Chairman



Michael E. Bender



C. S. Fang



C. Y. Kuo, Virginia Polytechnic
Institute and State University



Maynard M. Nichols

TABLE OF CONTENTS

	Page
ACKNOWLEDGEMENTS.....	iv
LIST OF TABLES.....	v
LIST OF FIGURES.....	vi
ABSTRACT.....	xi
CHAPTER I. INTRODUCTION.....	2
CHAPTER II. THE JAMES RIVER - DESCRIPTION AND OBSERVATIONS.....	10
CHAPTER III. GOVERNING EQUATIONS AND NUMERICAL METHODS.....	24
CHAPTER IV. MODEL VERIFICATION.....	49
CHAPTER V. MODELLING THE SPRING-NEAP STRATIFICATION CYCLE.....	93
CHAPTER VI. MODELLING MOVEMENT OF THE SALINITY INTRUSION.....	118
CHAPTER VII. EXPERIMENTS ON A MODEL ESTUARY.....	150
CHAPTER VIII. RECOMMENDATIONS FOR FUTURE INVESTIGATORS.....	265
CHAPTER IX. SUMMARY AND CONCLUSIONS.....	270
BIBLIOGRAPHY.....	279
VITA.....	283

ACKNOWLEDGEMENTS

This dissertation would not have been possible without the advice and ideas of my committee chairman, Dr. Albert Y. Kuo. I am also indebted to Dr. Frank Fang, former head of the Department of Physical Oceanography and Hydraulics, for committing the resources of the department to the collection of much of the data contained herein. Last but not least, let me thank my typist par excellence, Ms. Shirley Crossley.

LIST OF TABLES

Table	Page
4-1. Laboratory Flume Parameters.....	58
5-1. August-September 1980 Salinity Surveys.....	94
6-1. April-May 1978 Salinity Surveys.....	119
7-1. Characteristics of Idealized Trapezoidal Estuary.....	155
7-2. Results of Experiments on Model Estuary.....	172

LIST OF FIGURES

Figure	Page
2-1. The Tidal James River.....	19
2-2. Effect of Flow and Tide Range on Stratification at James River Bridge.....	20
2-3. Dimensionless Stratification vs. Mixing Parameter.....	21
2-4. Stratification and Tide Range at Km. 21, August 14 - September 2, 1980.....	22
2-5. Estuarine Behavior Following April 1978 Storm.....	23
3-1. Finite Difference Grid.....	48
4-1. Effect of Friction on Model Solution.....	72
4-2. Effect of Time Step on Model Solution.....	73
4-3. Effect of Time Step on Phase of Solution.....	74
4-4. Convergence of Solution as a Function of Bottom Friction.....	75
4-5. Effect of Distance Step on Model Solution.....	76
4-6. Effect of Distance Step on Phase of Model Solution.....	77
4-7. Calibration of Laboratory Bottom Roughness....	78
4-8. Laboratory and Model Longitudinal Salinity Distributions.....	79
4-9. Laboratory and Model Vertical Salinity Distributions.....	79
4-10. Laboratory and Flume Tidal Average Horizontal Velocities.....	80

Figure	Page
4-11. Laboratory and Flume Tidal Average Vertical Velocities.....	81
4-12. Model Geometry.....	82
4-13. Predicted vs. Tabulated James River Tide Range.....	83
4-14. James River Tide and Current Stations, August, 1977.....	84
4-15. Tide and Current at Km. 47.....	85
4-16. Tide and Current at Km. 73.....	86
4-17. Tide and Current at Km. 112.....	87
4-18. Predicted vs. Measured Salinity, July, 1977...	88
4-19. Predicted vs. Measured Salinity, August, 1977.	89
4-20. Predicted vs. Measured Salinity, July, 1974...	90
4-21. Predicted vs. Measured Salinity, April, 1978..	91
4-22. Predicted vs. Measured Salinity, May, 1975....	92
5-1. Tide Range at Km. 21., August 14 - September 2..	98
5-2. Predicted and Observed Longitudinal Salinity, August 14.....	99
5-3. Predicted and Observed Longitudinal Salinity, August 19.....	100
5-4. Predicted and Observed Longitudinal Salinity, August 22.....	101
5-5. Predicted and Observed Longitudinal Salinity, August 27.....	102
5-6. Predicted and Observed Longitudinal Salinity, September 2.....	103
5-7. Observed and Predicted Salinity Profile August 14.....	104
5-8. Observed and Predicted Salinity Profile August 19.....	106

Figure	Page
5-9. Observed and Predicted Salinity Profile August 22.....	108
5-10. Observed and Predicted Salinity Profile August 27.....	110
5-11. Observed and Predicted Salinity Profile September 2.....	112
5-12. Predicted and Observed Stratification at Km. 23.....	114
5-13. Predicted and Observed Stratification at Km. 32.....	115
5-14. Predicted and Observed Stratification at Km. 50.....	116
5-15. Predicted and Observed Stratification at Km. 66.....	117
6-1. Tide Range at Km. 21, April 25 - May 9.....	126
6-2. Predicted and Observed Longitudinal Salinity, April 25.....	127
6-3. Predicted and Observed Longitudinal Salinity, April 28.....	128
6-4. Predicted and Observed Longitudinal Salinity, April 29.....	129
6-5. Predicted and Observed Longitudinal Salinity, April 30.....	130
6-6. Predicted and Observed Longitudinal Salinity, May 2.....	131
6-7. Predicted and Observed Longitudinal Salinity, May 7.....	132
6-8. Observed and Predicted Salinity Profile, April 25.....	133
6-9. Observed and Predicted Salinity Profile, April 28.....	135
6-10. Observed and Predicted Salinity Profile, April 29.....	137

Figure	Page
6-11. Observed and Predicted Salinity Profile, April 30.....	139
6-12. Observed and Predicted Salinity Profile, May 2.....	141
6-13. Observed and Predicted Salinity Profile, May 7.....	143
6-14. Predicted and Observed Salinity at Km. 21.....	145
6-15. Predicted and Observed Salinity at Km. 33.....	146
6-16. Predicted and Observed Salinity at Km. 39.....	147
6-17. Predicted and Observed Stratification at Km. 21.....	148
6-18. Predicted and Observed Stratification at Km. 33.....	149
7-1. Salinity Regimes of Idealized Trapezoidal Estuary.....	175
7-2. Longitudinal Salinity Distribution of Idealized Estuary at Steady State.....	176
7-3. Vertical SBF Salinity of Idealized Estuary at Steady State.....	177
7-4. Response to Upstream Wind Step Function.....	178
7-5. Response to Downstream Wind Step Function.....	185
7-6. Response to Step-Function Increase in Tide Range.....	192
7-7. Response to Step-Function Decrease in Tide Range.....	199
7-8. Response to Step-Function Increase in Flow.....	206
7-9. Response to Step-Function Decrease in Flow.....	213
7-10. Response to Step-Function Increase in Salinity Boundary.....	222
7-11. Response to Step-Function Decrease in Salinity Boundary.....	229

Figure	Page
7-12. Response to Upstream Wind Pulse.....	236
7-13. Response to Downstream Wind Pulse.....	243
7-14. Response to Pulse Increase in Flow.....	250
7-15. Response to Spring-Neap Tidal Cycling.....	257

ABSTRACT

A two-dimensional, longitudinal-vertical model for partially-mixed estuaries has been developed. The model provides intratidal predictions of surface level, velocity, and salinity through a semi-implicit finite-difference solution to the continuity and momentum equations and an explicit finite-difference solution to the salinity equation.

The model was verified through comparison with analytical solutions, laboratory data, and prototype data. Following verification, the model was used to simulate the destratification-stratification cycle which occurs in the James River Estuary, Virginia, coincident with the spring-neap tidal cycle. In a second application to the James, a simulation of the movement of the salinity intrusion following a storm-generated freshwater flow pulse was conducted.

Investigations were conducted into the reaction of a hypothetical estuary to step-like and pulse-like alterations in wind stress, tide range, boundary conditions and flow. It was noted that the reaction time-scale of the estuary was much longer than the time-scale of alterations in the forcing functions. Thus, in prototype estuaries in which forcing functions are periodic and/or randomly superimposed, truly steady-state conditions are never attained.

TWO-DIMENSIONAL, INTRATIDAL MODEL STUDY OF SALINITY
INTRUSION STRUCTURE AND MOTION IN PARTIALLY-MIXED ESTUARIES

CHAPTER I.

INTRODUCTION

An estuary is a body of water in which fresh, upland runoff meets and mixes with the saline water of the sea. The nature of the mixing process and the physical structure of the region in which mixing takes place may vary, and depend upon the volume of freshwater runoff, the geometry of the estuary, the salinity of the adjacent seawater, and the energy input from tides and wind.

Estuaries of the Virginia coast are characterized as "partially mixed". Within the mixing region, a gradient of salinity may be observed in both the longitudinal and vertical directions. The longitudinal gradient exists due to the fixed boundary conditions of fresh and salt water at each end of the estuary. The vertical gradient is due to the buoyancy of the freshwater which moves downstream in a surface layer perched upon a denser, more saline lower layer.

In the lower layer, salt water is driven upstream due to the pressure gradient created by the density difference of the salt and fresh water. As it moves upstream this saline flow mixes with and is entrained into

the surface layer and returns downstream resulting in a net two-layered circulation - downstream in the upper layer and upstream in the lower layer.

As salt water in the lower layer moves upstream and becomes diluted with water from the upper layer, the salinity of the lower layer decreases until the upstream pressure gradient created by longitudinal density differences is no longer sufficient to overcome the downstream gradient created by the hydrostatic head of the freshwater flow. At the location where these forces balance, a point of no net motion exists in the lower layer. Salt water cannot intrude upstream of this point which forms the limit of upstream motion in the lower layer and the limit of salinity intrusion.

The location of the upstream limit of the salinity intrusion is dependent upon the volume of freshwater flow, the geometry of the estuary, the salinity at the downstream boundary of the estuary, and the amount of tidal and wind mixing present. As the flow, boundary conditions, and other influences vary over time, the salinity intrusion moves up and down the estuary in response.

Freshwater flow and tidal energy influence not only the longitudinal salinity gradient but the vertical gradient as well. Large runoff volumes and small amounts of energy available for mixing result in sharp vertical gradients of salinity. Estuaries in which the surface

water is much less saline than the bottom water are referred to as "stratified". In the limiting case, a salt wedge is formed and no mixing exists between surface and bottom (Pritchard, 1967). If the runoff volume is small and the tidal mixing large, only a slight vertical salinity gradient will exist. In the limiting case of no vertical salinity gradient, the estuary is said to be "well mixed" (Pritchard, 1967).

Partially mixed estuaries occupy an intermediate position between salt-wedge and well-mixed estuaries. Stratification exists in partially mixed estuaries but is of variable degree depending on the relative amounts of runoff and mixing energy available. At times these estuaries may be highly stratified. At other times they may approach the well-mixed condition. If the energy input is cyclical (as from spring-neap tidal cycling) alternate stratification and destratification may be evident (Haas, 1977).

Wind also influences the circulation and salinity of a partially-mixed estuary through local and non-local effects. Surface currents are generally in the same direction as the local wind stress (Elliott, 1976). Thus downstream winds tend to enhance circulation and stratification while upstream winds may reverse the typical circulation pattern and reduce stratification. Non-local meteorological effects can affect stratification through alteration of sea level at the mouth of the estuary (Wang and Elliott, 1978).

A. Objectives of Present Study

The ability to predict the location and movement of the head of the salt intrusion and the condition of stratification in an estuary is of theoretical and practical importance. Based on observations of freshwater flow and salinity, an empirical salinity model may be formulated. A preferable approach, however, is to derive a predictive mathematical model based upon the principles of estuarine physics and verified against field observations. A model consistent with physical principles can be utilized as an experimental tool to test the influence on salinity of alternate parameter magnitudes and formulations; such experiments are impossible to conduct in a prototype estuary. The model can also be used to provide rational, reliable forecasts of the estuarine salinity distribution to individuals and organizations economically dependent upon the quality of estuarine water. At present, however, no predictive model exists which may be applied over the extended time scales of motion of the salinity intrusion while detailing the intratidal variations of salinity and circulation.

The features which must be included in such a model are apparent. The model must simulate the salinity structure and the currents, tidal heights, and mixing processes which determine this structure in at least two spatial dimensions - the longitudinal and the vertical.

The model must provide time-variable or transient predictions consistent with the observed time scales of motion of the intrusion. To be of most use, the model should also be based on sound theoretical principles.

The objective of this study is to develop a two-dimensional, time variable model which incorporates these features. Once formulated, the model will be verified via the simulation of prototype events and then utilized to explore the behavior of an idealized estuary.

B. Review of Previous Studies

It is the intent of this study to develop a two-dimensional longitudinal-vertical model. The proposed model differs from two-dimensional depth-integrated models of the type developed by Leendertse (1970) which operate along the longitudinal and lateral axes.

Several models of the time-variable, longitudinal-vertical hydrodynamic and salinity structures of estuaries have been previously formulated. These models, of the developmental type, have been used to test the thesis that two-dimensional modelling is feasible and to explore the effects of alternate parameter formulations and boundary conditions. Rigorous verification against field data has not been performed. Neither have the existing models been applied to phenomena which are time-variable in the scale of movement of the salinity intrusion. Rather, the models have been employed to simulate intratidal changes in circulation and salinity in estuaries for which conditions are steady from cycle to cycle. Failure to apply the models to more

lengthy time periods has been due primarily to the excessive computer time required for computations of this nature and to the lack of a suitable data base.

Hamilton (1975) developed a time-variable, two-dimensional model for estuaries of rectangular cross-section based on an explicit finite-difference solution to the laterally-integrated conservation of volume, momentum, and mass equations. A model simulation of one tidal cycle in the Rotterdam Waterway produced qualitative agreement with field observations of current and salinity.

In a succeeding paper, Hamilton (1977) presented a revised semi-implicit numerical scheme which employed time steps fifteen to thirty times longer than his previous explicit scheme. Applied to a hypothetical channel, the model was used to investigate the effects of alternate eddy viscosity formulations on the estuarine salt balance.

Blumberg (1975) utilized a "leapfrog" explicit finite-difference scheme to solve the conservation of volume, momentum, and salt equations in an application of a two-dimensional model to the Potomac River Estuary. Blumberg also addressed the problem of formulation of the eddy viscosity parameter and found that a functional dependence of viscosity on vertical stability is necessary to produce model results comparable to field observations.

The specification of the downstream boundary condition on salt in a time-variable estuarine model is problematic

since the salinity structure at the mouth of the estuary is dependent both upon conditions in the adjacent sea and in the estuary. Determination of the boundary as a function of external factors only without consideration of conditions in the estuary reduces the predictive ability of the model. Elliott (1976) addressed this issue by extending Blumberg's model to include a portion of Chesapeake Bay as well as the Potomac Estuary. By this means, the downstream boundary was moved seaward from the region of primary interest, enhancing the predictive nature of the model in the vicinity of the Potomac River mouth.

Kuo et al (1978) extended the application of the two-dimensional longitudinal-vertical model to estuarine sediment transport and formation of the turbidity maximum. In an application to the Rappahannock River Estuary, agreement was achieved between model results and field data of tidal height and current. Predictions of the salinity gradient and formation of a turbidity maximum consistent with observations were also obtained.

The results of explicit and semi-implicit integration schemes were compared by Wang and Kravitz (1980) in applications to a hypothetical estuary and to the Potomac River. The semi-implicit integration scheme made possible "order-of-magnitude" savings in computer time compared to the explicit scheme although it was less accurate than the

explicit scheme in the prediction of surface oscillations. Both methods produced good agreement in computations of salinity and velocity.

Although they are not time-variable, the analytical model of Hansen and Rattray (1965) and the numerical model of Festa and Hansen (1974) are also significant predecessors to this study. From their analyses of idealized estuaries, conceptual understanding of prototype behavior and bases for comparison with more detailed models may be obtained.

Hansen and Rattray (1965) developed a pair of stream-function equations describing circulation and salt balance in an estuary. By defining three salinity regimes, they were able to obtain similarity solutions describing the vertical salinity and velocity profiles in the inner and central regimes. The effects of wind stress on these idealized profiles were also investigated.

Festa and Hansen (1976) investigated the effects of altering depth and river discharge on estuarine circulation and salinity by means of a two-dimensional, steady-state numerical model based on vorticity and salt-balance equations. They found that decreasing the discharge allowed the head of salt intrusion to move upstream. Although estuarine circulation weakened, it became more extensive as runoff decreased. Increasing the depth resulted in enhanced circulation and inward migration of the head of salt intrusion.

CHAPTER II.

THE JAMES RIVER - DESCRIPTION AND OBSERVATIONS

The James River originates in the Appalachian mountains of Virginia at the confluence of the Jackson and Cowpasture Rivers. From there, the river flows approximately 530 kilometers in a southeasterly direction to Chesapeake Bay. From the mouth at Sewell's Point (km 0) to the fall-line at Richmond (km 160) the river is tidal (Fig. 2-1) with an average tide range varying from 76 cm at Sewell's Point to 58 cm near the Chickahominy River mouth (km 77) to 98 cm at Richmond.

Freshwater flow at Richmond averages $215 \text{ m}^3/\text{sec}$. Typically, flows vary from approximately $1400 \text{ m}^3/\text{sec}$ during spring floods to approximately $25 \text{ m}^3/\text{sec}$ during droughts although extremes outside this range have been noted. Salt generally intrudes upstream from Chesapeake Bay to the vicinity of Jamestown Island (km 68) but the intrusion may approach Hopewell (km 120) or be forced downstream as far as Newport News (km 24) in response to low-flow and flood events.

Near its juncture with Chesapeake Bay, the James River forms the harbor of Hampton Roads. Within Hampton Roads, three-dimensional distributions of circulation

and salinity occur, rendering this portion of the river unsuited to the two-dimensional approximation employed herein. Upstream of the James River Bridge (km 21), however, lateral parameter variations are small compared to longitudinal and vertical variations and may be neglected. Thus, a two-dimensional approximation is valid. The portion of the river between the fall-line (km 160) and the James River Bridge (km 21) will be considered the subject of this study.

Within the region of interest, the James receives two major tributaries, the Appomattox (km 124) and Chickahominy (km 77) Rivers. Flows in these tributaries average $47 \text{ m}^3/\text{sec}$ and $8 \text{ m}^3/\text{sec}$ respectively.

The James River is channelized as far as Richmond to a minimum depth at mid-channel of approximately 8 m. Maximum depths in the estuary are typically 10-14 m and cross-sectional average depths vary from 3-9 m. Cross-sectional areas range from approximately 27000 m^2 near the James River Bridge to 1000 m^2 at Richmond.

A. Stratification-De-stratification Cycling

In a partially-mixed estuary such as the James, vertical gradients of salinity are created by the tendency of buoyant freshwater flow to "float" upon more dense, saline water. The steepness of the gradient is dependent upon the runoff volume and the availability of mixing energy, manifested as turbulent eddies which transport saline water upward and freshwater downward.

A primary source of mixing energy is the action of tides. This effect in the James River may be seen in Fig. 2-2 which shows surface-to-bottom stratification in the vicinity of km 21 as a function of predicted local tide range and daily runoff at Richmond. During intervals of low runoff and large range, the well-mixed condition is approached. During intervals of high flow and small tide range, stratification is observed.

The degree of stratification can be related to buoyancy and mixing energy through the non-dimensional parameter M (Hansen and Rattray, 1965).

$$M \equiv K_h K_z b^2 / R^2 \quad (2-1)$$

where

K_h = horizontal tidal dispersion

K_z = vertical turbulent diffusivity

R = river discharge

b = channel width

As M increases, stratification decreases until the limiting, well-mixed case.

While the ratio expressed in Eq. (2-1) is conceptually useful, it is difficult to evaluate the mixing parameters and relate them to tidal action. An alternative dimensionless quantity which expresses the ratio of buoyancy to mixing action is simply the ratio of fresh-water velocity to tidal velocity, u_f/u_t . This parameter

is more easily evaluated and is plotted against dimensionless stratification in Fig. 2-3 employing the same data as in Fig. 2-2. The positive correlation between stratification and the ratio u_f/u_t is apparent. Also of interest is the tendency for the data points to occupy two regions delineated by $\Delta s/s = 0.1$ and $u_f/u_t = 8 \times 10^{-3}$. For values of $u_f/u_t > 8 \times 10^{-3}$, observed stratification is generally greater than 10%. For values of $u_f/u_t < 8 \times 10^{-3}$, stratification is generally less than 10%.

The principal tidal component in the James River is the lunar semi-diurnal tide which has a period of 12.42 hours. Superimposed on this are several lesser components which produce a fortnightly spring-neap tidal cycle. During spring tide, the tide range in Hampton Roads exceeds 90 cm as compared to the average tide range of 76 cm.

Spring tides produce larger tidal currents and, hence, more intense mixing than neap tides. As may be deduced from Eq. (2-1) and observed in Figs. 2-2 and 2-3, stratification is lower during spring tides than neap tides, provided runoff is constant. As the spring-neap tidal cycle progresses, a stratification-destratification cycle may occur as well. This effect has been noted by Haas (1977) in the James, York, and Rappahannock estuaries of Virginia.

During August and September, 1980, a series of surveys were conducted by the Department of Physical Oceanography and Hydraulics of the Virginia Institute of Marine Science aimed at detailing stratification - destratification cycling in the James River. The longitudinal and vertical salinity distributions were sampled in seven surveys conducted on five different days in the interval August 14 to September 2. During this period, the tide range at Hampton Roads varied from 49 to 107 cm while freshwater flow averaged $46 \text{ m}^3/\text{sec}$. Details of the survey methodology and results are presented in Chapter V.

In Fig. 2-4, surface and bottom salinities sampled in the vicinity of the James River Bridge and tide range during the survey period are plotted (Note: diurnal inequalities have been removed from the tide data). The cyclical nature of stratification in the estuary and the relationship of the stratification-destratification cycle to the spring neap tidal cycle are apparent. Beginning with the survey of August 14, conducted in the mean-tide phase, stratification increased to a maximum during the neap-tide phase, as exemplified by the August 19 survey. From the neap-tide maximum, stratification was observed to decrease to a minimum on August 27 during spring tides. From the minimum, stratification again increased in response to decreasing tide range as exemplified by the survey of September 2.

The observations of August 14 - September 2 will form the basis for the application of the model, conducted in Chapter V, to the stratification-destratification cycle.

B. Longitudinal Movement of the Salinity Intrusion

The location of the upstream limit of the salinity intrusion is determined primarily by the force balance between the downstream hydrostatic head of the freshwater flow and the upstream pressure gradient exerted due to the longitudinal salinity gradient. The intrusion moves downstream with increasing runoff and upstream with decreasing runoff.

In estuaries such as the James, an annual cycle in the motion of the salinity intrusion may be observed. Concurrent with the high flows which occur in late winter and in spring, the intrusion is pushed to its most downstream location. During late summer and fall, low-flow conditions prevail and the intrusion gradually moves upstream until the high runoff associated with winter and spring recurs.

Superimposed on the long-term annual cycle are short-term motions due to pulse-like variations in flow from storm runoff. An extreme example of this phenomenon was observed in the aftermath of Tropical Storm Agnes in 1972. (Davis, ed.; 1974)

Between June 21 and June 23, 1972, Tropical Storm Agnes dumped 15 to 30 cm of rain on the previously saturated Chesapeake Bay watershed resulting in record flood stages in several Chesapeake tributaries. In the James River, peak flows in excess of sixty times normal were recorded. During the two-month period following the storm event, the structure and location of the salinity intrusion varied through four phases.

- (1) A period of strong stratification due to downstream movement of the surface salinity caused by increased freshwater runoff.
- (2) Reduced stratification due to depression of the bottom salinity which lagged the depression of the surface layer.
- (3) Increasing estuarine salinity accompanied by the reappearance of stratification. During the stratified phase, a rebound of salinity was observed in which the head of intrusion moved upstream of its pre-Agnes position.
- (4) Recovery to a roughly normal, partially mixed state.

A second example of short-term motion of the salinity intrusion occurred due to the pulse-flow associated with an April, 1978, storm. In two days, the storm increased runoff by twelve-fold from a steady, average value of $150 \text{ m}^3/\text{sec}$ prior to April 26 to a peak flow exceeding $1800 \text{ m}^3/\text{sec}$ on April 28 (Fig. 2-5). Five days following the peak, flow had decreased to $340 \text{ m}^3/\text{sec}$ before increasing in a second pulse to $830 \text{ m}^3/\text{sec}$ on May 5. Flows remained high throughout May, gradually returning to the level of mid-April by early June.

Prior to the April storm, both the location of the salinity intrusion (defined as the location of the 1‰ isohaline) and the salinity at the James River Bridge were constant although stratification decreased radically from April 19 to April 25 due to an increase in tide range from 67 cm to 99 cm (Fig. 2-5). In response to the storm flow which commenced on April 27, the intrusion moved downstream from km 53 to km 38 by April 29. Salinity at the James River Bridge was depressed about 7‰ from its value of 13.5‰ prior to the storm to a minimum of 6.1‰ on April 30. It then rebounded slightly to 7.6‰, a level maintained throughout early May. Simultaneously, the salinity intrusion continued to move downstream to approximately km 30 by May 7. With the return of mid-April flow levels (approx. 150 m³/sec) in early June, the intrusion moved back upstream and salinity at the bridge increased although neither had yet recovered to its pre-storm level.

The behavior of the estuarine salinity structure following the April, 1978, storm differs, in some respects, from the observations following the Agnes event. In 1978, surface and bottom salinities were depressed simultaneously rather than in two stages and a relatively constant surface-to-bottom salinity difference was maintained. Neither was a rebound of salinity in excess of pre-storm values observed although this phenomenon may have occurred in the interval between the May 7 and June 5 surveys.

Eight slackwater surveys were conducted in the James River by the Virginia Institute of Marine Science in the period from April 19 to June 5, 1978. Those surveys provide the salinity data presented in Fig. 2-5. Of them, five were grouped around the initial storm pulse and one was conducted during the recovery phase providing an excellent data base for modelling movement of the salinity intrusion. Details of the surveys and results of the modelling effort will be presented in Chapter VI.

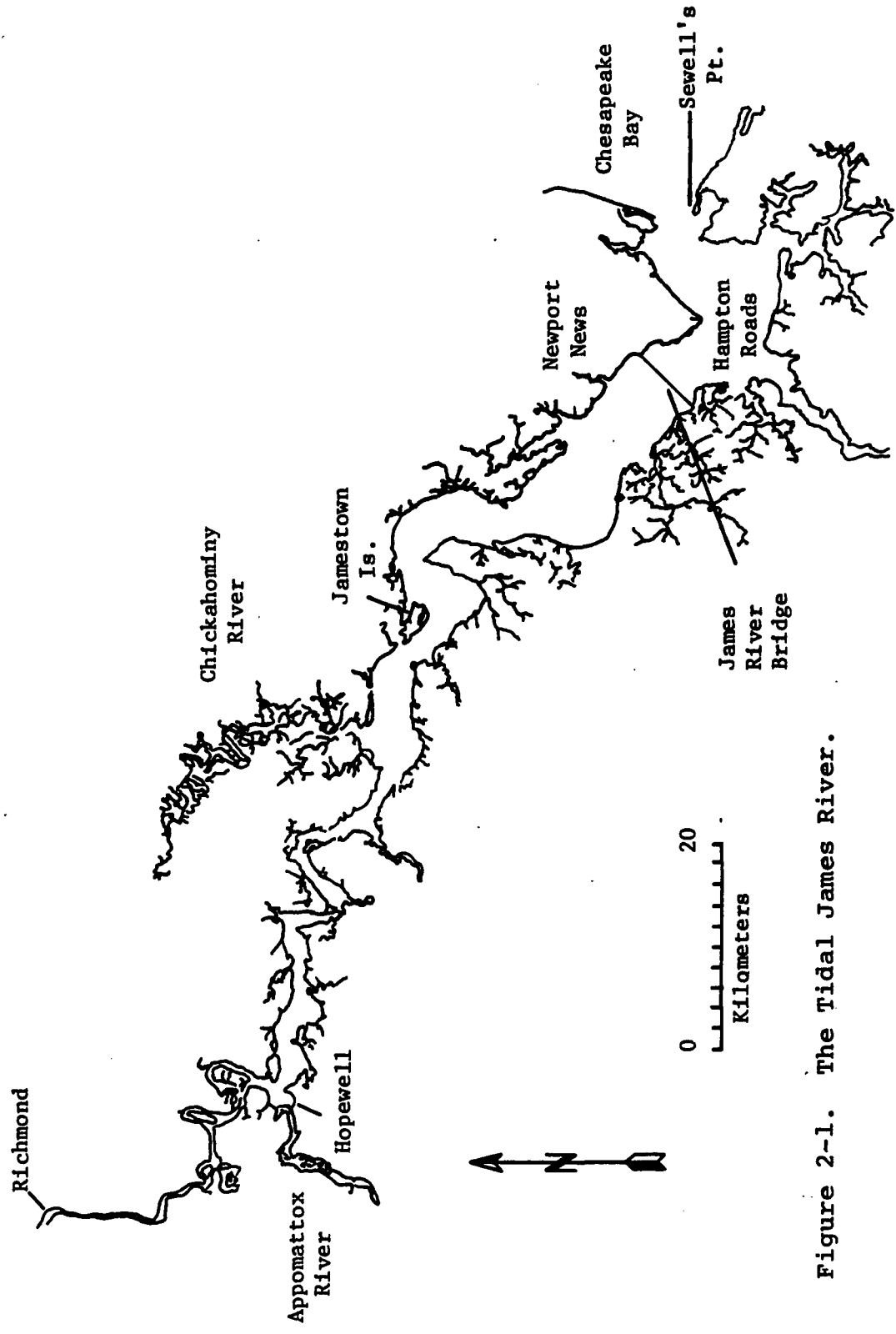


Figure 2-1. The Tidal James River.

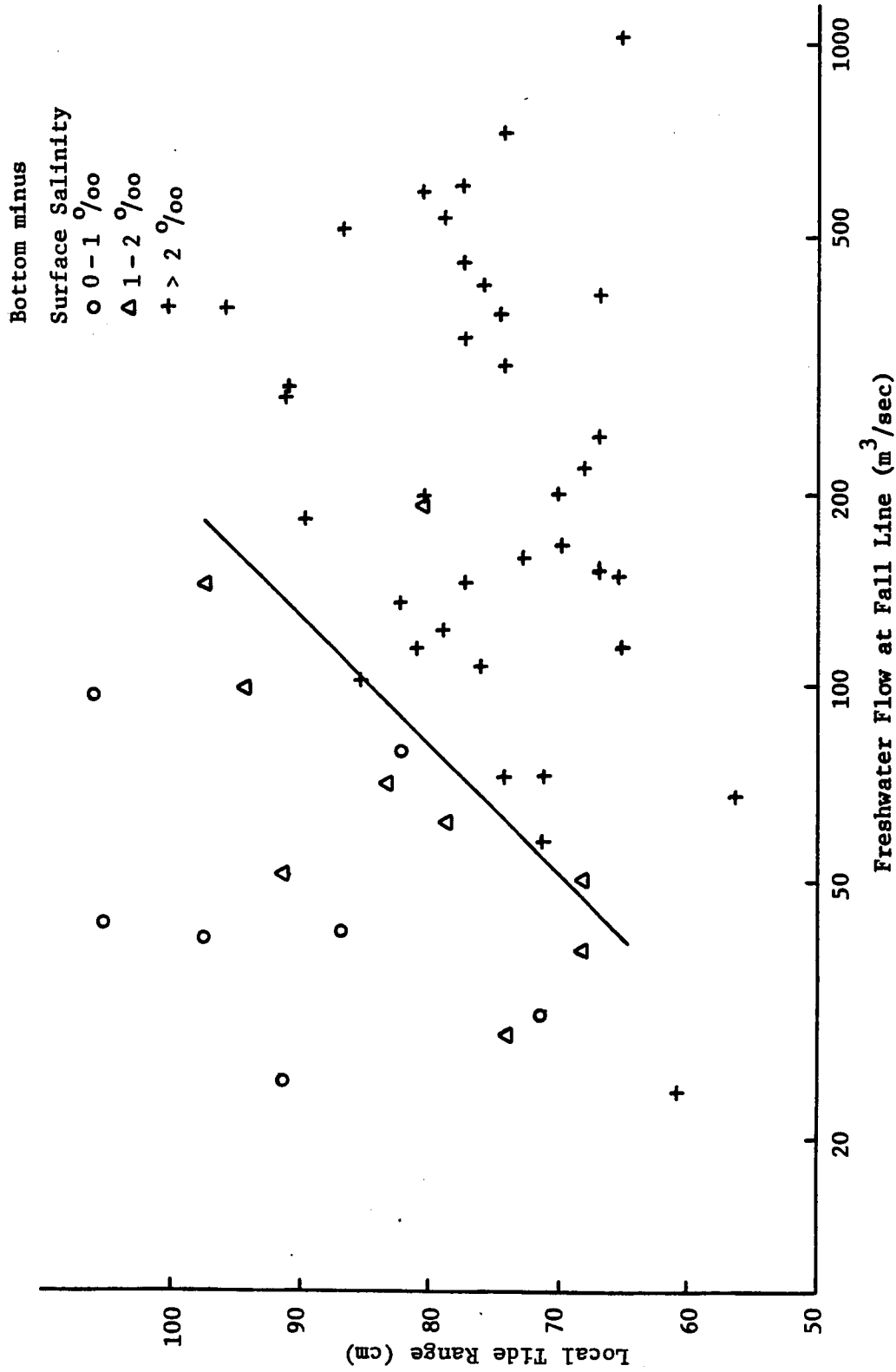


Figure 2-2. Effect of Flow and Tide Range on Stratification at James River Bridge.

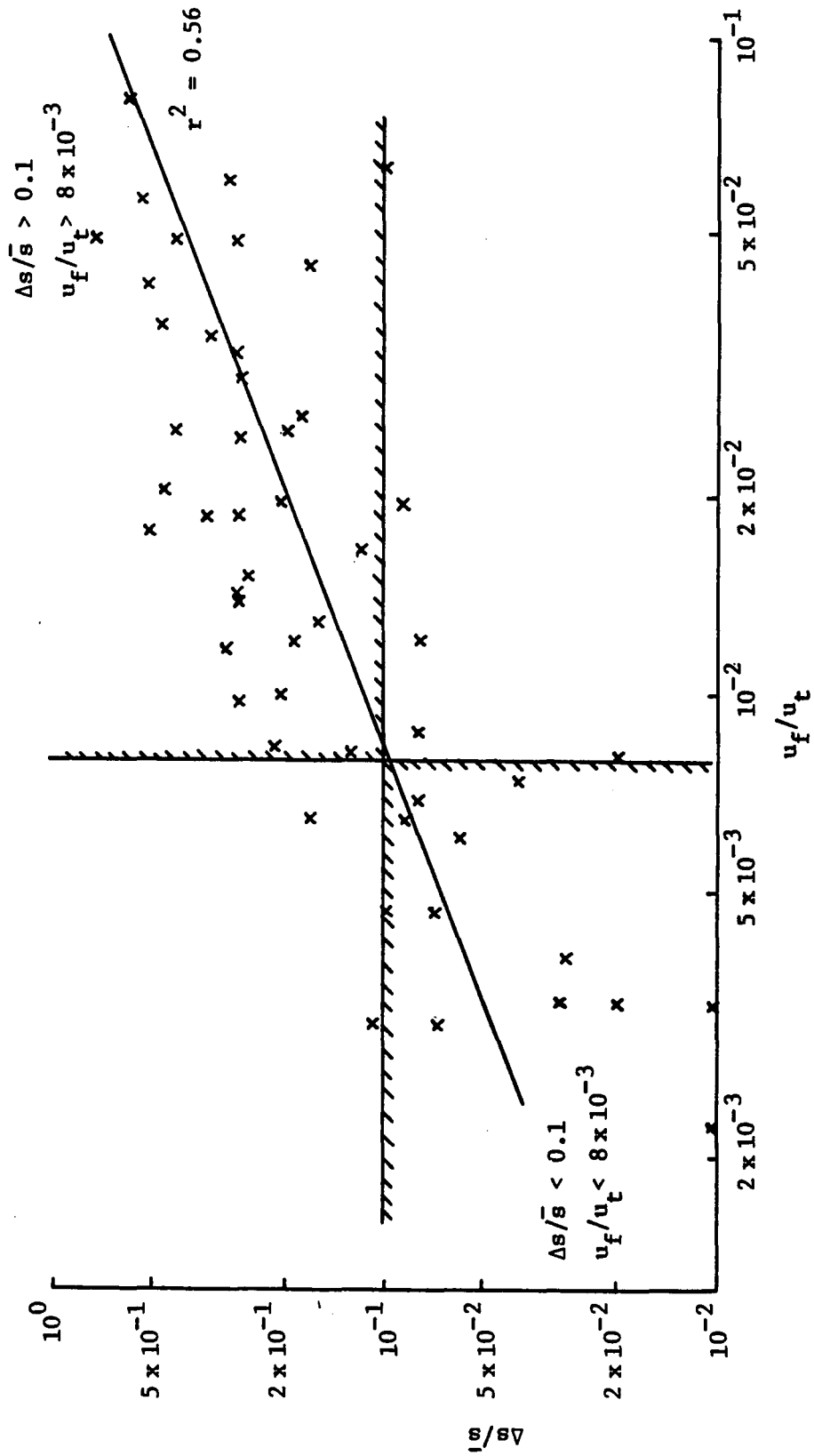


Figure 2-3. Dimensionless Stratification vs. Mixing Parameter.

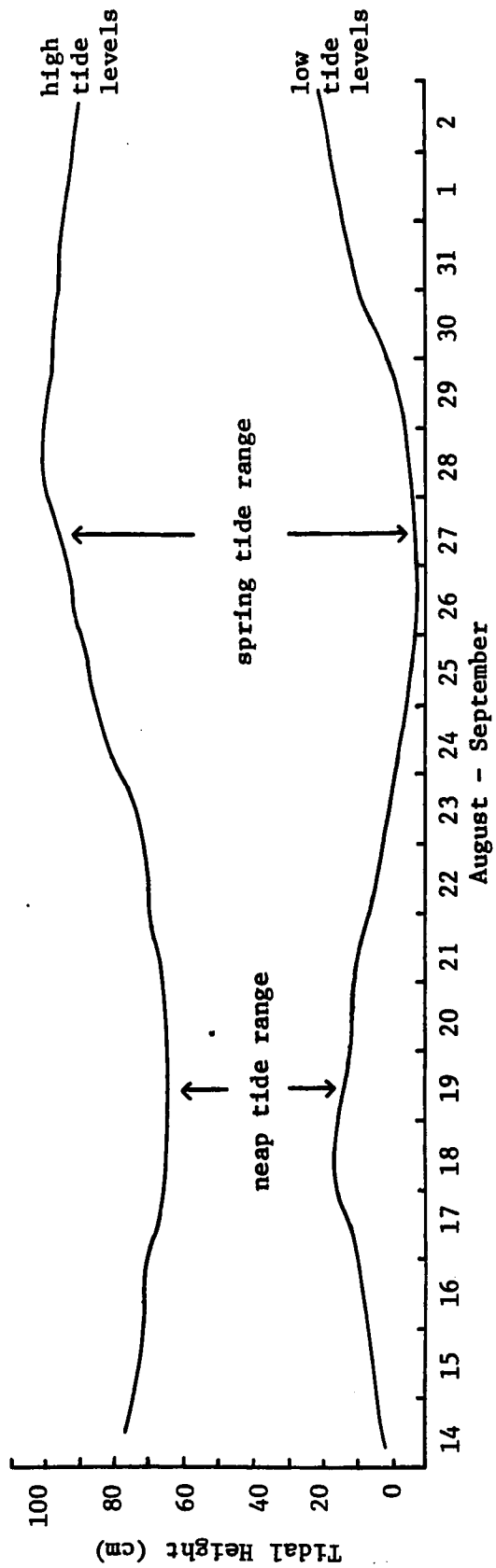
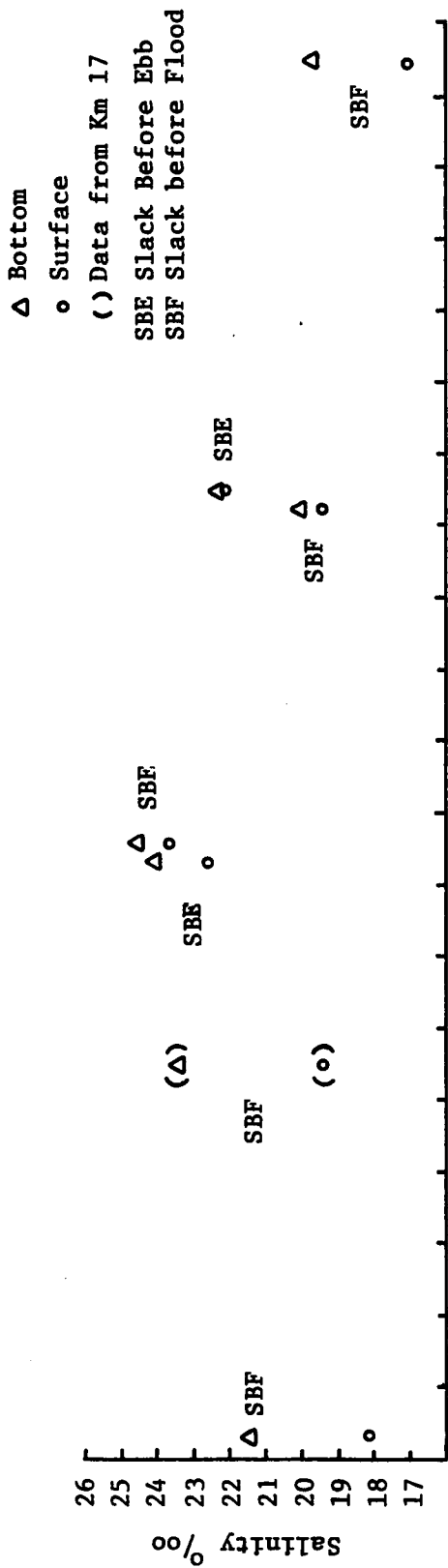


Figure 2-4. Stratification and Tide Range at Km. 21, August 14-September 2, 1980.

Note: Salinities are shown at SBF. April 19 & May 2 data are converted from SBE surveys.

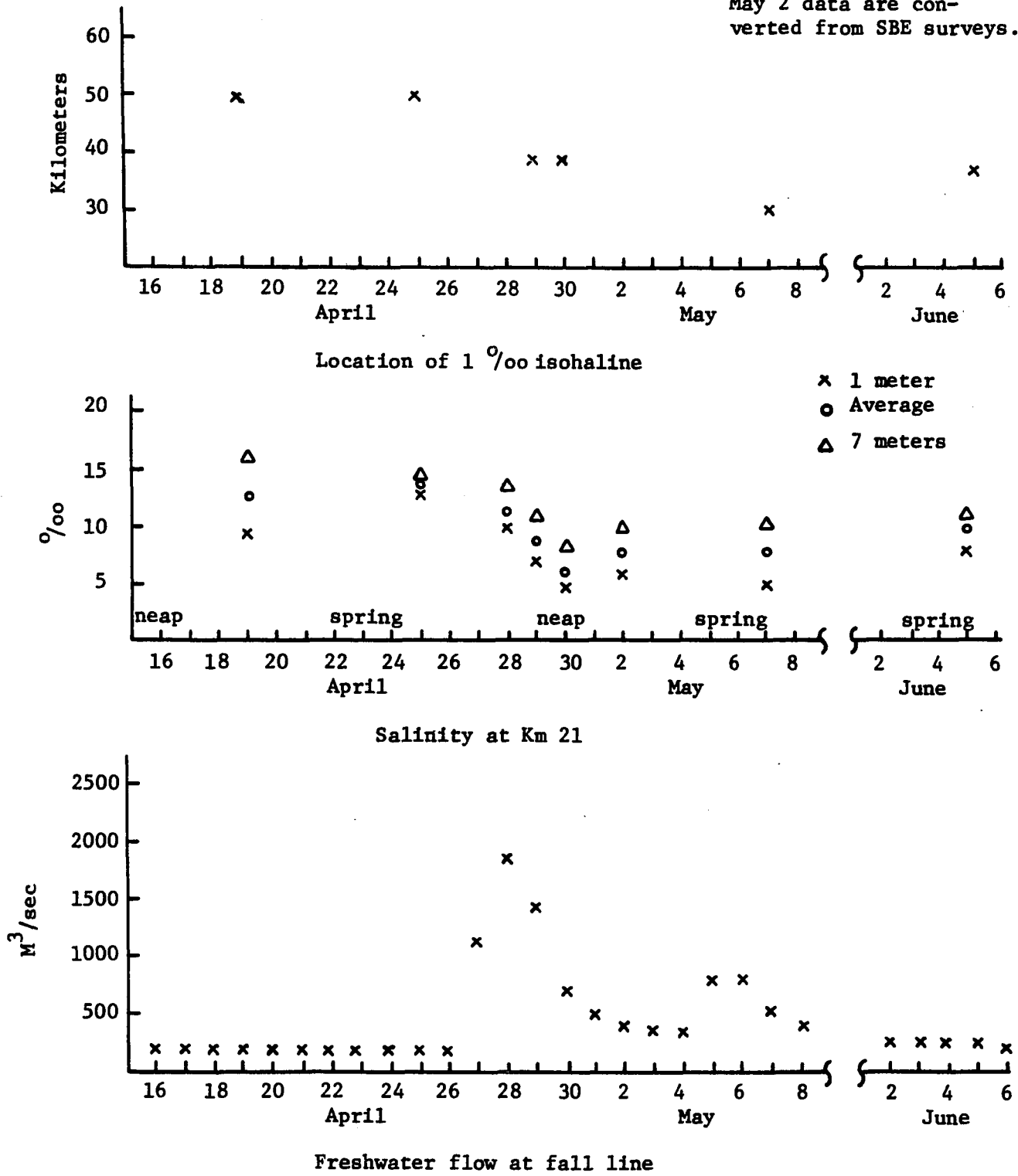


Figure 2-5. Estuarine Behavior Following April 1978 Storm.

CHAPTER III.

GOVERNING EQUATIONS AND NUMERICAL METHODS

A. Governing Equations

The hydrodynamic and salinity structures of an estuary may be mathematically described in space and time by means of a set of four equations together with appropriate boundary conditions. Three of the equations represent the conservation of volume, momentum, and salt, and the fourth relates the density of water to salinity. In tensor notation, the equations are:

$$\text{Conservation of Volume} \quad \frac{\partial u_i}{\partial x_i} = 0 \quad (3-1)$$

$$\begin{aligned} \text{Conservation of Momentum} \quad \frac{\partial u_i}{\partial t} + \frac{\partial}{\partial x_j} (u_j u_i) + 2\epsilon_{ijk} \Omega_j u_k = \\ - \frac{1}{\rho} \frac{\partial P}{\partial x_i} - g \delta_{3i} \\ - \frac{\partial}{\partial x_j} \overline{(u_i' u_j')} + \nu \frac{\partial^2 u_i}{\partial x_j \partial x_j} \\ i = 1, 2, 3 \end{aligned} \quad (3-2)$$

$$\begin{aligned} \text{Conservation of Salt} \quad \frac{\partial s}{\partial t} + \frac{\partial}{\partial x_i} (u_i s) = - \frac{\partial}{\partial x_i} \overline{(u_i' s')} \\ + D \frac{\partial^2 s}{\partial x_i \partial x_i} \end{aligned} \quad (3-3)$$

$$\text{Equation of State} \quad \rho = 1. + \alpha s \quad (3-4)$$

where

x_i = distance coordinate

t = time

u_i = velocity component

Ω_i = component of angular velocity of the earth

ρ = density

P = pressure

D = molecular diffusion

ν = kinematic viscosity

g = gravitational acceleration

s = salinity

u_i', s' = turbulent fluctuations of velocity and salinity respectively

α = an empirical constant $\approx 7.8 \times 10^{-4}$

A complete, general solution to the system of equations (3-1) - (3-4) does not exist. A number of simplifications and approximations can be made, however, to render the system amenable to solution. A primary simplification is to integrate eqs. (3-1) - (3-3) along one or more axes to produce a reduced set of equations. Since parameter variations across estuaries are usually small compared to longitudinal variations, lateral integration is frequently conducted. In some applications, integration along the vertical axis is also performed, but this

operation is inappropriate in a salt intrusion model since the descriptions of the salinity stratification and the vertical velocity profile are lost in the process.

Other simplifications common in the study of estuarine hydrodynamics include the Boussinesq approximation, the neglect of vertical acceleration, molecular viscosity, molecular diffusion and rotation of the earth, and a Fickian analogy to Reynold's stresses. Employing these together with lateral integration, the following differential equations are obtained from eqs. (3-1) - (3-3):

$$(Bu)_x + (Bw)_z = q \quad (3-5)$$

$$(Bu)_t + (Bu^2)_x + (Buw)_z = -\frac{B}{\rho_0} p_x \quad (3-6)$$

$$+ (N_x Bu_x)_x + (N_z Bu_z)_z$$

$$p_z = -\rho g \quad (3-7)$$

$$(BS)_t + (BuS)_x + (BwS)_z = (K_x BS_x)_x \quad (3-8)$$

$$+ (K_z BS_z)_z$$

where

x, z = subscripts denoting partial derivatives
in the longitudinal and vertical
directions, respectively

u, w = longitudinal and vertical velocity
components

p = pressure

ρ = density

S = salinity

B = local width

q = tributary inflow per unit area of x-z plane

N_X, N_Z = horizontal and vertical eddy viscosity

K_X, K_Z = horizontal and vertical eddy diffusivity

Equations (3-4) - (3-8) form the basis of the estuarine model. Integration of eqs. (3-5) - (3-8) with appropriate initial and boundary conditions provides a time-variable, longitudinal-vertical description of current velocity, tidal height, and salt concentration throughout the estuary.

B. The Finite-Difference Solution

Except under simplistic conditions, exact analytical integration of eqs. (3-5) - (3-8) is impossible and an approximate, numerical solution must be attempted. One type of numerical solution, to be utilized in this study, is based upon the substitution of discrete finite differences for continuous derivatives. Solution of the resulting system of finite-difference equations is then possible on a high-speed computer.

1. Vertical Integration - The first step in the finite-difference solution is to divide the estuary into horizontal layers of thickness Δz . Equations (3-5) - (3-8) are then applied to each layer and integrated vertically

across the layer thickness resulting in a set of hybrid differential-finite-difference equations:

$$\frac{\partial \eta}{\partial t} = \frac{1}{B} (w_b B_b - \frac{\partial}{\partial x} u B h + q h) \quad (3-9)$$

$$w_T = \frac{1}{B_T} (w_b B_b - \frac{\partial}{\partial x} u B h + q h) \quad (3-10)$$

$$\begin{aligned} \frac{\partial}{\partial t} u B h + \frac{\partial}{\partial x} u^2 B h + u_T w_T B_T - u_B w_B B_B = & \quad (3-11) \\ & - \frac{B}{\rho_0} \frac{\partial P}{\partial x} + \frac{\partial}{\partial x} N_x B h \frac{\partial u}{\partial x} + \tau_T - \tau_B \end{aligned}$$

$$\begin{aligned} \frac{\partial}{\partial t} s B h + \frac{\partial}{\partial x} s u B h + s_T w_T B_T - s_B w_B B_B & \quad (3-12) \\ = \frac{\partial}{\partial x} K_x B h \frac{\partial s}{\partial x} + (K_z B \frac{\partial s}{\partial z})_T - (K_z B \frac{\partial s}{\partial z})_B \end{aligned}$$

where

η = water surface level

h = layer thickness (= $\Delta z + \eta$ for surface layer)
= Δz otherwise

P = pressure integrated over layer thickness

T, B = subscripts denoting parameter evaluated
at the top or bottom of a layer

τ = shear stress

Equation (3-9) is the conservation of volume or continuity equation applicable at the free surface. $\eta=0$ is defined at the mean surface level and is evaluated positive upwards. Equation (3-10) is the continuity equation applicable below the free surface.

The shear stresses may be further defined as

$$\tau_T = (N_z B \frac{\partial u}{\partial z})_T \quad (3-13)$$

$$\tau_B = (N_z B_1 \frac{\partial u}{\partial z})_B + \rho g n^2 R^{-1/3} B_2 u |u| \quad (3-14)$$

where

n = Manning's friction coefficient

R = hydraulic radius

B_1 = width of fluid interface at bottom of layer

B_2 = width of solid-fluid interface at bottom of layer ($B_1 + B_2 = B$)

2. Stability Criteria and the Semi-Implicit

Method - The next step in the finite-difference solution of eqs. (3-9) - (3-11) is to discretize the remaining continuous variables and to represent the derivatives as ratios of the discretized variables e.g.

$$\frac{\partial \eta}{\partial t} \approx \frac{\eta^{t+\Delta t} - \eta^t}{\Delta t} \quad (3-15)$$

$$\frac{\partial u B h}{\partial x} \approx \frac{(u B h)_{x+\Delta x} - (u B h)_x}{\Delta x} \quad (3-16)$$

where

$\Delta t, \Delta x$ = discrete time and distance intervals

t = superscript indicating evaluation at time t , etc.

x = subscript indicating evaluation at distance x , etc.

Equations (3-15) and (3-16) are generalized finite-difference formulae. A variety of particular finite-difference approximations to derivatives can be formulated and substitution of differing approximations into equations (3-9) - (3-11) may result in widely disparate solutions. The formulation selected should provide a stable numerical solution which closely approximates the true solution to the differential equations. Simultaneously, the formulation must be cost-effective in terms of the computation time required to obtain a solution. Selection and/or formulation of a finite-difference approximation which meets these criteria is of fundamental importance.

Finite difference approximations to partial differential equations may be classified as explicit or implicit. In explicit schemes, all functions of the dependent variable except time derivatives are evaluated at time level t

$$\frac{a^{t+\Delta t} - a^t}{\Delta t} = f(a^t) \quad (3-17)$$

where

a = any dependent variable

The only unknown in eq. (3-17) is $a^{t+\Delta t}$ which may be evaluated directly (or explicitly).

In implicit schemes, one or more functions of the dependent variable, in addition to the time derivative, are evaluated at time level $t+\Delta t$

$$\frac{a^{t+\Delta t} - a^t}{\Delta t} = f(a^t, a^{t+\Delta t}) \quad (3-18)$$

Equation (3-18) cannot be solved directly for $a^{t+\Delta t}$ but must be solved by iterative means or by the solution of a set of simultaneous equations (implicitly).

Explicit schemes are easier to program and execute than implicit schemes but are subject to restrictive stability criteria. The following inequalities must hold for a stable convergent explicit solution of the momentum equation to result:

$$\Delta t \leq \frac{\Delta x}{\sqrt{gH}} \quad (3-19)$$

$$\Delta t \leq \frac{\Delta x^2}{2N_x} \quad (3-20)$$

$$\Delta t \leq \frac{\Delta z^2}{2N_z} \quad (3-21)$$

If the inequalities (3-19) - (3-21) are not satisfied, an incorrect and/or wildly oscillating solution may result.

In practice, the inequality (3-20) is seldom restrictive. The maximum time step is governed by ineq. (3-19) and/or (3-21). This time step governs the number of iterations required to advance the solution of eqs. (3-9) - (3-11) from the beginning to the end of an integration period. For a typical estuary and values of Δx and Δz , $\Delta t \approx 2$ to 5 minutes. Thus, the number of iterations required to complete a long-term integration, e.g. 7 days, is prohibitive.

Implicit schemes are less restricted or entirely free of stability requirements. Thus, larger values of Δt are permissible in implicit schemes than in explicit schemes and fewer iterations are required to complete an integration period. Implicit schemes are more difficult to formulate and program than explicit schemes, but long-term integrations and model simulations are feasible only through employment of implicit methods.

Kwizak and Robert (1971) have shown that the Courant condition (3-19) results from the explicit treatment of the continuity equation (3-9) and the pressure term in the momentum equation (3-11). By treating the continuity equation and the pressure term implicitly, the numerical solution is freed from the Courant constraint and lengthy time steps become feasible.

It is not possible to obtain a solution to the two-dimensional coupled system of eqs. (3-9) - (3-11) with a fully-implicit finite-difference scheme. Instead, eq. (3-11) is solved with all terms except the pressure term expressed explicitly. An implicit expression for the pressure term is obtained through solution of the one-dimensional depth-integrated continuity and momentum equations which can be solved implicitly. These equations are, respectively

$$\frac{\partial \eta}{\partial t} = - \frac{1}{B_s} \frac{\partial}{\partial x} \langle Bu \rangle + \frac{1}{B_s} \langle q \rangle \quad (3-22)$$

$$\frac{\partial}{\partial t} \langle Bu \rangle + \frac{\partial}{\partial x} \langle Bu^2 \rangle = -g\bar{b} (H+\eta) \frac{\partial \eta}{\partial x} \quad (3-23)$$

$$- \frac{\alpha g \bar{b}}{2\rho_0} (H+\eta)^2 \frac{\partial \bar{s}}{\partial x} - \frac{\tau_0}{\rho}$$

where

B_s = surface width

\bar{b} = depth-average width

\bar{s} = depth-average salinity

ρ_0 = depth-average density

H = total depth below mean water surface

$\langle \rangle$ = notation signifying depth integration i.e.

$$\langle a \rangle \equiv \int_{-H}^{\eta} a dz$$

N.B. The use of average width and salinity in the barotropic and baroclinic terms is only approximately correct but allows convenient notation. The computer program integrates these terms exactly.

Equations (3-22) and (3-23) are solved implicitly for $\eta^{t+\Delta t}$ which is used in the pressure term of eq. (3-11). The momentum equation is otherwise solved explicitly for $u^{t+\Delta t}$ and the resulting velocity field is substituted in eq. (3-10) to solve for $w^{t+\Delta t}$. Because $\eta^{t+\Delta t}$ is obtained implicitly while $u^{t+\Delta t}$ is obtained partly implicitly and partly explicitly, this method of integrating the two-dimensional longitudinal-vertical momentum and continuity equations is referred to as a "semi-implicit" method (Hamilton; 1977). Details of the method, as employed in this study, are presented in the next section.

3. Semi-Implicit Integration of the Momentum

Equation - The next step in the integration of eqs. (3-9) - (3-11) and (3-22) - (3-23) is to discretize the time and longitudinal distance variables. A variety of discretizations are possible. The scheme employed herein is based on the staggered grid shown in Figure 3-1. In this schematization, u , K_x , and N_x are evaluated at points set off $\Delta x/2$ from the points at which the remaining variables are evaluated. Similarly, w , K_z , and N_z are evaluated at points set off $\Delta z/2$ from the remaining variables. This arrangement allows advantageous expression of the boundary conditions to be discussed later.

The implicit, discrete form of eq. (3-22) is

$$\frac{\eta_i^{t+\Delta t} - \eta_i^t}{\Delta t} = - \frac{1}{B_s} \left\{ \frac{\langle u\bar{B} \rangle_{i+1}^{t+\Delta t} - \langle u\bar{B} \rangle_i^{t+\Delta t}}{\Delta x} \right\} + \frac{1}{B_s} \langle q_i \rangle \quad (3-24)$$

where

i = longitudinal node index

$$\bar{B}_i = (B_i + B_{i-1})/2$$

Equation (3-24) requires evaluation of the depth-integrated longitudinal transport at time $t+\Delta t$, $\langle u\bar{B} \rangle_i^{t+\Delta t}$. This term is obtained through solution of the discretized depth-integrated momentum equation.

$$\begin{aligned}
\frac{\langle \bar{B}u \rangle_i^{t+\Delta t} - \langle \bar{B}u \rangle_i^t}{\Delta t} + \frac{\langle \bar{B}u^2 \rangle_i^t - \langle \bar{B}u^2 \rangle_{i-1}^t}{\Delta x} = & \quad (3-25) \\
& - g\bar{b}(H+\bar{\eta}_i^t) \frac{(\eta_i - \eta_{i-1})^{t+\Delta t}}{\Delta x} \\
& - \frac{\alpha g \bar{b}}{2\rho_o} (H+\bar{\eta}_i^t)^2 \frac{(\bar{S}_i - \bar{S}_{i-1})^t}{\Delta x} - \frac{\tau_i^t}{\rho_o}
\end{aligned}$$

where

$$\bar{\eta}_i = (\eta_i + \eta_{i-1})/2.$$

Equation (3-25) may be solved for $\langle \bar{B}u \rangle_i^{t+\Delta t}$ as follows

$$\begin{aligned}
\langle \bar{B}u \rangle_i^{t+\Delta t} = \langle \bar{B}u \rangle_i^t - \frac{\Delta t}{\Delta x} \left\{ \overbrace{\left\langle \frac{B_i}{4} (u_{i+1} + u_i)^2 \right\rangle}^{J_i} \right. & \quad (3-26) \\
& \left. - \overbrace{\left\langle \frac{B_{i-1}}{4} (u_i + u_{i-1})^2 \right\rangle}^{J_{i-1}} \right\} \\
& - \frac{\Delta t}{\Delta x} \overbrace{g\bar{b}(H+\bar{\eta}_i^t) (\eta_i - \eta_{i-1})^{t+\Delta t}}^{K_i} \\
& - \frac{\Delta t}{\Delta x} \overbrace{\frac{\alpha g \bar{b}_i}{2\rho_o} (H+\bar{\eta}_i^t)^2 (\bar{S}_i - \bar{S}_{i-1})^t}^{L_i} - \frac{\Delta t \tau_i}{\rho_o} \overbrace{1}^{M_i}
\end{aligned}$$

The capital letters above the brackets denote these expressions in subsequent equations.

Equation (3-26) may be substituted in (3-24) to yield

$$\begin{aligned}
\eta_i^{t+\Delta t} = \eta_i^t - \frac{I}{B_s} \left\{ \overbrace{H_{i+1} - H_i - IJ_{i+1} + IJ_i - L_{i+1}}^{R_i} \right. & \quad (3-27) \\
& \left. + \overbrace{L_i - M_{i+1} + M_i} \right\} + \frac{\Delta t}{B_s} \langle q_i \rangle + \frac{I^2 K_{i+1}}{B_s} \left\{ \eta_{i+1} - \eta_i \right\}^{t+\Delta t} \\
& - \frac{I^2 K_i}{B_s} \left\{ \eta_i - \eta_{i-1} \right\}^{t+\Delta t}
\end{aligned}$$

or

$$\begin{aligned}
 - \frac{I^2 K_i}{B_s} \eta_{i-1}^{t+\Delta t} + \left\{ 1 + \frac{I^2 K_i}{B_s} + \frac{I^2 K_{i+1}}{B_s} \right\} \eta_i^{t+\Delta t} & \quad (3-28) \\
 - \frac{I^2 K_{i+1}}{B_s} \eta_{i+1}^{t+\Delta t} = R_i &
 \end{aligned}$$

Equation (3-28) is in the form of a tri-diagonal system of equations which may be solved by matrix methods for $\eta_i^{t+\Delta t}$. Two boundary conditions are required, one each at the upstream ($x=0$) and downstream ($x=L$) ends of the estuary. The conditions utilized are

$$\frac{\partial \eta}{\partial x} = 0 \quad \text{at } x = 0 \quad (3-29)$$

$$\eta = \eta_0(t) \quad \text{at } x = L$$

where

$\eta_0(t)$ represents the tidal fluctuations at the mouth

Once the values of $\eta_i^{t+\Delta t}$ are available from the solution of eq. (3-28), these values are used in the pressure term of the momentum equation (3-11). In order to conserve volume, values of $\eta_i^{t+\Delta t}$ needed for the $\frac{\partial}{\partial t} uBh$ term are obtained explicitly from a discrete form of the continuity equation (3-9) applied to the surface layer.

$$\begin{aligned}
 \frac{\eta_i^{t+\Delta t} - \eta_i^t}{\Delta t} = - \frac{1}{B_T} \left\{ \frac{\langle \bar{B}u \rangle_{i+1}^t - \langle \bar{B}u \rangle_i^t}{\Delta x} \right\} + \frac{1}{B_T} W_B B_B^t & \\
 + \frac{1}{B_T} q h & \quad (3-30)
 \end{aligned}$$

Equation (3-30) may be solved directly for $\eta_i^{t+\Delta t}$ at each node.

Even with implicit treatment of the pressure term, the diffusion constraint (3-21) still may preclude large time steps. This constraint is circumvented by treating the vertical viscosity terms implicitly as well (Elliott; 1976).

Two discrete forms of eq. (3-11) are necessary, one for the surface layer in which the thickness varies with time and a second for the subsurface layers in which volume is constant. The discrete equation for the surface layer is

$$\begin{aligned}
 & \left\{ \frac{\bar{B}_{i,k} u_{i,k}^{t+\Delta t} (\Delta z + \bar{\eta}_i^{t+\Delta t}) - \bar{B}_{i,k} u_{i,k}^t (\Delta z + \bar{\eta}_i^t)}{\Delta t} \right\} \\
 & \quad T1_{i,k} \\
 & + \frac{1}{\Delta x} \left\{ \frac{B_{i,k} (\Delta z + \eta_i^t) (u_{i+1,k}^t + u_{i,k}^t)^2}{4} \right. \\
 & \quad T1_{i-1,k} \\
 & \left. - \frac{B_{i-1} (\Delta z + \eta_{i-1}^t) (u_{i,k}^t + u_{i-1,k}^t)^2}{4} \right\} \\
 & \quad WUB \\
 & - B_B \frac{(w_{i-1,k} + w_{i,k})^t (u_{i,k} + u_{i,k+1})^t}{2} =
 \end{aligned}$$

$$\begin{aligned}
& \overbrace{-\frac{\bar{B}_{i,k}}{\rho_0} \frac{\partial P}{\partial x}}^{\text{PRESS}} + \frac{1}{\Delta x} \left\{ \overbrace{N_x B_{i,k} (\Delta z + \eta_i^t)}^{T2_{i,k}} \frac{(u_{i+1,k}^t - u_{i,k}^t)}{\Delta x} \right. \\
& \left. - \overbrace{N_x B_{i-1,k} (\Delta z + \eta_{i-1}^t) \frac{(u_{i,k}^t - u_{i-1,k}^t)}{\Delta x}}^{T2_{i-1,k}} \right\} \\
& - \overbrace{\frac{(N_{zi,k} + N_{zi-1,k})}{2} \frac{B_B}{\Delta z} (u_{i,k}^{t+\Delta t} - u_{i,k+1}^{t+\Delta t})}^{\text{VISB}} \\
& - \overbrace{\frac{\tau_B}{\rho}}^{\text{FRIK}}
\end{aligned} \tag{3-31}$$

where

k = vertical node index subscript

(= 1 for surface layer) (see Fig. 3-1)

$$\bar{\eta}_i = (\eta_i + \eta_{i-1})/2$$

$$\bar{B}_{i,k} = (B_{i,k} + B_{i-1,k})/2$$

$$B_B = (B_{i,k} + B_{i-1,k} + B_{i,k+1} + B_{i-1,k+1})/4$$

Note that N_x is considered constant in the derivation (since this term is small) and that the abbreviations of several expressions are noted above the brackets. The formulations of PRESS and FRIK will be detailed subsequently.

The equation for the subsurface layers is identical to eq. (3-31) except that the η_i^t and $\eta_i^{t+\Delta t}$ are everywhere zero and velocity and viscosity terms are added to account for vertical transfer of momentum through the upper boundary of the element

$$\begin{aligned} & \frac{\bar{B}_{i,k} \Delta z}{\Delta t} (u_{i,k}^{t+\Delta t} - u_{i,k}^t) + \frac{(T1_{i,k} - T2_{i-1,k})}{\Delta x} + WUT - WUB \\ & = - \text{PRESS} + \frac{(T2_{i,k} - T2_{i-1,k})}{\Delta x} + \text{VIST} (u_{i,k-1}^{t+\Delta t} - u_{i,k}^{t+\Delta t}) \\ & \quad - \text{VISB} (u_{i,k}^{t+\Delta t} - u_{i,k+1}^{t+\Delta t}) - \text{FRIK} \end{aligned} \quad (3-32)$$

where

$$WUT = B_T \frac{(w_{i-1,k-1} + w_{i,k-1})^t}{2} \frac{(u_{i,k-1} + u_{i-1,k-1})^t}{2}$$

$$B_T = (B_{i,k-1} + B_{i-1,k-1} + B_{i,k} + B_{i-1,k})/4$$

$$\text{VIST} = \frac{(N_{z_{i,k-1}} + N_{z_{i-1,k-1}})}{2} \frac{B_T}{\Delta z}$$

Gathering terms in eq. (3-32) yields

$$\begin{aligned} & - u_{i,k-1}^{t+\Delta t} \frac{\Delta t}{\bar{B}_{i,k} \Delta z} \text{VIST} + u_{i,k}^{t+\Delta t} \left\{ 1 + \frac{\Delta t}{\bar{B}_{i,k} \Delta z} (\text{VIST} - \text{VISB}) \right\} \\ & - u_{i,k+1}^{t+\Delta t} \frac{\Delta t}{\bar{B}_{i,k} \Delta z} \text{VISB} = u_{i,k}^t - \frac{\Delta t}{\bar{B}_{i,k} \Delta z} \frac{(T1_{i,k} - T1_{i-1,k})}{\Delta x} \end{aligned}$$

$$\begin{aligned}
& - \frac{\Delta t}{\bar{B}_{i,k} \Delta z} (WUT - WUB) - \frac{\Delta t}{\bar{B}_{i,k} \Delta z} (\text{PRESS} + \text{FRIK}) \\
& + \frac{\Delta t}{\bar{B}_{i,k} \Delta z} \frac{(T2_{i,k} - T2_{i-1,k})}{\Delta x} \qquad (3-33)
\end{aligned}$$

Equation (3-33) is a generalized representation of a tridiagonal system of equations which must be solved by matrix methods for $u_{i,k}^{t+\Delta t}$. The value of k ranges from 1 in the surface layer to N in the bottom layer. Two boundary conditions are necessary in the vertical direction.

$$N_z \frac{\partial u}{\partial z} = 0 \quad \text{at } z = \eta \qquad (3-34)$$

$$w \frac{\partial u}{\partial z} = 0 \quad \text{at } z = -H$$

At this point, the advantage of the vertically staggered grid becomes obvious. N_z and w are set to zero at the surface and bottom, respectively, and the conditions in eq. (3-34) are automatically satisfied.

The complete solution for $u_{i,k}^{t+\Delta t}$ throughout the estuary is a recursive one. At each longitudinal node i , the tridiagonal system (3-33) is solved for $u_{i,k}^{t+\Delta t}$ where k ranges from 1 to N . The index i is then advanced one step and eq. (3-33) is solved again. Two boundary conditions on u_i are required at the head and mouth of the estuary. These conditions are

$$u = U_0 \quad \text{at } x = 0 \quad (3-35)$$

$$\frac{\partial^2 u}{\partial x^2} = 0 \quad \text{at } x = L$$

where

U_0 is a specified upstream velocity.

4. Calculation of the Vertical Velocity - Once the values of $u_{i,k}^{t+\Delta t}$ are known, the vertical velocities, $w_{i,k}^{t+\Delta t}$ are calculated through the discrete form of the continuity equation (3-10)

$$w_{i,k-1}^{t+\Delta t} = \frac{1}{B_{TW}} \left\{ B_{BW} w_{i,k}^{t+\Delta t} - \frac{(\bar{B}_{i,k} \Delta z u_{i,k}^{t+\Delta t} - \bar{B}_{i-1,k} \Delta z u_{i-1,k}^{t+\Delta t})}{\Delta x} + q_i \Delta z \right\} \quad (3-36)$$

where

$$B_{TW} = (B_{i,k-1} + B_{i,k})/2$$

$$B_{BW} = (B_{i,k} + B_{i,k+1})/2$$

Vertical velocities are calculated from the bottom to the surface using the condition that w at the bottom interface is always zero.

5. Evaluation of the Pressure Term - The term PRESS in eq. (3-31) requires discretization and evaluation of $\frac{\partial P}{\partial x}$. From the hydrostatic equation (3-7)

$$p(z) = \rho g(\eta - z) \quad (3-37)$$

where

z = distance from mean water surface (positive upwards)

Thus,

$$\frac{\partial p}{\partial x} = \frac{\partial}{\partial x} \rho g(\eta - z) \quad (3-38)$$

As used in eq. (3-31), however, $\frac{\partial P}{\partial x}$ is the integral over the layer thickness of $\frac{\partial p}{\partial x}$. Thus, for the surface layer,

$$\frac{\partial P}{\partial x} = \int_{-\Delta z}^{\eta} \frac{\partial}{\partial x} \rho g(\eta - z) dz \quad (3-39)$$

Applying Liebnitz' rule, eq. (3-39) may be expressed

$$\frac{\partial P}{\partial x} = \rho g(\eta + \Delta z) \frac{\partial \eta}{\partial x} + \frac{g(\eta + \Delta z)^2}{2} \frac{\partial \rho}{\partial x} \quad (3-40)$$

The discrete form, for the surface layer, of (3-40) is

$$\begin{aligned} \text{PRESS} = & - \bar{B}_{i,1} g(\Delta z + \bar{\eta}_i^t) \left\{ \frac{\eta_i^{t+\Delta t} - \eta_{i-1}^{t+\Delta t}}{\Delta x} \right. \\ & \left. + \frac{(\Delta z + \bar{\eta}_i^t) (\rho_{i,1}^t - \rho_{i-1,1}^t)}{2\rho_0 \Delta x} \right\} \end{aligned} \quad (3-41)$$

Note that the barotropic term is evaluated at $t+\Delta t$. This is consistent with the semi-implicit method. Strictly, the baroclinic term should also be considered at $t+\Delta t$. Computational simplicity is gained by treating this term at time level t , however, and stability was found not to be affected.

Once the pressure gradient is evaluated in the surface layer, the gradient in the subsurface layers may be computed through the relationship

$$\frac{\partial P}{\partial x_{k+1}} = \frac{\partial P}{\partial x_k} + \frac{g\Delta z}{2} \left\{ \frac{\partial \rho_k}{\partial x} + \frac{\partial \rho_{k+1}}{\partial x} \right\} \quad (3-42)$$

6. Evaluation of the Friction Term - The term FRIK in eqs. (3-31) and (3-32) is computed

$$\text{FRIK} = g n^2 R^{-1/3} (\bar{B}_{i,k} - \bar{B}_{i,k+1}) u_{i,k}^t (u_{i,k}^t) \quad (3-43)$$

7. Discretization of the Conservation of Mass Equation - The conservation of mass (or salinity) equation, (3-12), remains to be discretized and integrated. In order to circumvent a stability requirement analogous to ineq. (3-21), namely $\Delta t \leq \Delta z^2 / 2K_z$, the vertical diffusion terms are treated implicitly in a manner similar to the momentum equation (Elliott; 1976). The resulting discretized equation is, for the surface layer,

$$\begin{aligned} & \left\{ B_{i,k} (\Delta z + \eta_i^{t+\Delta t}) S_{i,k}^{t+\Delta t} - B_{i,k} (\Delta z + \eta_i^t) S_{i,k}^t \right\} \\ & + \frac{1}{\Delta x} \left\{ T3_{i,k} - T3_{i-1,k} \right\} - \text{WSB} = -\text{DIFB}(S_{i,k} \\ & - S_{i,k+1})^{t+\Delta t} + \frac{1}{\Delta x} \left\{ T4_{i,k} - T4_{i-1,k} \right\} \quad (3-44) \end{aligned}$$

where

$$\begin{aligned} T3_{i,k} &= u_{i+1,k} \bar{B}_{i,k} (\Delta z + \bar{\eta}_{i+1}) \frac{(S_{i+1,k} + S_{i,k})}{2} \\ \text{WSB} &= B_{BW} w_{i,k} \frac{(S_{i,k} + S_{i,k+1})^t}{2} \end{aligned}$$

$$\text{DIFB} = K_{z_{i,k}} \frac{B_{Bw}}{\Delta z}$$

$$T^4_{i,k} = K_x \bar{B}_{i+1,k} (\Delta z + \eta_{i+1}^t) (S_{i+1,k} - S_{i,k})^t$$

The parameter $\eta_i^{t+\Delta t}$ for use in eq. (3-44) is obtained explicitly from eq. (3-30).

The discretized form of eq. (3-12) for the sub-surface layers is similar to eq. (3-44) except that η is set to zero and terms are needed to express the vertical transport and diffusion of salt through the upper boundary of the layer. The generalized form of the discrete salinity equation is

$$\begin{aligned} & - S_{i,k-1}^{t+\Delta t} \frac{\Delta t}{B_{i,k} \Delta z} \text{DIFT} + S_{i,k}^{t+\Delta t} \left\{ 1 + \frac{\Delta t}{B_{i,k} \Delta z} (\text{DIFT} - \text{DIFB}) \right\} \\ & - S_{i,k+1}^{t+\Delta t} \frac{\Delta t}{B_{i,k} \Delta z} \text{DIFB} = S_{i,k}^t - \frac{\Delta t}{B_{i,k} \Delta z} \frac{(T^3_{i,k} - T^3_{i-1,k})}{\Delta x} \\ & - \frac{\Delta t}{B_{i,k} \Delta z} (\text{WST} - \text{WSB}) + \frac{\Delta t}{B_{i,k} \Delta z} (T^4_{i,k} - T^4_{i-1,k}) \quad (3-45) \end{aligned}$$

where

$$\text{DIFT} = k_{z_{i,k-1}} \frac{B_{Tw}}{\Delta z}$$

$$\text{WST} = B_{Tw} w_{i,k-1} \frac{(S_{i,k-1} + S_{i,k})^t}{2}$$

Equation (3-45) represents a tridiagonal system of equations with k ranging from 1 in the surface layer to N in the bottom layer. The system may be solved by

matrix methods given the vertical boundary conditions.

$$K_z \frac{\partial S}{\partial z} = 0 \quad \text{at } z = \eta \quad (3-46)$$

$$w \frac{\partial S}{\partial z} = 0 \quad \text{at } z = -H$$

The complete solution for $S_{i,k}^{t+\Delta t}$ throughout the estuary is a recursive one. At each longitudinal node i , the tridiagonal system of equations (3-45) is solved for $S_{i,k}^{t+\Delta t}$. The index i is then advanced one step and eq. (3-45) is solved again. Two longitudinal boundary conditions on S are needed. These conditions are

$$\begin{aligned} S &= 0 \quad \text{at } x = 0 \\ S(z) &= S_0(z,t) \quad \text{at } x = L \end{aligned} \quad (3-47)$$

where

$$S_0(z,t) = \text{specified boundary salinity}$$

8. Stability of the Conservation of Mass

Equation - Although the vertical diffusion terms are evaluated implicitly, eq. (3-45) is solved explicitly in the longitudinal direction and is subject to several stability and convergence constraints. Roache (1972) presents these constraints as

$$K_x \leq \frac{\Delta x^2}{2\Delta t} \quad (3-48)$$

$$K_x \geq \frac{u^2 \Delta t}{2} \quad (3-49)$$

$$K_x \geq \frac{u \Delta x}{2} \quad (3-50)$$

The inequality (3-48) arises from the explicit treatment of the longitudinal dispersion term and is seldom restrictive for typical values of Δx and Δt . Inequality (3-49) is due to the explicit treatment of the advection term and is restrictive and stringent; violation of this constraint results in terminal instabilities in the numerical computation. Inequality (3-50) is less restrictive. If the quantity $u \Delta x / K_x$, known as the "cell Reynolds number", is greater than 2, the computation remains stable but oscillations or "wiggles" develop in the solution. Thus, violation of (3-50) causes the solution to the numerical approximation to diverge from the solution to the original differential equation and the inequality should be viewed as a convergence rather than a stability criterion.

If the inequalities (3-48) - (3-50) are obeyed, a stable, convergent solution to the explicit conservation of mass equation will result.

9. Summary - The steps involved in the semi-implicit integration of the two-dimensional conservation of volume, momentum, and mass equations (3-5) - (3-8)

may be summarized as follows:

- a. Solve the one-dimensional continuity equation (3-28) implicitly for surface level, $\eta^{t+\Delta t}$.
- b. Solve the continuity equation applied to the surface layer (3-30) explicitly for a second estimate of surface level, $\eta^{t+\Delta t}$.
- c. Solve the momentum equation (3-33) for horizontal velocity, $u^{t+\Delta t}$. Use the surface level obtained implicitly in the pressure term and the surface level obtained explicitly elsewhere.
- d. Solve the two-dimensional continuity equation (3-36) for the vertical velocity, $w^{t+\Delta t}$.
- e. Solve the conservation of mass equation (3-45) for salinity, $S^{t+\Delta t}$.

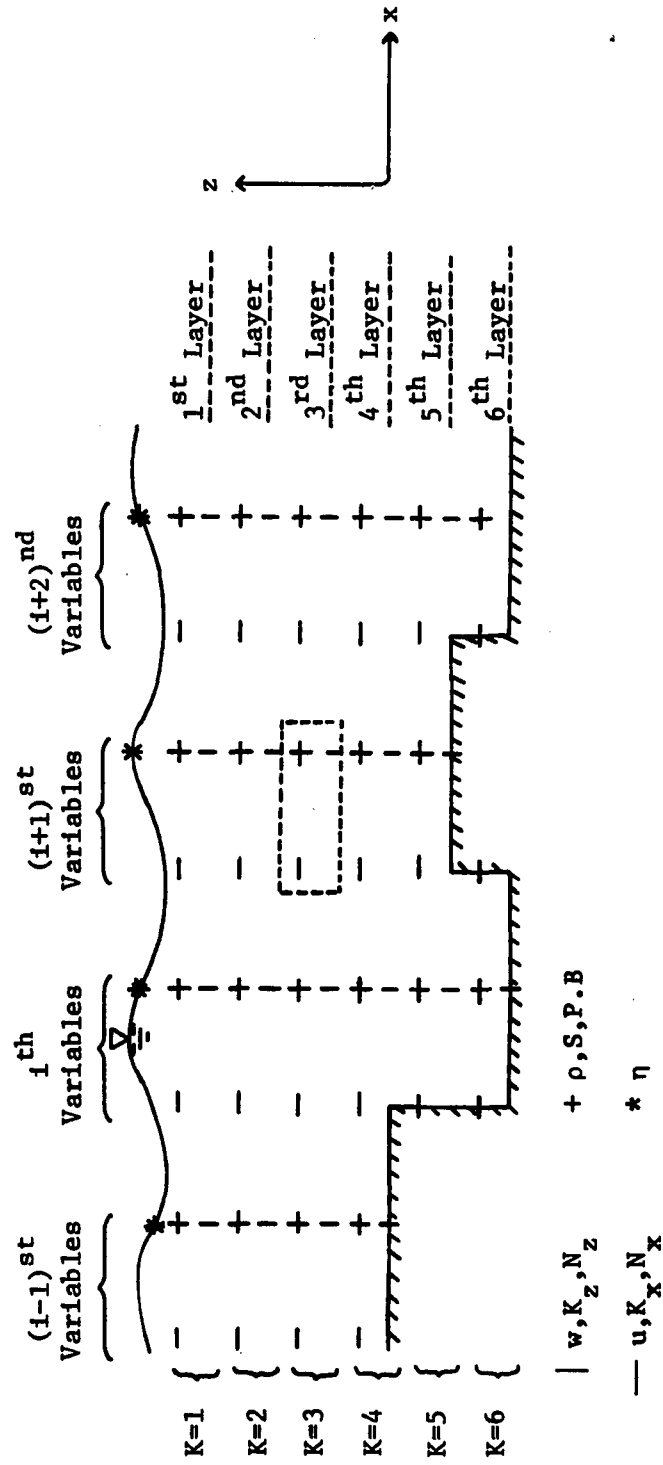


Figure 3-1. Finite Difference Grid.

CHAPTER IV.

MODEL VERIFICATION

The model formulated in the preceding chapter must be verified before it can be used in a predictive manner. The verification confirms both the model formulation and the transformation of the formulae into computer code.

Verification is conducted in three steps:

Comparison of the Model with Analytical Solutions

Comparison of the Model with Laboratory Experiments

Comparison of the Model with Prototypes

A. Comparison with Analytical Solutions

A numerical approximation to a differential equation or set of equations should provide a stable, convergent solution. A stable solution is one which does not oscillate or grow wildly as the number of time steps becomes large. A convergent solution agrees with the solution of the original differential equation.

The problems of stability and convergence may be approached in two ways. The first is to derive and adhere to a set of mathematical constraints (e.g. (3-19) - (3-21)) which insure these properties. Derivation of these constraints is intractable, however, without a

number of simplifying assumptions which restrict the applicability of the guidelines. A second approach, adopted here, is to test the numerical solution empirically by comparison with a known, analytical solution. Stability is confirmed by conducting the numerical integration until a steady or quasi-steady solution is achieved. Convergence is investigated through comparison of the model solution, employing various values of Δx and Δt , with the analytical solution.

The model predictions of tidal range are tested against the solution to the one-dimensional, linearized equations of continuity and motion applied to a frictionless, rectangular channel which is closed at one end. These equations are

$$\frac{\partial \eta}{\partial t} = -h \frac{\partial u}{\partial x} \quad (4-1)$$

$$\frac{\partial u}{\partial t} = -g \frac{\partial \eta}{\partial x} \quad (4-2)$$

The solution to eqs. (4-1) - (4-2), with appropriate boundary conditions, for surface level as a function of location and time is given by Ippen and Harleman (1966) as

$$\eta = 2a \cos(\sigma t) \cos(kx) \quad (4-3)$$

where

η = surface level,

$2a$ = tidal amplitude at the closed end of the channel,

$\sigma = 2\pi/T$; T is the tidal period,
 $k = 2\pi/CoT$, the wave number,
 $C_o = \sqrt{gh}$,
h = channel depth,
t = time,
x = distance from head of channel

An expression for tidal amplitude, A, at any location on the channel, normalized by the amplitude at the mouth, A_o , may be derived from eq. (4-3).

$$\frac{A}{A_o} = \left| \frac{\cos(kx)}{\cos(kl)} \right| \quad (4-4)$$

where l is the length of the channel.

Parameters for use in eqs. (4-3) and (4-4) were selected to roughly correspond to the James River to provide guidelines for the selection of Δx and Δt in the application of the model to the prototype. These parameters are

T = 12 hours l = 140 km
h = 10 meters $A_o = 10$ cm

1. The Effect of Bottom Friction - Explicit finite-difference solutions to the frictionless equations of continuity and motion (eqs. (4-1), (4-2)) are known to be unstable due to the effects of negative numerical viscosity (Harlow and Ansdén; 1970). To test the effects of friction on the two-dimensional semi-implicit model,

the model was run to a quasi-steady state (approximately 10 tidal cycles) with values of Manning's n progressively reduced from 0.20 to 0.0. Values of $\Delta t = 1200$ secs and $\Delta x = 4000$ m were utilized. The results, presented in Fig. 4-1, show a convergence of the model solution towards the frictionless solution as n is decreased. In contrast to explicit methods, the semi-implicit method is stable at $n=0.0$ although the solution does not agree precisely with theory, especially near the nodal point.

This behavior may be understood by examining the implicit solution to (4-1) and (4-2). The linearized equations may be expanded

$$\frac{\eta'_i - \eta_i}{\Delta t} = -h \frac{u'_{i+\frac{1}{2}} - u'_{i-\frac{1}{2}}}{\Delta x} \quad (4-5)$$

$$\frac{u'_i - u_i}{\Delta t} = -g \frac{\eta'_{i+\frac{1}{2}} - \eta'_{i-\frac{1}{2}}}{\Delta x} \quad (4-6)$$

where the prime superscript indicates evaluation at time level $t+\Delta t$.

Substituting eq. (4-6) into eq. (4-5) yields

$$\eta'_i = \eta_i - \frac{h\Delta t}{\Delta x} \left\{ u_{i+\frac{1}{2}} - \frac{g\Delta t}{\Delta x} (\eta'_{i+1} - \eta'_i) - u_{i-\frac{1}{2}} + \frac{g\Delta t}{\Delta x} (\eta'_i - \eta'_{i-1}) \right\} \quad (4-7)$$

Using the following Taylor-series expansions

$$\eta'_i = \eta_i + \Delta t \frac{\partial \eta_i}{\partial t} + \frac{\Delta t^2}{2} \frac{\partial^2 \eta_i}{\partial t^2} + \text{HOT (higher-order terms)}$$

$$\eta_{i+1} = \eta_i + \Delta x \frac{\partial \eta_i}{\partial x} + \frac{\Delta x^2}{2} \frac{\partial^2 \eta_i}{\partial x^2} + \text{HOT}$$

$$\eta_{i-1} = \eta_i - \Delta x \frac{\partial \eta_i}{\partial x} + \frac{\Delta x^2}{2} \frac{\partial^2 \eta_i}{\partial x^2} + \text{HOT} \quad (4-8)$$

$$u_{i+\frac{1}{2}} = u_i + \frac{\Delta x}{2} \frac{\partial u_i}{\partial x} + \frac{\Delta x^2}{4} \frac{\partial^2 u_i}{\partial x^2} + \text{HOT}$$

$$u_{i-\frac{1}{2}} = u_i - \frac{\Delta x}{2} \frac{\partial u_i}{\partial x} + \frac{\Delta x^2}{4} \frac{\partial^2 u_i}{\partial x^2} + \text{HOT}$$

and dropping higher-order terms (HOT), eq. (4-7) becomes

$$\frac{\partial \eta}{\partial t} + \frac{\Delta t}{2} \frac{\partial^2 \eta}{\partial t^2} = -h \frac{\partial u}{\partial x} + gh\Delta t \frac{\partial^2 \eta}{\partial x^2} \quad (4-9)$$

Note $\frac{\partial^2 \eta}{\partial t^2} = \frac{\partial}{\partial t} \frac{\partial \eta}{\partial t} = \frac{\partial}{\partial t} (-h \frac{\partial u}{\partial x}) = -h \frac{\partial}{\partial x} \frac{\partial u}{\partial t} = gh \frac{\partial^2 \eta}{\partial x^2}$

Thus, from (4-9)

$$\frac{\partial \eta}{\partial t} = -h \frac{\partial u}{\partial x} + \frac{gh\Delta t}{2} \frac{\partial^2 \eta}{\partial x^2} \quad (4-10)$$

Equation (4-10), the implicit numerical analog of (4-1), contains a second order term which is proportional to Δt and behaves as viscosity.

Analogous expansion and substitution into eq. (4-6) yields

$$\frac{\partial u}{\partial t} = -g \frac{\partial \eta}{\partial x} + gh \frac{\Delta t}{2} \frac{\partial^2 u}{\partial x^2} \quad (4-11)$$

Again, numerical viscosity proportional to Δt is inherent in the implicit solution to the frictionless equation.

This numerical viscosity is responsible both for the stability of the semi-implicit scheme and the failure of the scheme to reproduce the frictionless solution even with zero bottom friction. As the time step increases and the computations become more efficient, numerical viscosity increases.

2. The Effects of the Time Step - As the time step, Δt , is reduced, the numerical viscosity inherent in the implicit method will decrease and the model solution should approach the theoretical frictionless solution. To verify this behavior in the model, three runs were performed with $\Delta t = 600$ secs, 1200 secs, and 1800 secs. All runs were conducted for 10 tidal cycles. The distance step, Δx , was held constant in all runs at 4000 m and n was set to zero. The magnitudes of the time and distance steps selected for this test were determined by their potential use as parameters in the application of the model to the James River. In contrast to the implicit method, eq. (3-19) gives a maximum time step of $\Delta t = 400$ secs for an explicit integration with $\Delta x = 4000$ m.

The results of the three model runs are compared to the theoretical solution, eq. (4-4), in Fig. 4-2. At the node, the run with the smallest time step agrees

most closely with the theoretical solution, as expected. Near the head, however, the run with $\Delta t = 600$ secs gives the poorest agreement.

The effect of the time step on the phase of the tidal wave is also of interest. In Fig. 4-3, the tidal height at the closed end of the channel is plotted versus time for the tenth tidal cycle. Due to numerical viscosity, the computed solution leads the theoretical solution. The difference in phase between the three computed solutions is small, but the run with $\Delta t = 600$ secs is closest to the theoretical phase.

From Fig. 4-3 it can be noted that at $\Delta t = 600$ secs, the height of the high tide is significantly less than the depression of the low tide. It is this behavior which contributed to the failure of the run to agree more closely with the theoretical amplitude near the head of the channel.

To determine if the model had reached steady state, a second run of 14 cycles duration was conducted with $\Delta t = 600$ secs. The oscillatory behavior in Fig. 4-4 was noted. At small time steps and zero bottom friction, the semi-implicit model is non-convergent although it is stable; the solution does not oscillate wildly or "blow up". This behavior is apparently due to a non-linear wave interaction which is damped by numerical viscosity at larger time steps. The non-linearity may also be

damped by the addition of bottom friction. A fourteen cycle run with $n = .015$ and $\Delta t = 600$ secs proved convergent and stable (Fig. 4-4).

3. The Effects of the Distance Step - Alteration of the distance step, Δx , should have little effect on the predicted solution as the truncation errors involved in the Taylor-series expansions about Δx are higher-order terms compared to the truncation errors in the expansion about Δt which produce the numerical viscosity. To confirm this behavior in the solution, a series of three model runs were made with $\Delta x = 2000, 4000,$ and 8000 m. Again, these values were selected as having potential use in application of the model. All runs were conducted for 10 tidal cycles with $\Delta t = 1200$ secs and $n = 0.0$.

The model predictions of tidal amplitude and phase are compared with the theoretical solution in Figs. 4-5 and 4-6. As expected, varying the distance step, Δx , within reasonable limits has little effect on the computed solution.

B. Comparison with Laboratory Experiments

In the preceding section, it has been shown that the two-dimensional implicit model provides results which agree with the solutions to the one-dimensional, linearized wave equations. Next, it is worthwhile to test the model results in two-dimensions against a known solution. A variety of analytical solutions to the

two-dimensional equations of momentum, volume and salt exist, (e.g. Hansen and Rattray; 1965, Fisher, Ditmars and Ippen; 1972, Hunter; 1975). These solutions are cumbersome, however, require a number of simplifying assumptions, and are primarily steady-state analyses. An alternate approach to verification in two-dimensions is to test the model against laboratory experimental data. The work of Harleman and Ippen (1967) provides such a data base.

The aforementioned authors investigated the behavior of the estuarine salinity intrusion through a series of experiments conducted in a 100 meter long flume. Freshwater was input to one end of the flume while the opposite end was connected to a basin of fixed salinity. Tidal oscillations in surface level were generated in the basin. Longitudinal and vertical measures of salinity and horizontal velocity were obtained at several locations in the flume throughout the simulated tidal periods. These data allowed the average salinity and horizontal and vertical velocity fields to be derived.

Numerical model results are tested against Experiment 16. Laboratory parameters for this experiment are listed in Table 4-1. Further details of this and other experiments may be found in Ippen and Harleman (1961) and Harleman and Ippen (1967).

Table 4-1. Laboratory Flume Parameters

Length = 100 meters	Tidal Amplitude = 1.5 cm
Depth = 15.1 cm	Tidal Period = 600 secs
Width = 22.7 cm	Salinity at Mouth = 29.2 ⁰ /oo
Freshwater Flow = 200 cm ³ /sec	

1. Model Parameter Selection - Employment of the numerical model in the simulation of laboratory experiments requires the selection of both analytical and numerical parameters. Among these are the viscosity and diffusion terms, the space and time increments, and Manning's n in the bottom friction term.

a) Viscosity and Diffusion Terms - Both functional forms and magnitudes must be assigned to the viscosity and diffusion terms of equations (3-11) and (3-12). The vertical terms are considered first.

The functional form(s) selected must consider the magnitude of turbulent diffusion in homogeneous flow, the decrease in diffusion due to vertical stratification, and the relationship between the diffusivity of mass (eddy diffusivity) and the diffusivity of momentum (eddy viscosity). In addition, the eddy terms should be time-variable in order to provide the most realistic distributions of velocity and salinity (Blumberg; 1975, Hamilton; 1977).

The simplest approach to diffusion in homogeneous flow is to relate turbulent diffusion linearly to

velocity

$$K_o = au \quad (4-12)$$

where

K_o = eddy diffusion in a homogeneous water column

Officer (1976) has shown that the effect of stratification on vertical diffusion can be quantified through the Richardson number. A generalized form of this relationship is

$$K_z = \frac{K_o}{(b+c R_i)^n} \quad (4-13)$$

where

R_i = local Richardson number $\equiv \frac{g}{\rho} \frac{\partial \rho}{\partial z} / \left(\frac{\partial u}{\partial z}\right)^2$

b, c, n = empirical constants

A linear relationship is assumed between eddy diffusivity and eddy viscosity

$$N_z = \gamma K_z \quad (4-14)$$

The empirical constants for the laboratory flume were evaluated through trial and error. Successive model runs were conducted employing different constants until tidal-average eddy diffusivities in the range reported by Harleman and Ippen (1967) were obtained. The constants employed were

$$a = 0.085 \text{ cm}$$

$$b, c, n = 1.0$$

$$\gamma = 1.0$$

Taylor's formula was used to evaluate the longitudinal dispersion due to transverse velocity shear. For an open channel, this formula is

$$K_x, N_x = 20 R u^* \quad (4-15)$$

where

R = channel hydraulic radius

u^* = shear velocity

b) Space and Time Increments - The laboratory flume was divided into thirty longitudinal segments each 3.33 meters in length. Five vertical layers, 3.0 cm thick, were utilized. A time step of 10 seconds or 1/60th of a scale tidal cycle was employed.

c) Bottom Roughness Coefficient - Manning's n for the laboratory flume was obtained by running the model with different values of n until agreement was achieved with the tide ranges reported for Experiment 29. (Ippen and Harleman; 1961). A value of $n = 0.024$ was utilized. Results of the calibration are shown in Fig. 4-7.

2. Results of Flume Simulation - The tidal-average longitudinal and vertical distributions of salinity for the laboratory and the numerical model are shown in Figs. 4-8 and 4-9. The agreement is excellent. The numerical model accurately reproduces the length of the salinity intrusion and the salinity stratification.

Comparison of the tidal-average horizontal and vertical velocities are shown in Figures 4-10 and 4-11. For these parameters, agreement is less ideal although the general circulation characteristics are reproduced. A net two-dimensional flow is developed, but the model circulation is not as strong as that indicated in the lab. To some extent, this disparity is due to the nature of velocity measurements. Due to velocity non-uniformities generated by shear at the channel walls, velocity measurements at the center of a channel over-estimate the lateral-average velocity predicted by the model. Over-estimates of horizontal velocities lead to over-estimates of vertical velocities which are derived from horizontal measurements and the principle of continuity. Thus the model should be expected to predict weaker circulation than indicated by measurements.

The balance of the discrepancy between the laboratory and model circulation patterns may be attributed to incomplete specification of the downstream boundary conditions. Spatial and temporal variations in salinity at the mouth of the flume were unknown. Boundary conditions were adopted by "back fitting" to the tidal average stratification upstream of the mouth. Besides the incomplete specification of salinity, the velocities at the mouth can only be imperfectly represented. The boundary condition $\frac{\partial^2 u}{\partial x^2} = 0$ (eq. 3-35) is necessary for closure, but cannot be proven to be valid.

Of particular interest in the Harleman and Ippen experiments is the cell-like circulation indicated. Net vertical circulation is downward in the lower portion of the salinity intrusion and upward near the head of the intrusion. The model reproduces this circulation except at the mouth. At that point, the model indicates upward circulation; the experiments indicate downward circulation. At this most downstream point, however, both the model predictions and laboratory estimations of circulation are based on extrapolations and, hence, the results of both must be viewed with caution.

C. Comparison with the Prototype

The numerical model has been shown to accurately predict the tidal-average, two-dimensional salinity and velocity fields observed in laboratory experiments conducted under steady conditions in a uniform rectangular channel. The final test of the model is against intra-tidal current and tide data collected in the James River estuary. In several separate runs, the model is tested against observations of salinity in the same estuary.

1. Model Parameter Selection - Employment of the numerical model in a prototype simulation requires the specification of the river geometry, selection of space and time increments, specification of the viscosity and diffusion terms, estimation of the bottom friction factors, and specification of boundary conditions.

a) Space and Time Increments - Space and time increments in a numerical model must be selected to provide a realistic representation of the prototype, subject to the constraints of model stability, accuracy, and computational feasibility. Based upon the numerical experiments detailed earlier in this chapter and upon several preliminary model runs, the following parameter values were selected:

$$\Delta x = 4000 \text{ m}$$

$$\Delta z = 2 \text{ m}$$

$$\Delta t = 1242 \text{ secs (1/36 tidal cycle)}$$

b) Model Geometry - The James River geometry was derived from bathymetry data collected at sixty-six transects between kilometers 21 and 160 by the U. S. Army Corps of Engineers and the Virginia Institute of Marine Science (unpublished data). Inspection of the data showed this portion of the river could be divided into five reaches of roughly uniform cross-section. Model geometry was obtained by averaging, at 2 m depth intervals, the widths of all bathymetry transects within each reach. Deep "holes" which exert little effect on circulation were omitted to save computer time. The resulting model geometry is compared to the estuarine bathymetry in Fig. 4-12.

c) Vertical Viscosity and Diffusion Terms - Proper specification of the functional form and magnitude

of the vertical viscosity and diffusion terms is crucial in two-dimensional modelling. These parameters determine not only the vertical salinity and velocity profiles, but the length of the salinity intrusion as well (Hansen and Rattray; 1965).

As in the laboratory, eqs. (4-13) and (4-14) were utilized to quantify the eddy parameters. Empirical constants were evaluated through trial-and-error fit of the calculated longitudinal and vertical salinity distributions to field data. Best results were obtained with the following relationships

$$K_z = \frac{0.33 u}{1 + 0.5 R_i} \quad (4-15)$$

$$N_z = 5K_z \quad (4-16)$$

In the event the computed diffusivity fell below $0.2 \text{ cm}^2/\text{sec}$, a minimum value, $K_z = 0.2 \text{ cm}^2/\text{sec}$, was specified in order to "smooth" the numerical computations.

Employment of eq. (4-15) produced tidal-average eddy diffusivities in the range $0.3 - 3.0 \text{ cm}^2/\text{sec}$ for typical stratification in the James. These values are comparable to those employed by Blumberg (1975) in his intratidal Potomac River model and by Hansen and Rattray (1968) in their analytical study of the James River estuary. The eddy diffusivities employed herein are smaller, however, than the tidal-average values reported

by Pritchard (1967), 2-10 cm²/sec, for the James River and much smaller than the intratidal values employed by Bowden and Hamilton (1975), 5-150 cm²/sec, and derived from data collected in the Mersey estuary.

d) Longitudinal Dispersion Terms - In the prototype, longitudinal dispersion is primarily the result of shear dispersion due to velocity non-uniformities and other geometric effects. These terms may frequently be neglected as small.

In the model, however, longitudinal dispersion of salt is required due to inequalities (3-49) and (3-50). For typical maximum values of u and the selected increments of Δt and Δx , the value of K_x required to smooth numerical oscillations ($\approx 10^7$ cm²/sec) is far larger than the value of K_x required for numerical stability ($\approx 1.5 \times 10^6$ cm²/sec). The dispersion produced by satisfying (3-50) is large enough to become the dominant process in the longitudinal transport of salt - an unrealistic situation.

It was noted empirically that ineq. (3-50) could be violated provided that salinity gradients were not sharp and that small spatial oscillations were tolerated. The final relation used for longitudinal dispersion of salt was

$$K_x = 10^3 + \frac{u\Delta x}{8} \quad (4-17)$$

Equation (4-17) provided sufficient dispersion to maintain stability and minimize numerical oscillations without dominating the longitudinal transport term.

Longitudinal dispersion in the momentum equation was set to a small constant value, $N_x = 1000 \text{ cm}^2/\text{sec}$.

e) Downstream Boundary Conditions - Specification of downstream boundary conditions in an estuarine model is problematical. During ebb flows, boundary conditions are partially dependent on parameters which are predicted upstream. During flood flows, boundary conditions are determined by influences outside the domain of the model. At all times, boundary conditions must be enforced which provide realism while maintaining the predictive ability of the model.

Simple extrapolation of velocity at the most downstream node (eq. 3-35) was found satisfactory for velocity predictions. The spatial and temporal variation of salinity (eq. 3-47) proved impossible to specify while maintaining both realism and predictive ability, however. The problem was solved by extending the model several segments beyond the region of interest into Hampton Roads (Fig. 2-1). Circulation in Hampton Roads is three-dimensional and no effort was made to represent this area in detail. By extending the model, however, a constant, vertically uniform downstream salinity could be specified. A few segments upstream of the boundary,

the model established intratidal and vertical salinity variations dependent only on internal computations. Thus, within the region of interest, maximum predictability was obtained while only a simple boundary condition was required.

f) Base Flow - Measurements of freshwater flow into the James River above the fall-line are available from a U.S.G.S. gauging station located at Richmond. Two major tributaries to the James, the Appomattox and Chickahominy Rivers are also gauged at their fall-lines. Information on flows into the James from lesser tributaries and from groundwater intrusion is non-existent, however.

A customary practice in estimating non-gauged inflows is to increment the gauged inflows by the ratio of ungauged drainage area to gauged area. Above Richmond, the drainage area of the James is approximately 17500 km². Below Richmond this area (excluding gauged tributaries) is approximately 3300 km² (Seitz; 1971). Thus, by a common "rule of thumb", gauged flows at Richmond could be increased by 20% to account for ungauged flows. This analogy is faulty for two reasons, however. First, the drainage area upstream from Richmond is disparate in topography and well-removed in distance from the downstream drainage area. There is no reason to expect storm patterns and runoff relationships in the Appalachian Mountains to

be identical to those of the coastal plain. Secondly, the groundwater contributions of coastal aquifers cut by the river are ignored. It is known, for example, that the river trenches a water-bearing aquifer in the reach between Richmond and Hopewell (Kms. 120-160). During the 1940's, this aquifer supplied Hopewell with withdrawals as large as $124 \text{ m}^3/\text{sec}$ (Cederstrom; 1945).

The groundwater contribution may be of great importance, especially during periods of low flow, since groundwater levels (and thus groundwater contributions) change on a much longer time scale than surface flows (Linsley, Kohler and Paulhus; 1975).

Model results suggest that significant groundwater flow exists. In preliminary model calibrations against data collected during low-flow periods, salt intruded too far upstream unless a constant base flow was added. No alternate combinations of other model parameters would prevent the intrusion without disrupting another aspect of the predictions. Addition of a constant distributed base flow of $1 \text{ m}^3/\text{sec}/\text{km}$ of river length provided consistent salinity predictions compared to several independent sets of data, however. This distributed flow was used in all model runs and is assumed to represent the combined effects of both groundwater intrusion and ungauged surface runoff.

g) Bottom Friction - Application of the model requires calibration of bottom friction, quantified as Manning's "n". Bottom friction was obtained through repeated model runs conducted with different values of n. Best agreement between the model predictions and the tide ranges published in NOAA tide tables was obtained with $n = 0.022$. Comparison between the predicted and tabulated tide ranges is shown in Fig. 4-13.

2. Intratidal Verification - The intratidal predictive capability of the model was tested against tide and current data collected during August, 1977. Tide and current data were available from the three locations shown in Fig. 4-14. Comparisons of the field data with model predictions are shown in Figs. 4-15 to 4-17 for the stations at Kms. 47, 73, and 112, respectively.

The agreement between predictions and data is most satisfactory. Any apparent under-estimation of current velocities by the model is due to the nature of the measurements; the current measurements are of mid-channel velocity while the model predicts the lateral-average velocity. Due to the shear created by the channel sides and shoals, mid-channel velocities should be greater than lateral-average values.

A genuine discrepancy exists in the difference in phase between the predictions and data. The model generally leads the field data just as it led the analytical

solution (Figs. 4-3 and 4-6). Again, the phase error may be attributed to numerical viscosity inherent in the semi-implicit integration method.

3. Longitudinal Salinity Profiles - As a final verification, the model was tested against longitudinal salinity profiles sampled during different flow conditions in the James River.

An effort was made to select data collected under "steady" conditions. That is, a period in which variations in the freshwater flow during the preceding 14 or more days were small. This ideal is seldom attained, especially during moderate-to-high-flow intervals. Even during constant-flow periods, the river never achieves "steady state" due to wind events, spring-neap tidal cycling, and salinity changes at the downstream boundary. Indeed, the continually varying state of the river necessitates the two-dimensional, time-variable model developed herein. Never-the-less, examination of steady-state performances is the first step in development of a time-dependent model.

In the verifications which follow, no attempt was made to duplicate the vertical structure of the prototype. This vertical structure varies on a time scale of days in response to spring-neap tidal cycling and wind while the longitudinal structure varies on a much longer time scale in response to variations in flow and downstream

salinity. Thus, while the longitudinal profile approaches steady-state during constant-flow intervals, the vertical profile is never at steady-state. Simulation of the vertical salinity structure is left for the transient applications in subsequent chapters.

Five constant-flow periods were selected. During some of the periods, more than one survey was available. The periods, survey dates and flows are as follows.

Period	Survey(s)	Flow at Richmond
July, 1977	July 28 August 10	27 m ³ /sec
August, 1980	August 14 August 22 August 27 (2) September 2	51 m ³ /sec
July, 1974	July 3	118 m ³ /sec
April, 1978	April 19 April 25	181 m ³ /sec
May, 1975	May 22	317 m ³ /sec

Model predictions at slack-before-flood (SBF) and slack-before-ebb (SBE) are compared to the field surveys in Figs. 4-18 to 4-22. Good agreement is achieved throughout the range of flows and the model is seen to accurately represent steady conditions in the river. In subsequent chapters, the model will be employed to simulate spring-neap tidal cycling and transient flow events.

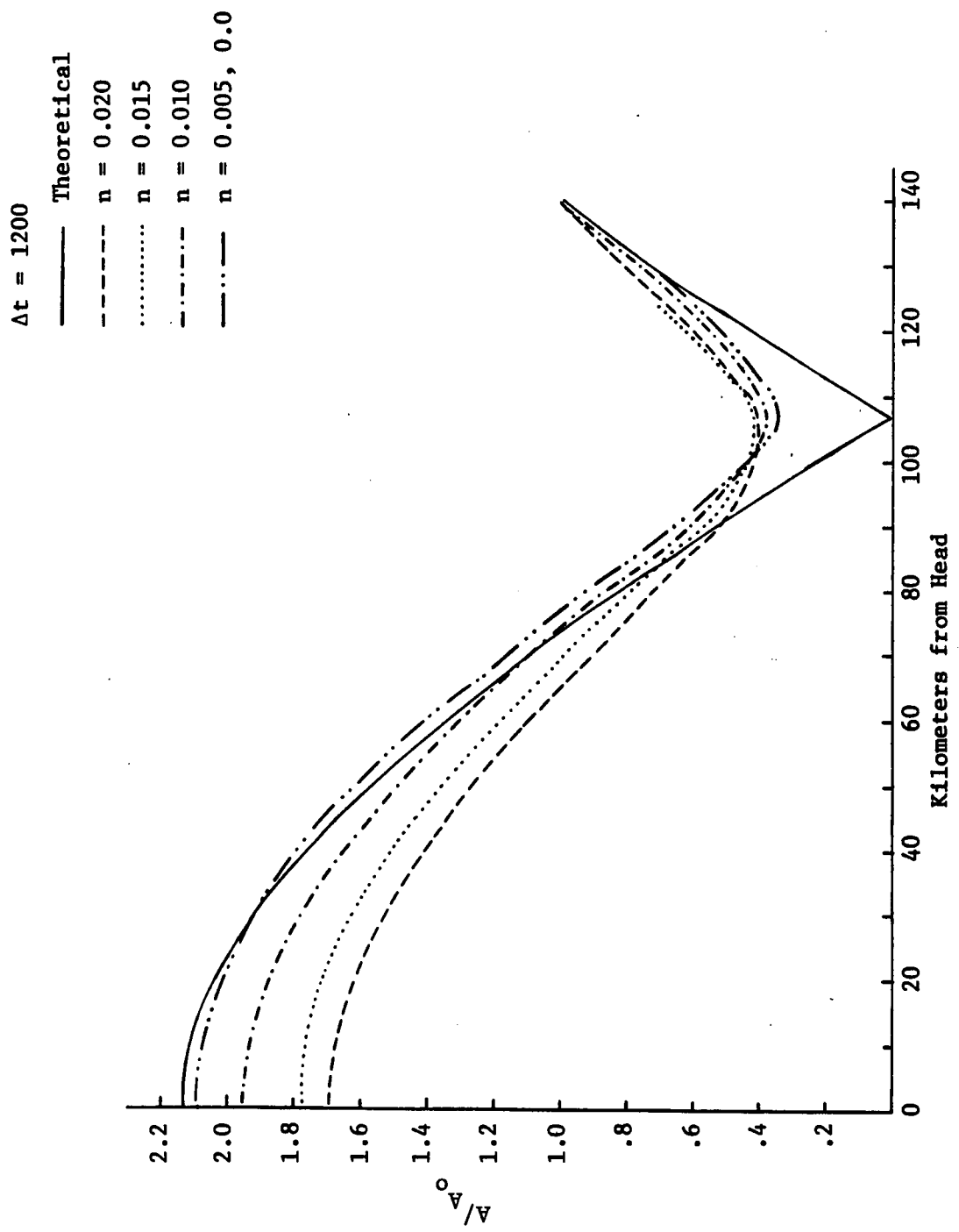


Figure 4-1. Effect of Friction on Model Solution.

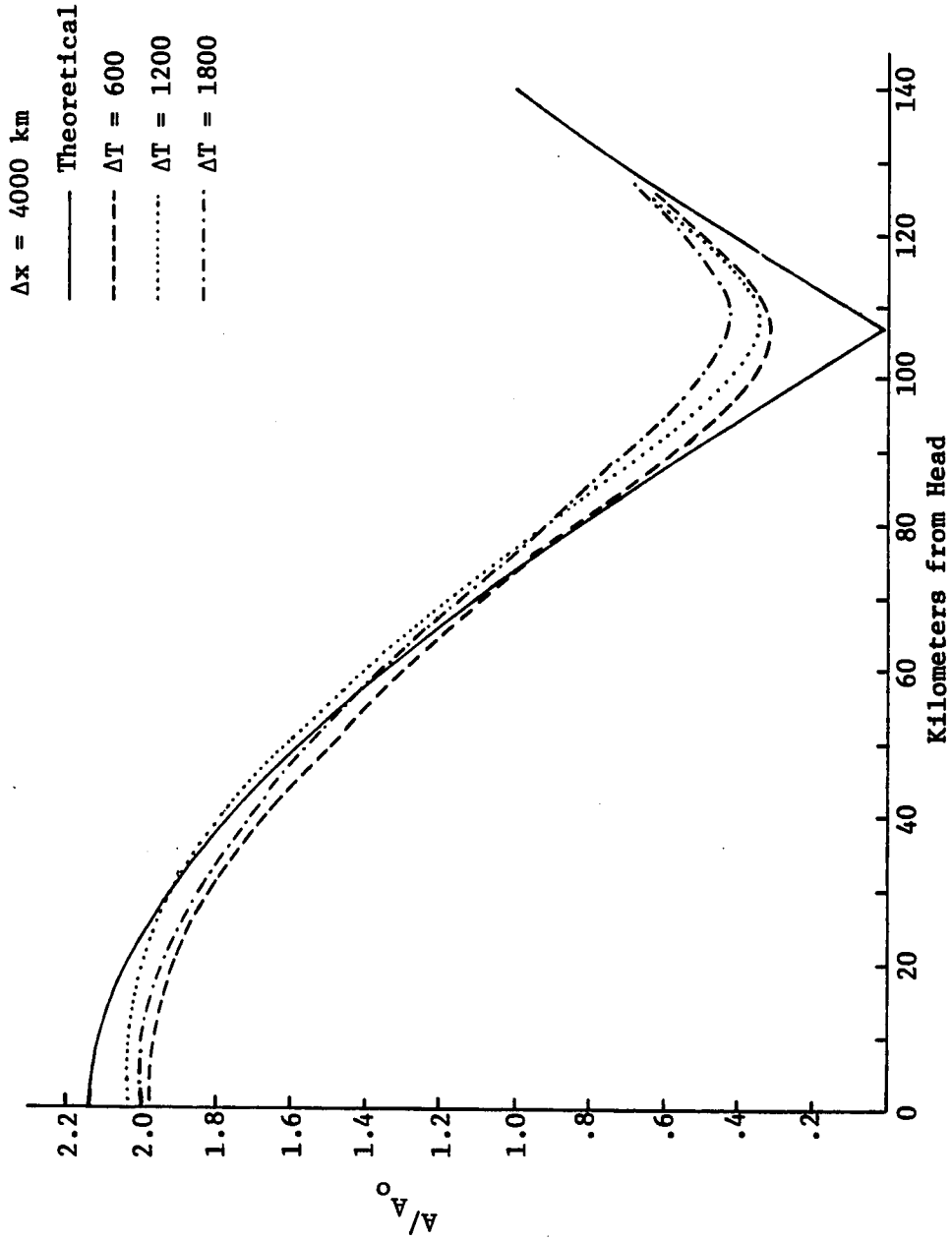


Figure 4-2. Effect of Time Step on Model Solution.

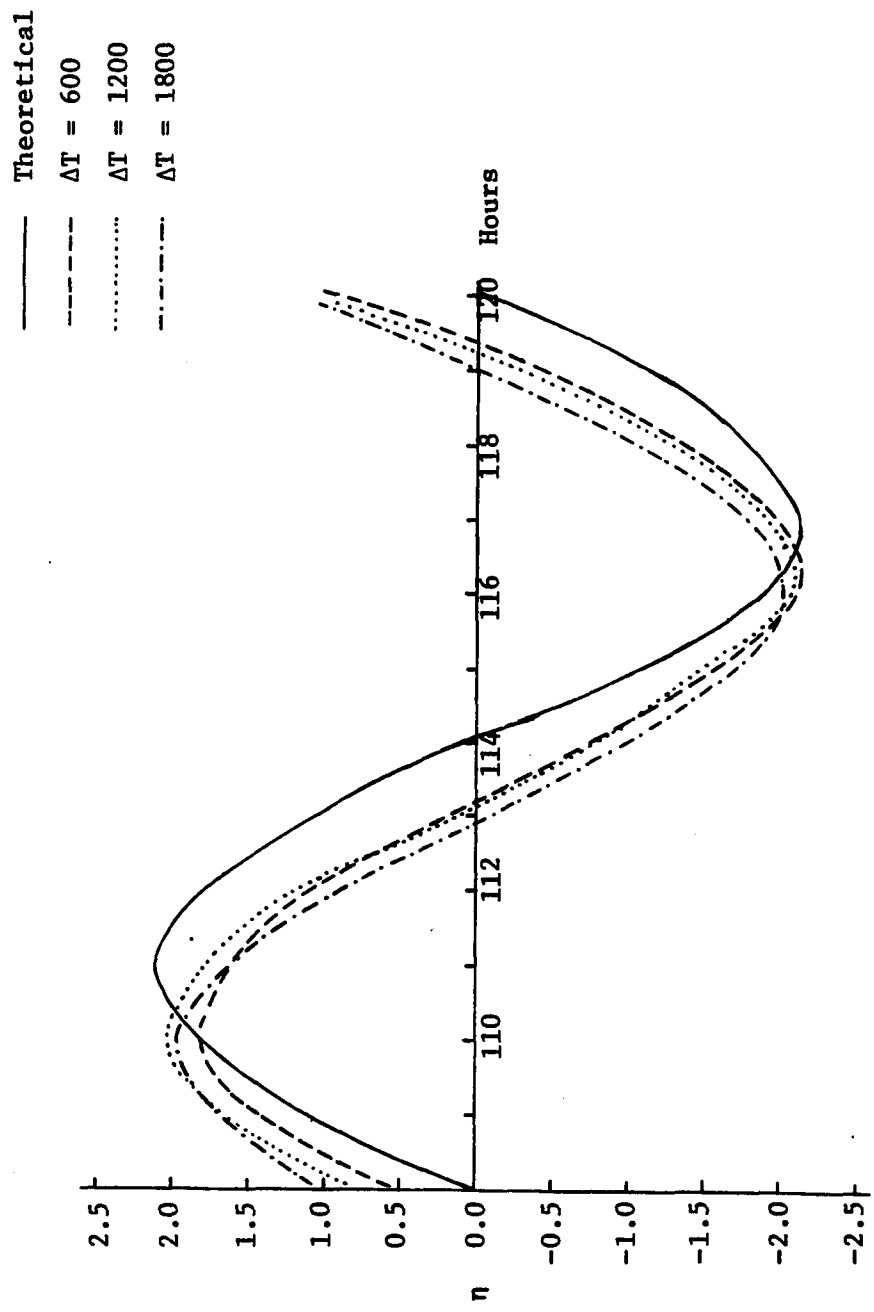


Figure 4-3. Effect of Time Step on Phase of Solution.

$\Delta t = 600$ $\Delta x = 4000$ m

— $\eta = 0.015$

- - - $\eta = 0.0$

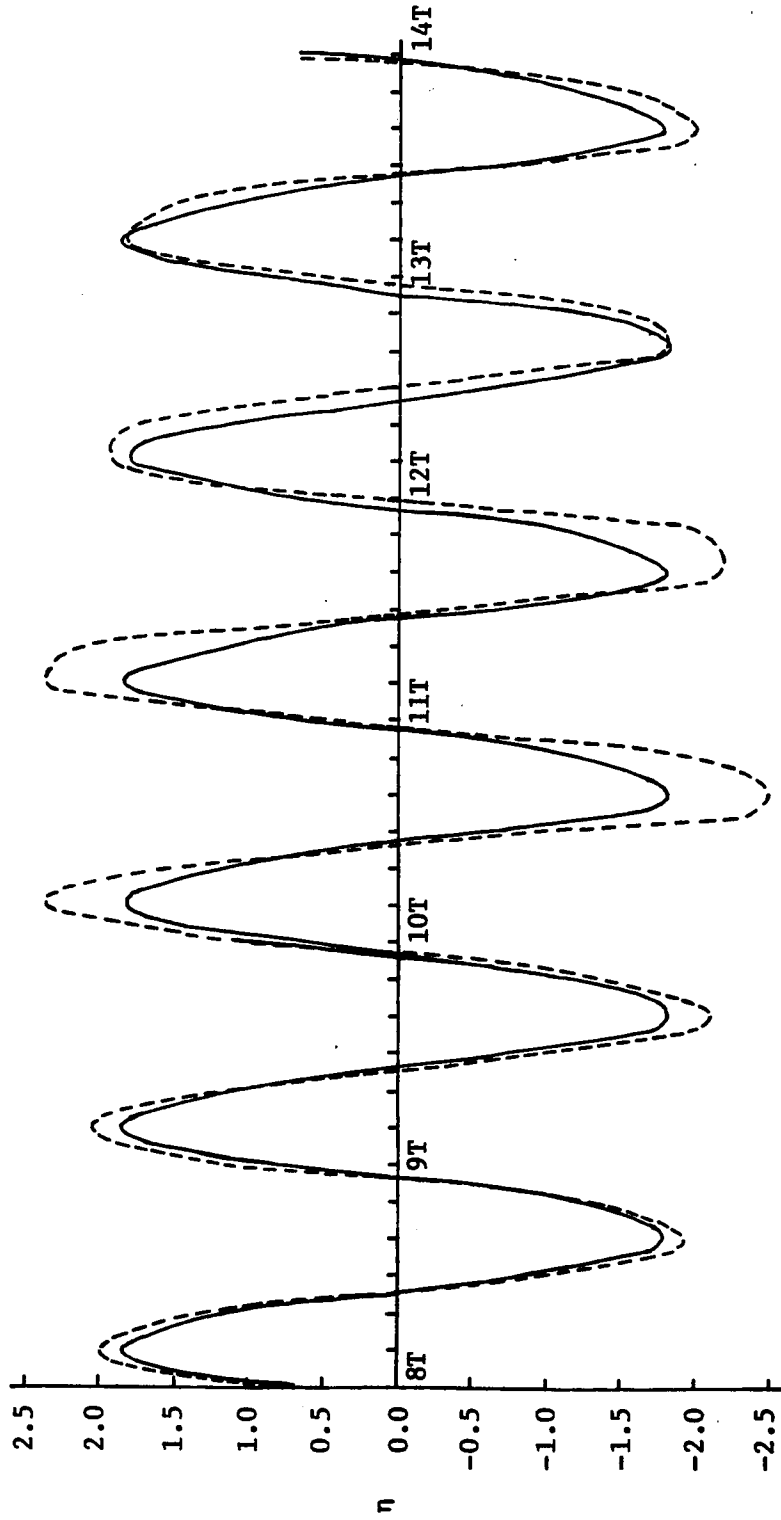


Figure 4-4. Convergence of Solution as a Function of Bottom Friction.

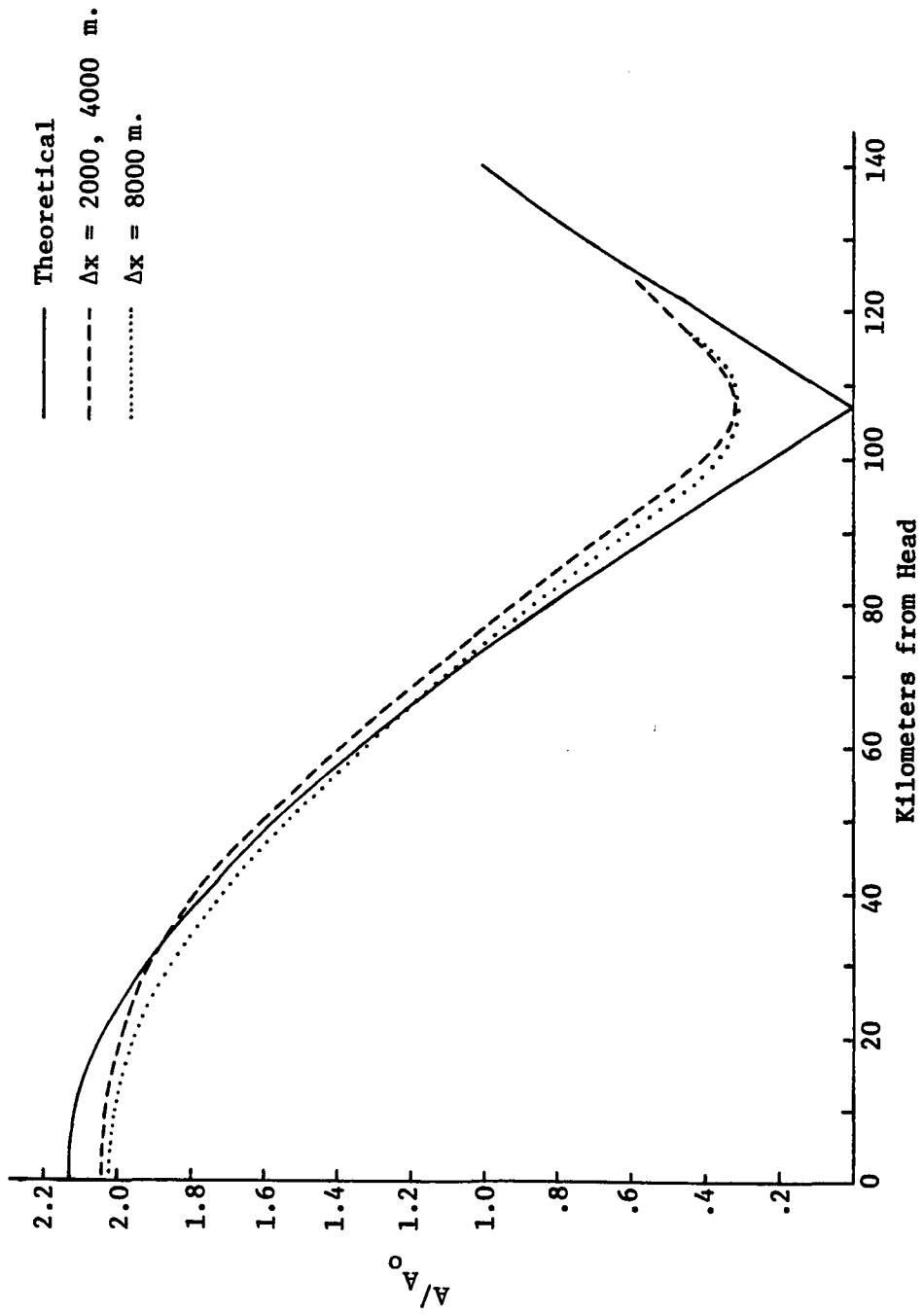


Figure 4-5. Effect of Distance Step on Model Solution.

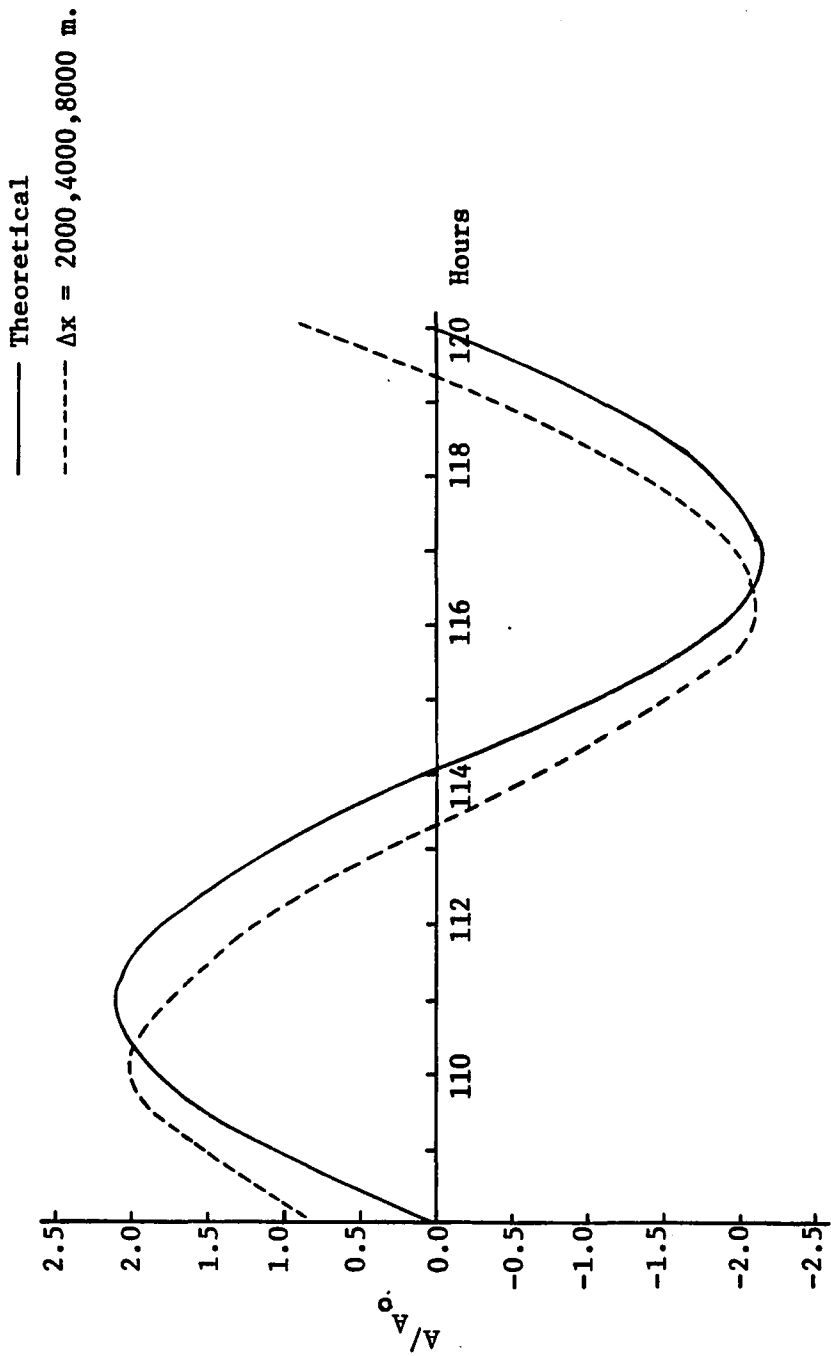


Figure 4-6. Effect of Distance Step on Phase of Model Solution.

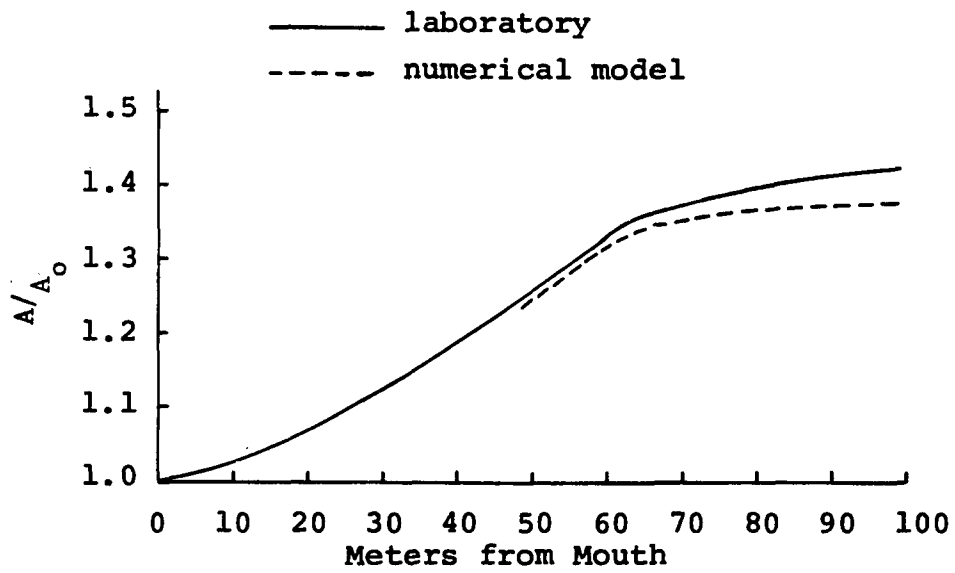


Figure 4-7. Calibration of laboratory bottom roughness.

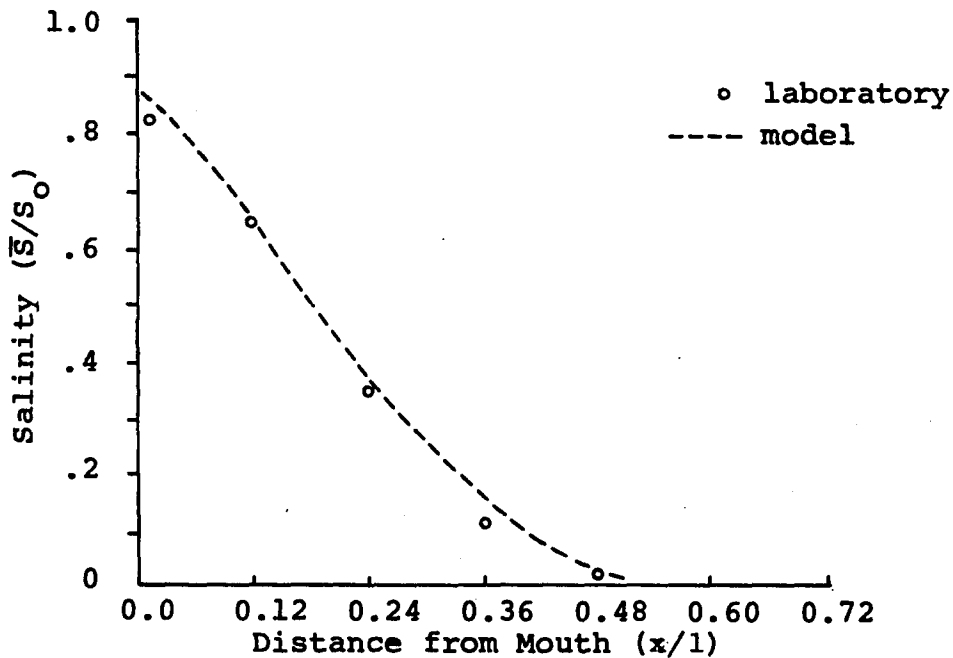


Figure 4-8. Laboratory and model longitudinal salinity distributions.*

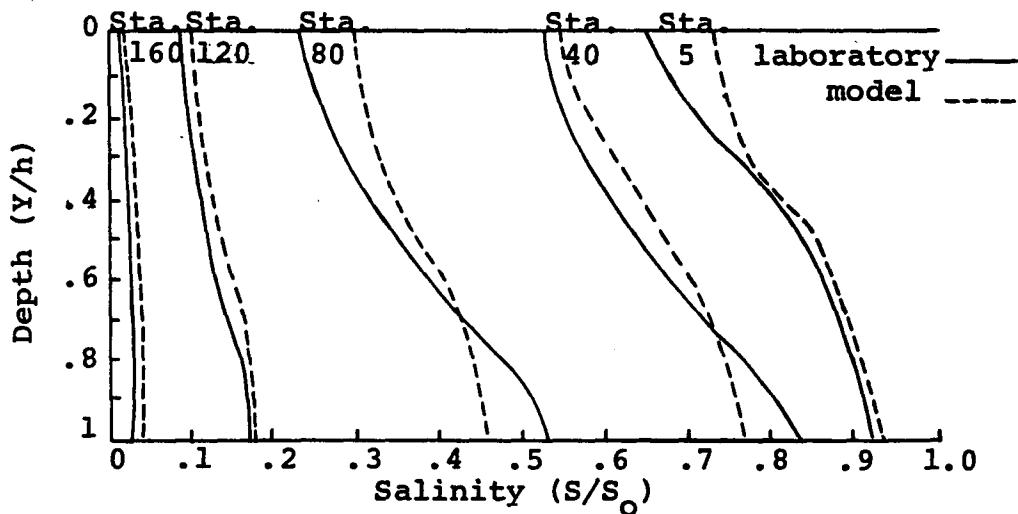


Figure 4-9. Laboratory and model vertical salinity distributions.*

* Laboratory data from Harleman and Ippen (1967). Station numbers correspond to feet from mouth of flume.

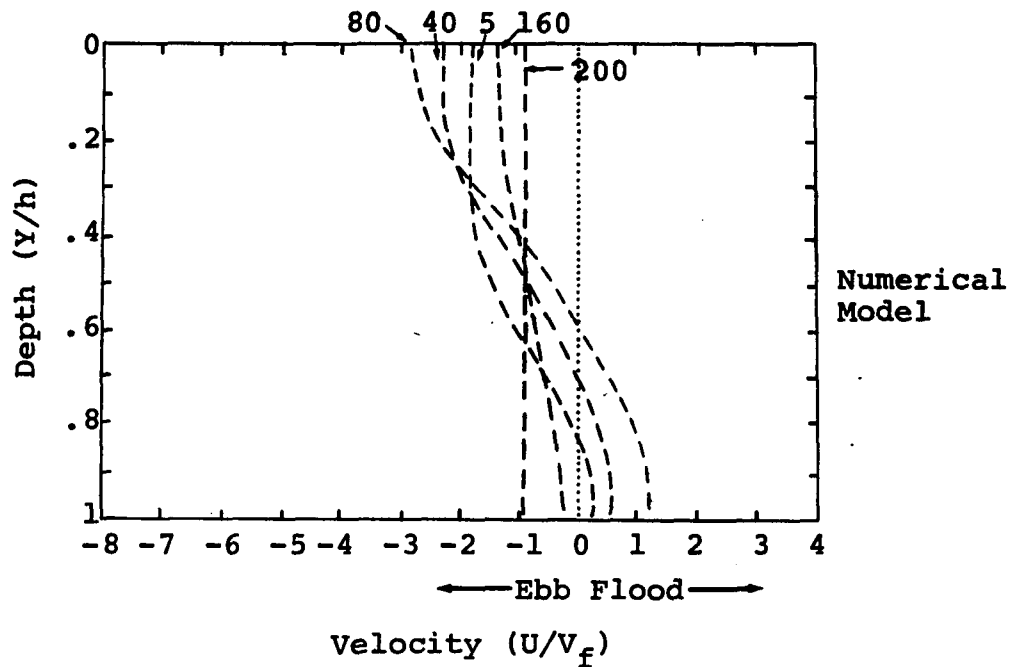
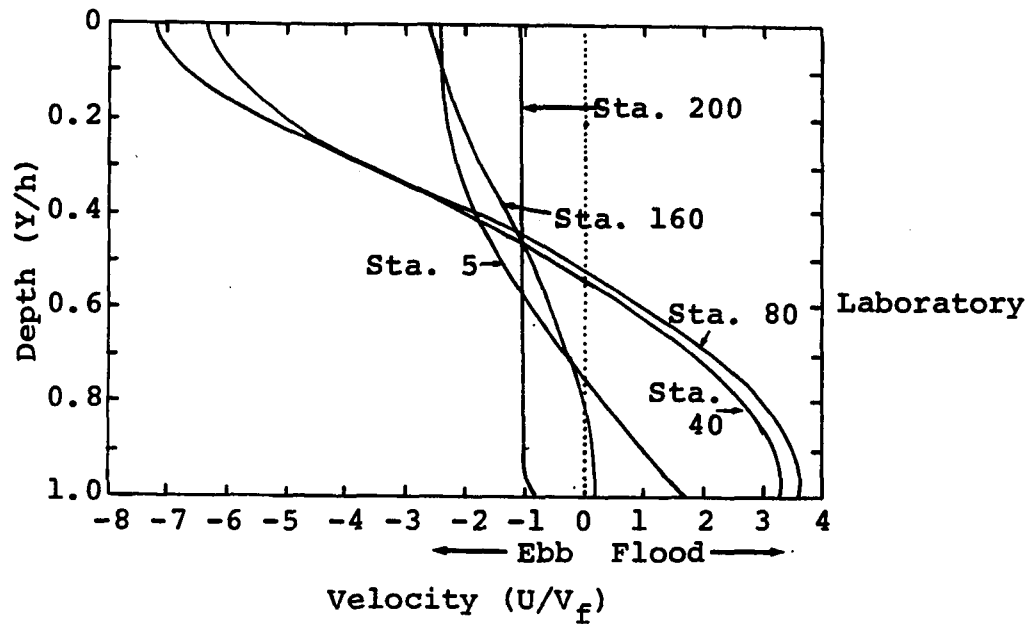


Figure 4-10. Laboratory and flume tidal average horizontal velocities.*

* Laboratory data from Harleman and Ippen (1967). Station numbers correspond to feet from mouth of flume.

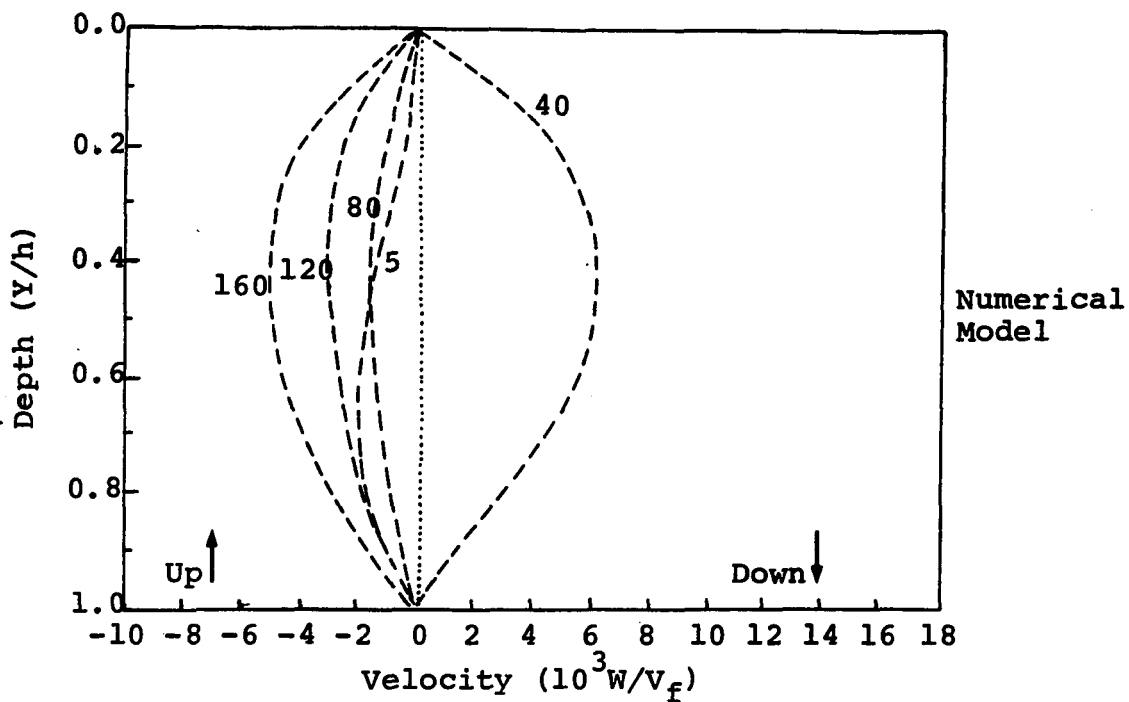
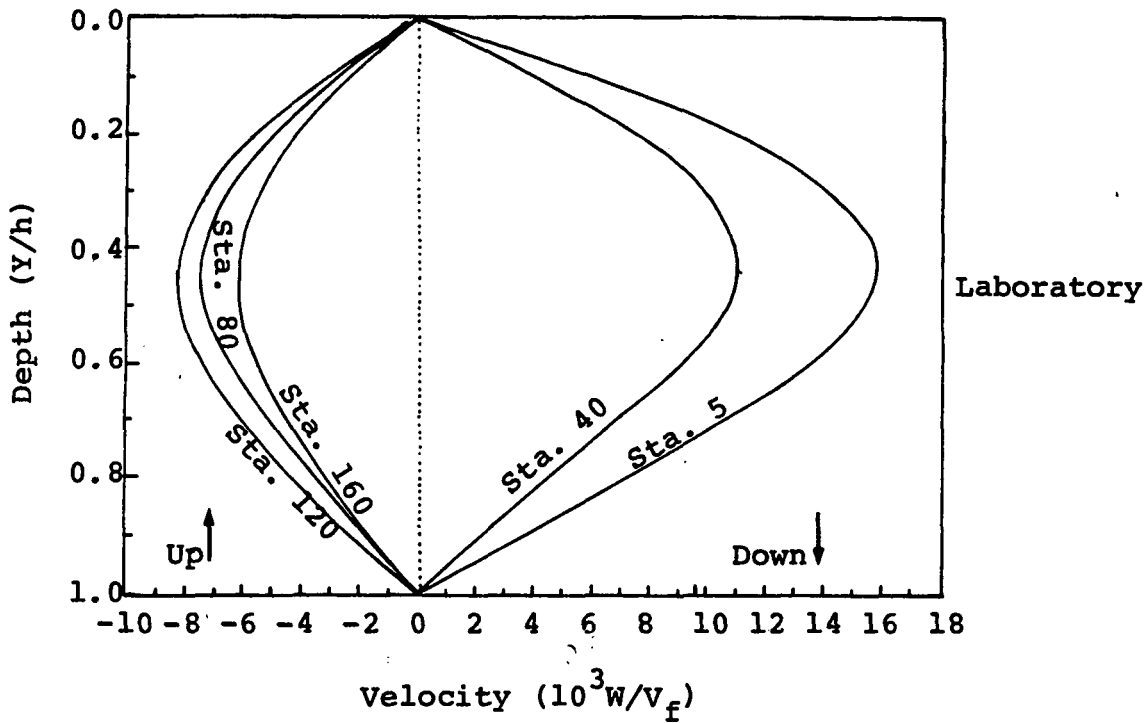


Figure 4-11. Laboratory and flume tidal average Vertical velocities.*

* Laboratory data from Harleman and Ippen (1967). Station numbers correspond to feet from mouth of flume.

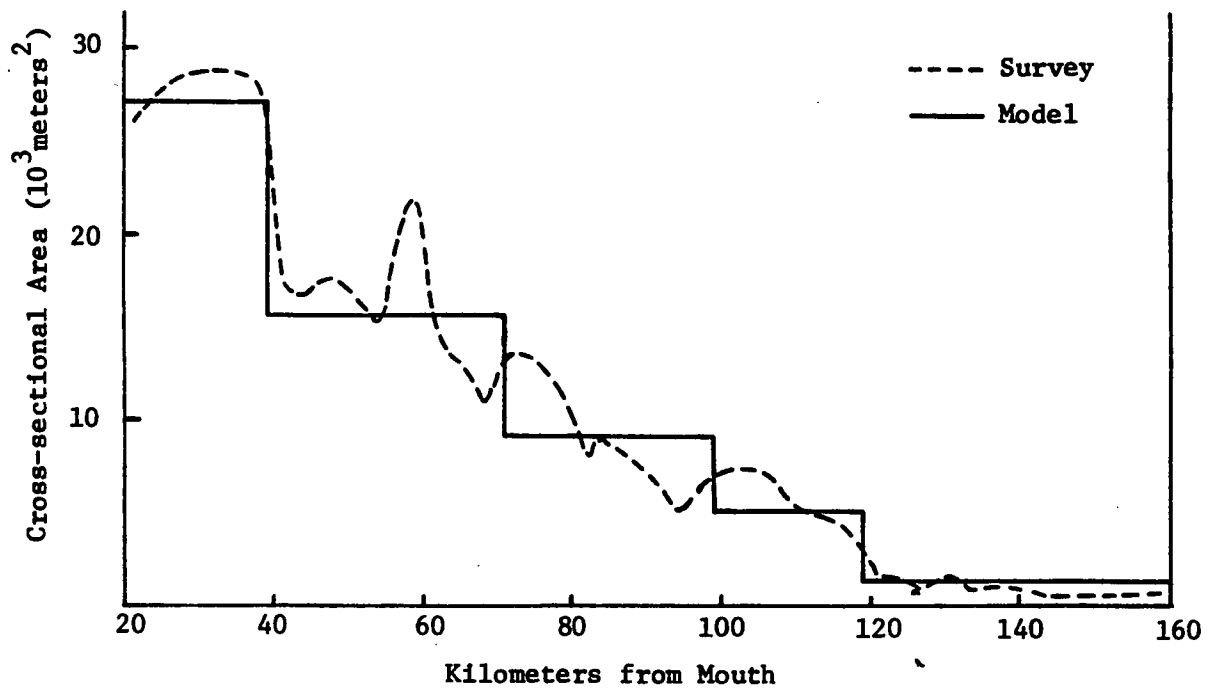
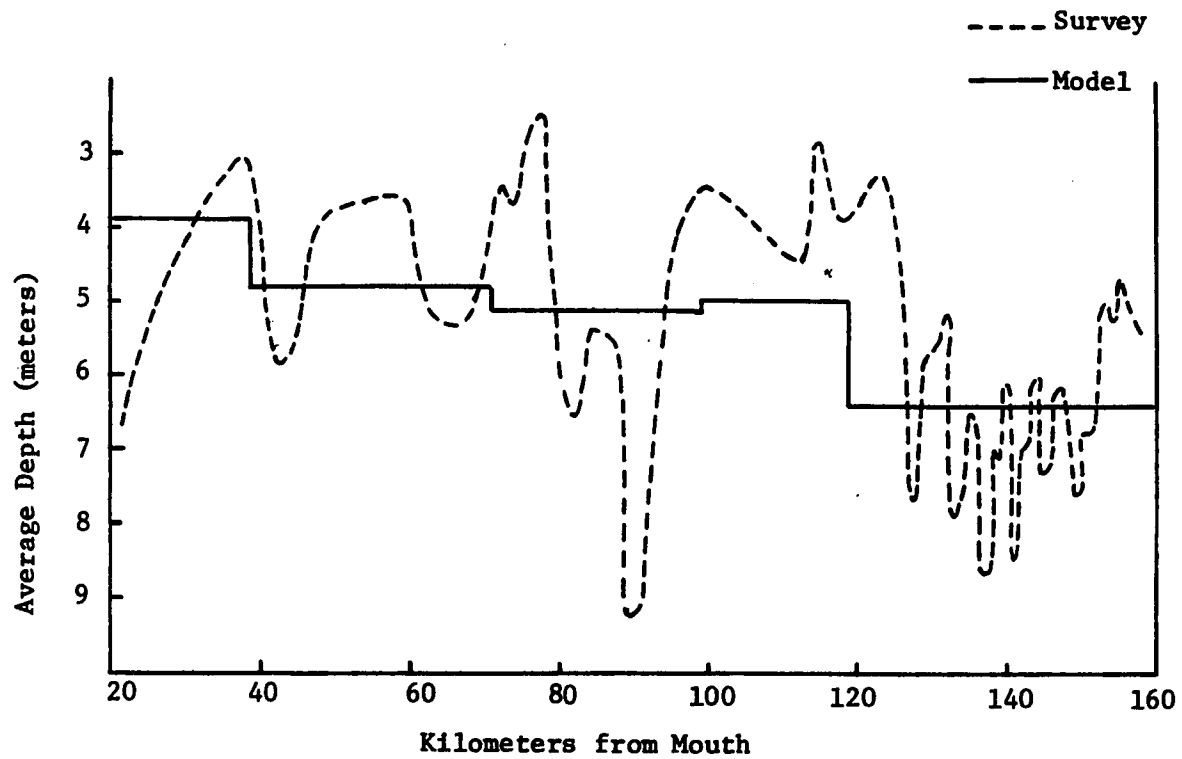


Figure 4-12. Model Geometry.

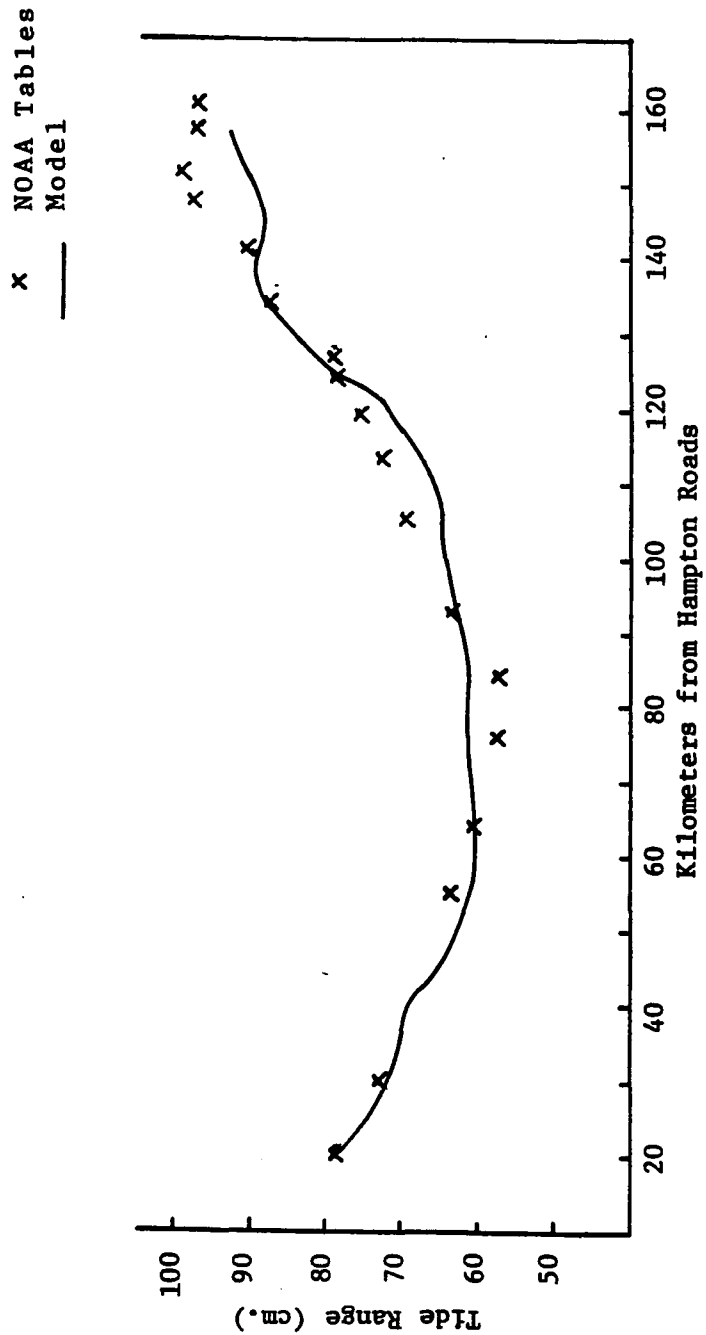


Figure 4-13. Predicted vs. Tabulated James River Tide Range.

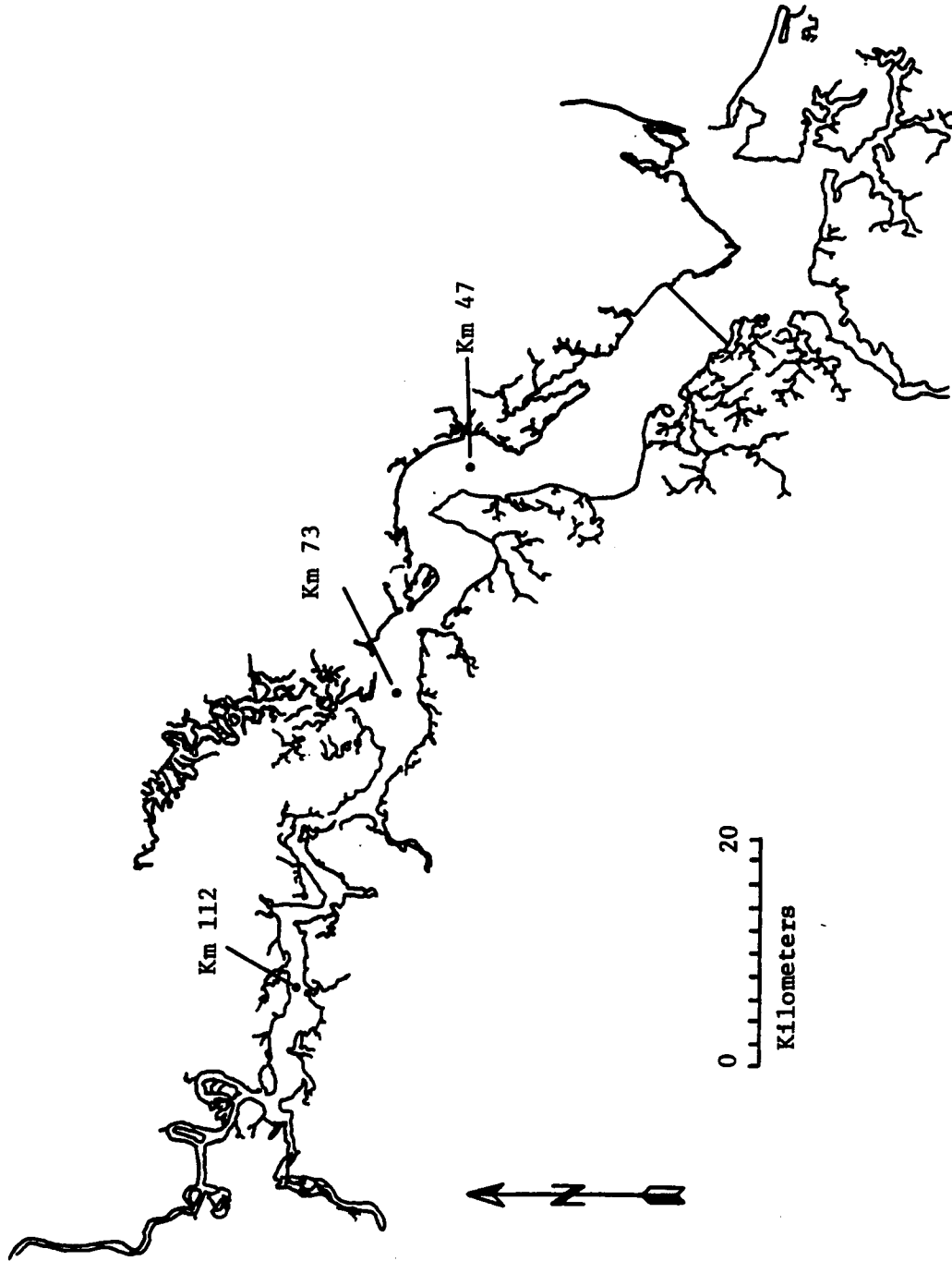


Figure 4-14. James River Tide and Current Stations, August, 1977.

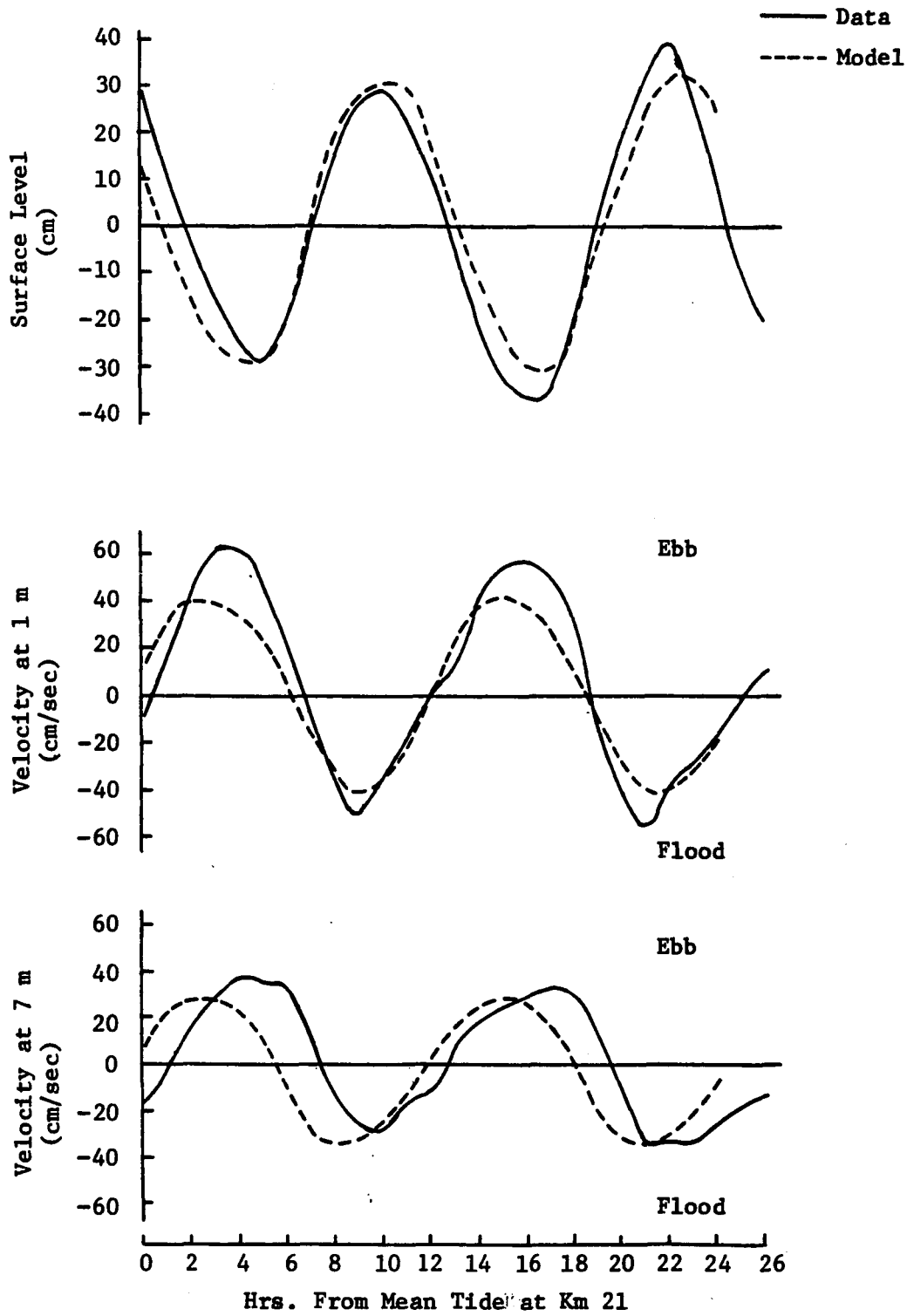


Figure 4-15. Tide and Current at Km. 47.

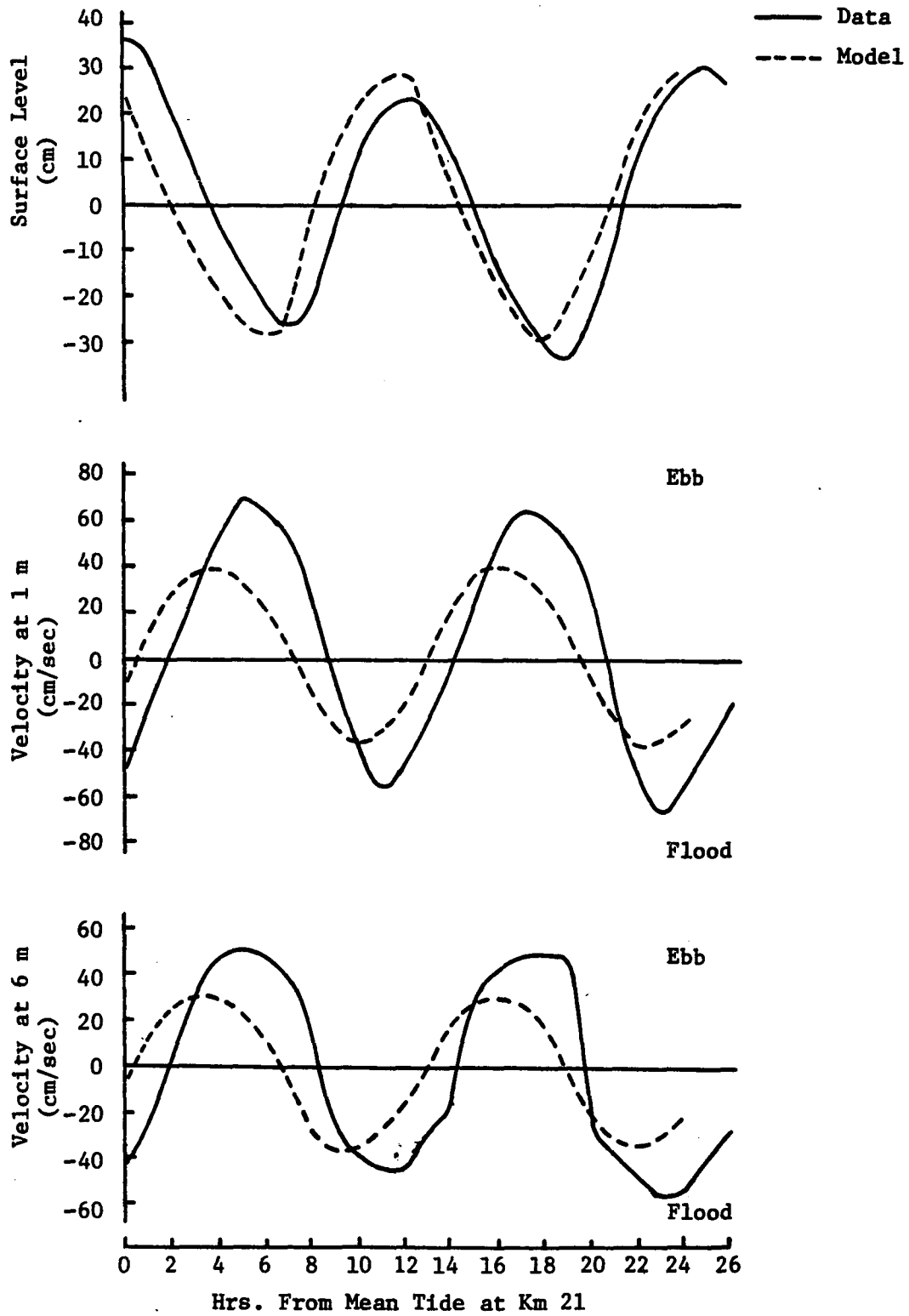


Figure 4-16. Tide and Current at Km. 73.

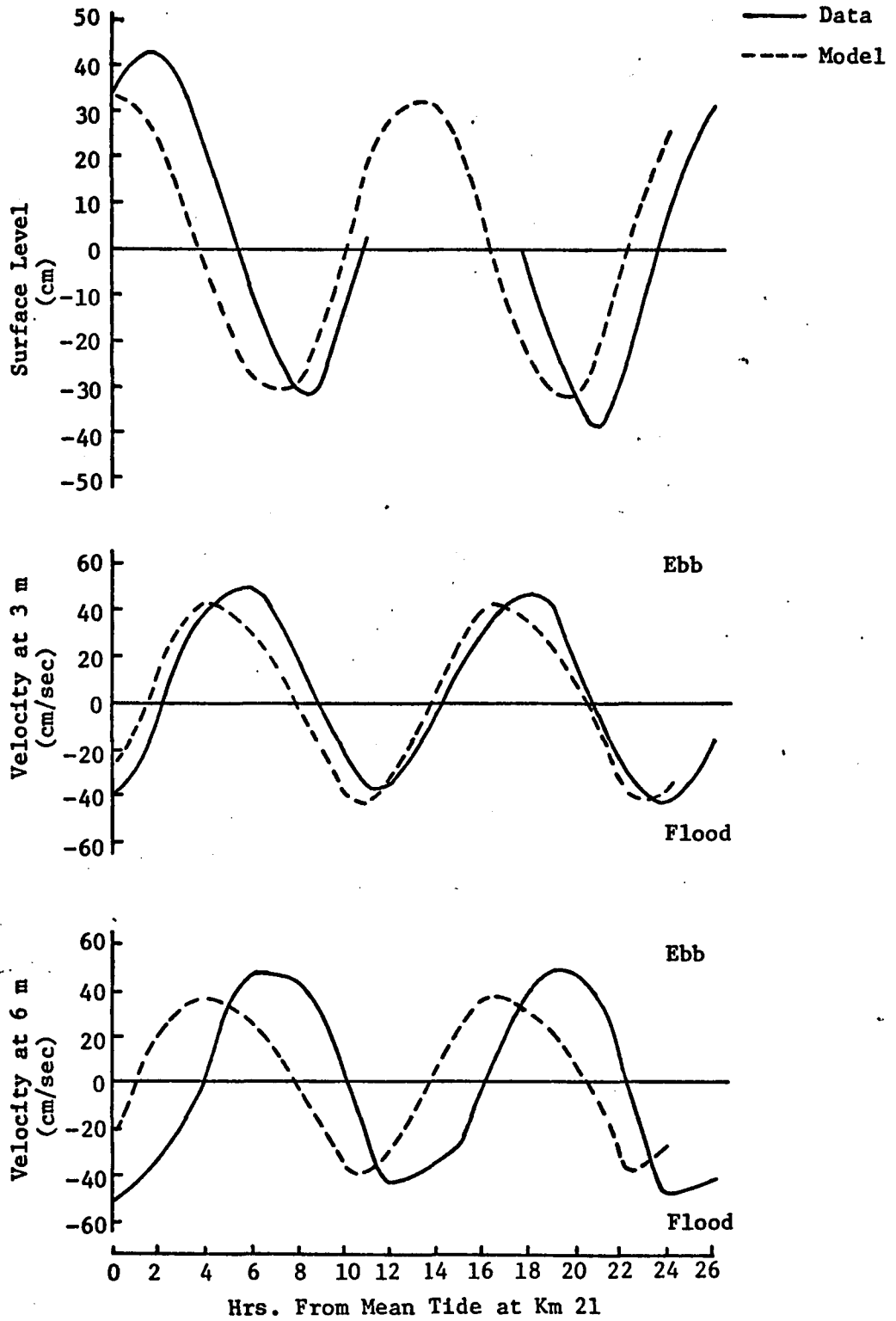


Figure 4-17. Tide and Current at Km. 112.

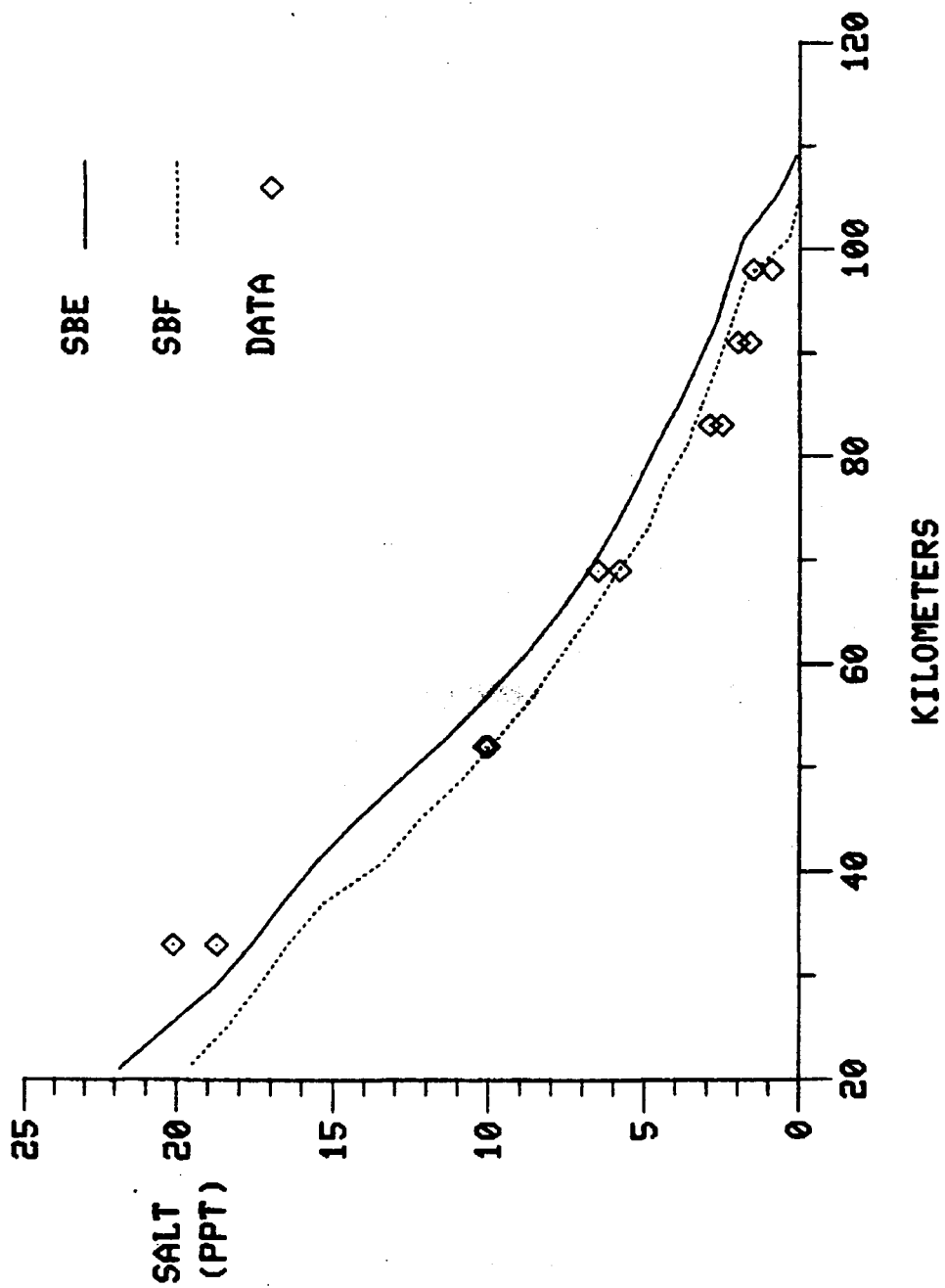


Figure 4-18. Predicted vs. Measured Salinity, July, 1977.

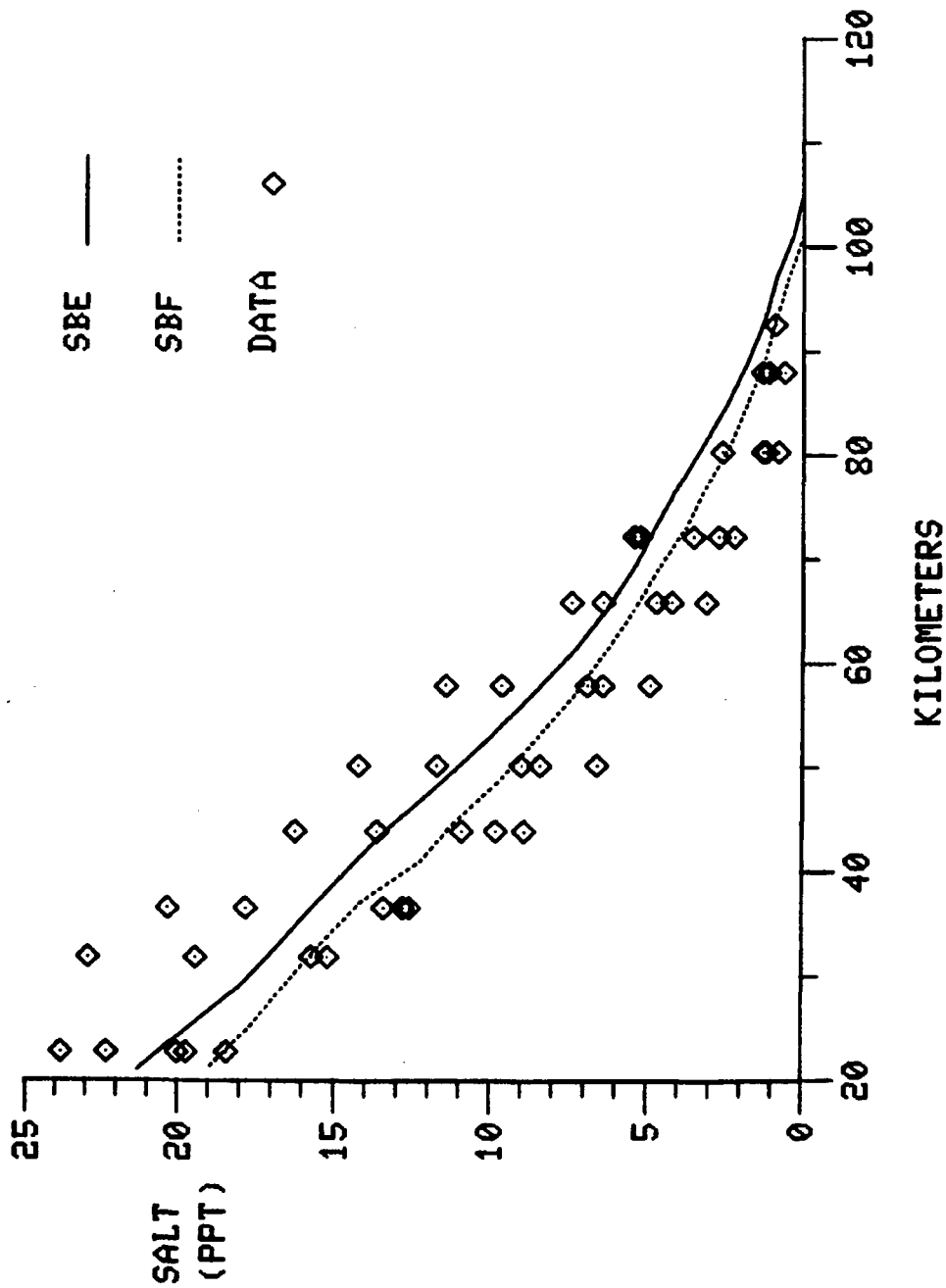


Figure 4-19. Predicted vs. Measured Salinity, August, 1980.

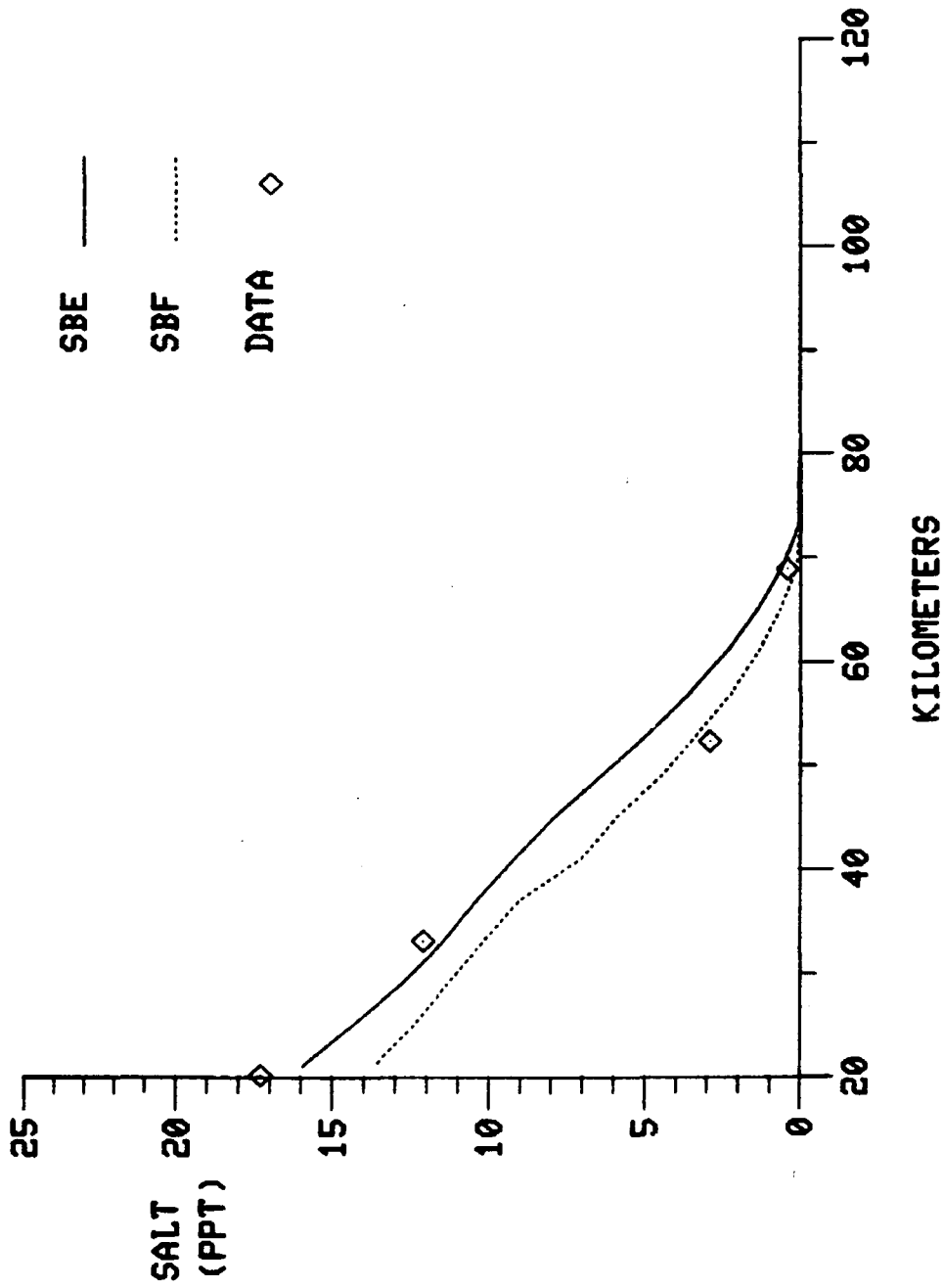


Figure 4-20. Predicted vs. Measured Salinity, July, 1974.

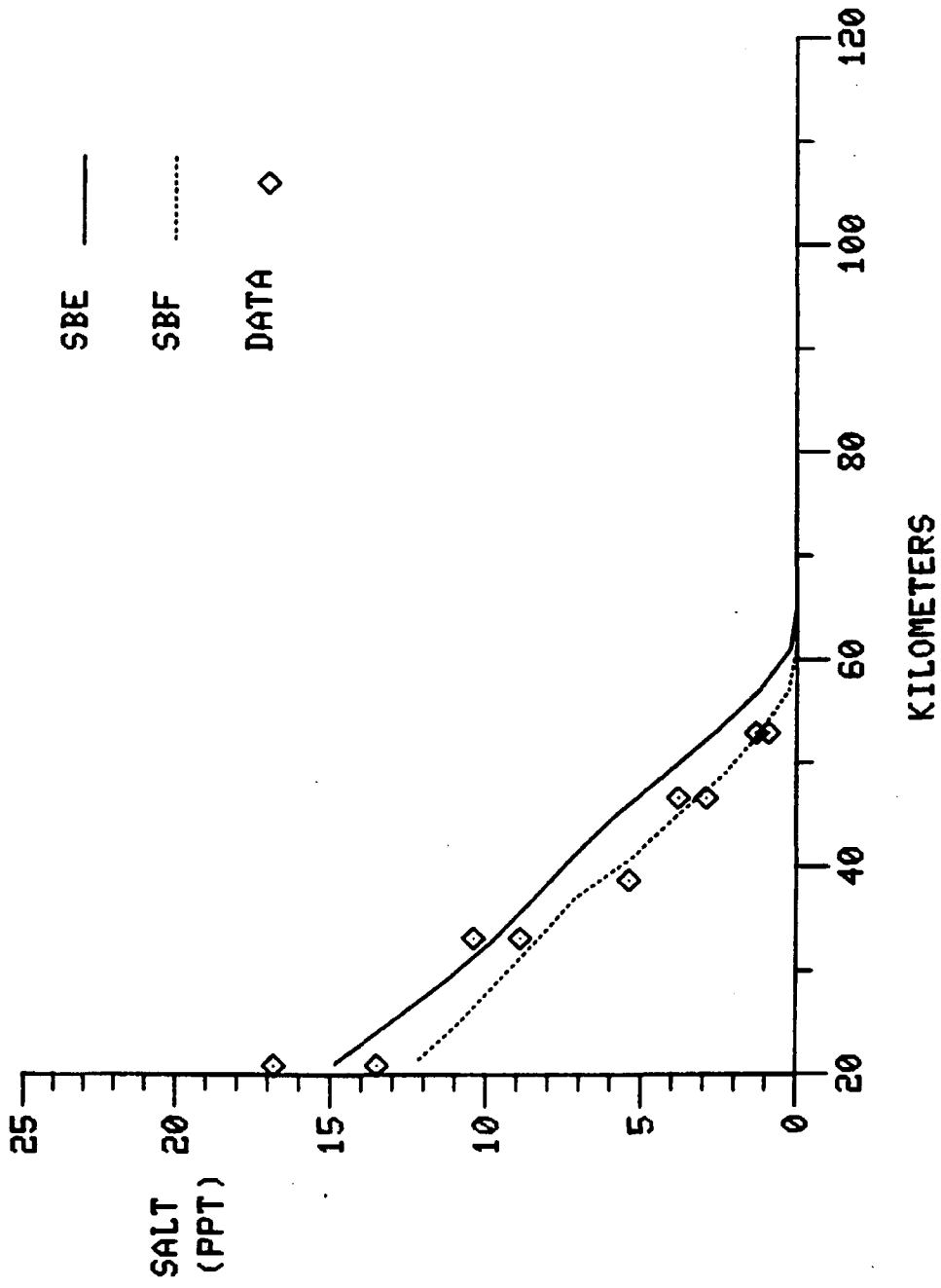


Figure 4-21. Predicted vs. Measured Salinity, April, 1978.

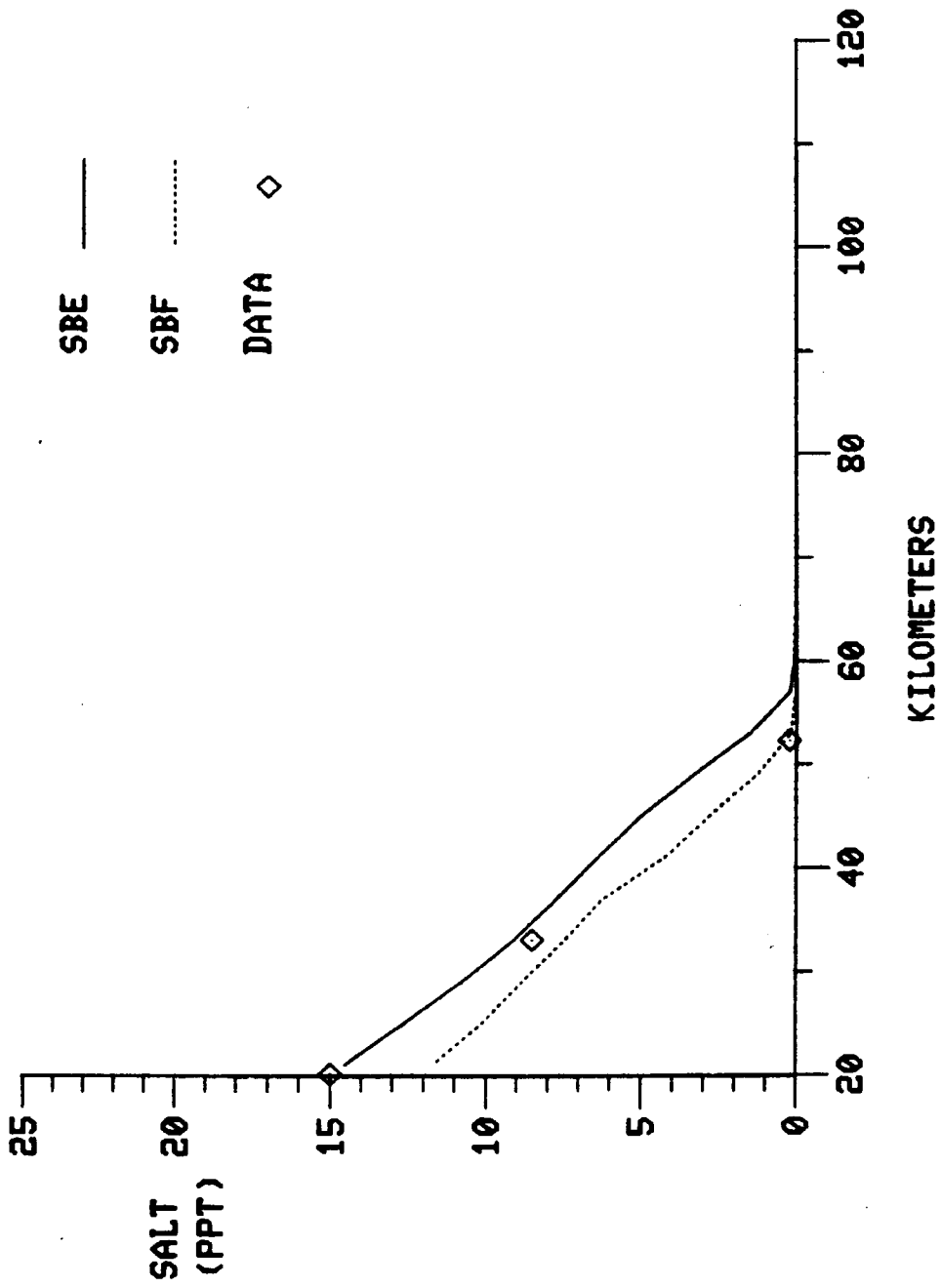


Figure 4-22. Predicted vs. Measured Salinity, May, 1975.

CHAPTER V.

MODELLING THE SPRING-NEAP STRATIFICATION CYCLE

Observations in the James River indicate the estuary undergoes periodic stratification and destratification in response to the spring-neap tidal cycle. This phenomenon has been described in Chapter II. In this chapter, application of the two-dimensional model to the stratification-destratification cycle is detailed.

A. Field Surveys

Model application was based upon a series of salinity observations made in the James River between August 14 and September 2, 1980. Seven surveys were conducted on five different days at slack-before-flood (SBF) or slack-before-ebb (SBE). Stations were placed 5 to 10 km. apart, from the mouth of the river to the head of the salt intrusion, so that a single survey vessel moving upstream from Sewell's Point could sample each station at approximately slackwater.* Conductivity and temperature readings were taken in-situ at two-meter intervals from the surface to the bottom and converted to salinity using standard formulae. The date, tidal

* Sample stations for the August 19 survey were located 15 to 20 km. apart.

phase, and tide range in Hampton Roads of each survey are presented in Table 5-1. Longitudinal and vertical salinity distributions for each survey are presented in Figs. 5-2 - 5-6 and 5-7a - 5-11a, respectively.

Table 5-1. August-September 1980
Salinity Surveys

Date	Phase	Tide Range in Hampton Roads (cm)
August 14	SBF	76
August 19	SBF	58
August 22	SBE	61
August 22	SBF	76
August 27	SBF	104
August 27	SBE	101
September 2	SBF	76

B. Model Application

Application of the model to a simulation of time-varying phenomena requires specification of freshwater runoff, a tidal forcing function, a set of salinity boundary conditions, and a set of initial conditions.

1. Freshwater Runoff - Freshwater runoff at the fall-line prior to and during the sample period was initially low and declined steadily from 70 m³/sec on August 1 to 33 m³/sec by September 1. An average flow rate of 55 m³/sec for the two-week period preceding the surveys was used to set the initial conditions and the daily hydrograph for the James River at Richmond was employed during the simulation.

Flow in the Appomattox was similarly low, averaging $8 \text{ m}^3/\text{sec}$ prior to the surveys and $1.5 \text{ m}^3/\text{sec}$ during the sample period. Flow in the Chickahominy was negligibly small.

2. Tidal Forcing Function - A time series of surface levels in Hampton Roads was generated by a harmonic analysis program which employs the same constants used by NOAA in their tidal predictions for Hampton Roads (Boon and Kiley; 1978). This time series was then adjusted by a constant multiplier in order to reproduce the tide record at km 21, the downstream limit of interest in the model. The surface level at km 21 for the simulation period is shown in Fig. 5-1.

3. Salinity Boundary Conditions - A constant, vertically-uniform downstream salinity boundary condition of 26 ‰ was employed throughout the simulation.

4. Initial Conditions - A set of initial conditions was produced by running the model, utilizing the average flow for the two week period preceeding the survey and the August 14 tidal amplitude, until the conditions observed in the August 14 survey were reproduced. These initial conditions are shown in Figs. 5-2 and 5-7b.

C. Simulation Results

The model was used to simulate the 38 tidal cycles from August 14 to September 2. The results are presented in several formats. First shown are a series of predicted

versus measured depth-average longitudinal salinity distributions (Figs. 5-2 - 5-6). Next, the observed and predicted salinity profiles are compared (Figs. 5-7 - 5-11). Finally, time-series of predicted and observed relative stratifications are presented (Fig. 5-12 - 5-15).

Longitudinal salinity distributions at both SBE and SBF are shown for the August 22 and August 27 surveys. Otherwise, only the available SBF longitudinal distributions are shown. Comparisons between the predicted and observed salinities are generally good. The length of the salt intrusion is especially well predicted.

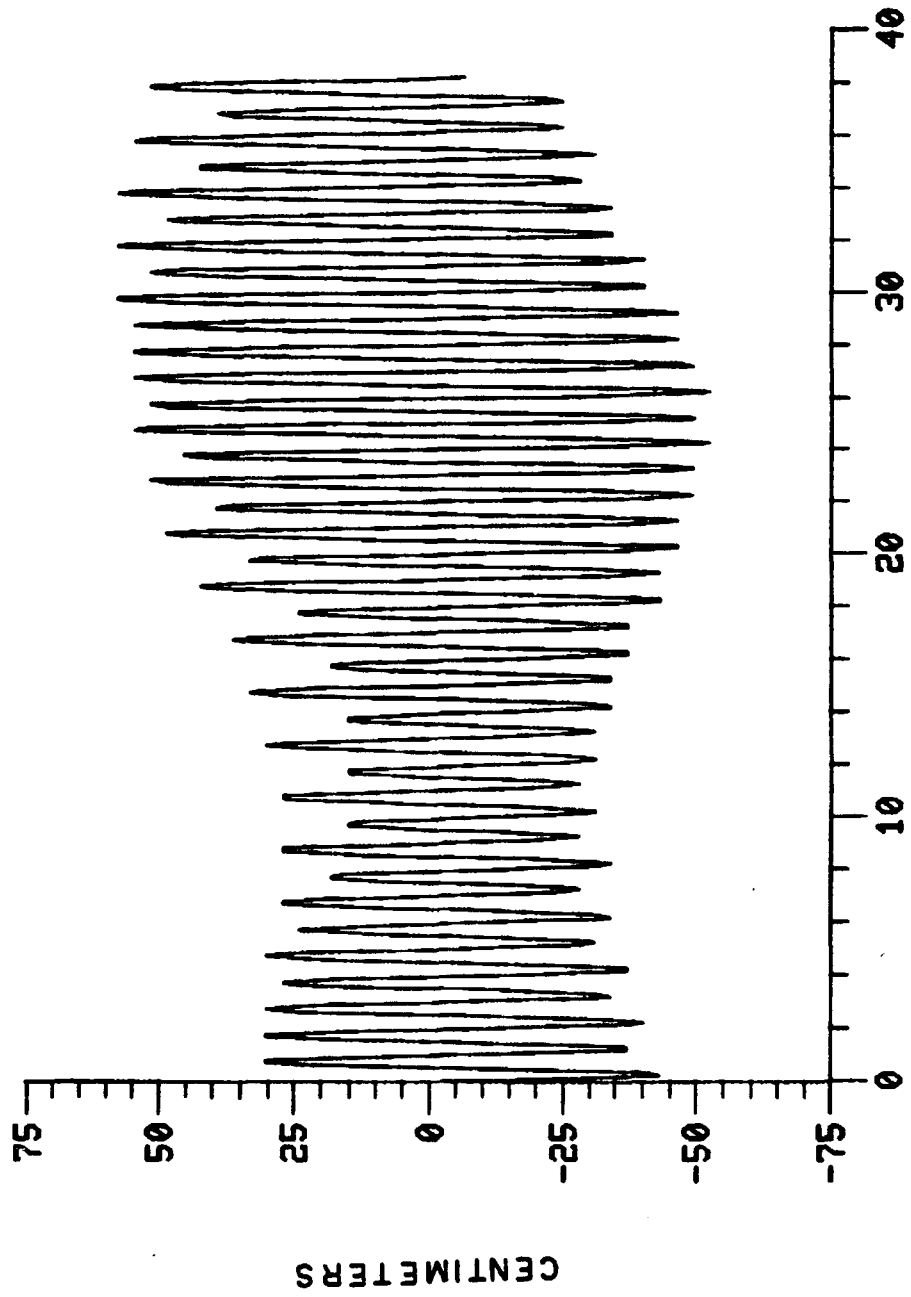
In order to form a consistent set, vertical salinity profiles are shown at SBF only. The observations (Figs. 5-7a - 5-11a) are shown on separate sheets from the predictions (Figs. 5-7b - 5-11b) to improve clarity. For these profiles, agreement between the model and field data is less ideal than the longitudinal distributions. The agreement is still extremely good, however, considering that a two-dimensional, time variable salinity field is being modelled.

Time-series of predicted and observed stratifications are shown in the last series of graphs (Figs. 5-12 - 5-15). Note that relative stratification, $\Delta s/\bar{s}$, is shown on the vertical axis. In this series, the cyclic nature of stratification predicted by the model is most evident although the cycling is partially obscured

in some of the field data. Notably, observed stratification at km 23 and 66 during tidal cycle 16 (Aug. 22) is minimal when it should be elevated due to the neap tidal range.

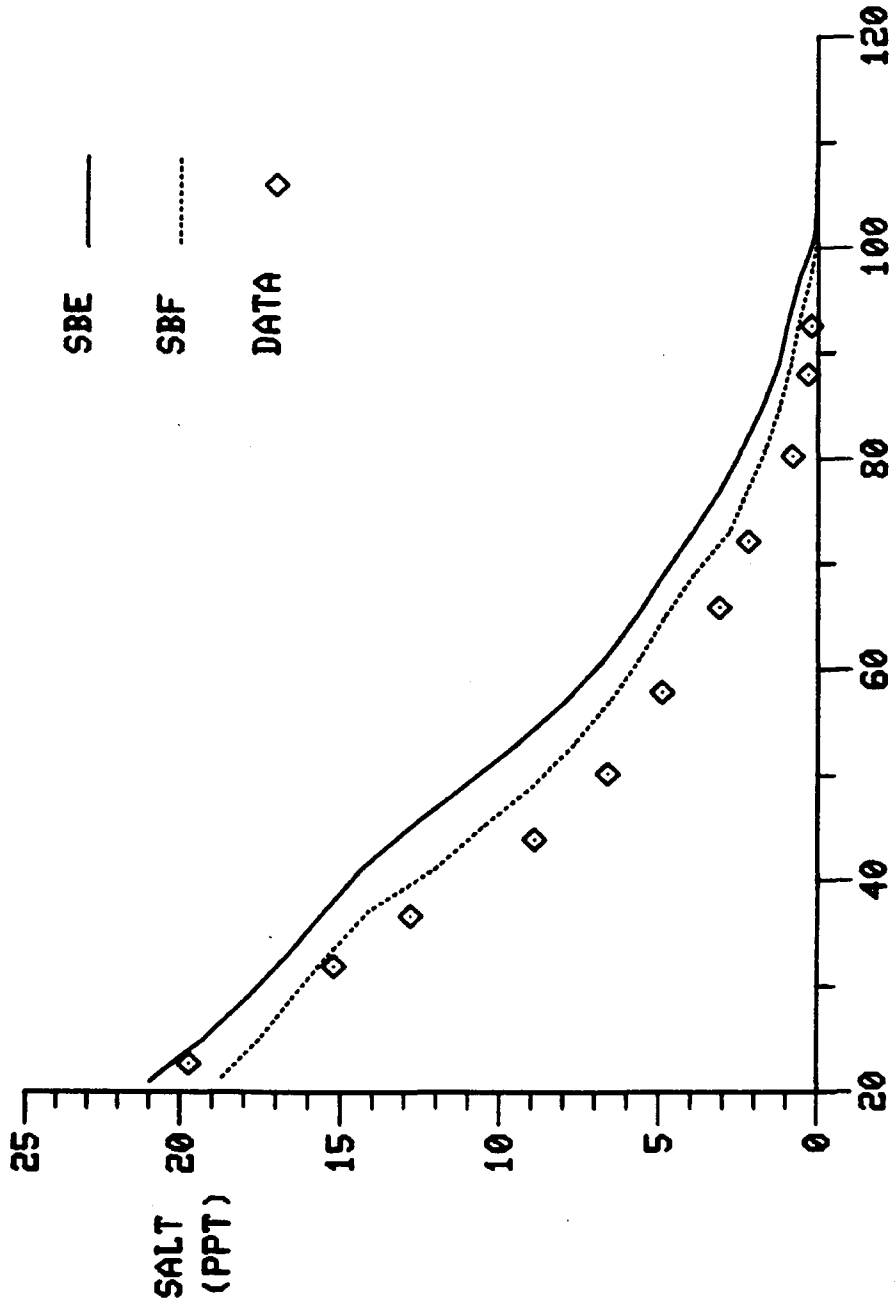
Examination of the August 22 field data (Fig. 5-9a) shows several anomalous observations. Station 23 is vertically well-mixed while stations 32 - 50 are highly stratified. Furthermore, stations 37 and 50 exhibit higher salinities at depths below 3 meters than adjacent downstream stations. These anomalies may be attributed to a wind event which took place from August 20 - 23. During this event, northeast winds prevailed and peaked on the 22nd with a daily resultant speed of 5.5 m/sec. For the month, southeast winds prevailed with a resultant speed of 0.9 m/sec. The wind-induced circulations and vertical mixing due to the Aug. 20 - 23 event are not included in the model and may account for the discrepancies between predictions and observations at tidal cycle 16.

In the absence of wind or other influences not included in the model, agreement between predicted and observed stratification-destratification cycling is good, especially considering that, as in the vertical profiles, the relative stratification parameter is dependent on both time and the two-dimensional salinity distribution.



TIDAL CYCLES

Figure 5-1. Tide Range at Km. 21., August 14 - September 2.



KILOMETERS

Figure 5-2. Predicted and Observed Longitudinal Salinity, August 14.

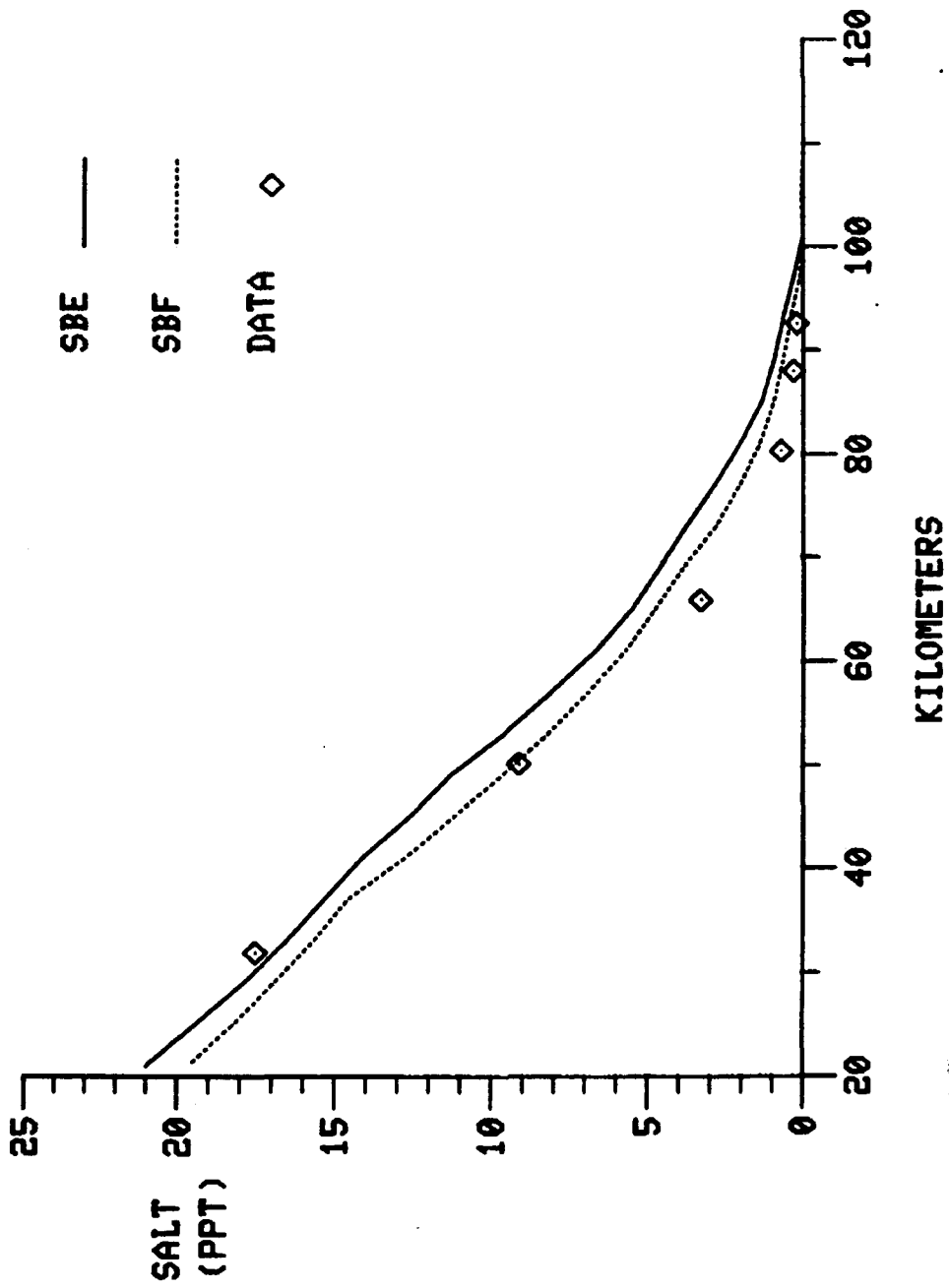
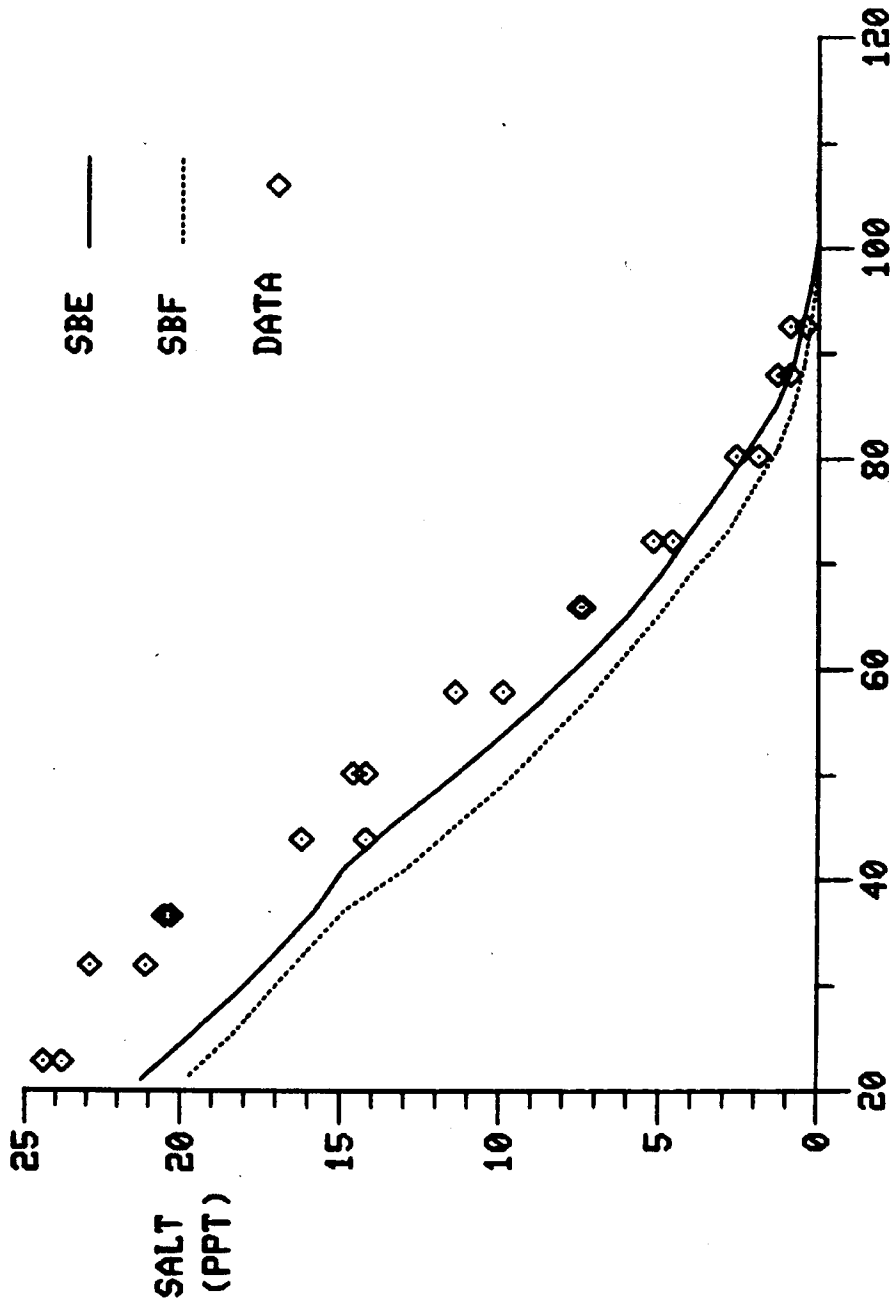
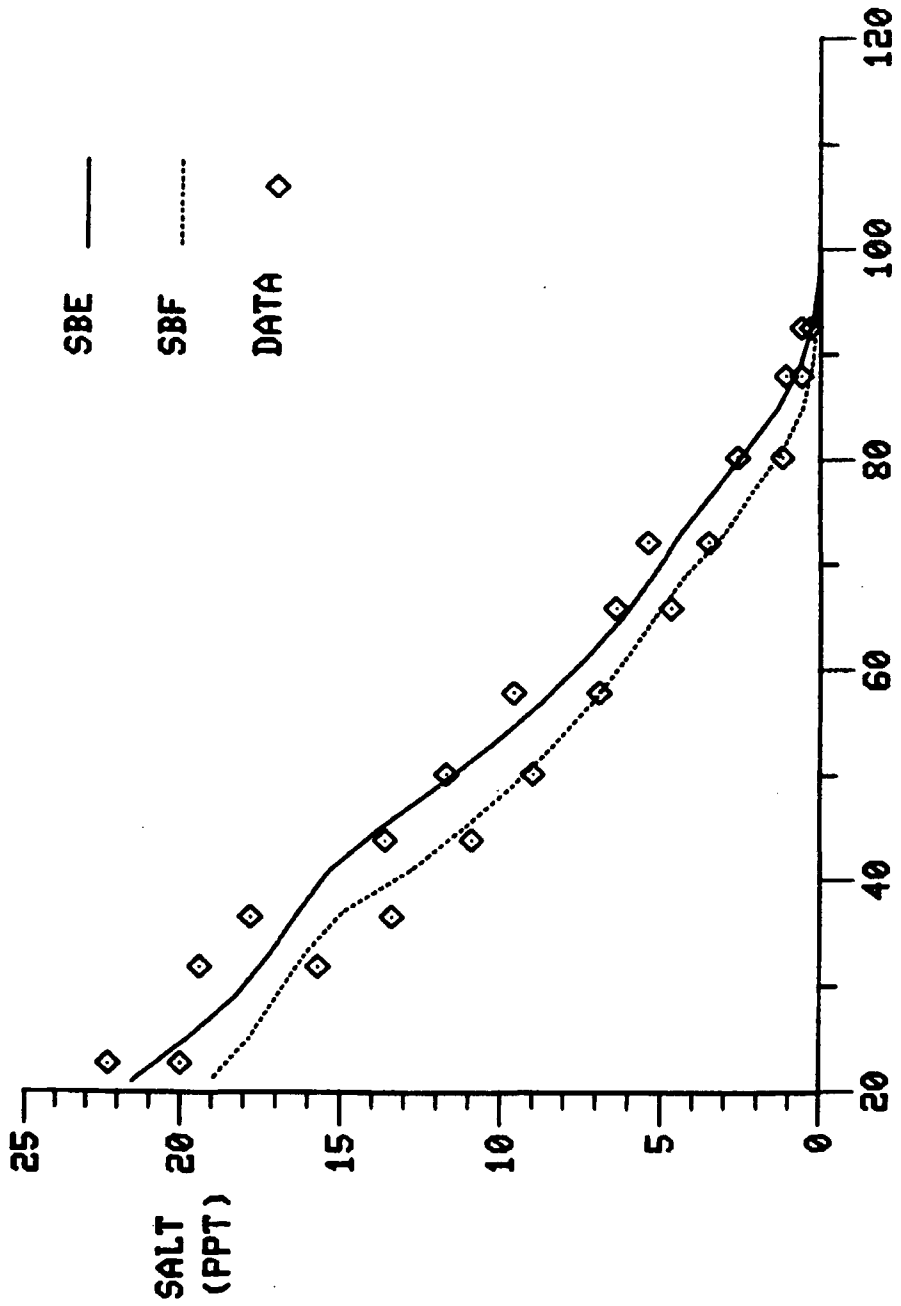


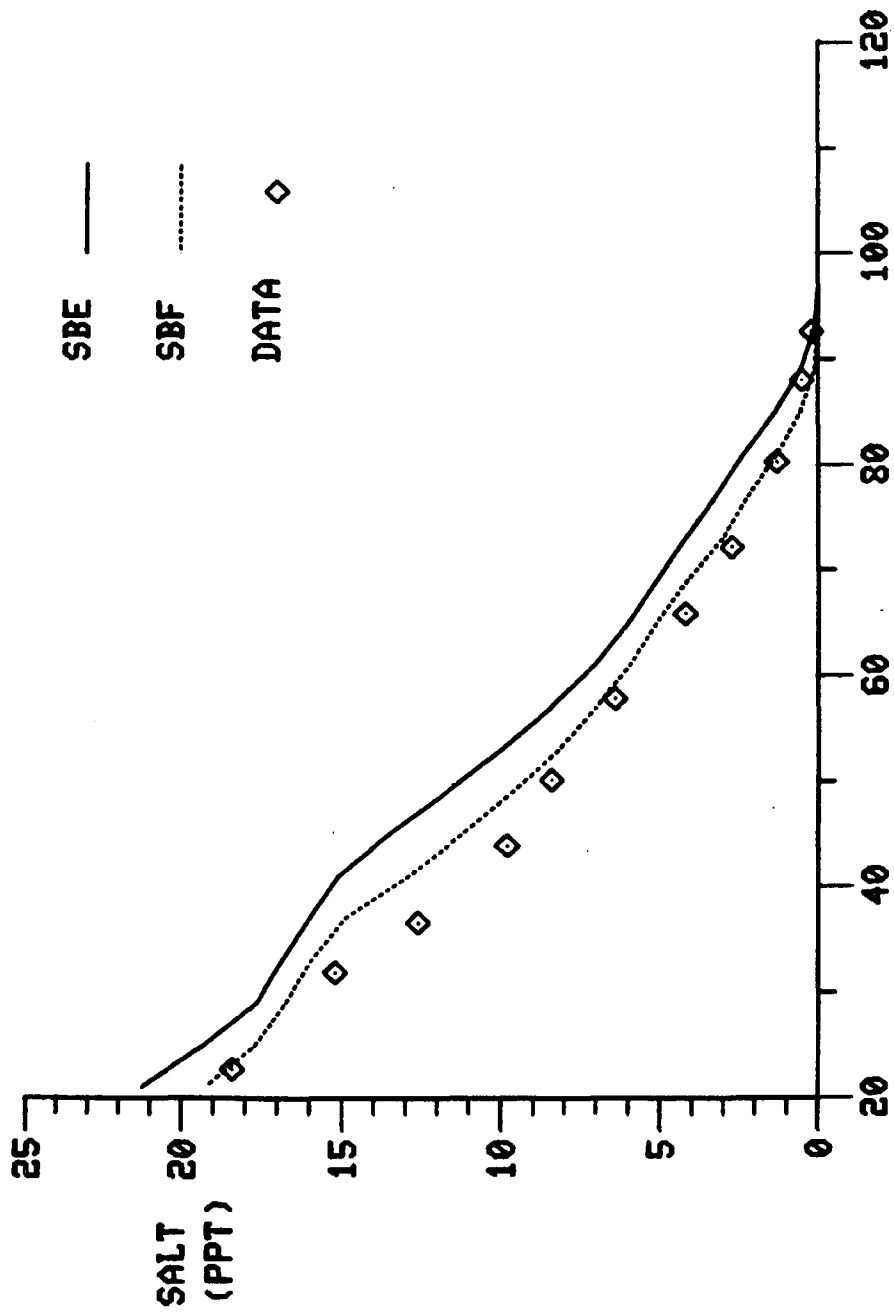
Figure 5-3. Predicted and Observed Longitudinal Salinity, August 19.



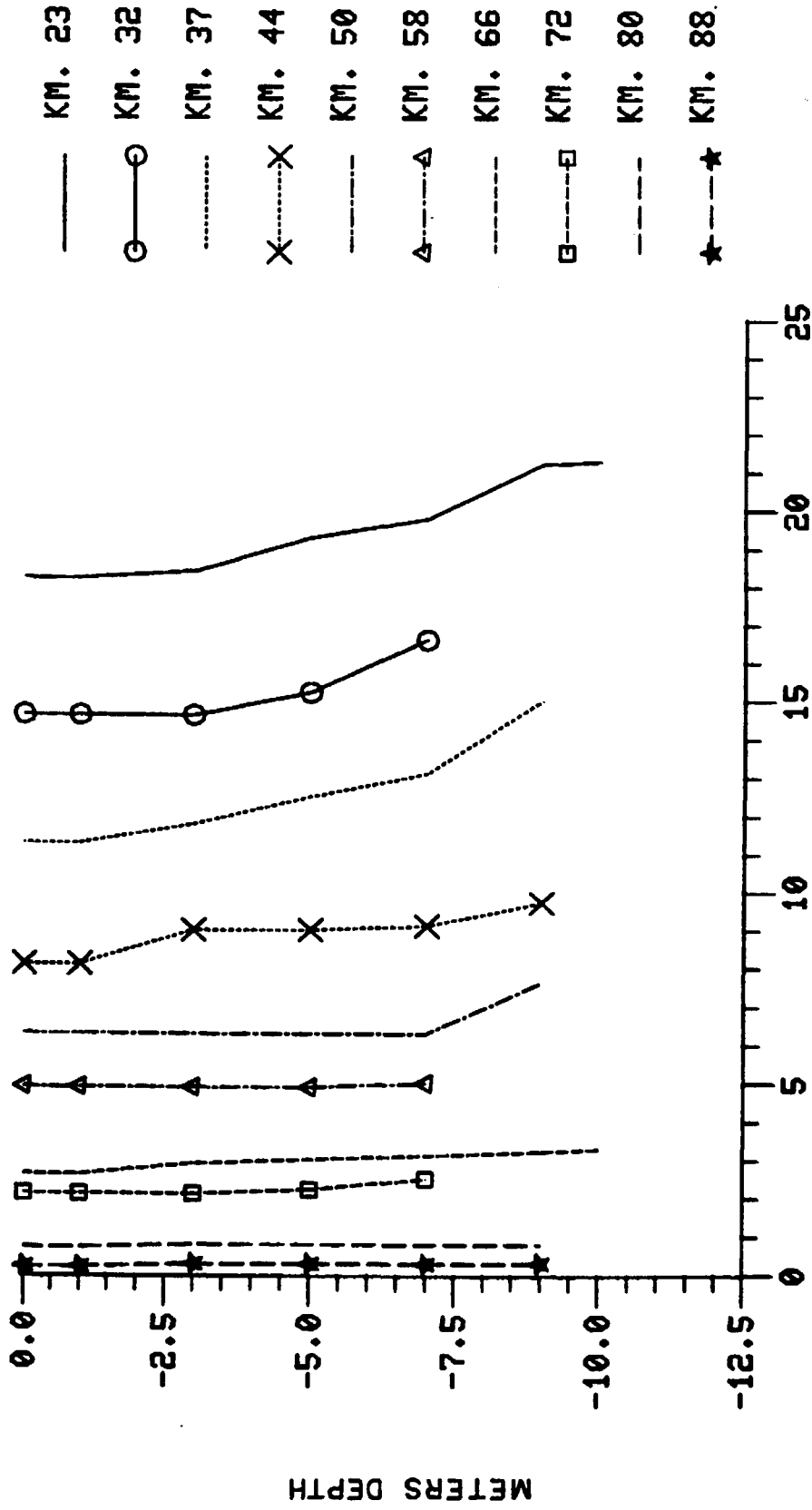
KILOMETERS
Figure 5-4. Predicted and Observed Longitudinal Salinity,
August 22.



KILOMETERS
Figure 5-5. Predicted and Observed Longitudinal Salinity,
August 27.

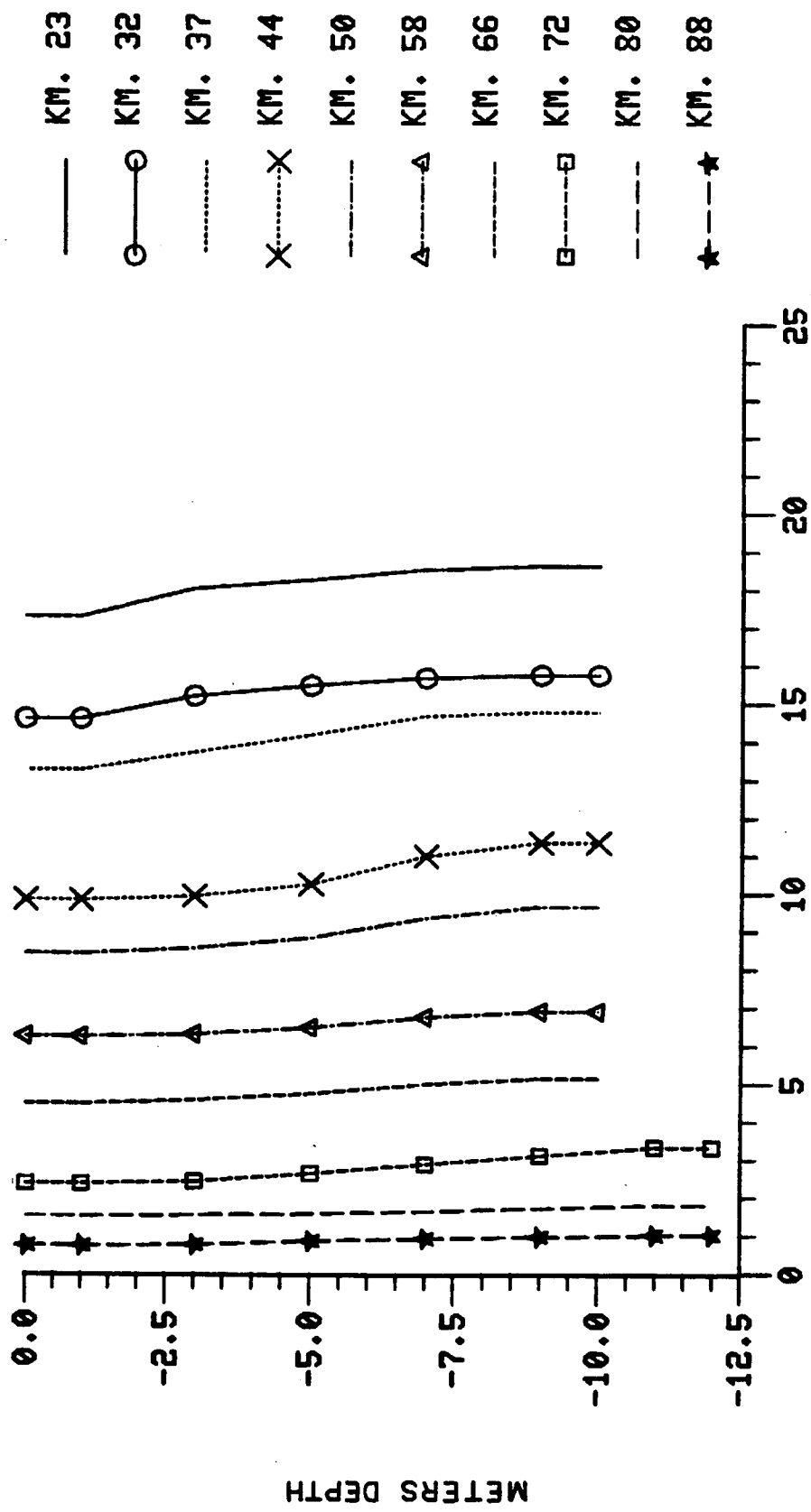


KILOMETERS
 Figure 5-6. Predicted and Observed Longitudinal Salinity,
 September 2.



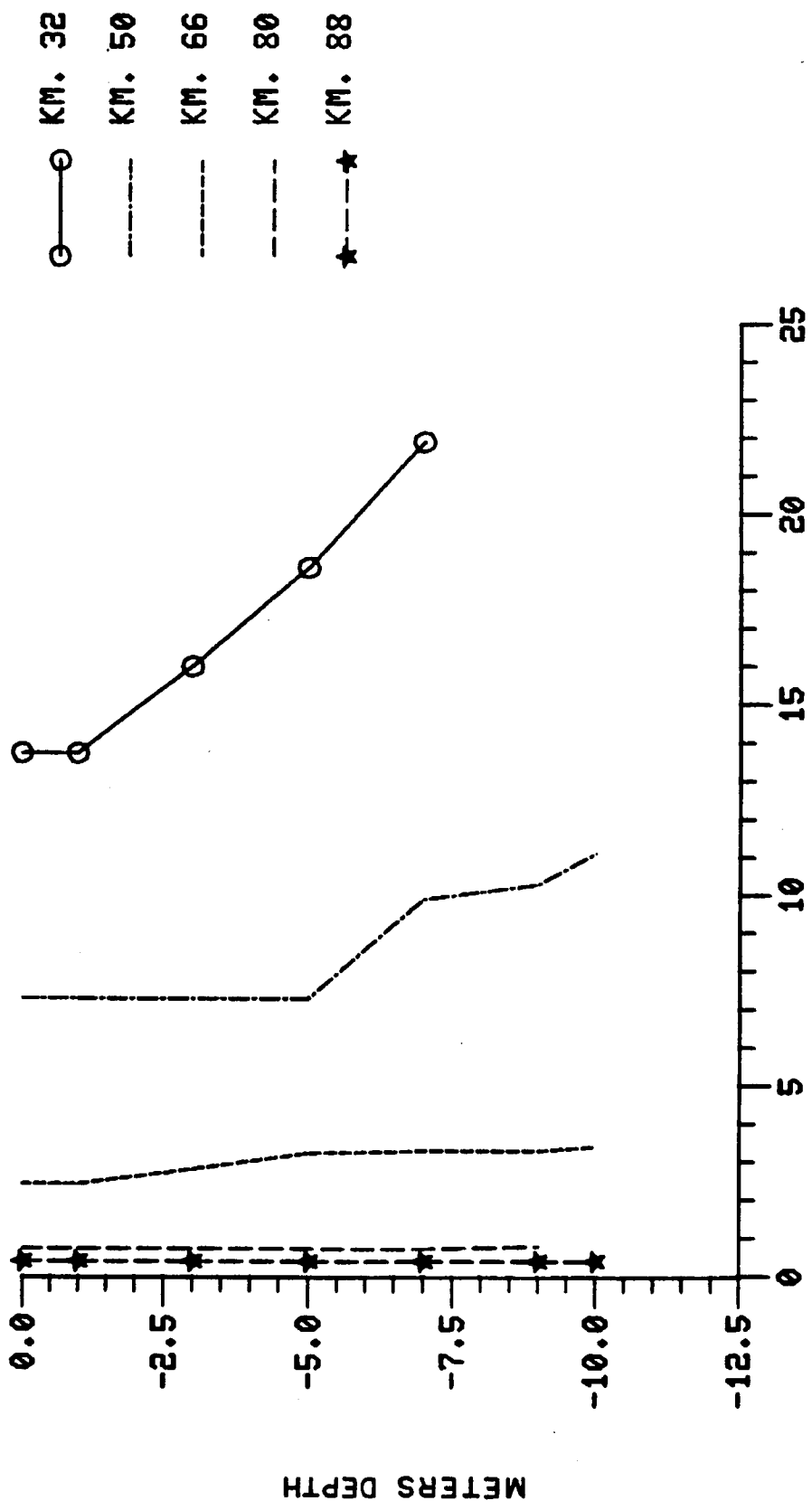
SALINITY (PPT)

Figure 5-7a. Observed Salinity Profile August 14.

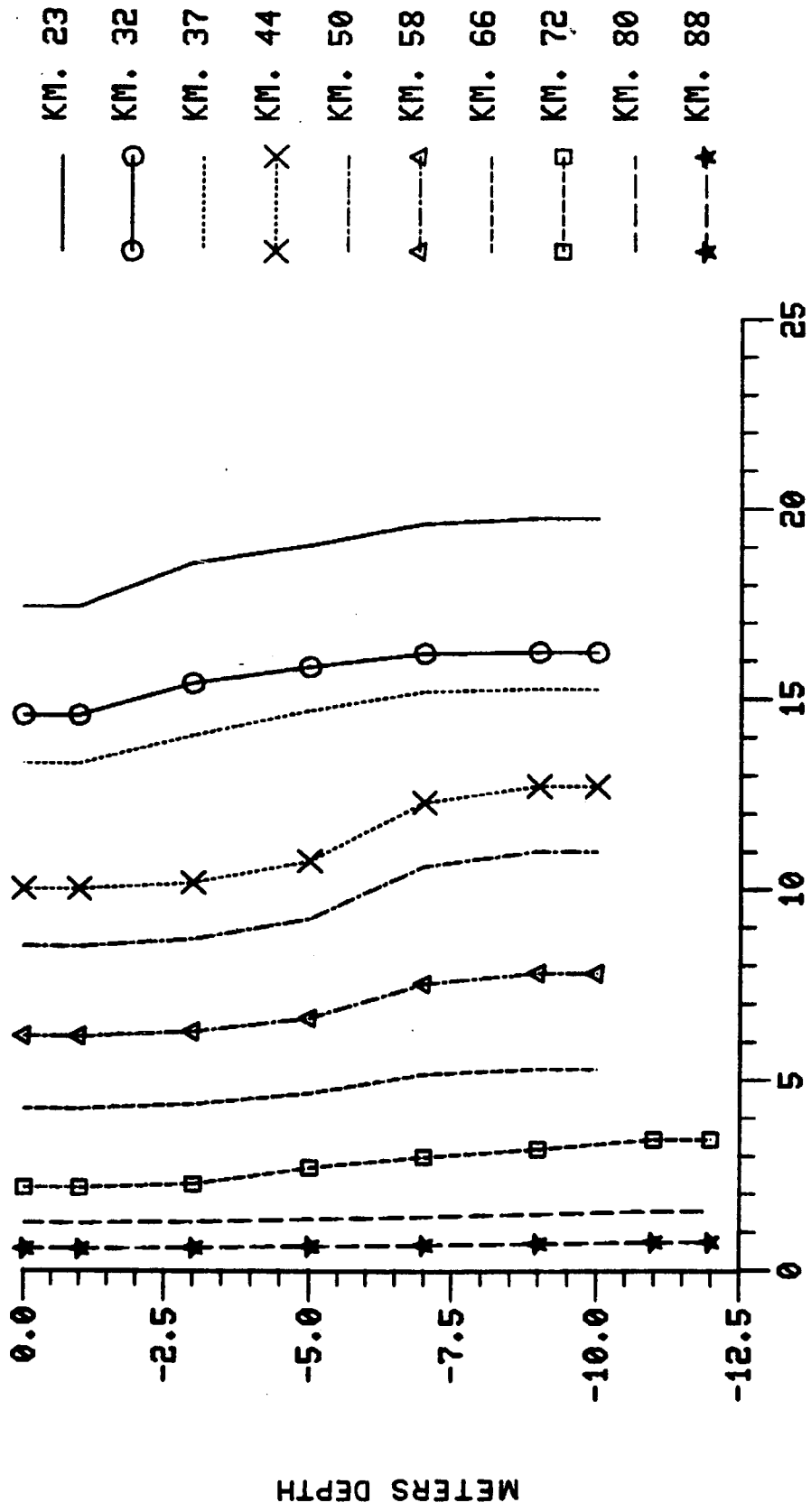


SALINITY (PPT)

Figure 5-7b. Predicted Salinity Profile August 14.



SALINITY (PPT)
Figure 5-8a. Observed Salinity Profile August 19.



SALINITY (PPT)
 Figure 5-8b. Predicted Salinity Profile August 19.

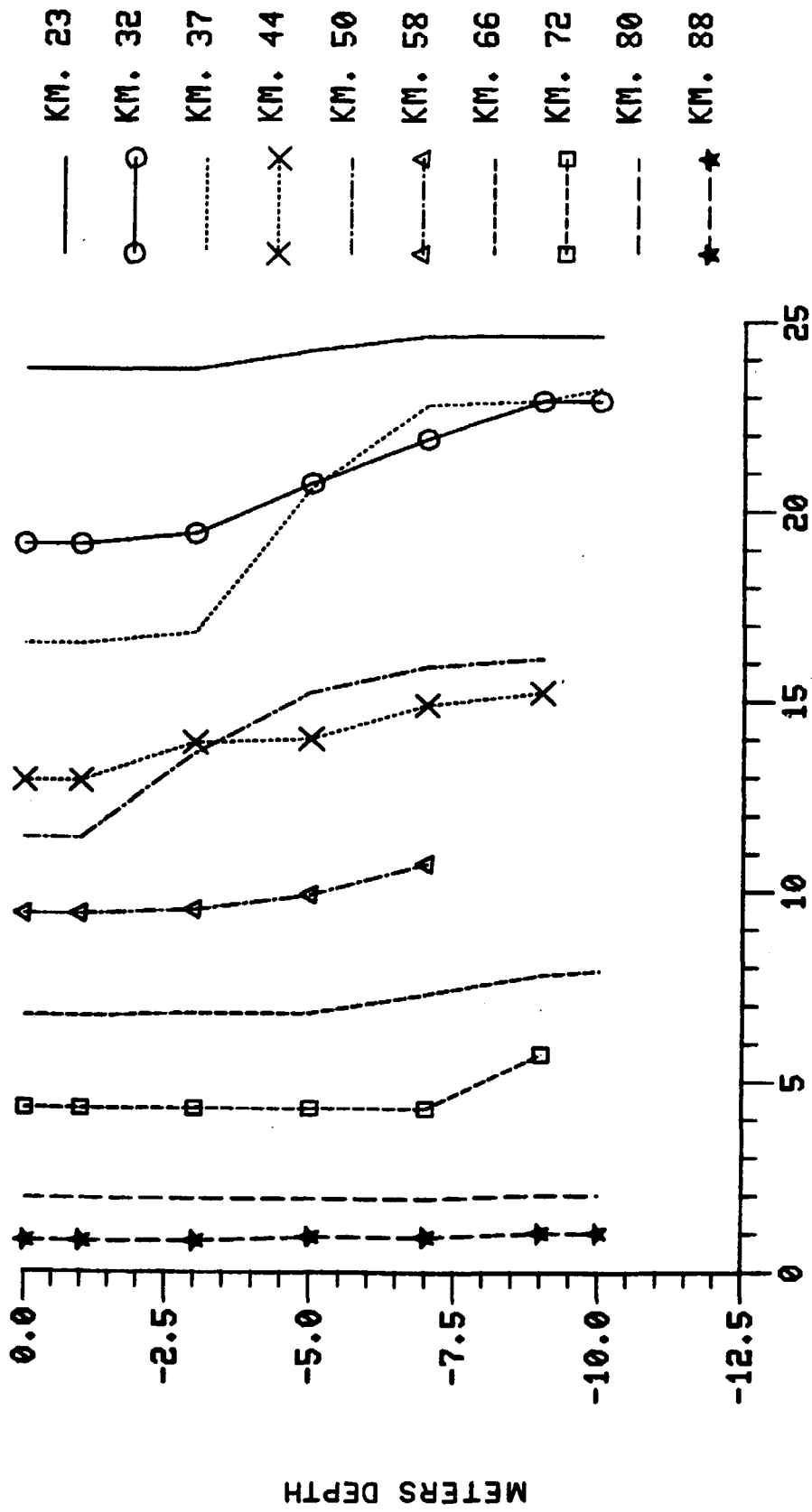


Figure 5-9a. Observed Salinity Profile, August 22.

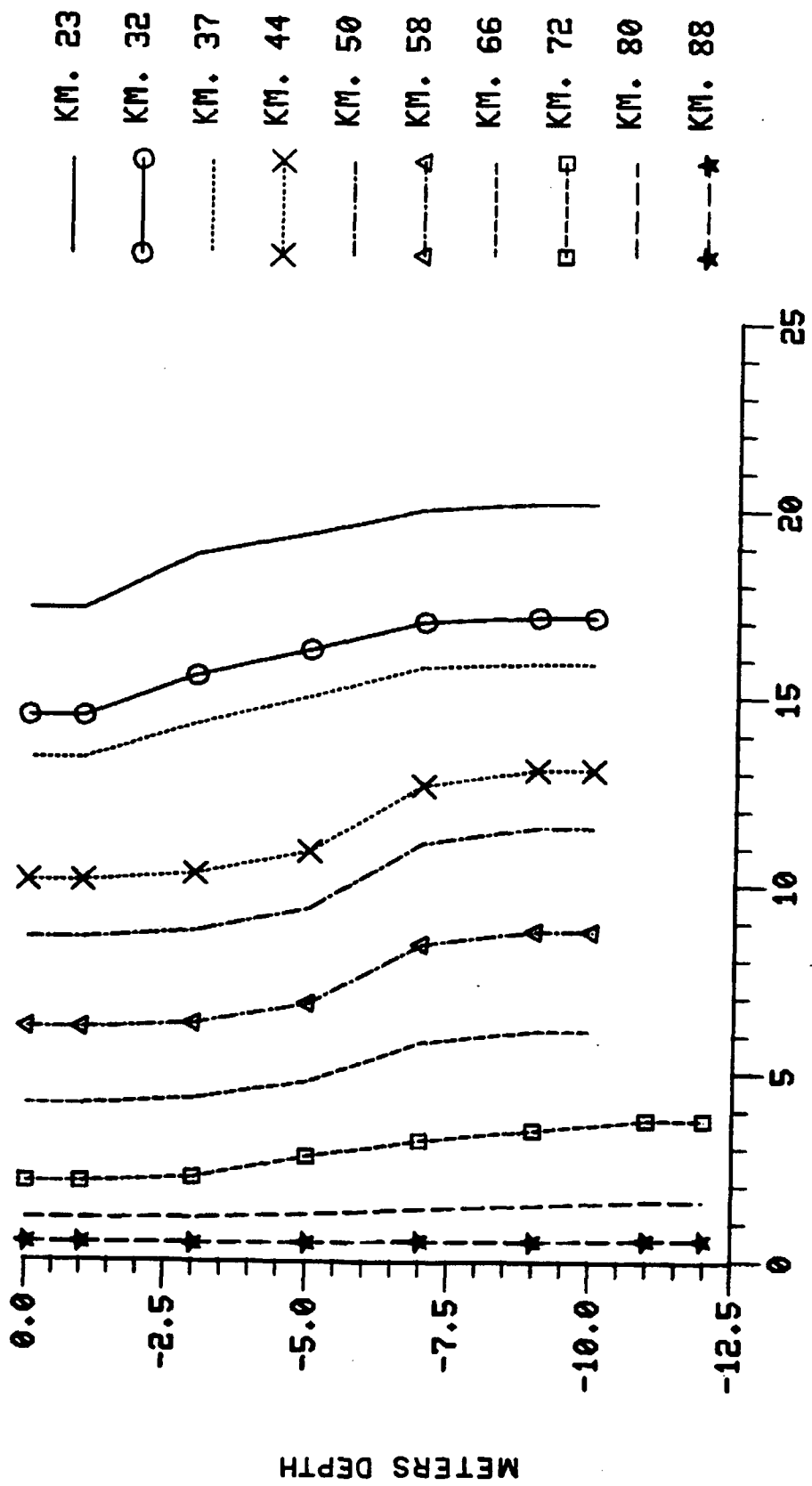


Figure 5-9b. Predicted Salinity Profile August 22.

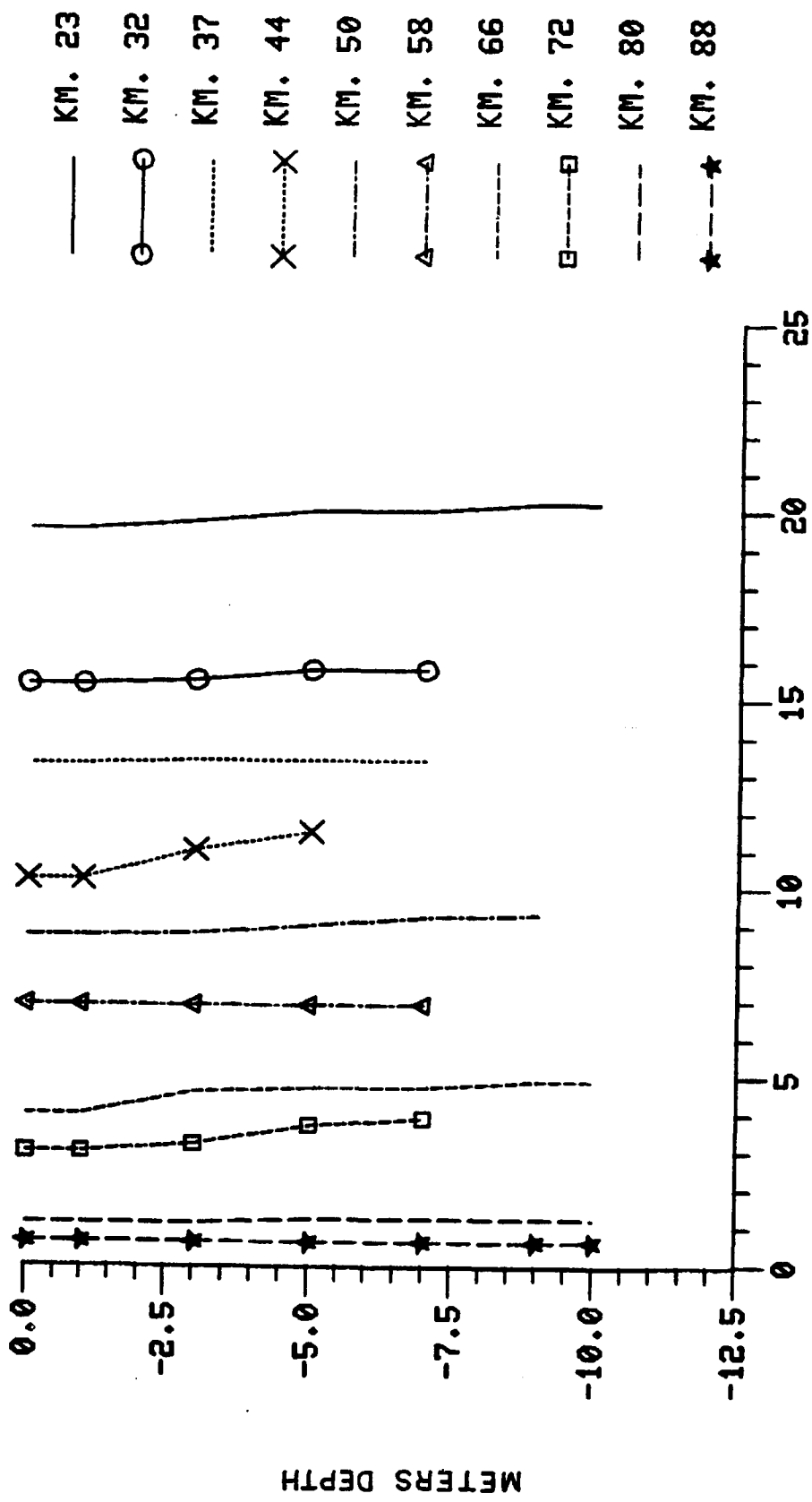
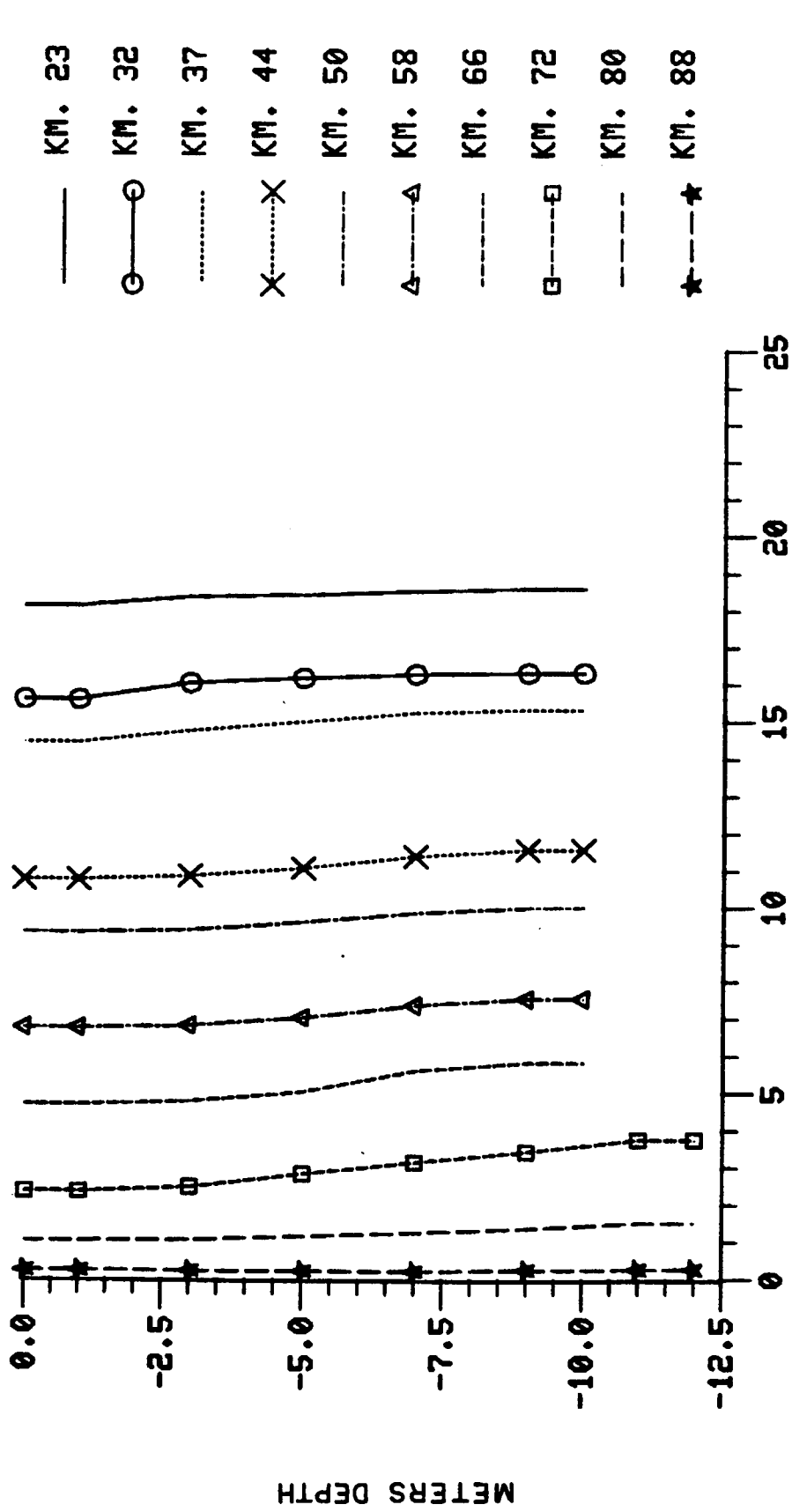


Figure 5-10a. Observed Salinity Profile August 27.

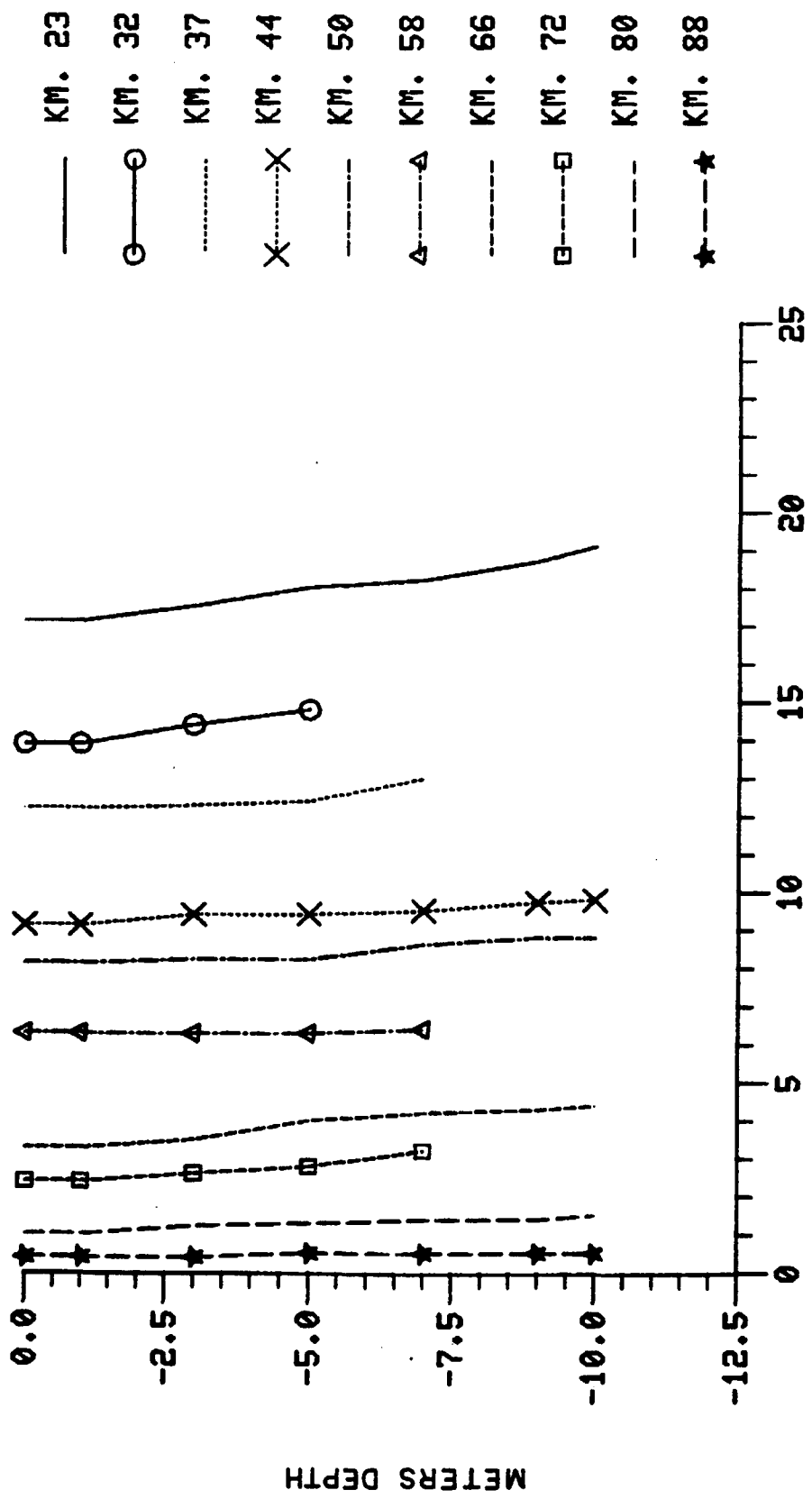
SALINITY (PPT)

METERS DEPTH



SALINITY (PPT)

Figure 5-10b. Predicted Salinity Profile August 27.



SALINITY (PPT)

Figure 5-11a. Observed Salinity Profile September 2.

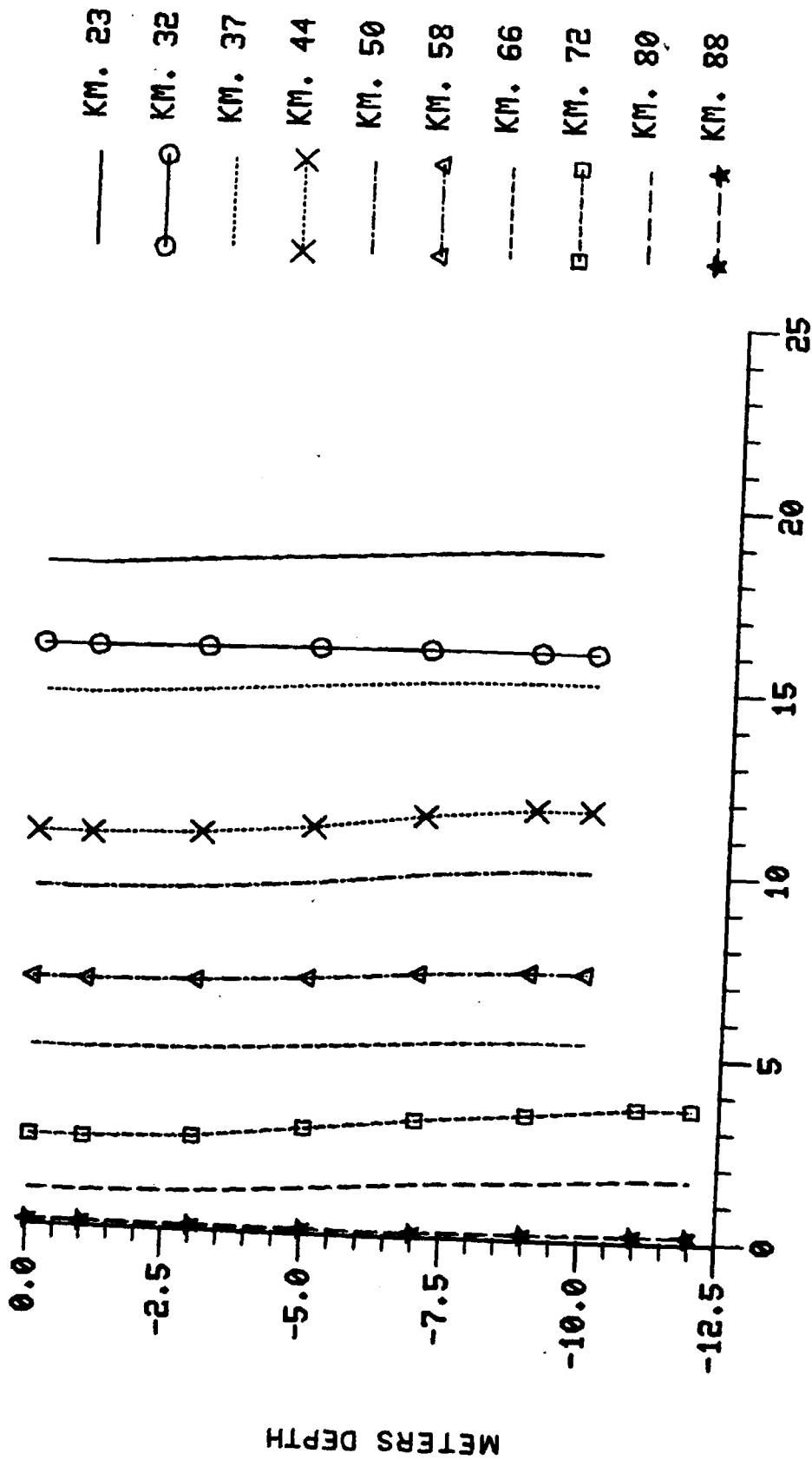
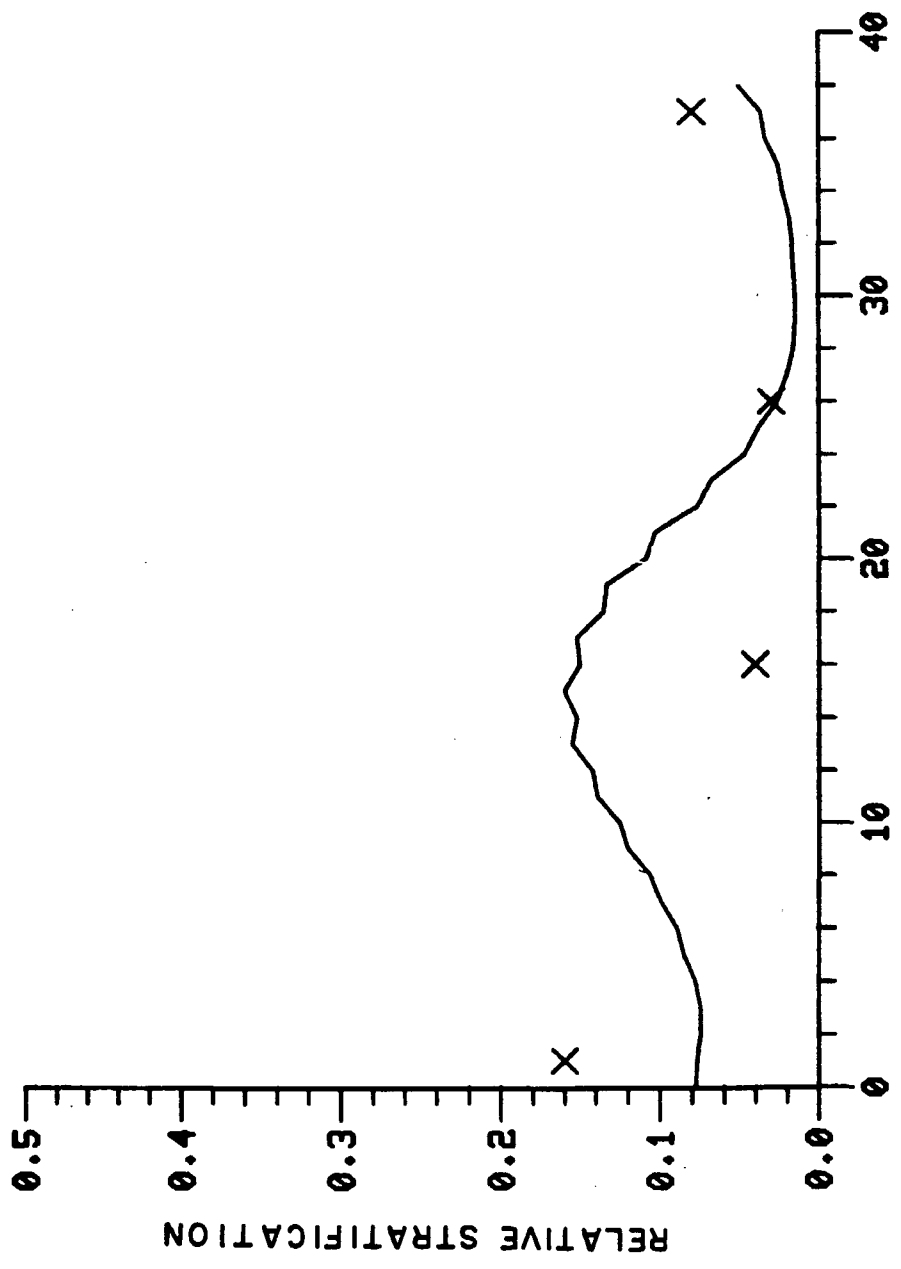
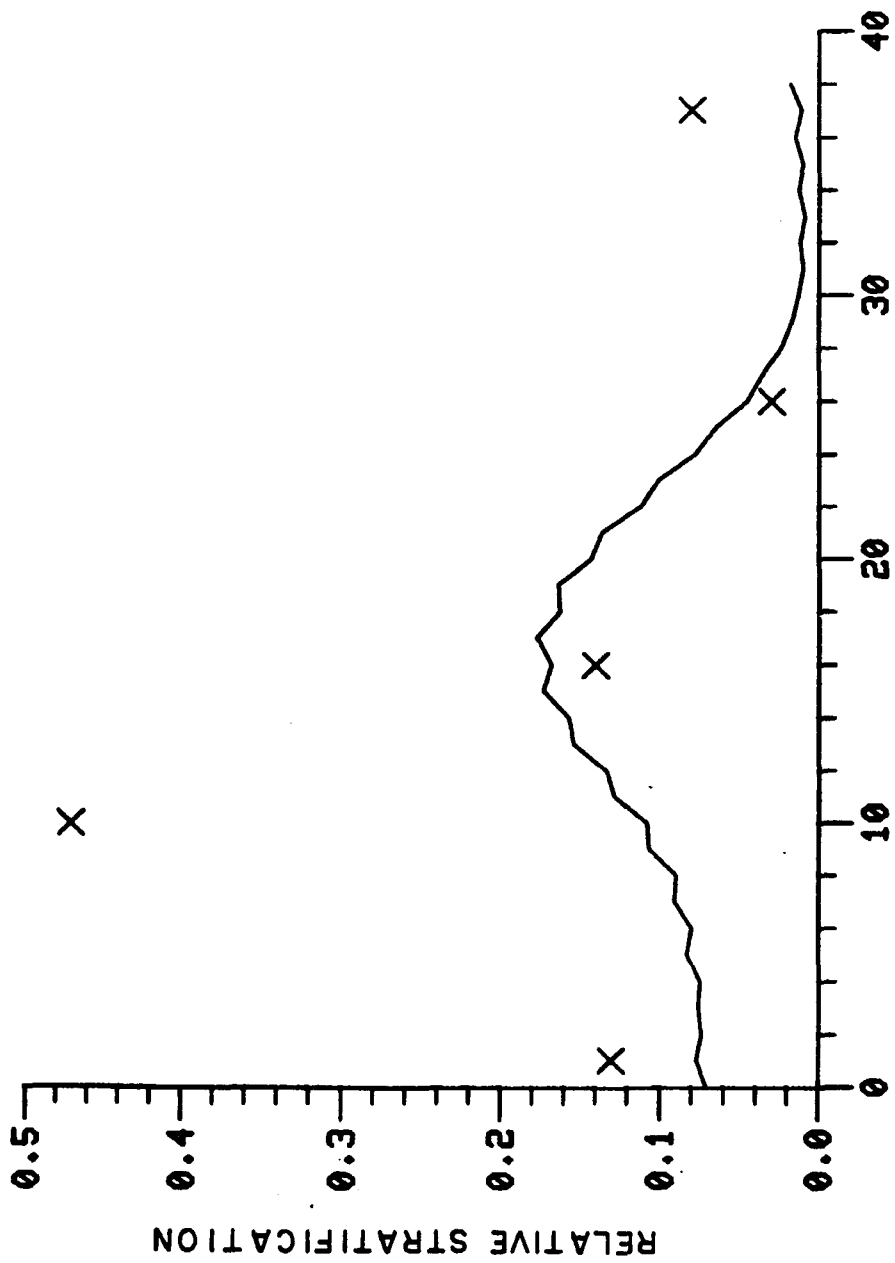


Figure 5-11b. Predicted Salinity Profile September 2.



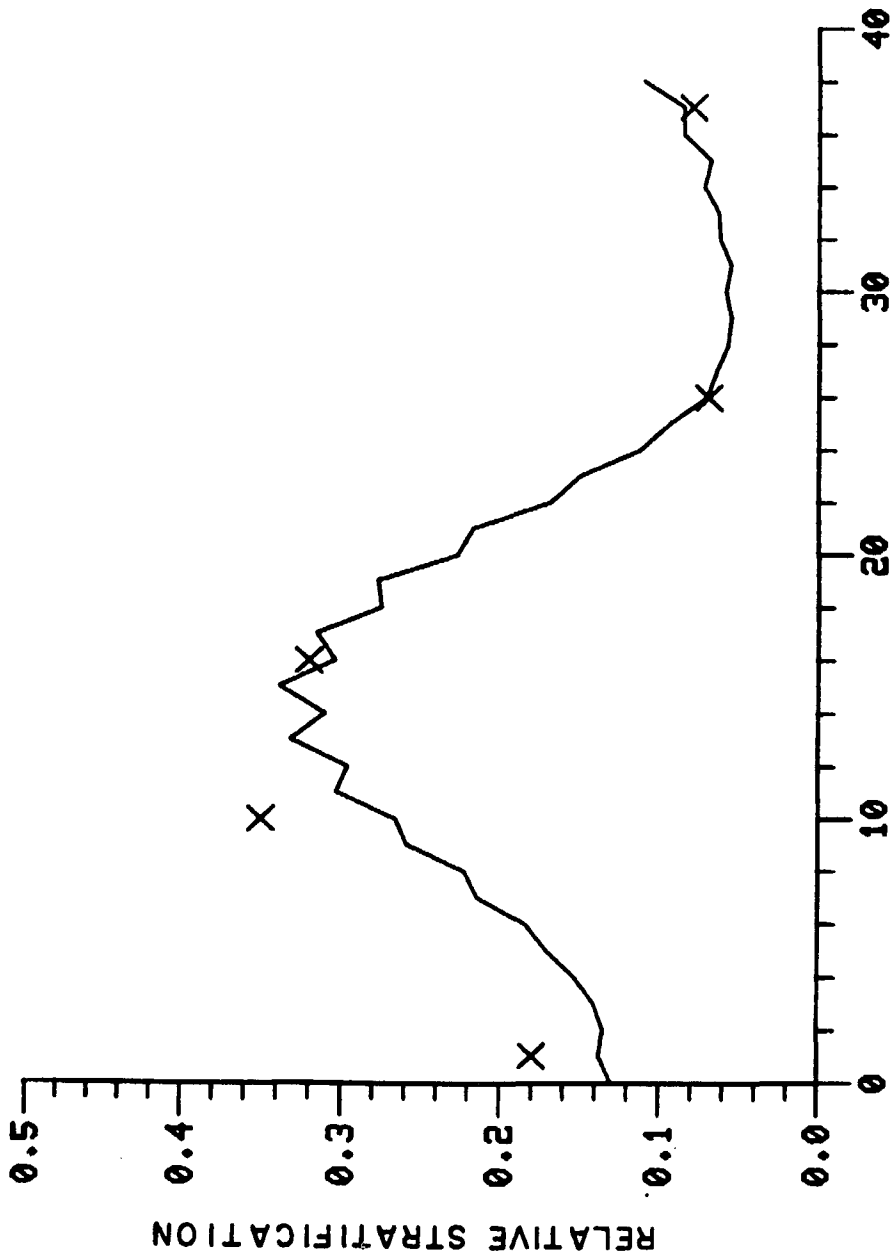
TIDAL CYCLES

Figure 5-12. Predicted and Observed Stratification at Km. 23.



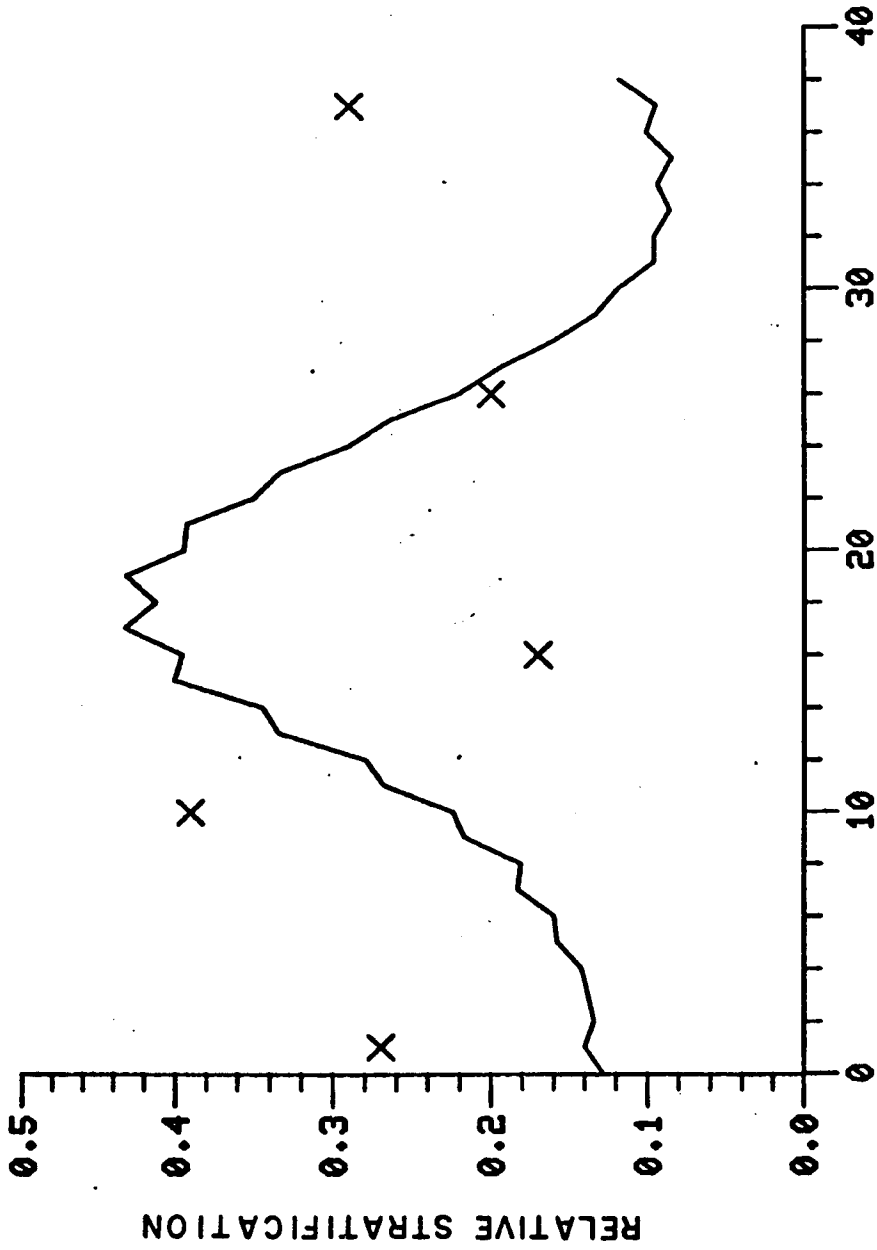
TIDAL CYCLES

Figure 5-13. Predicted and Observed Stratification at Km. 32.



TIDAL CYCLES

Figure 5-14. Predicted and Observed Stratification at Km. 50.



TIDAL CYCLES

Figure 5-15. Predicted and Observed Stratification at Km. 66.

CHAPTER VI.

MODELLING MOVEMENT OF THE SALINITY INTRUSION

The salinity intrusion of an estuary is subject to displacement longitudinally and alteration in vertical structure as a result of both long-term and short-term variations in freshwater runoff. The response of the James River estuary to storm-generated flow pulses has been described in Chapter II. In this chapter, application of the two-dimensional model to a rapid seaward translation of the salt intrusion is detailed.

A. Field Surveys

Model application is based upon a series of salinity observations made in the James River between April 25 and May 7, 1978. During this interval, the salinity intrusion was displaced approximately 25 km due to a twelve-fold increase in flow over a period of 48 hours (Fig. 2-5). Prior to and during the storm pulse, six salinity surveys were conducted at SBE or SBF. Stations were spaced approximately 10 to 20 km apart and extended from the vicinity of Newport News (km 20) to above the head of the salt intrusion (km 39 to 67). At each station, conductivity and temperature readings were taken in-situ, at two-meter intervals from the surface

to a depth of 7-11 m, for later conversion to salinity values. The date, tidal phase, and freshwater flow at Richmond for each survey are presented in Table 6-1. Longitudinal and vertical salinity distributions are shown in Figs. 6-2 - 6-7 and 6-8a - 6-13a.

Table 6-1. April-May 1978 Salinity Surveys

Date	Phase	Flow Rate at Richmond (m^3/sec)
April 25	SBF	141
April 28	SBF	1870
April 29	SBF	1410
April 30	SBF	697
May 2	SBE	406
May 7	SBF	501

B. Model Application

Application of the model to the simulation of time-varying phenomena requires specification of freshwater runoff, a tidal forcing function, a set of salinity boundary conditions, and a set of initial conditions.

1. Freshwater Runoff - For the ten-day period preceding the storm pulse, freshwater runoff at the fall-line was relatively constant at approximately $150 \text{ m}^3/\text{sec}$. During the initial storm pulse, flow increased to $1870 \text{ m}^3/\text{sec}$ on April 28 then declined to $330 \text{ m}^3/\text{sec}$ by May 4. On May 5, a secondary storm pulse of $823 \text{ m}^3/\text{sec}$ occurred. The hydrograph for the simulation period, as used in the model, is shown in Fig. 2-5.

Similar to the James, flow in the Appomattox was steady prior to the storm, and averaged $26 \text{ m}^3/\text{sec}$. Only a single storm pulse was noted, however, and occurred on May 2 with a flow of $344 \text{ m}^3/\text{sec}$. Flow in the Chickahominy averaged $6 \text{ m}^3/\text{sec}$ prior to the storm and peaked at $43 \text{ m}^3/\text{sec}$ on May 1. Daily hydrographs for both these tributaries were used in the model.

2. Tidal Forcing Function - As in the spring-neap simulation, tide levels at the open boundary were generated as the sum of constituent harmonics using appropriate constants specified by NOAA. The tide level at km 21 for the simulation period is shown in Fig. 6-1.

3. Salinity Boundary Conditions - Assigning boundary conditions in a time-varying model subject to reversing flows is problematical. The specified conditions must be consistent with the adjacent estuary both during ebb intervals when the salinity at the mouth is largely influenced by processes within the estuary and during flood intervals when the salinity at the mouth is dominated by external processes.

For a highly transient case, the desirable boundary conditions are a vertically and temporally complete set of salinity measurements at the mouth of the prototype. This ideal cannot be realized, however. Neither can the constant downstream salinity employed during the spring-neap simulation be applied as this assumption is physically unrealistic.

In order to provide boundary conditions, the following assumptions were made:

- (a) During ebb flows, salinity at the mouth is determined solely by conditions upstream.
- (b) During flood flows, a constant salinity gradient, $\frac{\partial s}{\partial x}$, prevails at the mouth.

The first assumption is appropriate during high-flow conditions and enhances the predictive nature of the model. The second condition is less well-grounded but is necessary for closure in the absence of detailed data.

In order to impose the boundary conditions, several terms in eq. (3-44) are modified for application at the open boundary. First, the advection term is changed from central to backwards differencing in order to eliminate dependence on the boundary segment during ebb flows.

$$T3_{NT,k} = u_{NT,k} \bar{B}_{NT,k} S_{NT}, \quad u \geq 0$$

$$T3_{NT,k} = u_{NT+1,k} \bar{B}_{NT,k} S_{NT+1,k} \quad u < 0$$
(6-1)

where

NT = most downstream model segment.

Second, diffusion through the mouth is set equal to diffusion through the next most upstream segment

$$T4_{NT,k} = T4_{NT-1,k}$$
(6-2)

Boundary condition (b) is imposed during flood intervals by setting

$$S_{NT+1,k} = S_{NT,k} + \text{SINC} \quad u < 0 \quad (6-3)$$

where

SINC = specified constant

For this simulation, SINC = 0.5 was found suitable.

4. Initial Conditions - A set of initial conditions was produced by running the model, utilizing the average flow for the ten-day period preceeding the surveys and the April 25 tidal amplitude, until the conditions observed in the April 25 survey were reproduced. These initial conditions are shown in Figs. 6-2 and 6-8a.

5. Convergence of the Salinity Computations - Stability and convergence of the salinity computations have been discussed in Chapters III and IV. It was noted that the cell-Reynolds-number criterion, eqn. (3-50), required dispersion large enough to dominate the longitudinal transport computations. Violation of restriction (3-50) was permissible, however, in the presence of "mild" salinity gradients.

In preliminary simulations of the 1978 storm event, wave-like oscillations in salinity were observed to form in the downstream portion of the estuary. The oscillations occurred towards the end of the simulation, when the longitudinal salinity gradient was steepest. Due to the sharp gradient, longitudinal dispersion, as

as computed by eq. (4-17), was no longer sufficient to "smooth" the computations. As the oscillations occurred only at the end of the simulation and were confined largely to the downstream portion of the estuary, beyond the region of interest, the effects on the simulation were minor. Extension of the simulation for a longer time period showed, however, that the oscillations would eventually propagate upstream and invalidate the salinity calculations.

If a longer simulation was to be conducted, the salinity oscillations would have to be eliminated. Since K_x cannot be increased without introducing excess dispersion, Δx would have to be reduced until restriction (3-50) was satisfied, entailing greatly increased computation time compared to simulation of events in which the longitudinal salinity gradient is relatively mild.

C. Simulation Results

The model was used to simulate a 28 tidal cycle period encompassing the April 25 to May 7 surveys. The results are presented in several formats. First shown are comparisons of predicted vs. measured depth-average longitudinal salinity distributions (Figs. 6-2 - 6-7). Next, the observed and predicted SBF salinity profiles are compared (Fig. 6-8 - 6-13). Finally, time-series of predicted and observed salinities and relative stratifications are shown for stations providing sufficient data (Figs. 6-14 - 6-18).

The comparisons between the predicted and observed longitudinal salinity distributions are excellent. The model accurately depicts the downstream motion of the intrusion and the general depression of salinity throughout the estuary including the vicinity of the open boundary. Only on May 7 is there significant discrepancy between predictions and observations; the length of the intrusion appears to be overestimated. The data point at km 30 is likely spurious, however, as it represents an unreasonable downstream movement of the intrusion from the survey of May 2.

Predicted and observed salinity profiles also compare well. (Note that Fig. 6-12 shows observations at SBE and predictions at SBF.) Discrepancies occur primarily above km 33 for the April 28-29 surveys; near the head of the intrusion the model shows more stratification than the prototype. Lower-than-expected observed stratification in these instances may be attributed to wind mixing associated with the April 26-27 storm. On these two days daily resultant wind speeds averaged 12 m/sec - far in excess of the typical wind speeds of 1-2 m/sec for which the vertical mixing parameter was evaluated.

The time series plots (Figs. 6-14 - 6-18) most clearly show the behavior of the model in the simulation of estuarine response to the transient pulse. At kms. 21, 33, and 39, a delay occurs between the beginning of

the flow pulse (cycle 2) and the initial motion of the intrusion (cycle 5). In response to the pulse, salinity rapidly declines throughout the estuary over a period of 6-7 cycles and then holds steady in the upper estuary while continuing to decline at a lesser rate near the mouth. Salinity at all stations exhibits a secondary decline after cycle 22 in response to the May 2 storm pulse.

As with the depth-average salinities, there is a lag between the storm pulse and the onset of any change in stratification. Relative stratification is first affected at cycle 5 and increases until cycle 15. After cycle 15, stratification declines slightly to a steady value approximately four times the pre-storm level. Fig. 6-1 suggests that the increase in stratification beyond cycle 10 and the decrease after cycle 15 may be partly attributed to the influence of the spring-neap tidal cycle rather than to the storm pulse, however.

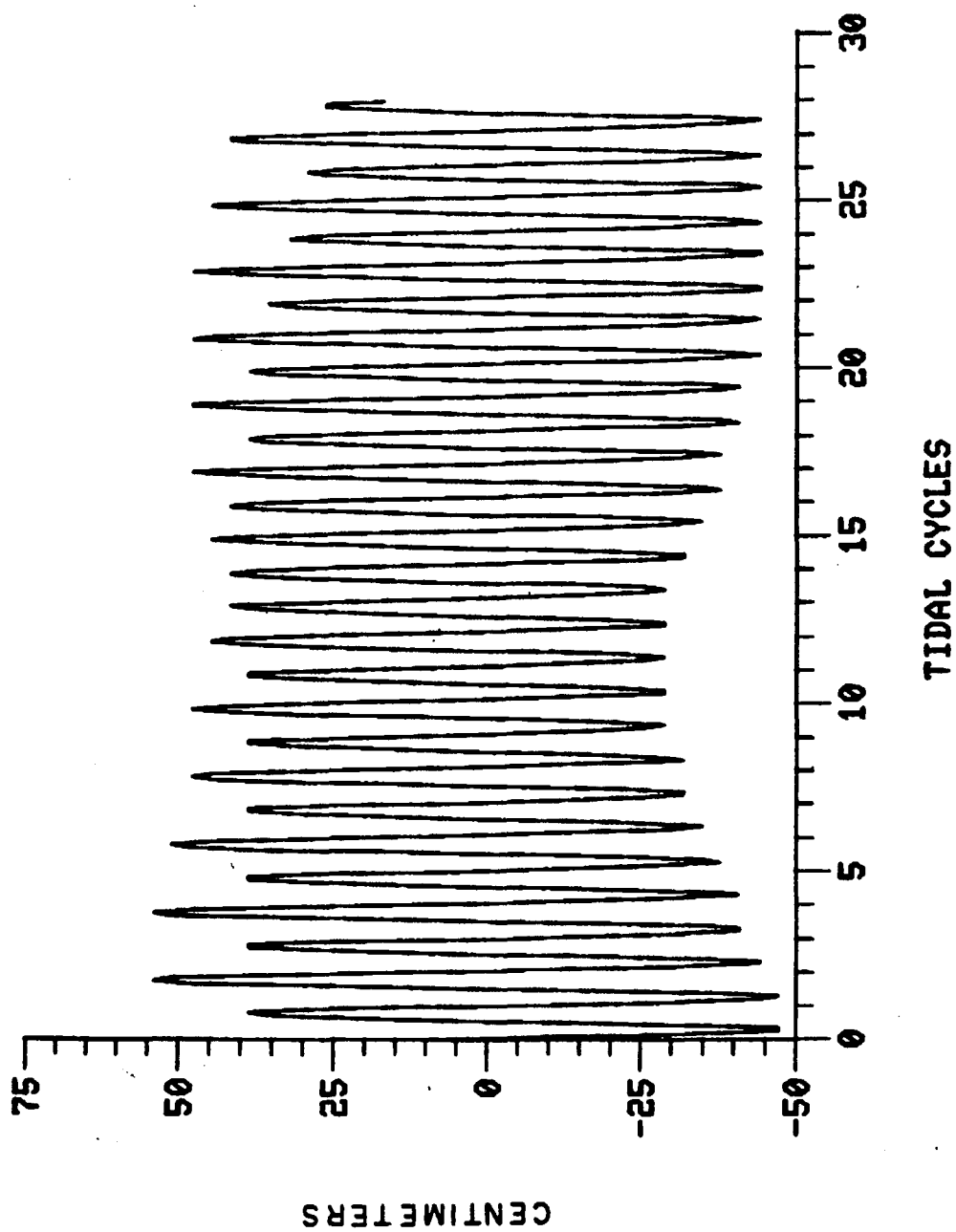


Figure 6-1. Tide Range at Km. 21, April 25 - May 9.

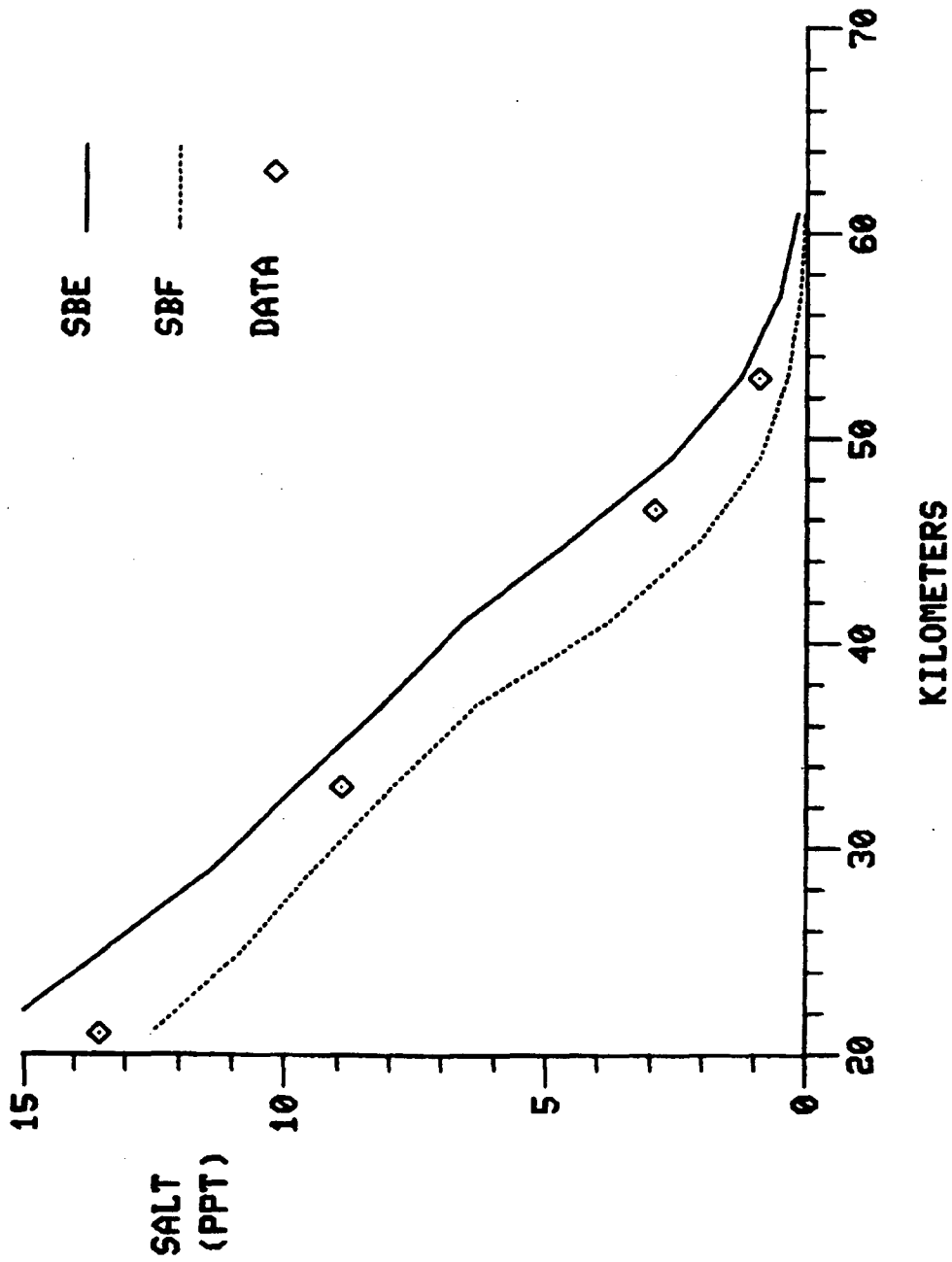
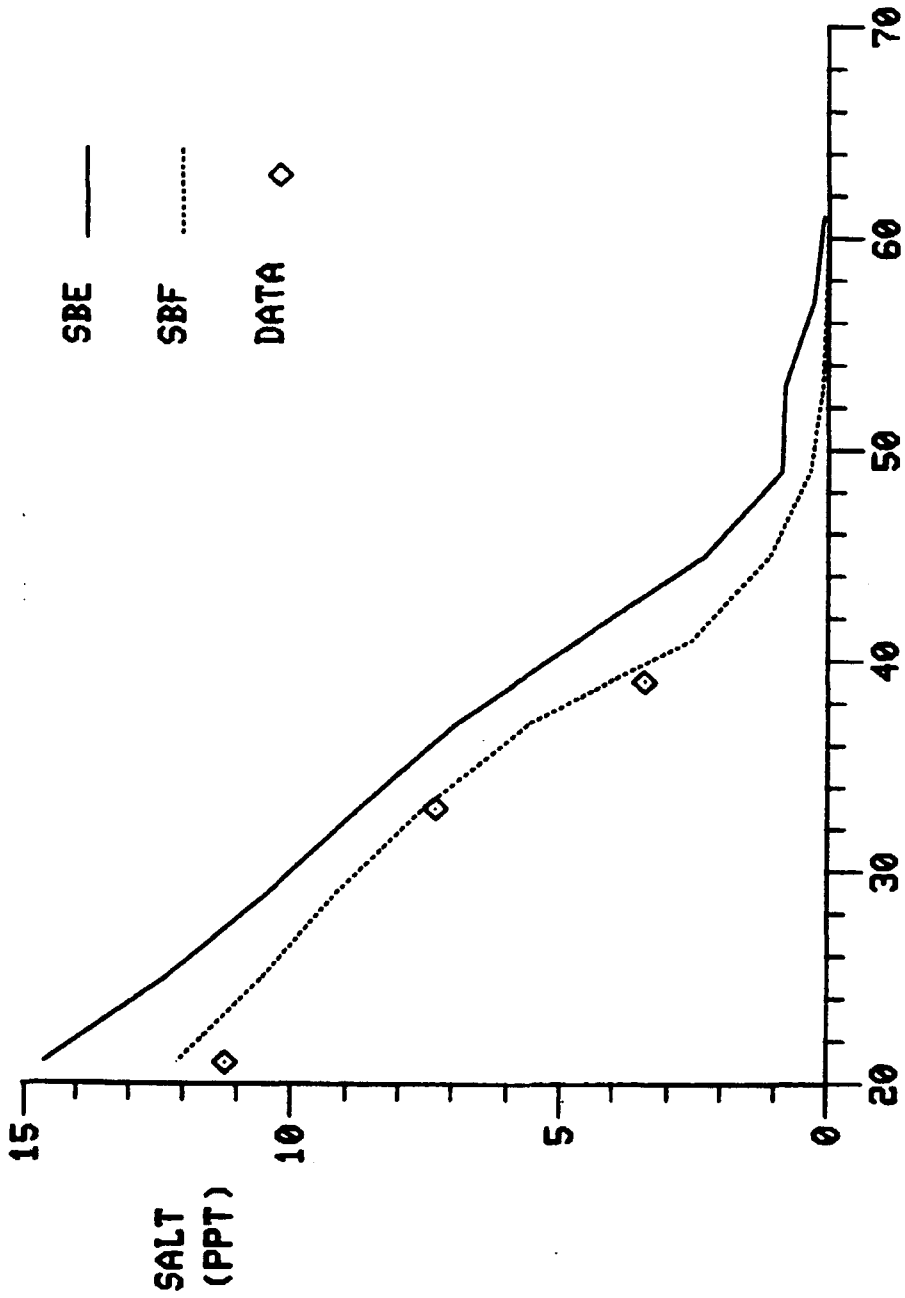


Figure 6-2. Predicted and Observed Longitudinal Salinity, April 25.



KILOMETERS
Figure 6-3. Predicted and Observed Longitudinal Salinity, April 28.

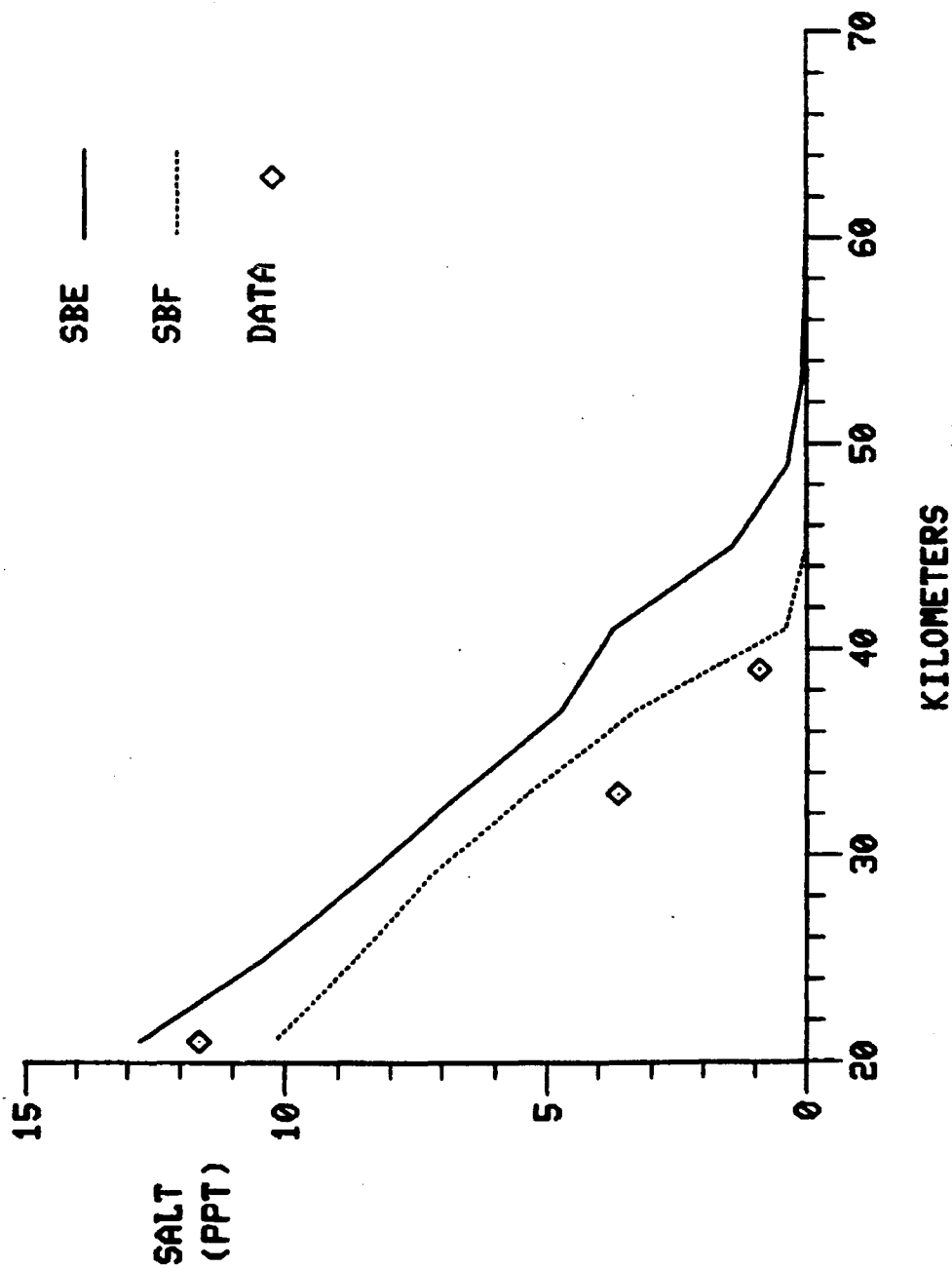
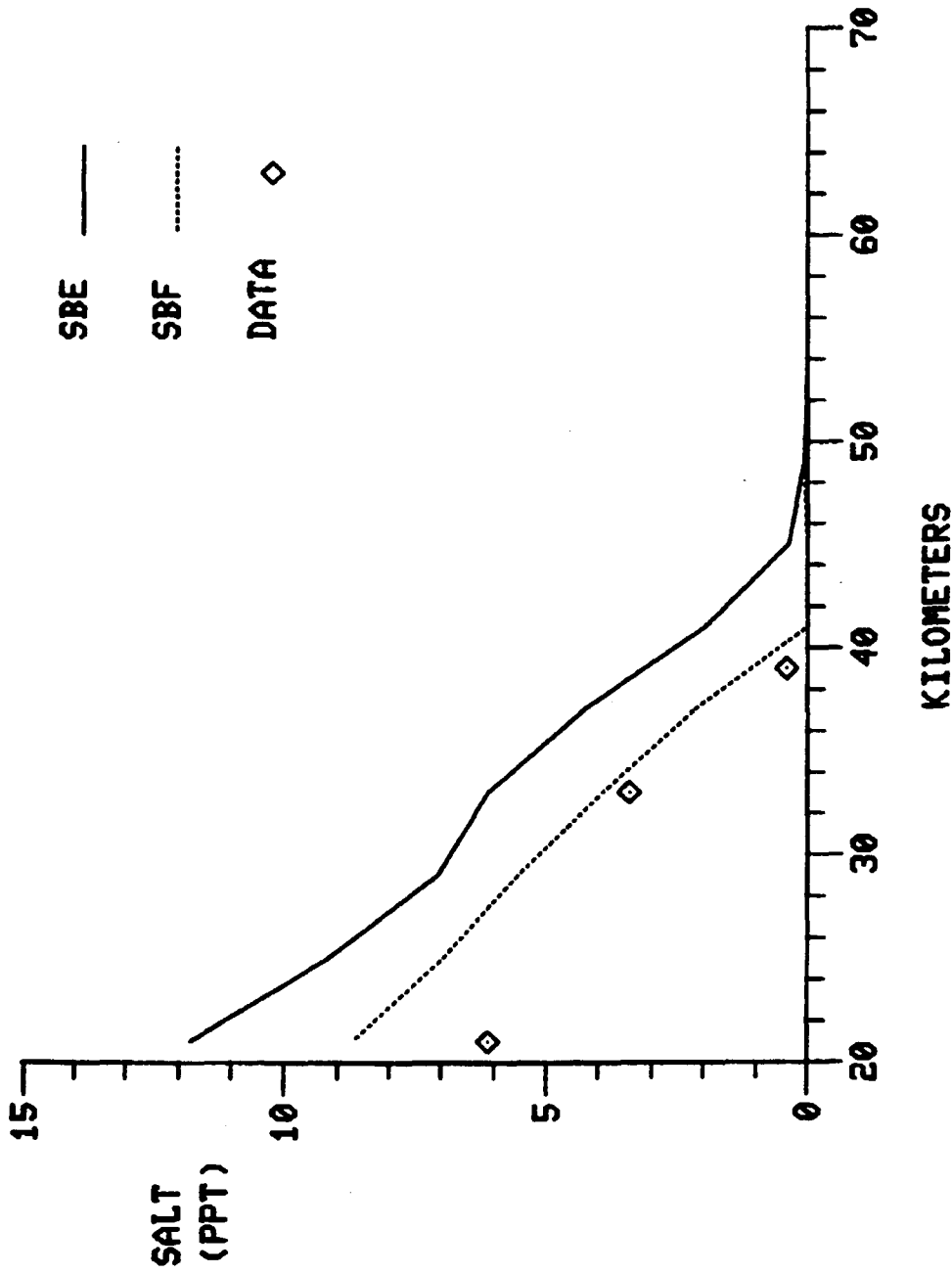


Figure 6-4. Predicted and Observed Longitudinal Salinity, April 29.



KILOMETERS
Figure 6-5. Predicted and Observed Longitudinal Salinity, April 30.

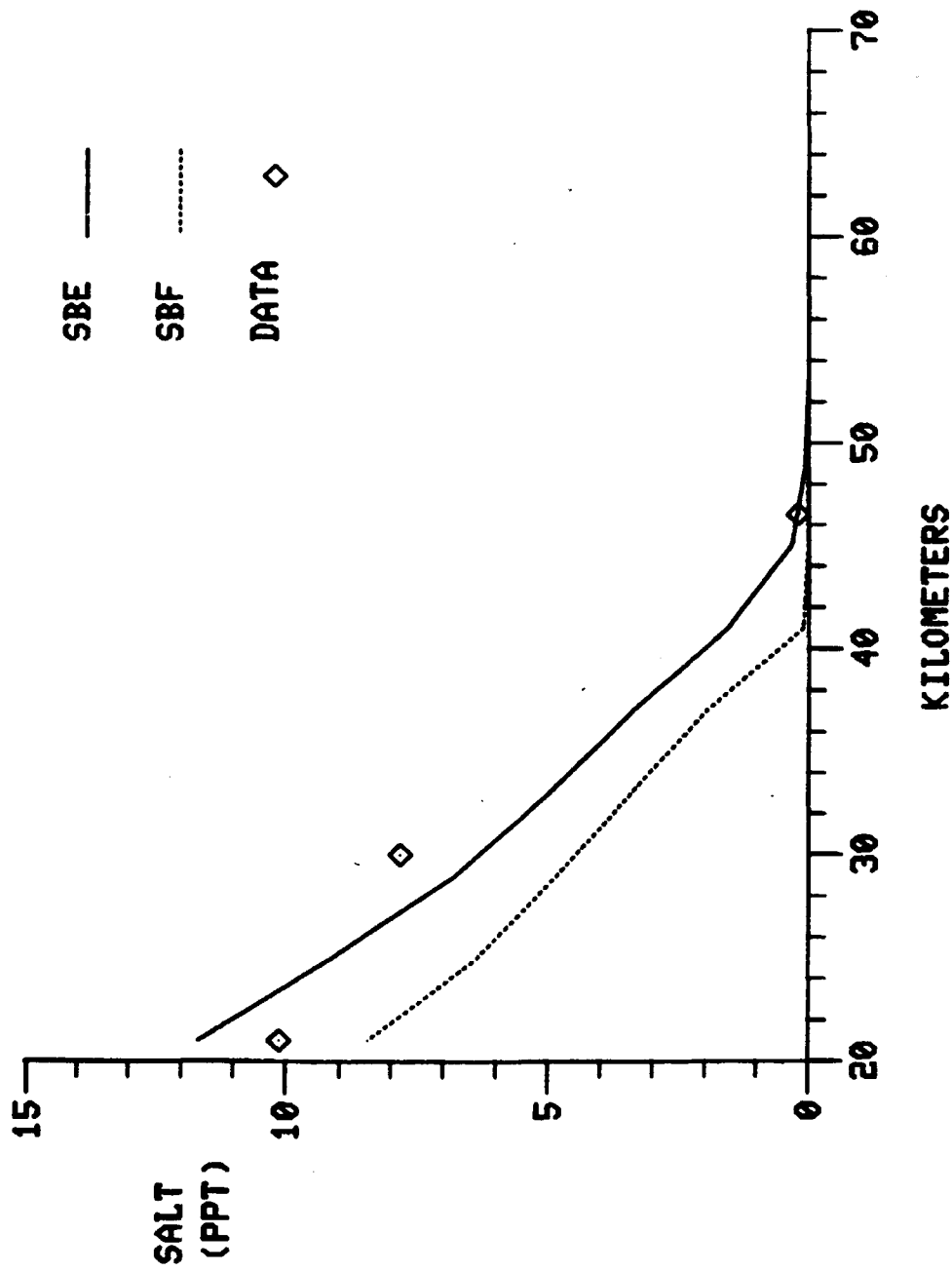


Figure 6-6. Predicted and Observed Longitudinal Salinity, May 2.

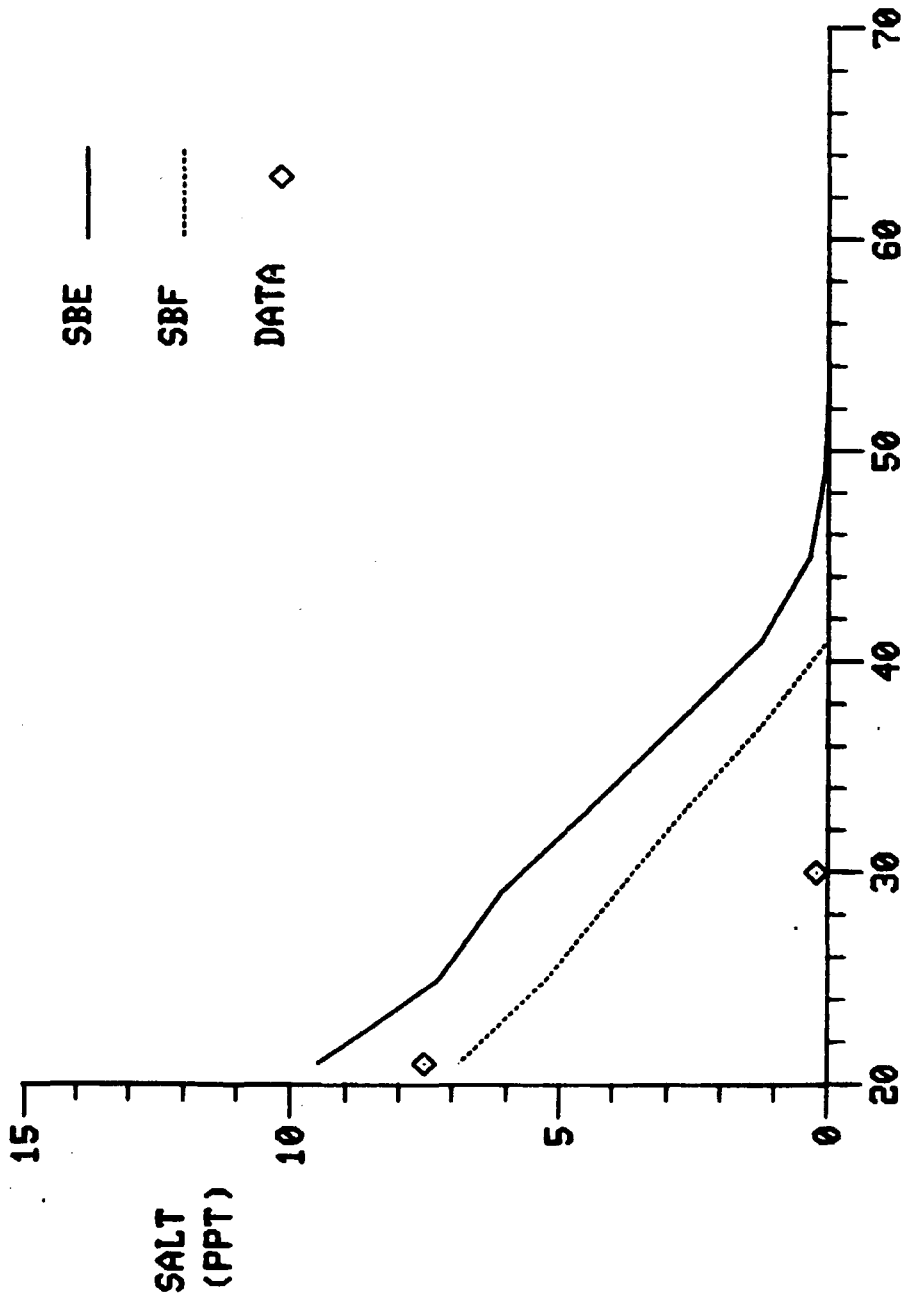


Figure 6-7. Predicted and Observed Longitudinal Salinity, May 7.

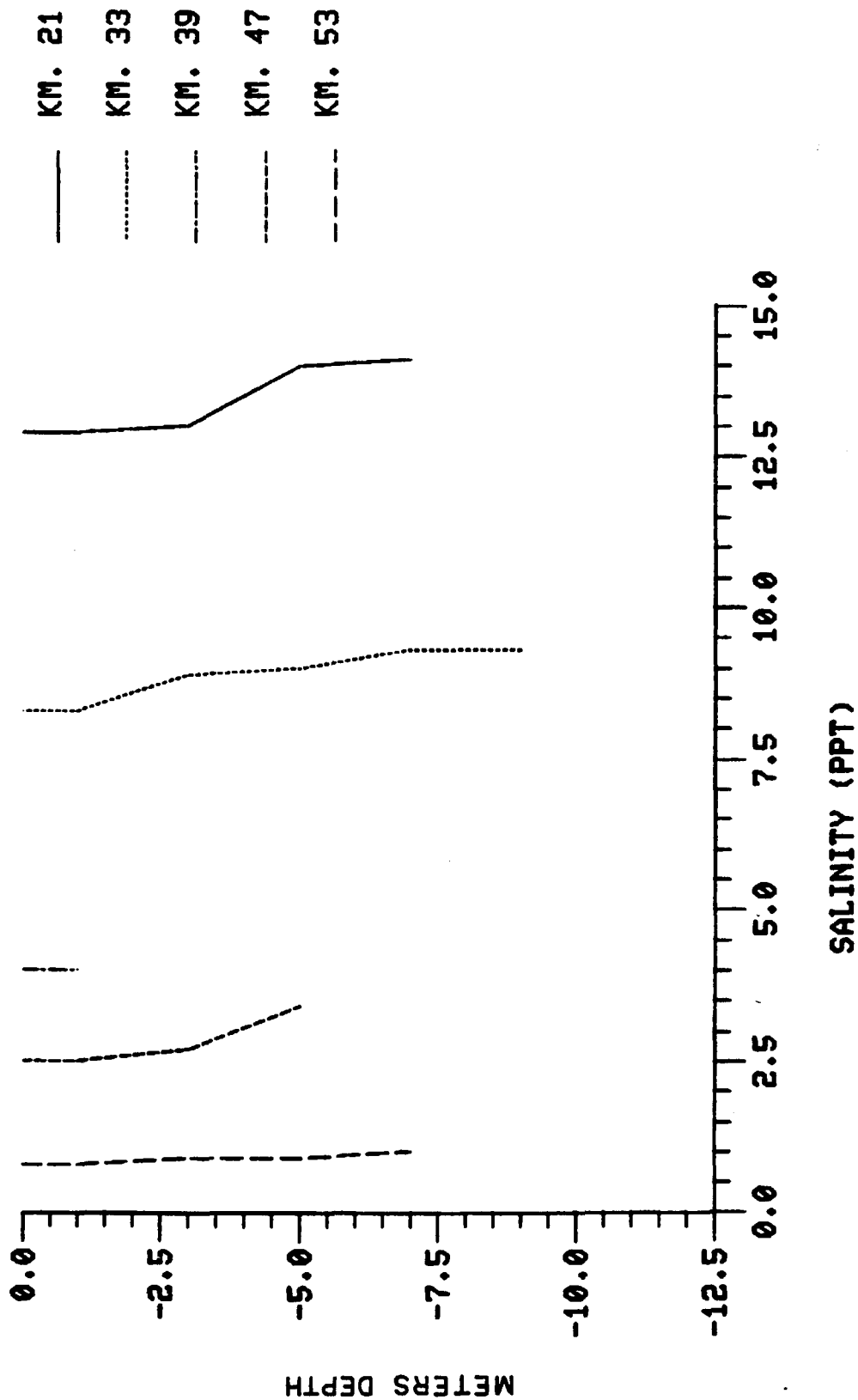


Figure 6-8a. Observed Salinity Profile April 25.

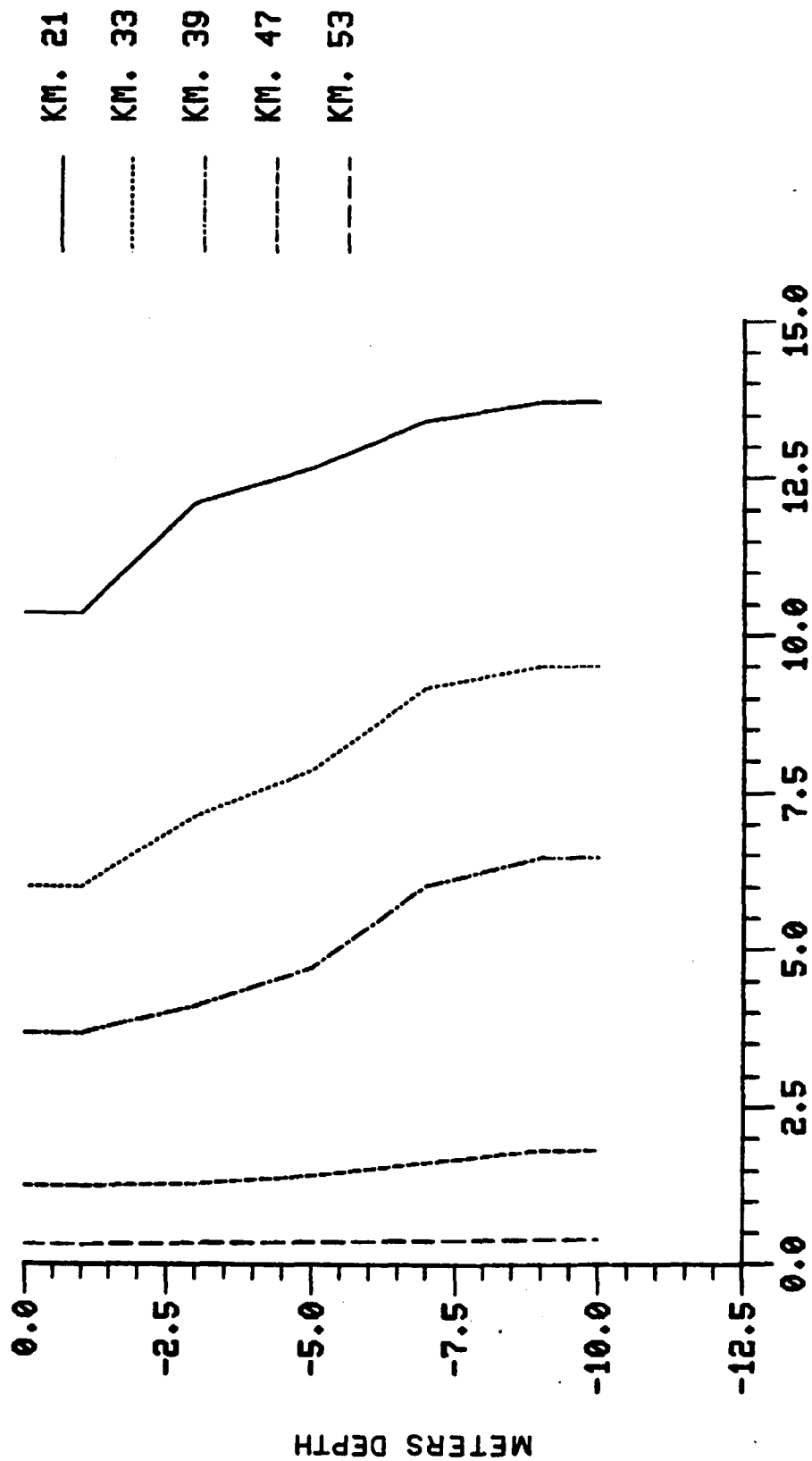
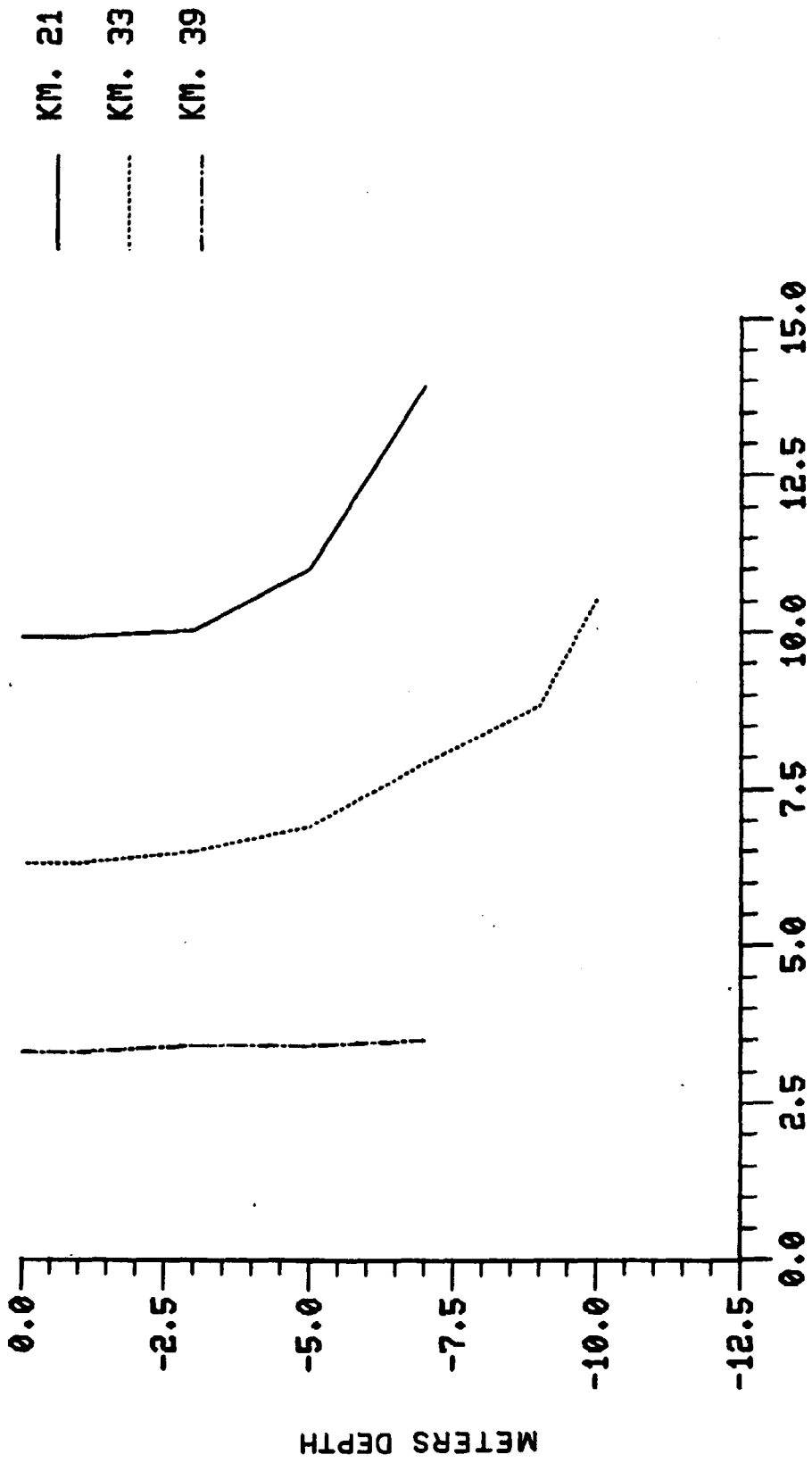


Figure 6-8b. Predicted Salinity Profile April 25

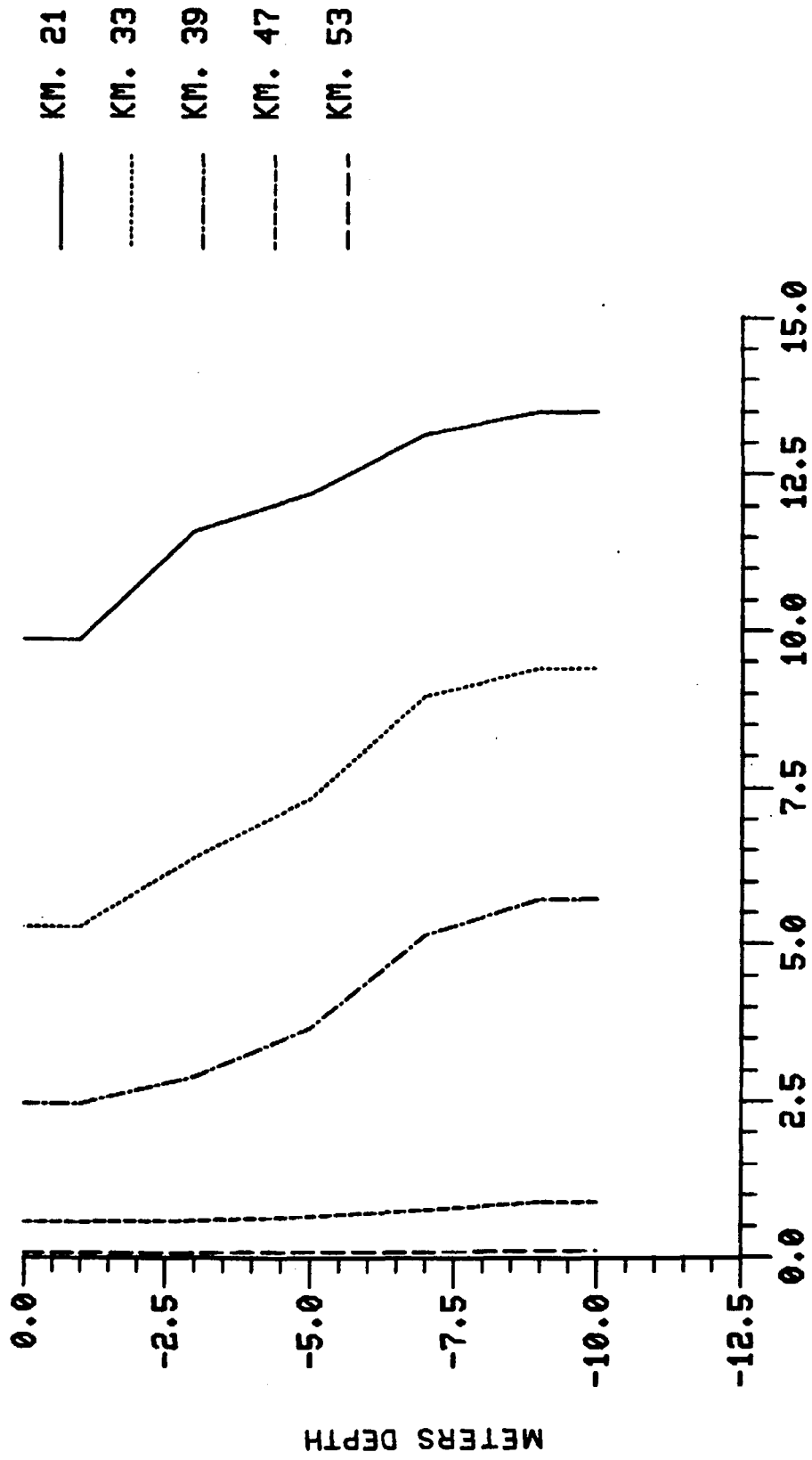
SALINITY (PPT)

METERS DEPTH

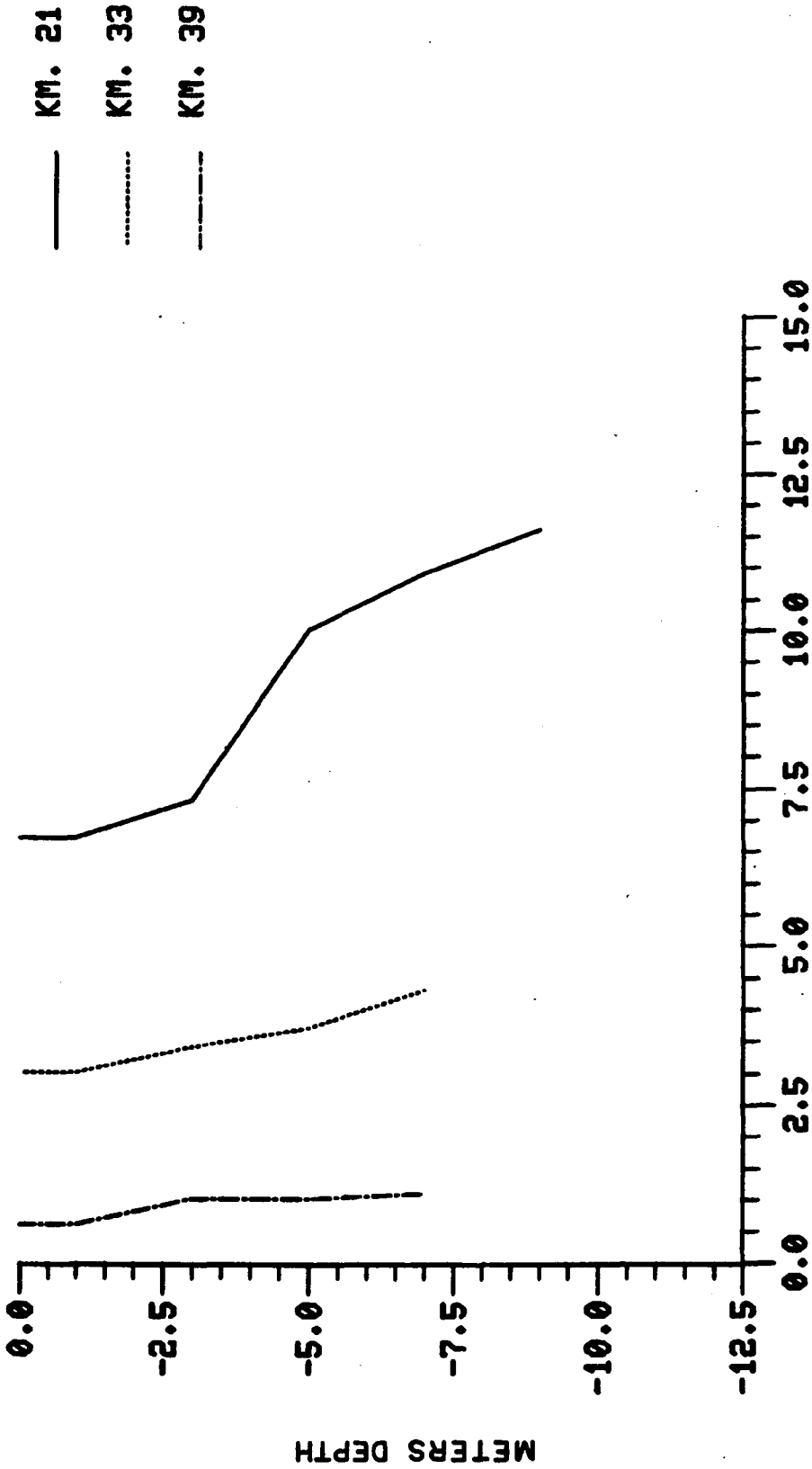


SALINITY (PPT)

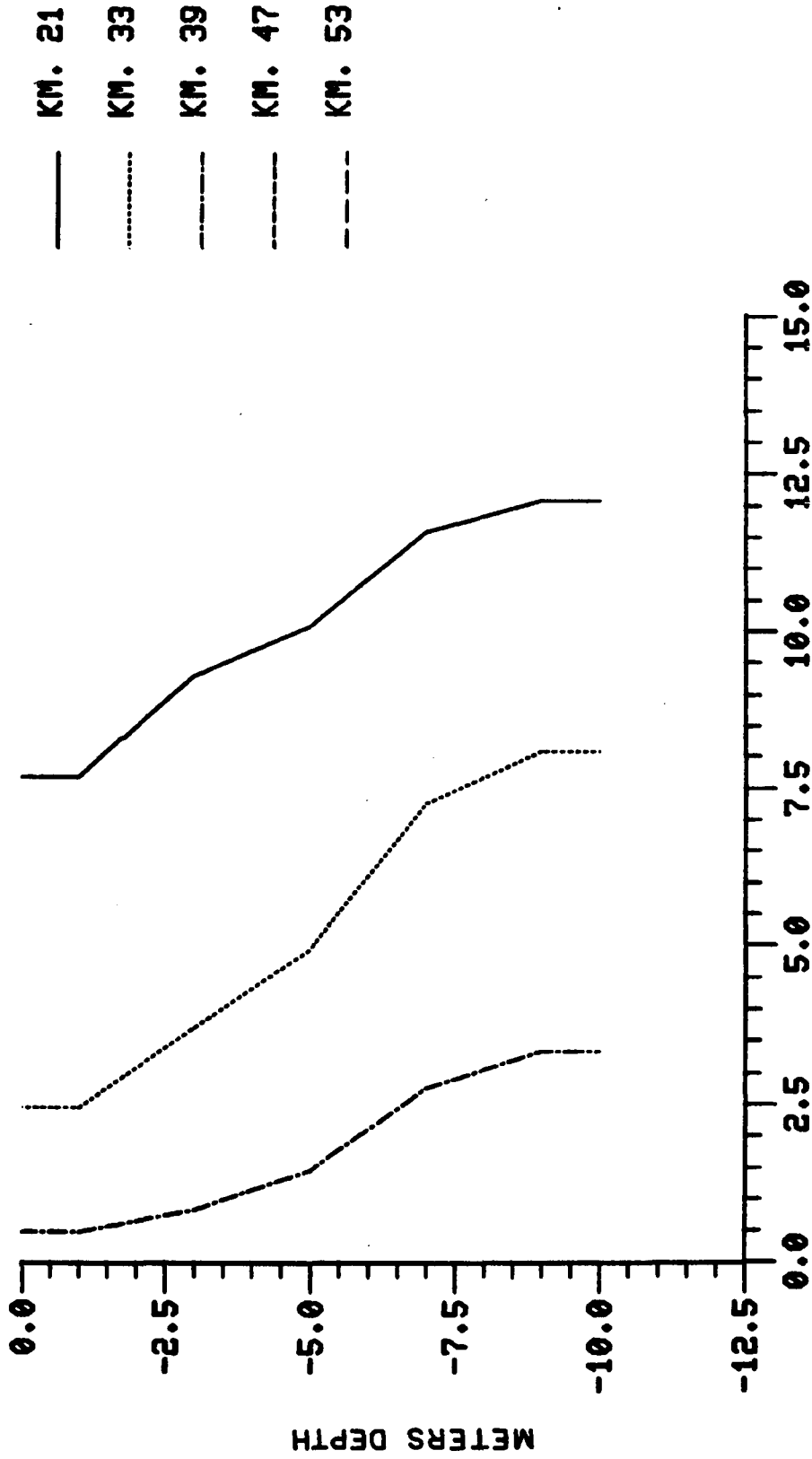
Figure 6-9a. Observed Salinity Profile April 28.



SALINITY (PPT)
Figure 6-9b. Predicted Salinity Profile April 28.

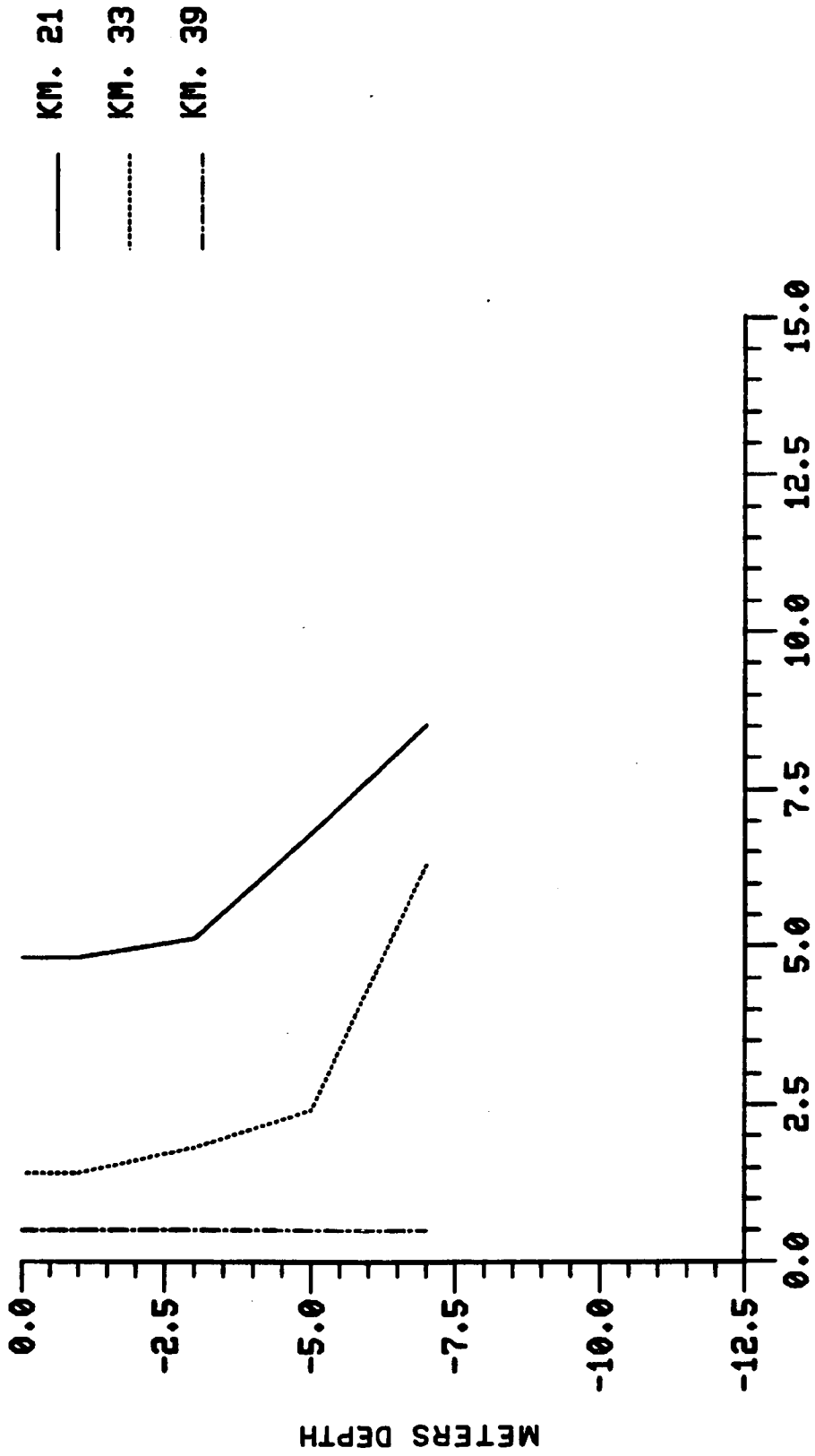


SALINITY (PPT)
Figure 6-10a. Observed Salinity Profile April 29.



SALINITY (PPT)

Figure 6-10b. Predicted Salinity Profile April 29.



SALINITY (PPT)

Figure 6-11a. Observed Salinity Profile April 30.

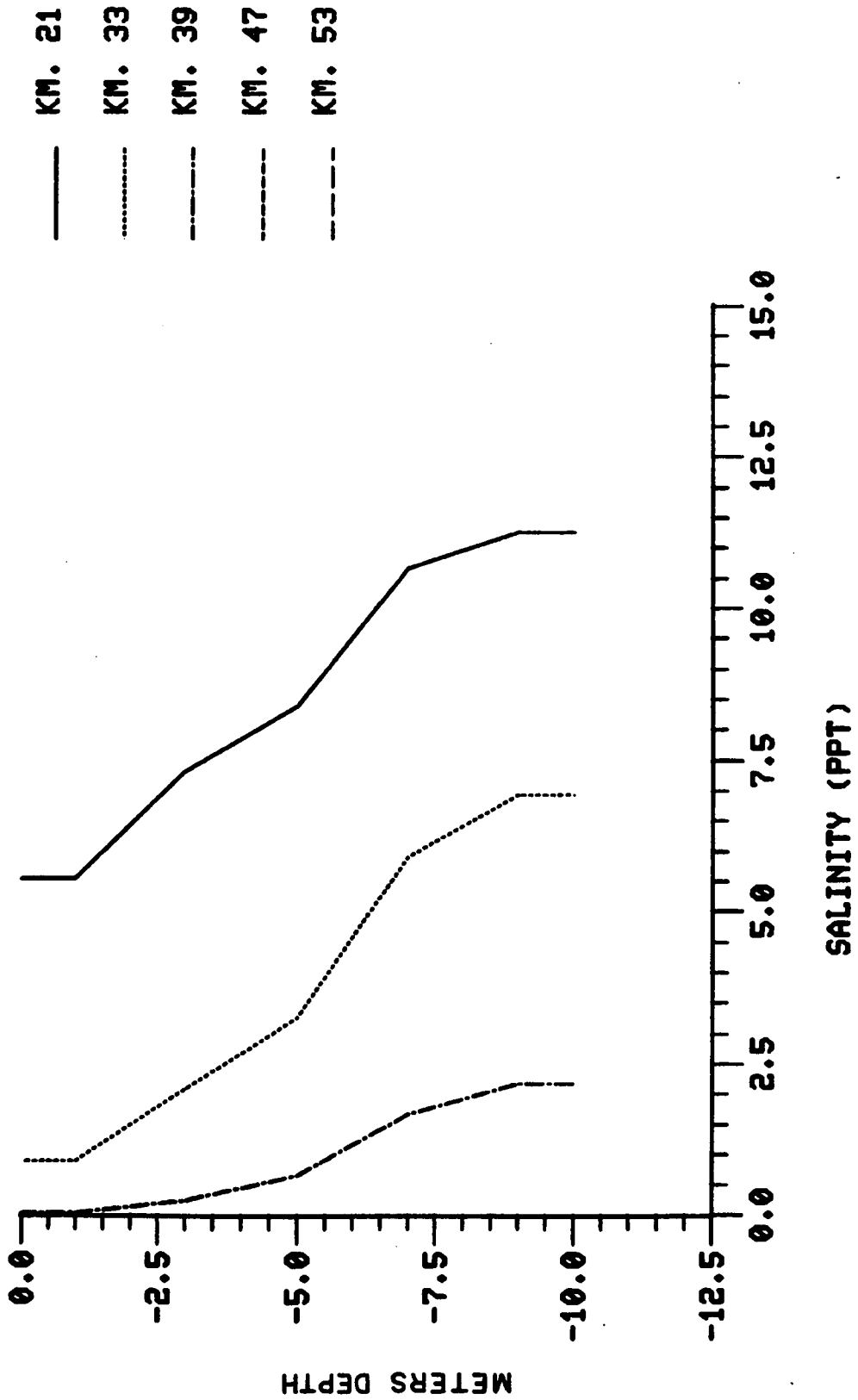
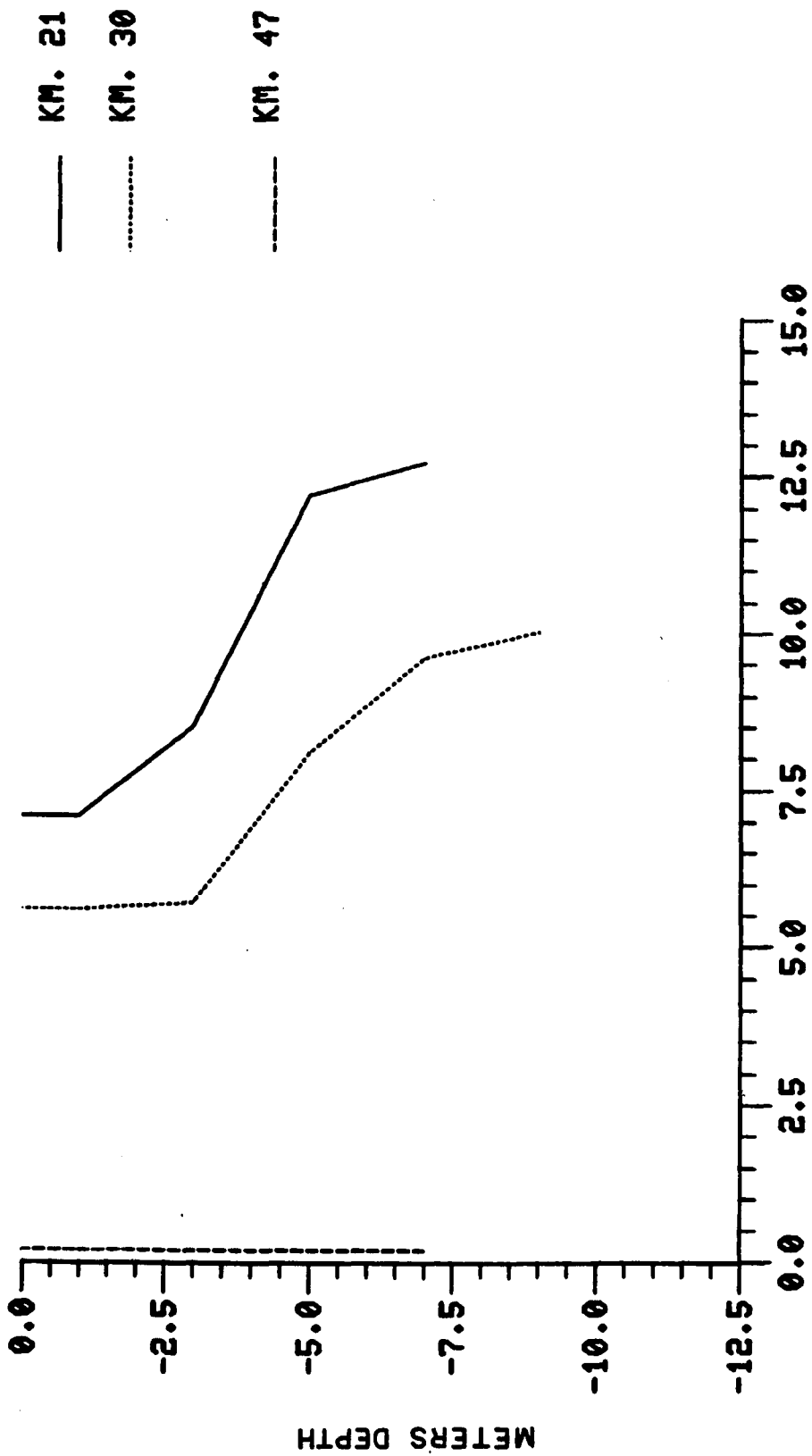
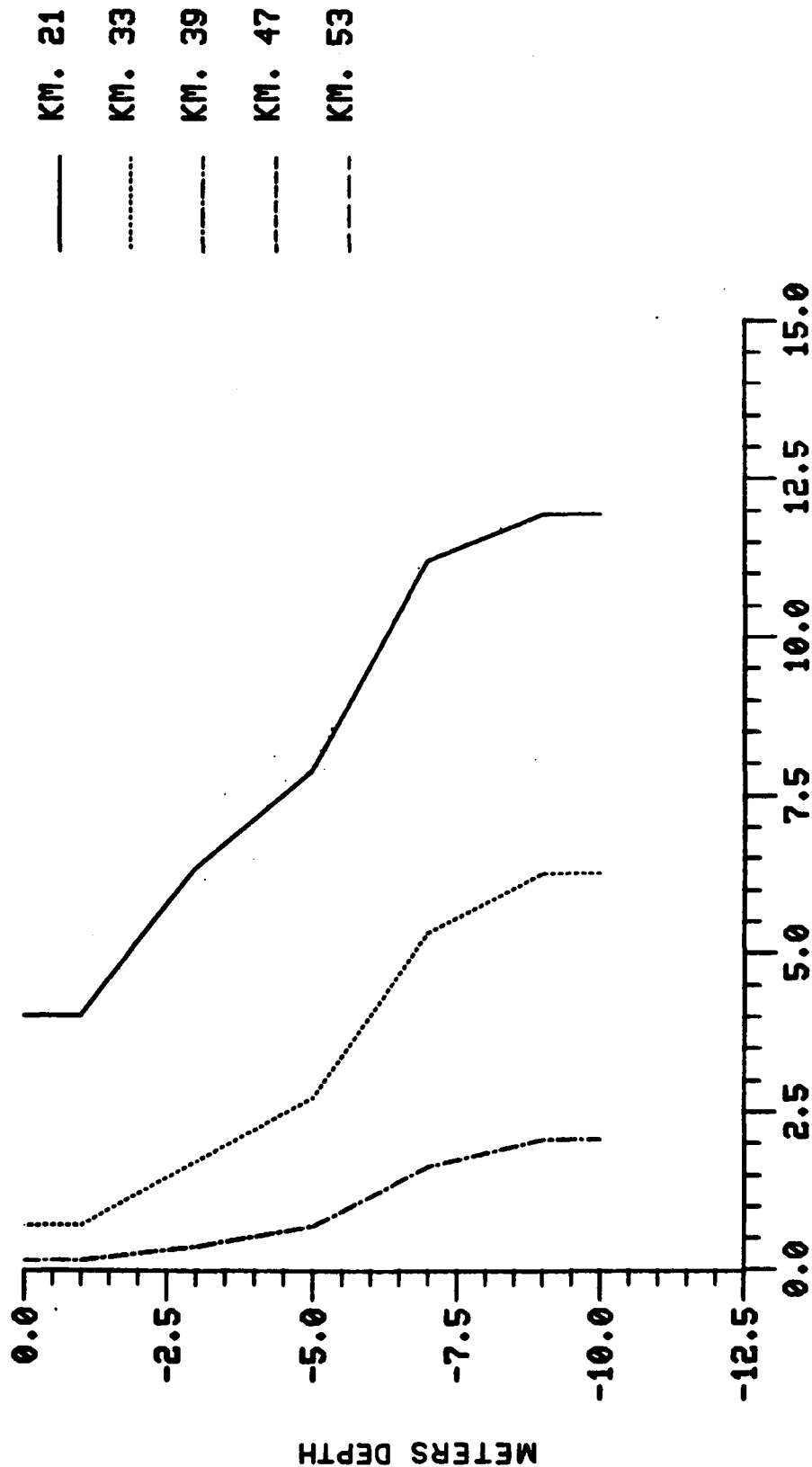


Figure 6-11b. Predicted Salinity Profile April 30.

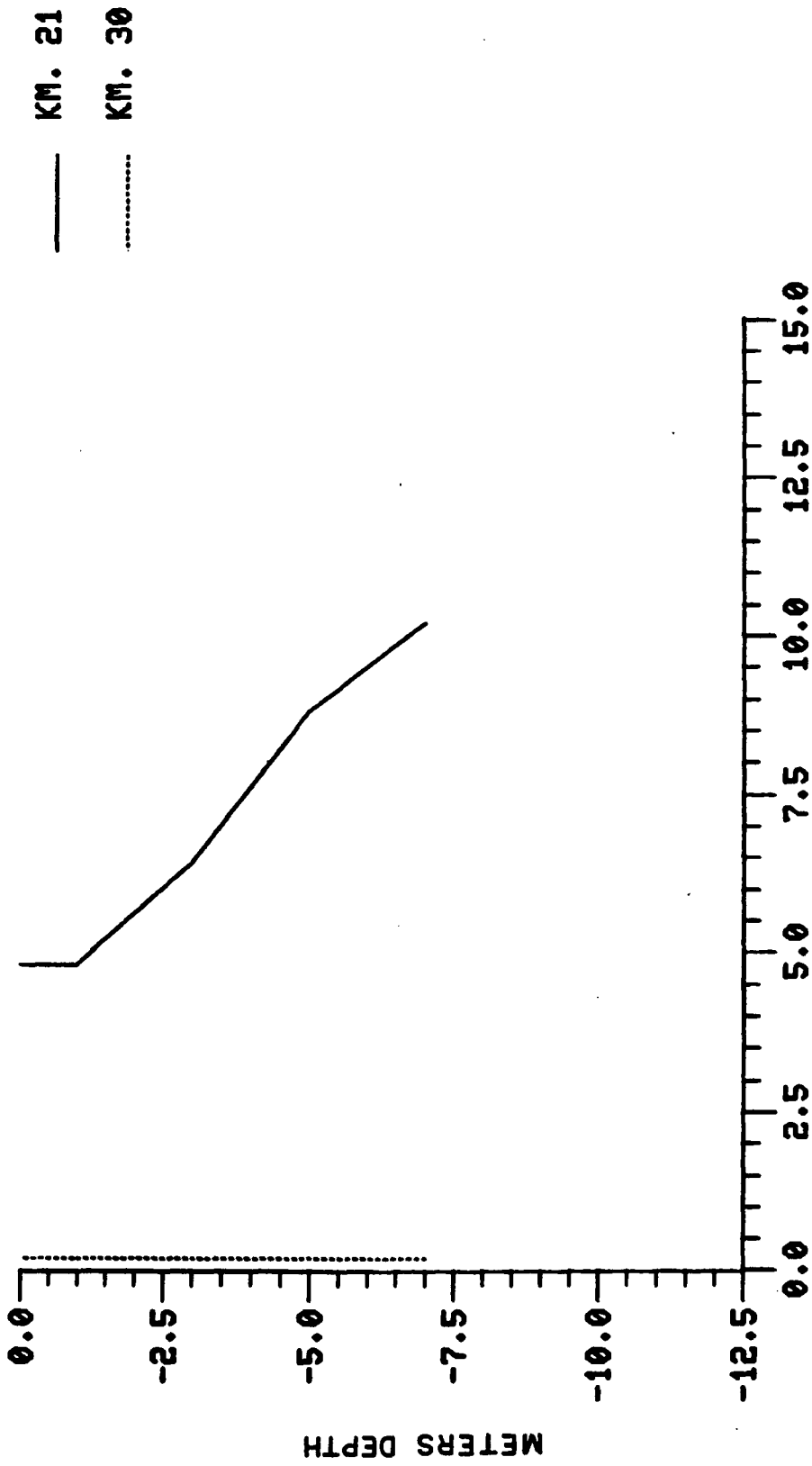


SALINITY (PPT)

Figure 6-12a. Observed Salinity Profile May 2 (SBE).

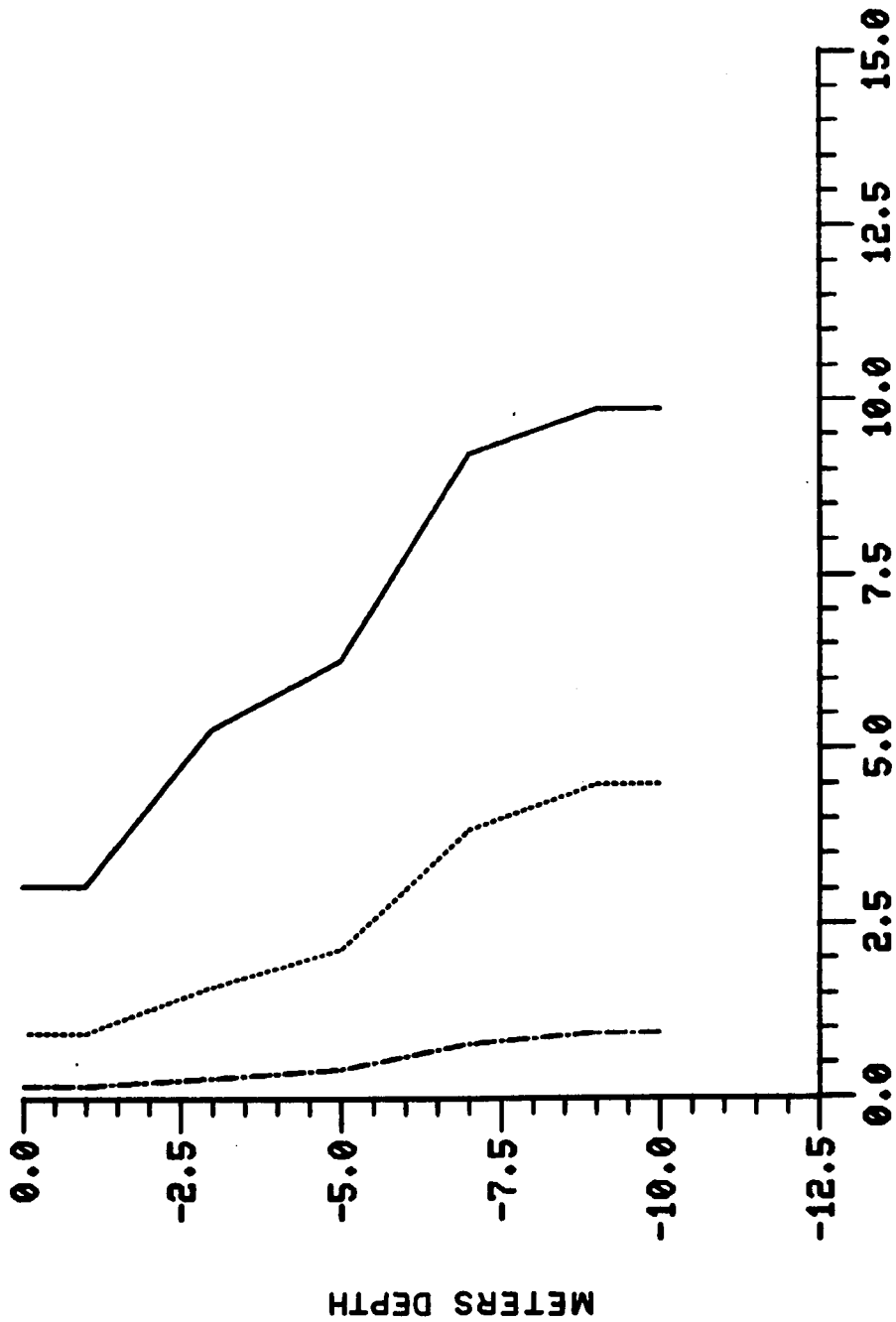


SALINITY (PPT)
Figure 6-12b. Predicted Salinity Profile May 2.



SALINITY (PPT)

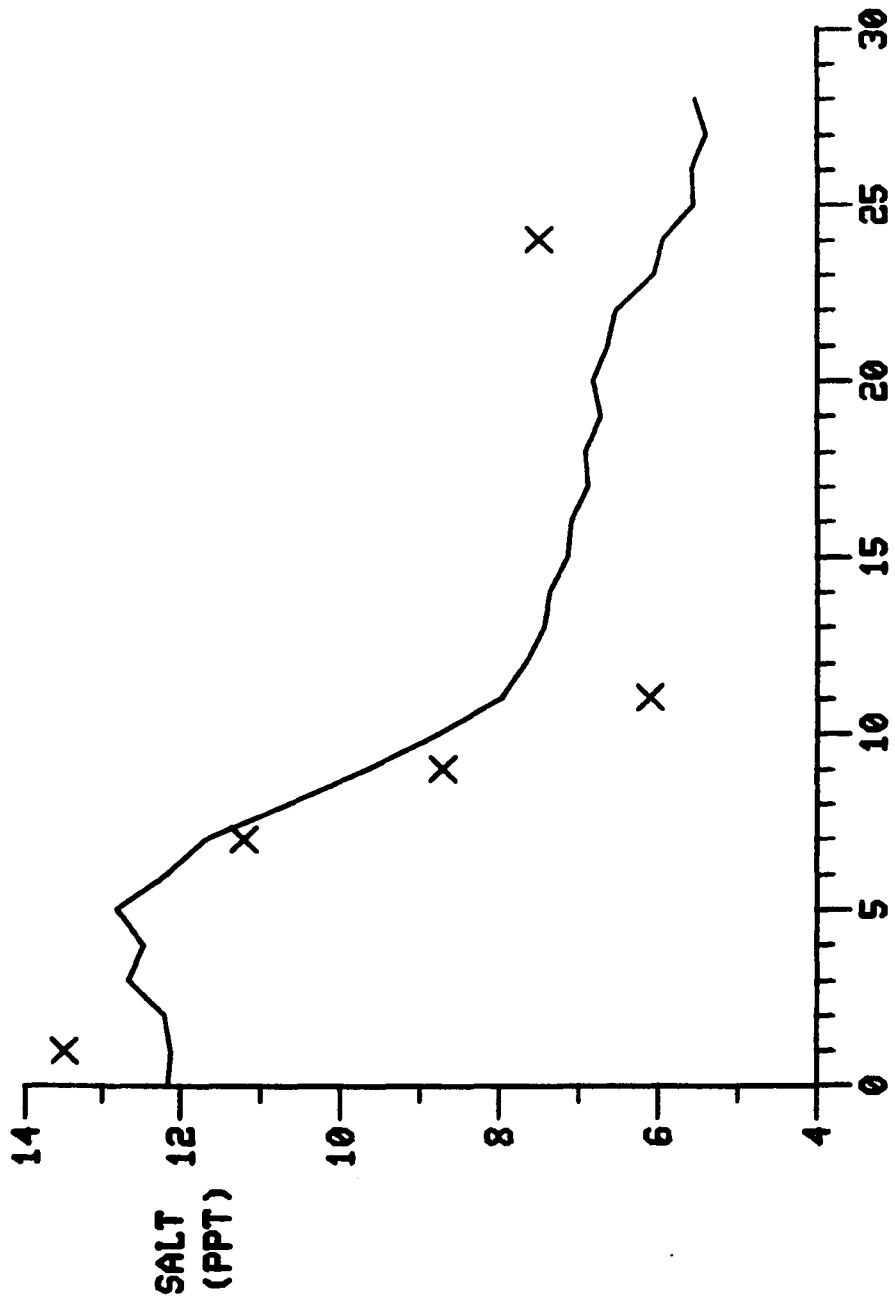
Figure 6-13a. Observed Salinity Profile May 7.



— KM. 21
 KM. 33
 - - - - KM. 39
 - - - - KM. 47
 - . - . KM. 53

SALINITY (PPT)

Figure 6-13b. Predicted Salinity Profile May 7.



TIDAL CYCLES

Figure 6-14. Predicted and Observed Salinity at Km. 21.

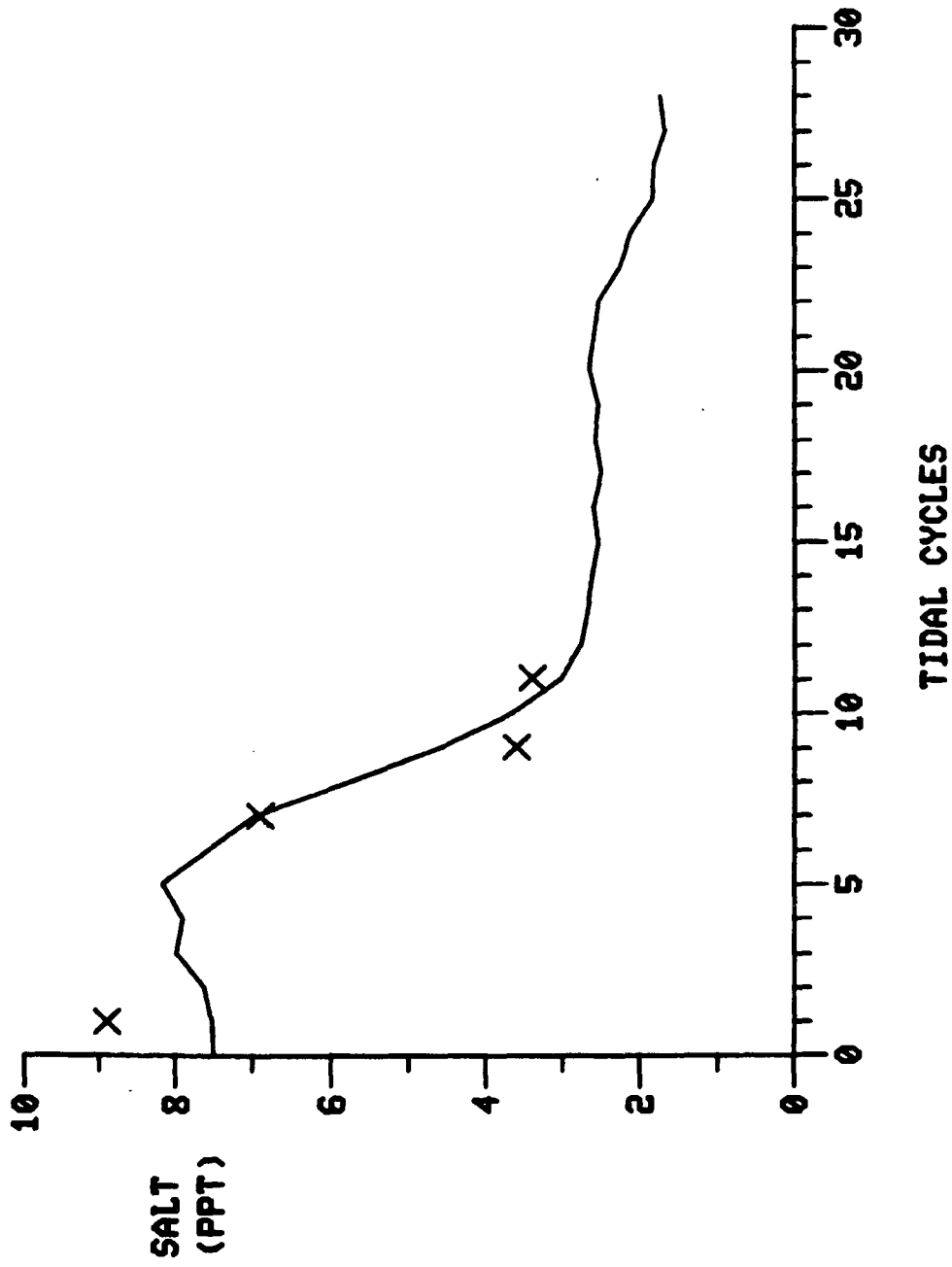
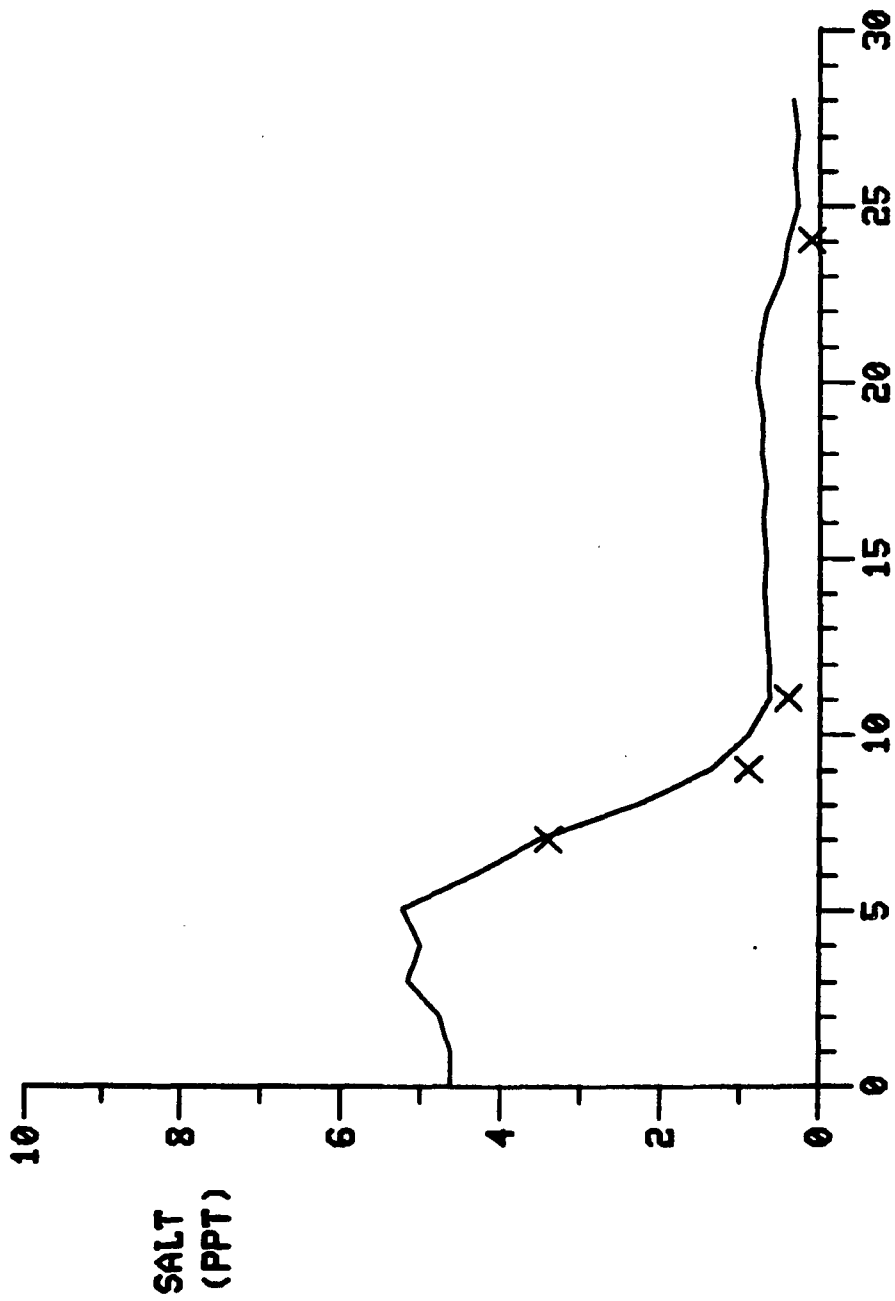
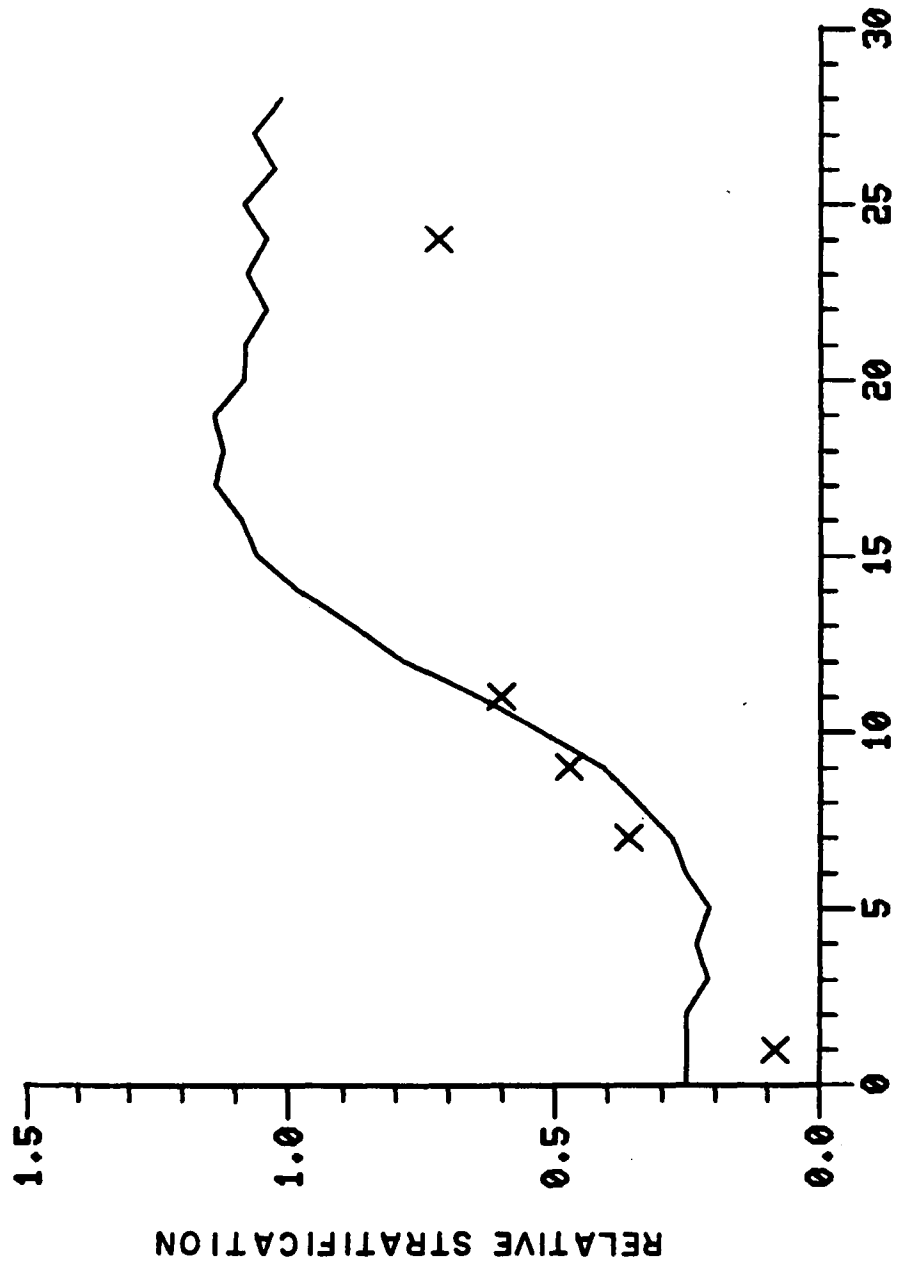


Figure 6-15. Predicted and Observed Salinity at Km. 33.



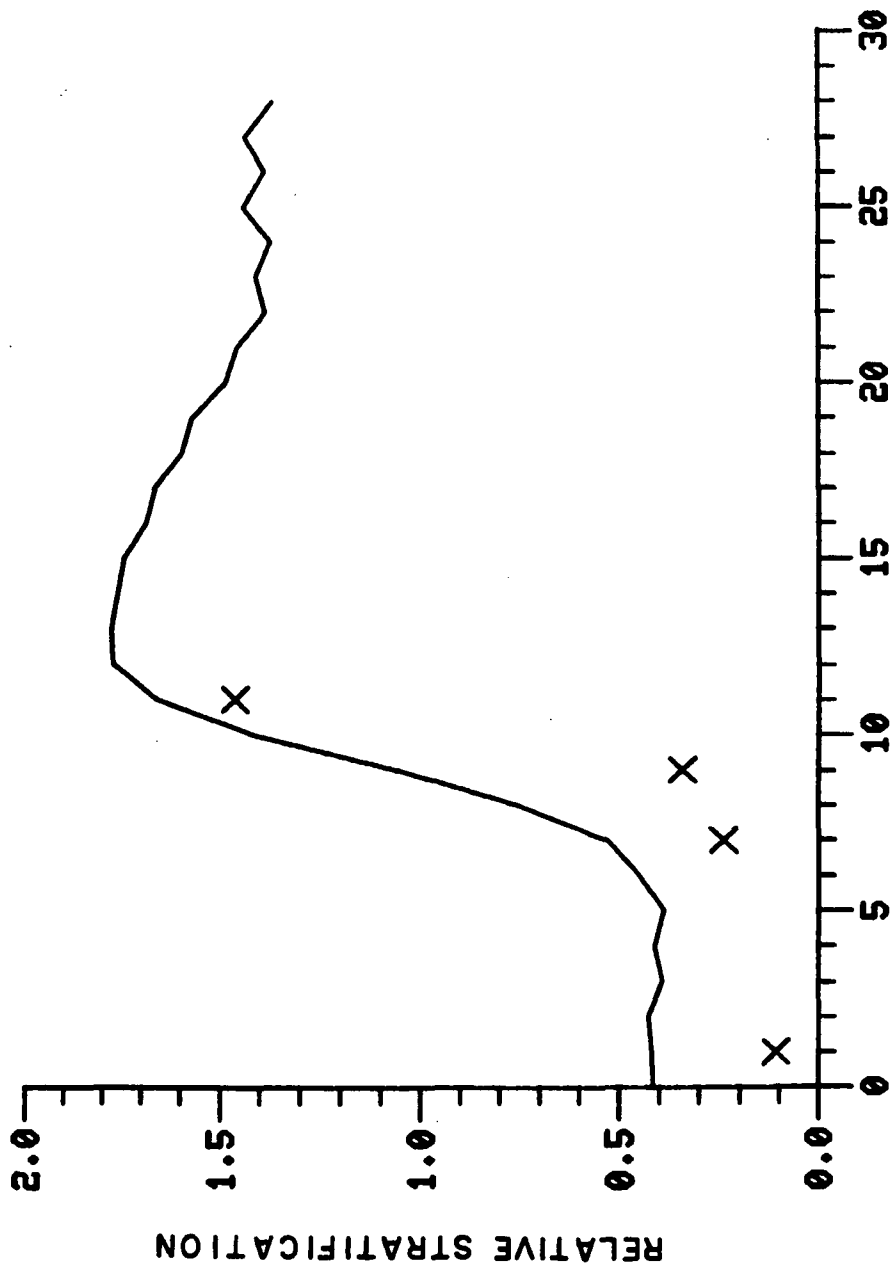
TIDAL CYCLES

Figure 6-16. Predicted and Observed Salinity at Km. 39.



TIDAL CYCLES

Figure 6-17. Predicted and Observed Stratification at Km. 21.



TIDAL CYCLES

Figure 6-18. Predicted and Observed Stratification at Km. 33.

CHAPTER VII.

EXPERIMENTS ON A MODEL ESTUARY

The first set of objectives of this study are complete. A two-dimensional, real-time estuarine model has been developed and verified in the simulation of prototype behavior. At this point, the model is available for use as an experimental tool in the examination of estuarine response to a variety of external forcing functions including wind, tide, freshwater flow, and downstream boundary conditions. A review of previous relevant studies, a description of the methodology employed in this study, and the results of the experiments are presented in the balance of this chapter.

A. Review of Previous Studies

No comprehensive investigation of the transient estuarine response to the above-mentioned forcing functions has yet been conducted. A series of analytical and numerical model studies have examined the estuarine response, in two dimensions, to some forcing functions, however, and it is useful to review these studies for comparison with the results presented herein.

Hansen and Rattray (1965) developed a pair of steady-state stream-function equations describing

circulation and salt balance in an estuary. They proceeded to solve the equations by defining three salinity regimes (Fig. 7-1). In the central regime, stratification was considered independent of location. In the inner and outer regimes, stratification was considered to decline as a function of distance from the central regime. Similarity solutions describing the vertical salinity and velocity profiles in the inner and central regimes were presented.

In the central regime, they found that the strength of gravitational circulation and the degree of salinity stratification increased as a function of the estuarine Reyleigh number.

$$Ra = \frac{gkS_o D^3}{A_v K_{ho}} \quad (7-1)$$

where

g = gravitational acceleration

$$k = \frac{1}{\rho} \frac{\partial \rho}{\partial s}$$

S_o = reference salinity

D = depth of channel

A_v = vertical eddy viscosity

K_{ho} = reference value of longitudinal dispersion

Stratification was also found to be inversely proportional to a mixing parameters, M , which denotes the ratio of vertical mixing to runoff-induced stratification

$$M = \frac{K_v K_{ho} B^2}{R^2} \quad (7-2)$$

where

K_v = vertical diffusivity

B = width of channel

R = freshwater flow

Hansen and Rattray presented a series of figures illustrating the modification of the velocity and salinity profiles by surface wind stress. A wind directed downstream was noted to increase net upstream circulation in the lower layer and to increase salinity stratification. An upstream-oriented wind decreased upstream circulation in the lower layer and decreased stratification.

Festa and Hansen (1976) investigated the effects of altering depth and river discharge on estuarine circulation by means of a steady-state two-dimensional model based on vorticity and salt-balance equations. They found that decreasing the river discharge allowed the salt intrusion and null-velocity point to move upstream. Although estuarine circulation weakened, it became more extensive as runoff decreased.

Depth was parameterized in their model through the Reyleigh number (eq. 7-1). Increasing the depth (and hence, Ra) resulted in increased circulation and inward migration of the salinity intrusion and null-velocity point.

A two-dimensional semi-implicit model was employed by Wang and Kravitz (1980) to examine the response of the Potomac River to an oscillating wind stress. Their work demonstrated that gravitational circulation in the Potomac could be completely masked by a surface stress of 0.25 dynes/cm^2 . Salinity was also subject to substantial change. Stratification was large at the end of a down-river wind event and small at the end of an up-river event.

B. Experimental Procedure

The goal of the experiments described herein is to investigate and describe the transient response of the salinity structure of a partially-stratified estuary to a variety of forcing functions. An investigation employing a verified model is ideal for a study of this nature since individual forces and responses may be examined while all other external influences are held constant. Since the numerical model solves the complete, time-variable equations of estuarine dynamics, a transient solution is available based on variable rather than constant parameters as in an analytic solution.

In order to free the results from the effect of channel geometry, an idealized estuary of constant depth and cross-section is hypothesized. The channel cross-section is trapezoidal, however, rather than rectangular, since preliminary experiments showed that unrealistic

velocity profiles resulted when bottom drag was transferred to the surface layers solely through viscous forces rather than by friction in shoal areas. The geometry, flow, and other characteristics of the idealized estuary are based roughly on those of the James River and are presented in Table 7-1. Eddy parameters and friction are the same as those used in the James River Model.

Before conducting the experiments, the model of the hypothetical estuary was first run until a steady state was attained (approximately 100 tidal cycles). These steady-state conditions are shown divided into salinity regimes in Fig. 7-1 and as longitudinal and vertical salinity distributions in Figs. 7-2 and 7-3. The steady-state conditions were employed as initial conditions in a series of model runs in which step-like forcing functions were introduced and held constant throughout the model run. In a second series of runs, pulse-like forcing functions were introduced for a short period and then restored to their original values. Step functions examined include wind, tidal amplitude, freshwater flow, and downstream boundary conditions. Pulse functions were wind and freshwater flow. An investigation of the spring-neap tidal cycle was also conducted in the series of pulse runs.

Results are shown graphically in several forms. For the step-function runs, depth-average longitudinal

Table 7-1. Characteristics of Idealized Trapezoidal Estuary

Length	160 km
Depth	10 m
Width at 1 Meter Depth	3000 m
3 Meters Depth	1800 m
5 Meters Depth	1000 m
7 Meters Depth	500 m
9 Meters Depth	200 m
Freshwater Flow Rate	150 m ³ /sec
Tide Range at Mouth	1 m
Salinity at Mouth	20 ‰

SBF salinity at the end of the model run and at initial steady state are first compared. Next, the SBF vertical salinity profile at the end of the sensitivity run (for comparison with Fig. 7-3) is shown. For both step-function and pulse-function runs, time series of SBF depth-average salinities and salinity stratifications are presented from among plots available at kms 20, 44, 68, and 92. The time-series plots of stratification show the surface and bottom salinity and the top-to-bottom difference on two vertical axes. The left axis is scaled for the surface and bottom values. The right axis is scaled for the bottom minus the surface salinity. Finally, a time-series plot of the location of the head of the salt intrusion, defined as the kilometer of the 1‰ isohaline, is shown.

C. Response to Step Functions

1. Wind - Wind velocity was converted to surface shear stress through the equation

$$\tau = C_D \rho_a V |V| \quad (7-3)$$

where

$$\begin{aligned} \tau &= \text{shear stress (dyne/cm}^2\text{)} \\ C_D &= \text{drag coefficient} \approx 10^{-3} \\ \rho_a &= \text{density of air} \approx 1.3 \times 10^{-3} \text{ gm/cm}^3 \\ V &= \text{wind speed (cm/sec)} \end{aligned}$$

By eq. (7-3), a wind speed of 1 m/sec yields a surface shear stress 0.013 dyne/cm². Initial model runs employing this value showed no discernable change in

salinity after 40 tidal cycles. A second series of runs was made using a shear stress of 0.33 dyne/cm^2 , corresponding to a wind speed of 5 m/sec (equivalent to the wind speed during the August 1977 wind event detailed in Chapter V). Wind was directed upstream for 80 tidal cycles in the first run (Figs. 7-4a - 7-4g) and downstream for 80 tidal cycles in the second run (Figs. 7-5a - 7-5g).

It can be seen that the effect of a 5 m/sec wind is immediate and dramatic. The upstream wind acts to reduce salinity throughout the estuary, moving the salt intrusion downstream, while the downstream wind acts to increase the estuarine salinity and moves the salt intrusion inland.

The upstream wind initially causes estuarine destratification. The destratified state is maintained in the central portion of the estuary (km 44) but near the mouth (km 20) the estuary restratifies after approximately 40 cycles and eventually attains greater stratification than in the initial conditions.

The downstream wind causes a brief, small decline in salinity and stratification in the lower and central portions of the estuary followed by a rapid increase in stratification. Near the mouth, stratification reaches a maximum and then declines, approaching a steady-state condition lower than the initial stratification. Near the head of the intrusion, however, stratification

continues to increase beyond 80 tidal cycles.

The initial response of the model estuary to wind stress is readily interpreted and is consistent with the results of Hansen and Rattray (1965) and Wang and Kravitz (1980). The upstream wind initially increases salinity near the surface as it impedes downstream transport. By the principle of continuity, as downstream surface transport is reduced, upstream gravitational circulation in the lower layer is also reduced, leading to lower salinities upstream. This effect is enhanced by reduced stratification which leads to larger eddy viscosity and diffusivity which further impede upstream circulation and short-circuit the upstream transport of salt.

The brief slight decline in salinity and stratification caused by the downstream wind is due to initial transport of salt out of the estuary. As downstream transport in the surface layer is enhanced, however, upstream circulation in the lower layers increases causing landward migration of the salt intrusion and increasing salinity in the lower layers upstream. Stronger stratification augments this effect by leading to diminished viscosities and diffusivities and thereby reducing frictional resistance to upstream circulation and the short-circuiting of salt transport.

The long-term effects of the wind forcing (e.g. the increase of stratification at km 20 under the upstream wind and the decrease of stratification under the

downstream wind) are less readily interpreted by conventional theory of the effects of wind on estuarine stratification. The long-term effects on stratification opposite to the short-term effects are due to migration of the salt intrusion and changes of zonation within the estuary. As the upstream wind moves the salt intrusion seaward, stratification at km 20 undergoes a transition in characterization from the outer to the central regime, accompanied by increased stratification. Conversely, a downstream wind transfers the central regime upstream and decreases stratification at km 20. A similar process is responsible for the continuous increase in stratification at km 92 during the downstream wind event. As the salinity intrusion is pushed upstream, km 92 changes in characterization from the reduced stratification of the inner regime to the increased stratification of the central regime.

The long-term effects due to wind described above are unlikely to be observed in a prototype since a steady wind directed along the axis of an estuary for 40 or more tidal cycles is unrealistic. An important characteristic of the response to forcing functions may be derived from these two experiments, however: The short-term response of stratification to a forcing-function may be augmented or opposed by long-term motions of the salinity intrusion.

2. Tide - The estuarine response to tide was analyzed in two model runs in which tide range at the mouth

was increased from 50 cm to 75 cm and decreased from 50 cm to 25 cm, respectively. Results of these runs are shown in Figs. 7-6a - 7-6g and 7-7a - 7-7g.

It can be seen that the increase in tidal amplitude leads to a rapid reduction in estuarine stratification. Salinity declines, and the salt intrusion moves seaward. Decreasing the tidal amplitude results in an increase in stratification, higher salinity, and landward movement of the salt intrusion. (Note that the small discontinuity in the time series of cycle 1 is an artifact caused by the way tide is handled in the model. A smooth curve should be visualized from cycle 0 to cycle 2.)

The response of the salinity structure to tidal forcing may be understood by noting that eddy viscosity and diffusivity are dependent upon instantaneous velocity (eqs. 4-15 - 4-16). As the tidal prism is enlarged or reduced, tidal currents increase or decrease resulting in corresponding changes in viscosity and diffusivity. The effect is magnified by the nature of the eddy function: e.g. increased diffusivity causes decreased stratification which leads to a further increase in diffusivity. Larger eddy parameters result in downstream movement of the salt intrusion through amplified frictional resistance to gravitational circulation and vertical rather than longitudinal transport of salt. Smaller eddy parameters have an opposite effect. These results may be understood

intuitively or through reference to Hansen and Rattray's (1965) and Festa and Hansen's (1976) observed dependence of circulation and stratification on the Rayleigh number (eq. 7-1) and a mixing parameter (eq. 7-2).

As in the experiments with wind, there is some long-term change in stratification due to longitudinal motion of the salinity intrusion. In the reduced tidal amplitude run, for example, this behavior may be noted as a downturn in stratification at km 20 after 20 tidal cycles. Again, this behavior would not be observed in a prototype since alterations in tidal amplitude act as periodic rather than step-functions.

3. Freshwater Flow - Response of the salinity intrusion to alterations in freshwater flow was examined in two model runs in which flow was tripled from $150 \text{ m}^3/\text{sec}$ to $450 \text{ m}^3/\text{sec}$ and decreased from $150 \text{ m}^3/\text{sec}$ to $30 \text{ m}^3/\text{sec}$, respectively. These values roughly correspond to high-flow and low-flow conditions in the James River. Results are shown in Figs. 7-8a - 7-8g for the high-flow run and Figs. 7-9a - 7-9i for the low-flow run.

As would be expected, the increased flow rate results in a decline in salinity and downstream motion of the salinity intrusion. The decreased flow causes an increase in salinity and upstream motion of the intrusion.

The effects on stratification are more complex than the longitudinal motions and less readily predictable

by conventional theory or by analysis of previous experiments, especially for the high-flow runs. By eq. 7-2, an increase in river flow would be expected to produce a reduced mixing parameter and, hence, increased stratification. An initial increase in stratification is indeed evidenced in the model as the high flow depresses surface salinity more rapidly than the bottom (Figure 7-8d). After approximately six tidal cycles, however, stratification decreases as the bottom salinity approaches the lower value of the surface. At km 44, stratification continues to decline as the salinity approaches zero (Figure 7-8f). At km 20, stratification reaches a minimum and then increases to approximately its initial value as the surface and bottom salinities reach steady state.

Decreasing river flow would be expected to reduce stratification (eq. 7-2). At km 20, this decline is noted but at kms 44 and 68, stratification increases as the bottom salinity advances more rapidly up the estuary than the surface salinity.

Once again, the unexpected behavior of the salinity stratification is the product of longitudinal migration of the limit of salt intrusion and relocation of the estuarine regimes. Unlike wind and tide, however, these longitudinal motions should be expected in a prototype estuary as the period of the model forcing function is practicable. That is, high- and low-flow intervals may persist for twenty or more days in a prototype estuary.

4. Boundary Conditions - The response of the model estuary to changes in salinity at the mouth was examined in two runs in which downstream salinity was increased from $20^{\circ}/\text{oo}$ to $24^{\circ}/\text{oo}$ and decreased from $20^{\circ}/\text{oo}$ to $16^{\circ}/\text{oo}$, respectively. Results are shown in Figs. 7-10a - 7-10g and Figs. 7-11a - 7-11g.

The effect of raising the downstream boundary condition is to increase salinity throughout the estuary. The influence commences at the mouth and works upstream slowly. Salinity at km 68 is unchanged after 30 tidal cycles; the salt intrusion is unmoved after 40 cycles. Stratification at km 20 is increased dramatically as salinity moves up the bottom layer of the estuary then slowly decreases as salinity advances in the surface layer. At km 68, stratification increases, but only after 30 or more tidal cycles.

Lowering the downstream boundary condition reduces salinity throughout the estuary. Again, the effects occur first near the mouth and move upstream gradually. After 40 tidal cycles, salinity and stratification near the head of the intrusion are unchanged. At km 20, salinity declines slowly while stratification remains roughly constant for 6 tidal cycles. After that, stratification decreases as the bottom salinity declines more rapidly than the surface, then attains a new steady value as the surface and bottom salinities decline jointly.

These responses to the alterations in boundary conditions may be inferred from the dependence of estuarine circulation and stratification on the Rayleigh number (eq. 7-1). Ra varies directly with S_0 and circulation and stratification change accordingly as S_0 is varied. The significance of the model response is in demonstrating the long period necessary for changes in boundary conditions to manifest themselves within the estuary. Except near the mouth, short-term fluctuations in the downstream salinity will have little influence on the estuarine circulation and salinity structure. This is particularly important in the execution of estuarine models when detailed information on the behavior of the downstream boundary is lacking.

D. Response to Pulse Functions

Estuaries are dynamic systems in which conditions are continuously changing in response to external influences of diverse time scales. The effects of random, short-term events such as storm flows may persist long after the events themselves have passed. Other influences, such as tidal fluctuations of surface level, vary on a regular, periodic basis. In this section, the extended response to several short-term and periodic forcing functions is examined, providing more realistic views of long-term estuarine response to wind, flow, and tide than are obtained from the step-function runs.

1. Wind - Examination of the transient response to a wind pulse was conducted by assuming a six-cycle wind event (A time scale typical of prototype events, Elliott; 1976). Upstream and downstream winds of 5 m/sec were imposed at the beginning of individual forty-cycle model runs. At the end of each six-cycle event, wind stress was returned to the zero value used in generating the initial conditions. Results are shown in Figs. 7-12a - 7-12g for the upstream wind and Figs. 7-13a - 7-13g for the downstream wind.

The short-term response to the upstream wind pulse is similar to that of the steady upstream wind. Salinity initially increases slightly and then declines throughout the estuary while stratification decreases. Stratification reaches a minimum coinciding with the cessation of the wind event although depth-average salinity continues to decline about two cycles longer. Recovery is extremely slow and depth-average salinity persists below its initial value past forty tidal cycles. Stratification recovers and then overshoots its initial value as surface salinity remains depressed while bottom salinity increases.

In response to the downstream wind pulse, salinity and stratification initially decrease slightly then increase. The increasing trend in both continues approximately two cycles past the end of the wind event. Again, recovery is prolonged, and elevated salinities persist

past forty tidal cycles. At km 20, stratification attains a value lower than initially while at km 68 a higher level is maintained.

Two primary results are noted from these model runs. The first is that the effects of a wind pulse on stratification are more pronounced than on the longitudinal salinity distribution. The second is that the estuarine response to a wind pulse persists long after the pulse itself has ceased. The small deviations in model salinity and stratification which exist beyond forty cycles would likely be masked in a prototype, but significant differences in stratification are maintained up to about tidal cycle twenty. Thus a period of twenty tidal cycles is proposed as the time-scale of estuarine response to a six-cycle wind event.

2. Storm Flow - The estuarine response to a storm-generated pulse in flow was examined in a model run by multiplying freshwater flow tenfold to $1500 \text{ m}^3/\text{sec}$ for a period of six tidal cycles and then returning to the average flow of $150 \text{ m}^3/\text{sec}$. These conditions roughly correspond to the April, 1978, storm event detailed in Chapters II and VI except that the post-storm flows in the prototype gradually returned to pre-storm values while in the model the return was instantaneous. The duration of the model run was eighty tidal cycles and the results are shown in Figs. 7-14a - 7-14g.

The response of the model to the storm pulse may be divided into several phases. In the first phase, salinity declines but stratification increases as surface salinity is depressed more rapidly than bottom salinity. In the second phase, depth-average salinity continues to decrease. Stratification decreases and reaches a minimum during this phase as surface salinity commences recovery while bottom salinity continues to decline. The third phase is characterized by an increase in depth-average salinity and a sharp increase in stratification to a maximum far in excess of the pre-storm value as bottom salinity recovers more rapidly than the surface. In the fourth phase, depth-average salinity and stratification slowly recover towards their pre-storm levels.

These model phases are remarkably similar to the observations conducted in the James River following the Agnes storm event as detailed by Hyer and Ruzicki (1974) and summarized in Chapter II. Only the rebound of salinity to a level exceeding the pre-storm value is lacking, reinforcing the author's suggestion that the rebound was due to conditions in Chesapeake Bay. Effects due to influences at or beyond the downstream boundary would not be reflected in the model due to the assumption of constant downstream boundary conditions.

As in the simulation of the wind pulses, the effects of the storm event are extended far beyond the duration of the event itself. Salinity in the mid-estuary

(km 44) continues to decline approximately twenty cycles after the cessation of the storm event and stratification maintains its minimum, likewise, until the twenty-sixth cycle. Near the mouth (km 20), the decline is less prolonged but still extends six cycles beyond the storm event. Recovery to steady conditions is slow with, bottom salinity advancing more rapidly than the surface leading to increasing then decreasing stratification as depth-average salinity returns to its initial value. By the 80th tidal cycle, however, neither the salinity nor the stratification have fully recovered.

3. Tide - The response of the model estuary to variation in tide range was examined through the simulation of two successive spring-neap tidal cycles. The model was run for a total of 66 lunar semi-diurnal tidal cycles. The first 10 cycles were dropped from analysis to allow a transition period from the steady state attained utilizing a constant tidal range to the quasi-steady state which occurs when tidal amplitude is varied periodically. The spring-neap cycling was generated by superimposing a solar semi-diurnal tide (N2) with a period of 12.0 hours and an amplitude of 25 cm on the lunar semi-diurnal tide (M2) of 12.42 hours period and 50 cm amplitude. The tidal variation at the mouth of the estuary for tidal cycles 10-66, approximately two complete spring-neap cycles, is shown in Fig. 7-15a. The response of the

estuary is shown in Figs. 7-15b - 7-15h.

Analysis commences at tidal cycle 10, with the tidal amplitude approximately midway between the 75 cm maximum and 25 cm minimum. From the mid-range, tidal amplitude proceeds through a minimum at cycle 15, a maximum at cycle 29, a second minimum at cycle 44 and a second maximum at cycle 58.

The effect of the spring-neap cycling on the depth-average salinity is periodic, but negligible. Fluctuations in salinity are about 0.5 ‰ in amplitude at km 20, where the longitudinal gradient is steep, and decline in the upstream direction until they are indiscernable at the head of the intrusion. A slight increasing trend in salinity, an artifact of the transition from steady to periodic tidal amplitude, is also noted. Neither of these effects would be observed in a prototype estuary, however. The small, periodic fluctuations would be masked by responses to other influences superimposed on the tidal cycling and by local variability, and the artificial, transitional, increase would not occur.

Of much greater significance than any variation in depth-average salinity is the periodic response of stratification to the spring-neap cycling. As would be expected, an increase in tide range results in a decrease in stratification while a decrease in tide range produces an increase in stratification. The effect is lagged, however, rather than instantaneous, so that maximum

stratification occurs roughly four cycles after minimum tide range and minimum stratification is delayed approximately four cycles past maximum tide range. This phase delay results in paradoxical instances in which stratification increases as the tide range grows larger and decreases as the tide range grows smaller.

A similar lag between extremes in tide range and stratification was noted by Haas (1977) in the York and Rappahannock Rivers. In those partially-mixed estuaries, "homogeneity was most highly developed about four days after sufficiently high spring tides." The lag is less noticeable in data collected from the James, however (Figs. 5-1 and 5-12 - 5-15). Presence of a lag in the model but not in the field data employed in this study suggests that reformulation of the eddy viscosity and diffusivity functions (eqs. 4-15 - 4-16) to allow greater variability as a function of tidal velocity might result in improved model accuracy. Alternately, prototype stratification-destratification cycling might be influenced by additional factors not included in the model.

E. Summary

Estuarine forcing functions may be divided into two categories: those which affect primarily stratification and those which affect both stratification and the longitudinal salinity distribution. In the former category are wind stress and tidal mixing. The latter category

includes runoff and salinity at the open mouth. Wind stress and changes in tidal mixing, applied over prolonged periods, are capable of altering the longitudinal salinity distribution as well, but under prototype conditions, variations in these forcing functions do not persist long enough to produce significant effects.

A summary of the results of the experiments detailed in this chapter is presented in Table 7-2. The table shows, for each experiment, the effects on stratification (increase or decrease) and the salt intrusion (moves upstream or downstream) and the approximate number of tidal cycles elapsed until the effects are first noted and until a new steady state is attained.

In order to distill the results of a dozen experiments into a single table, some simplifications and generalizations are necessary. Minor transients are ignored and asymptotic approaches to a steady state are considered complete when the deviations from steady state are judged to be indiscernable in a prototype.

Initial responses to the alterations in the forcing functions are rapid - usually within 0-2 tidal cycles of initiation of the impulse. Only in the case of a change in boundary conditions is the response prolonged. The appearance of changes in salinity and stratification twenty kilometers upstream of the mouth within 4-6 cycles after an alteration in boundary salinity indicates, however,

Table 7-2. Results of Experiments on Model Estuary

Model Run	Effect on Stratification	Movement of Intrusion	Cycles to Start	Cycles to Finish
Step Functions				
5 m/sec wind upstream	decreased	downstream	0	80
5 m/sec wind downstream	increased	upstream	0	80
tide range increased 25 cm	decreased	downstream	0	>40
tide range decreased 25 cm	increased	upstream	0	>40
flow tripled	varied	downstream	2	30
flow divided by five	varied	upstream	2	>40
salinity boundary increased 4‰	increased	upstream	varies with location	>40
salinity boundary decreased 4‰	decreased	downstream	varies with location	>40
Pulse Functions				
5 m/sec wind upstream	decreased	downstream	0	20
5 m/sec wind downstream	increased	upstream	0	20
flow increased tenfold	varied	downstream	2	>80
spring-neap tidal cycling	varied	none		

that, at least in the region adjacent to the boundary, estuarine response occurs in the same 0-2 cycle time scale associated with the other phenomena.

While the initial reactions are rapid, the complete responses to the altered forcing functions are lengthy. Approximately eighty tidal cycles are required for the estuary to attain steady state in response to a constant wind stress. More than forty tidal cycles are required for steady state to be attained in response to step-function alterations in tide range or downstream salinity. Since these response time scales are much longer than the time scales of variations in prototype forcing functions, estuaries such as the James do not achieve full equilibrium with respect to wind, tide, and boundary conditions. Only with respect to flow is equilibrium possible. The response time scales are still long (from thirty tidal cycles for a moderately high flow to more than forty cycles for drought flow) but in these instances the time scales of the forcing functions may be prolonged as well.

The responses to the pulse-functions are also lengthy. Twenty tidal cycles are required for the effects of a six-cycle wind event to pass. The effects of a major storm event are discernable after more than eighty tidal cycles. These long relaxation times confirm that under prototype conditions, when forcing functions are periodic

or randomly superimposed, an estuary is never truly at steady state.

Experimental results of particular interest are those which demonstrate the interaction of longitudinal salinity movement and stratification. Alterations in estuarine zonation can reinforce or counteract the initial reaction of stratification to an altered forcing function. Under prototype conditions, this effect is most likely to be noted in response to long-term changes in flow. Counter to expectations, an increase in flow can decrease stratification in portions of the estuary which are changed in characterization from the central to the inner regime. Conversely, a decrease in flow can increase stratification in reaches which are transformed from the inner to the central regime.

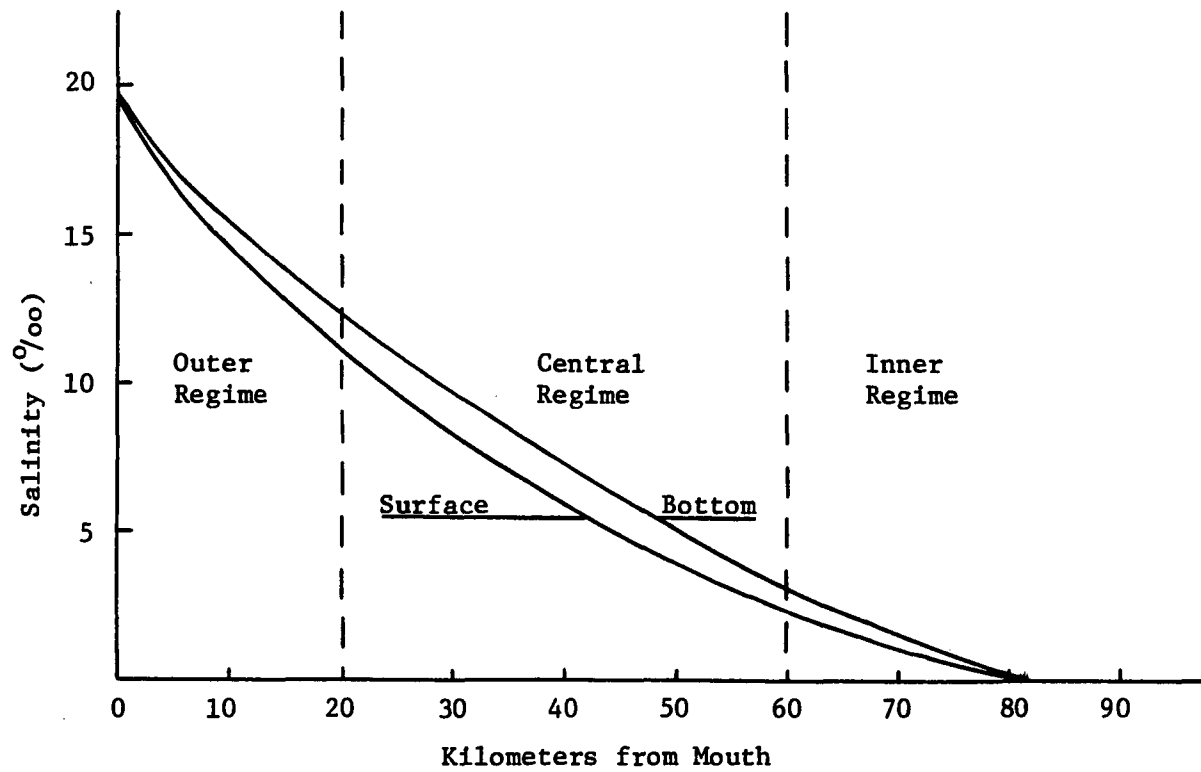


Figure 7-1. Salinity Regimes of Idealized Trapezoidal Estuary.

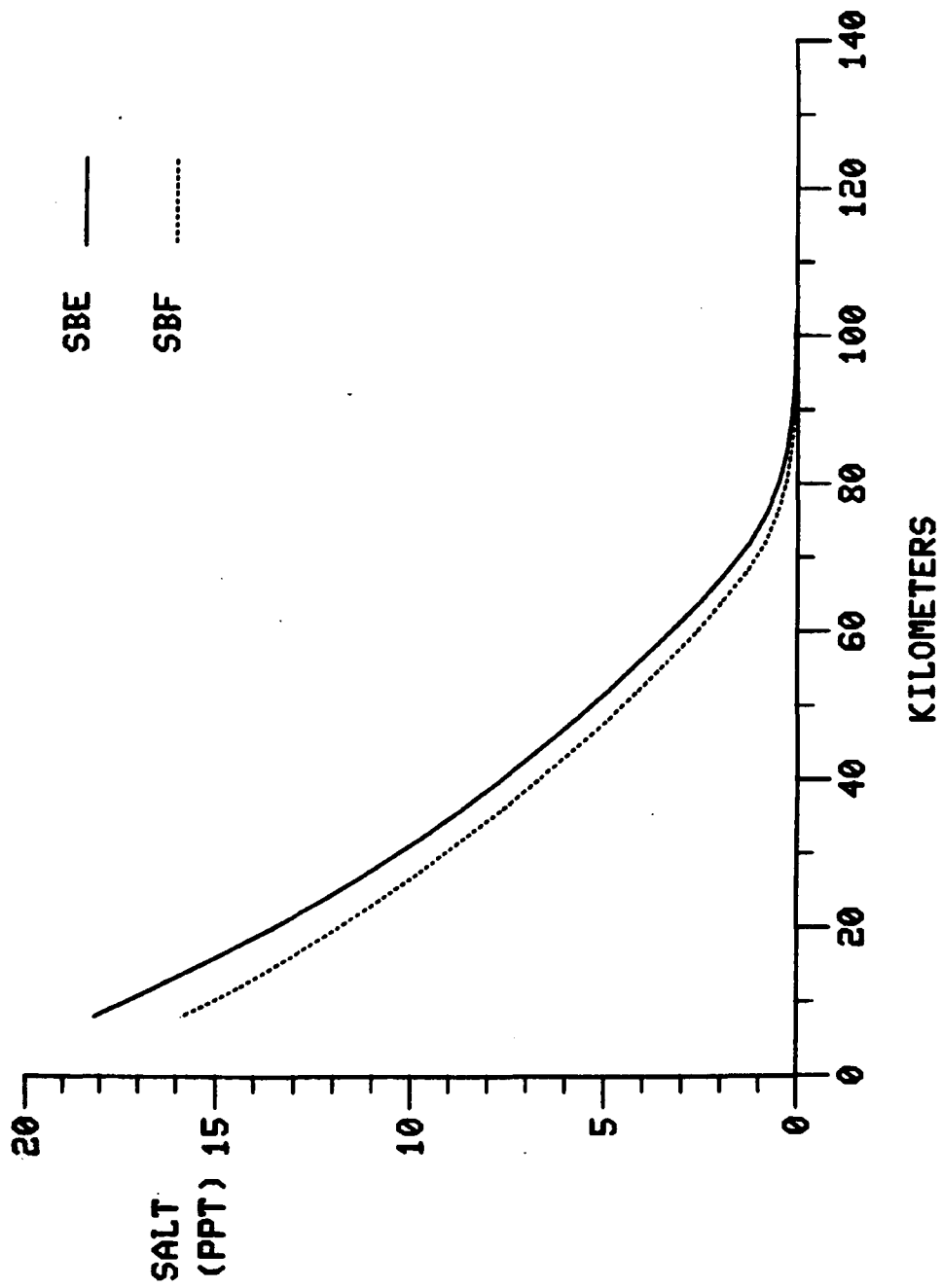
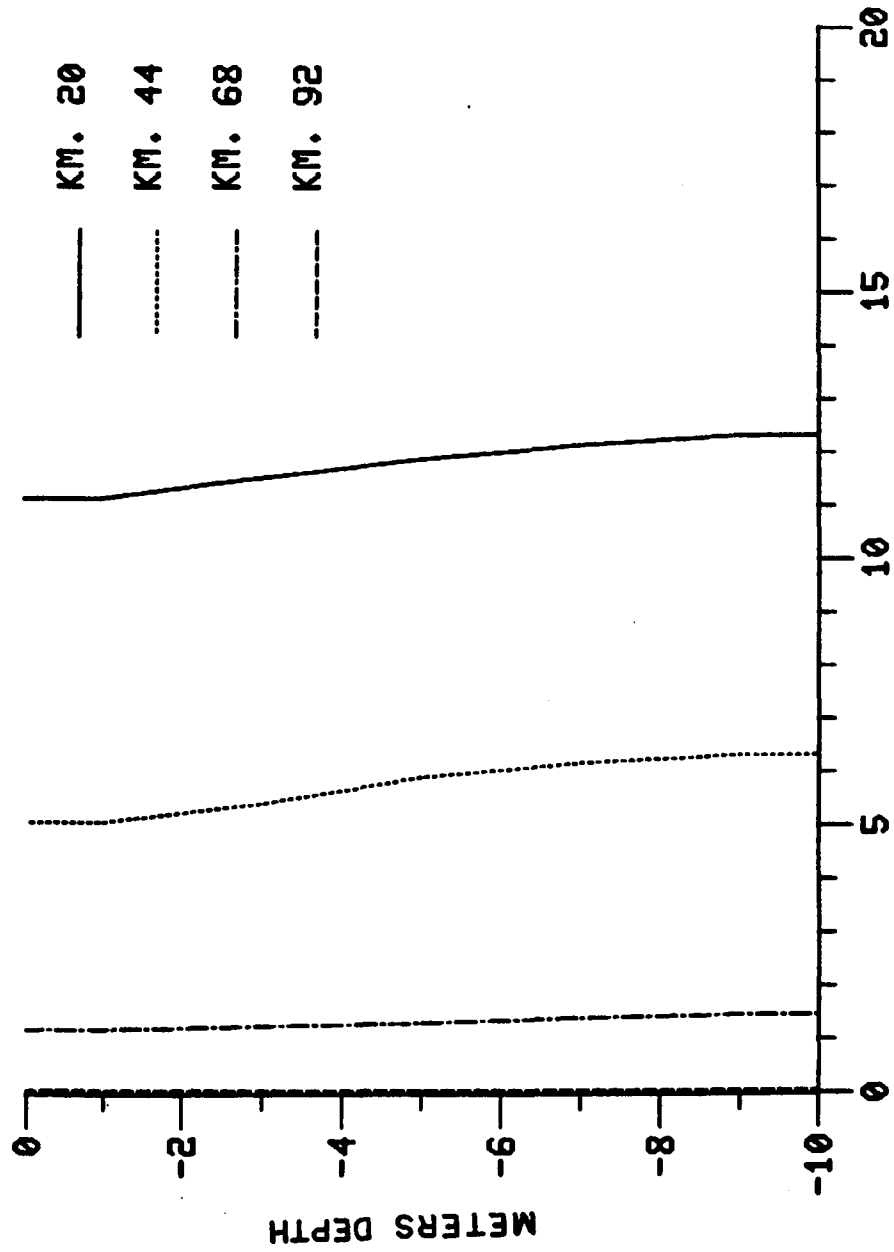


Figure 7-2. Longitudinal Salinity Distribution of Idealized Estuary at Steady State.



SALINITY (PPT)
Figure 7-3. Vertical SBF Salinity of Idealized Estuary at Steady State.

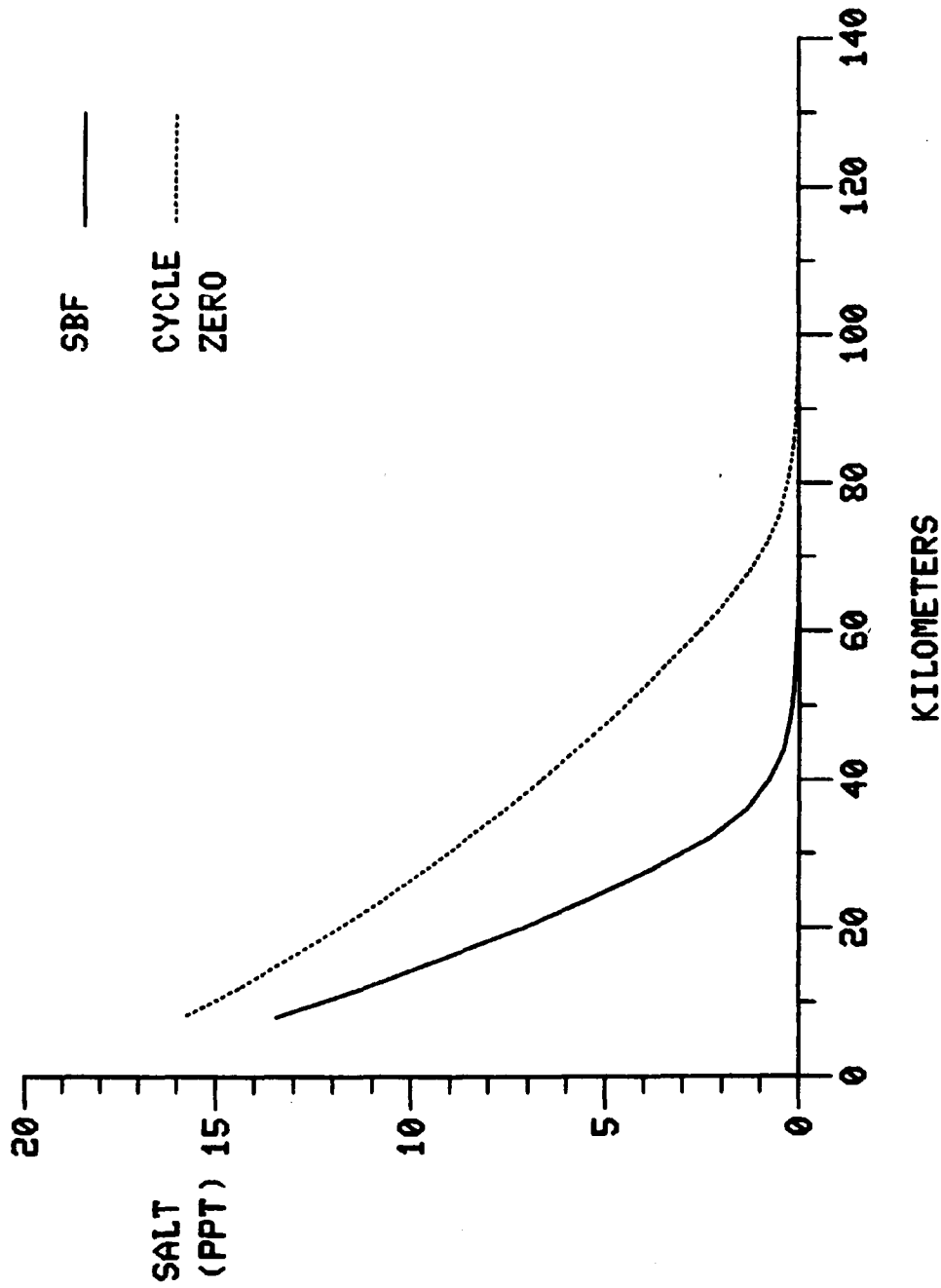
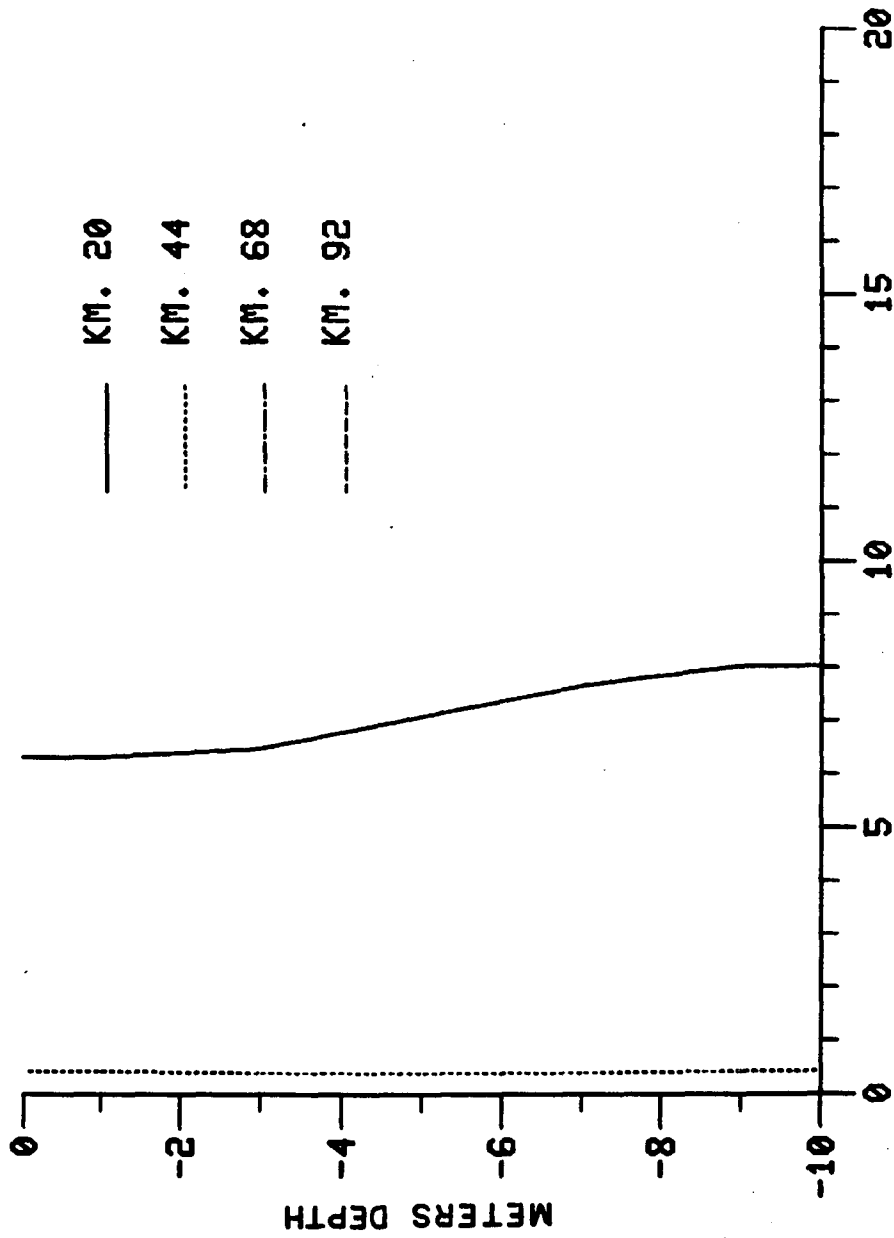
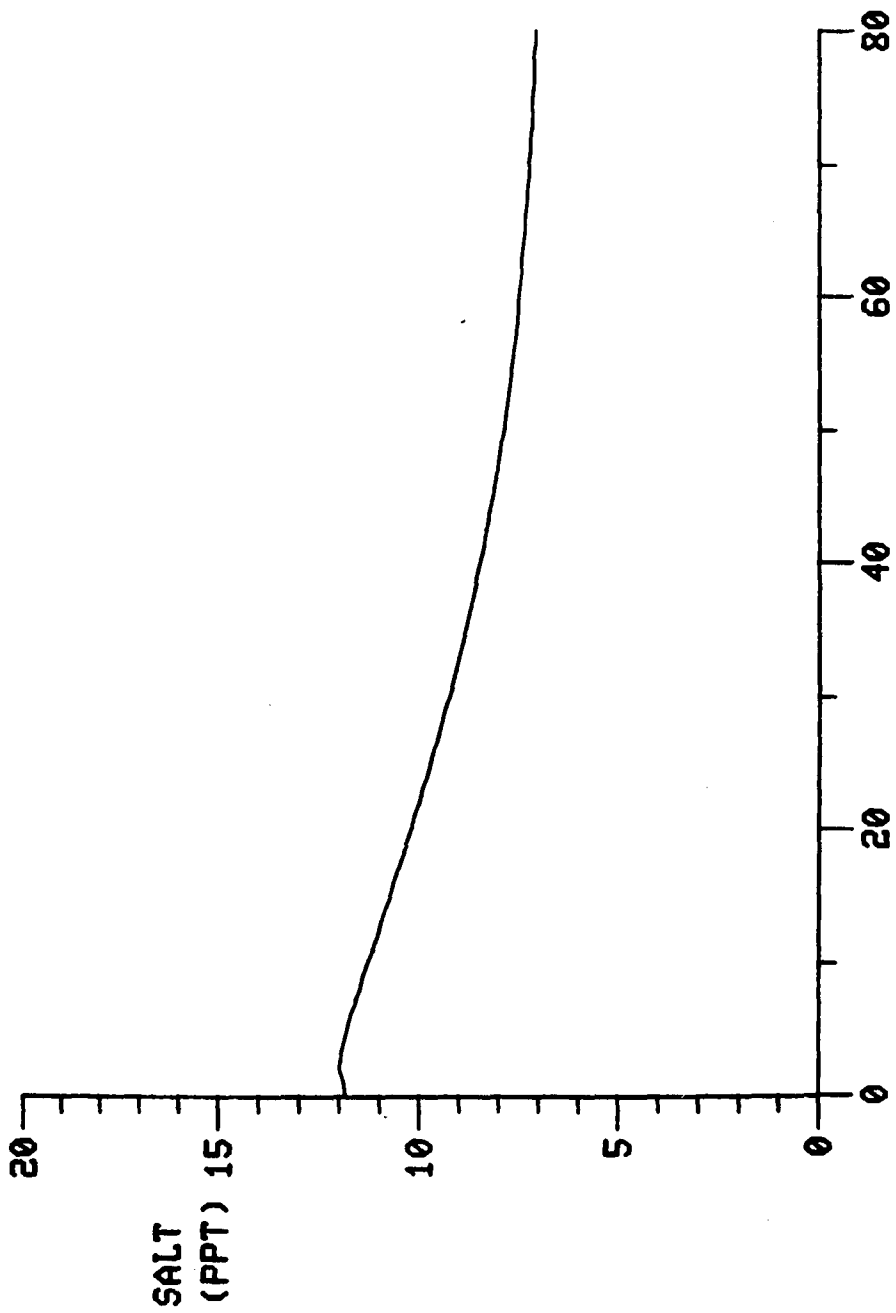


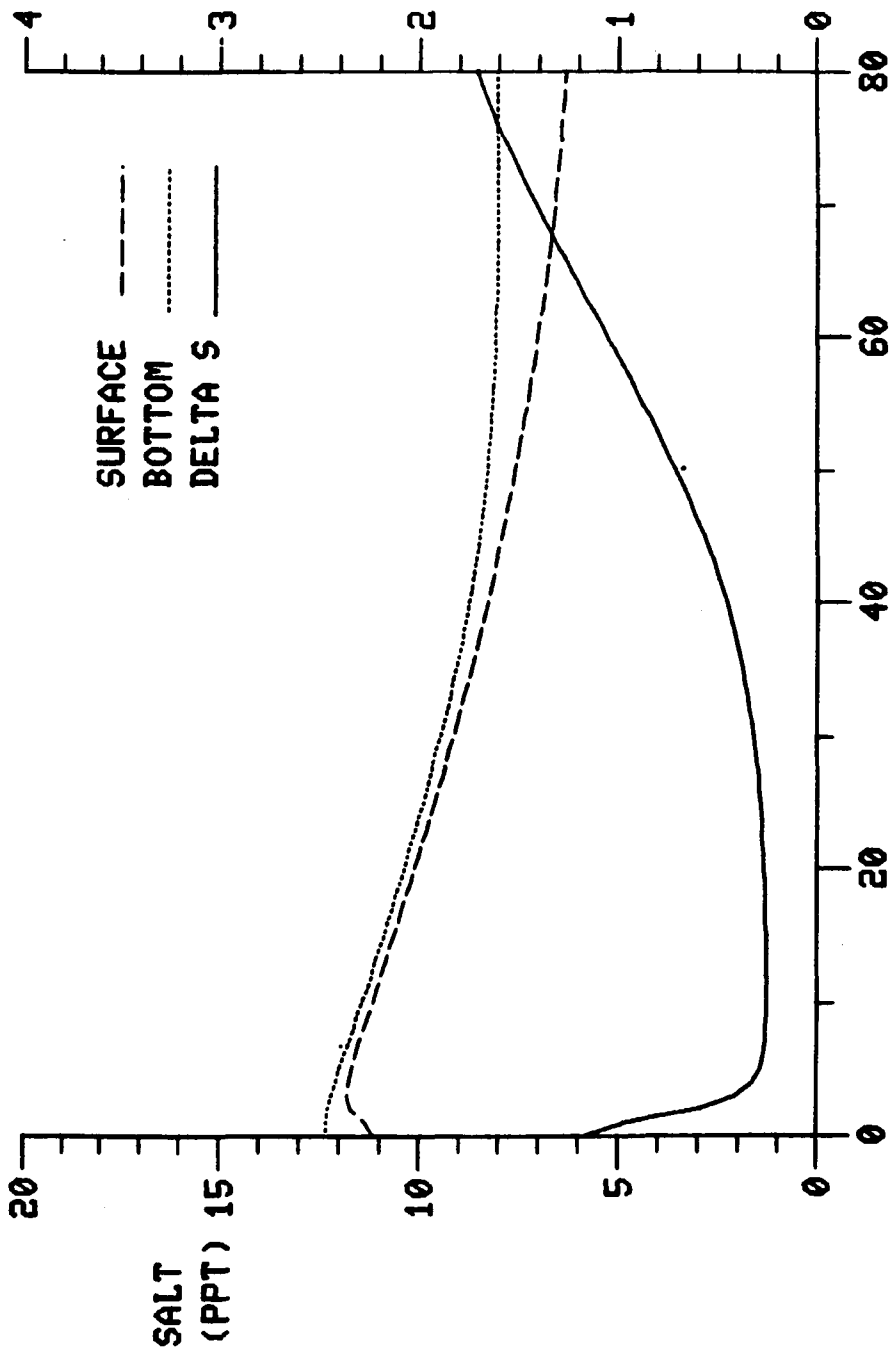
Figure 7-4a. Longitudinal Salinity After Upstream Wind Step Function.



SALINITY (PPT)
Figure 7-4b. Vertical SBF Salinity After Upstream Wind Step Function.

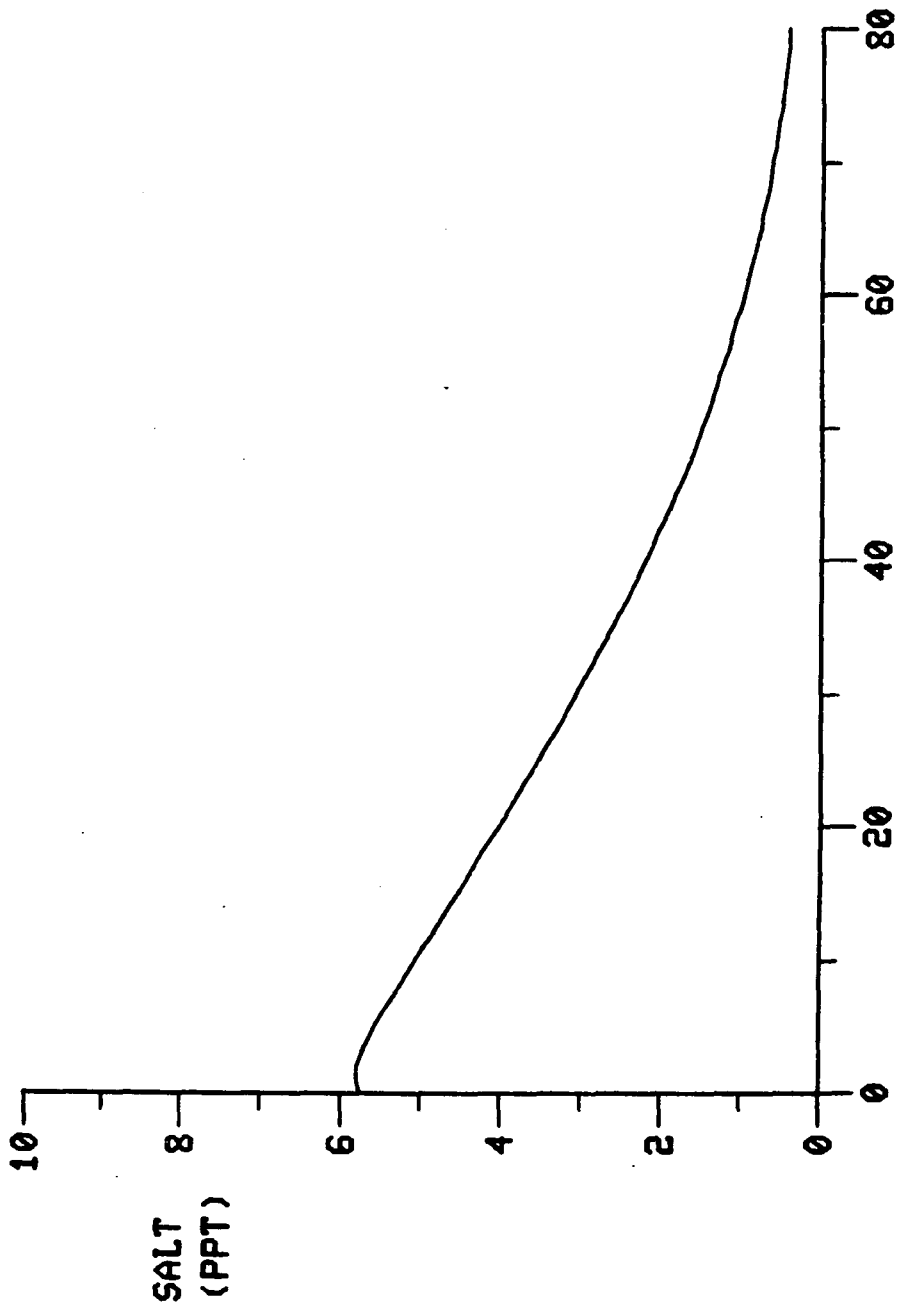


TIDAL CYCLES
Figure 7-4c. Time Series of Depth-Average Salinity at Kilometer 20, Upstream Step Function.

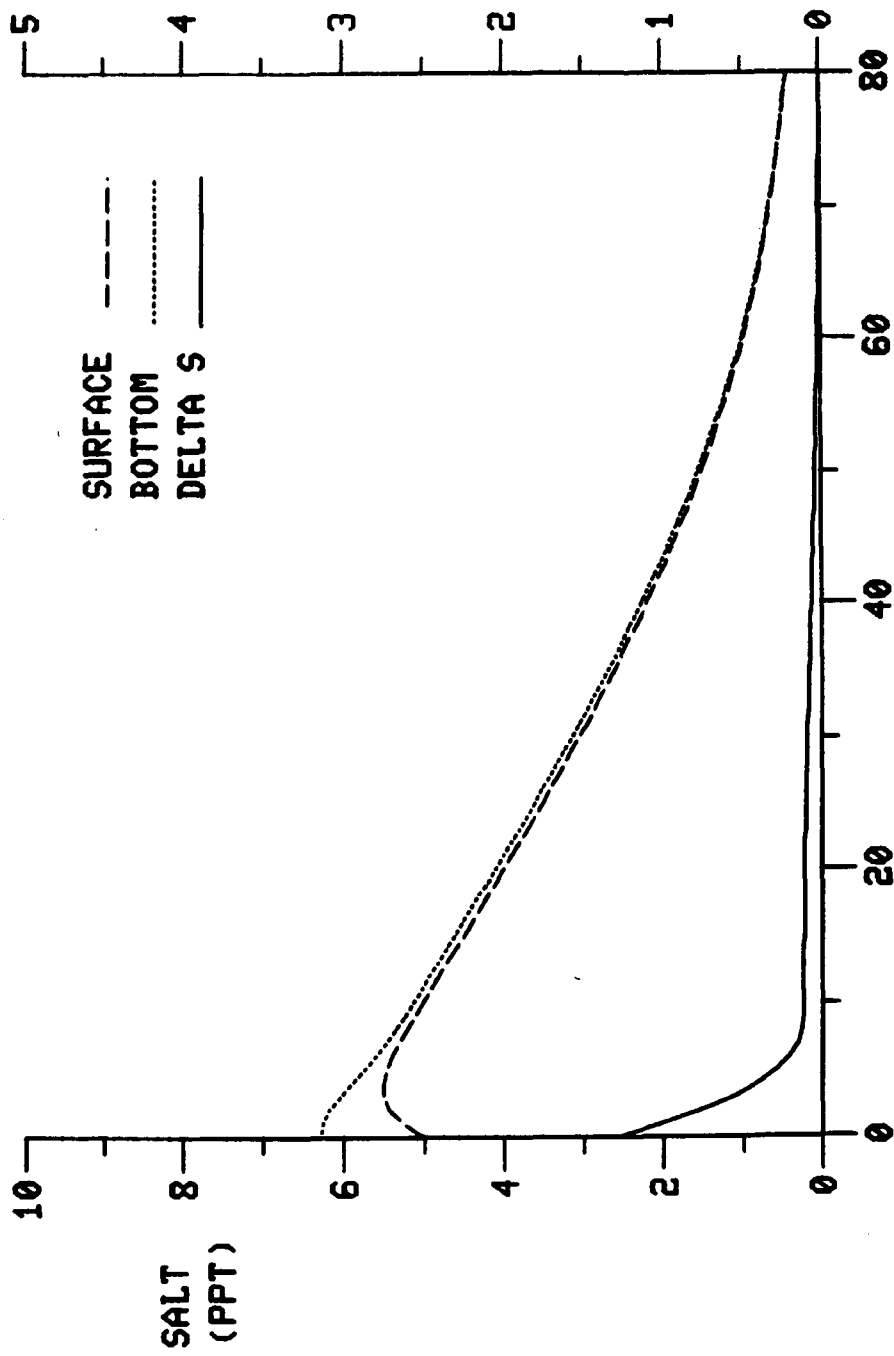


TIDAL CYCLES

Figure 7-4d. Time Series of Stratification at Kilometer 20, Upstream Wind Step Function.

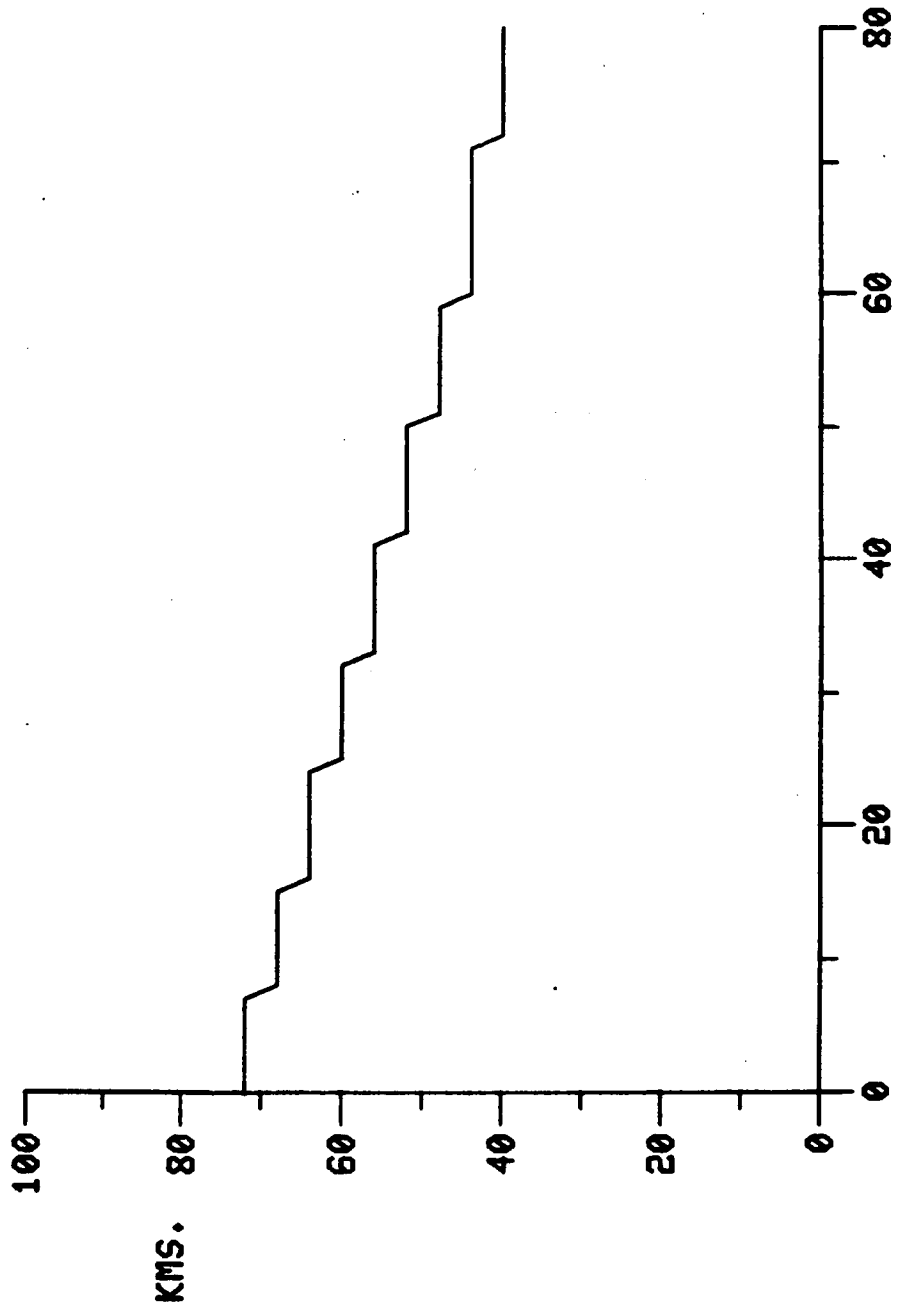


TIDAL CYCLES
 Figure 7-4e. Time Series of Depth-Average Salinity at Kilometer 44, Upstream Wind Step Function.



TIDAL CYCLES

Figure 7-4f. Time Series of Stratification at Kilometer 44, Upstream Wind Step Function.



TIDAL CYCLES
Figure 7-4g. Location of 1/00 Isohaline, Upstream Wind Step Function.

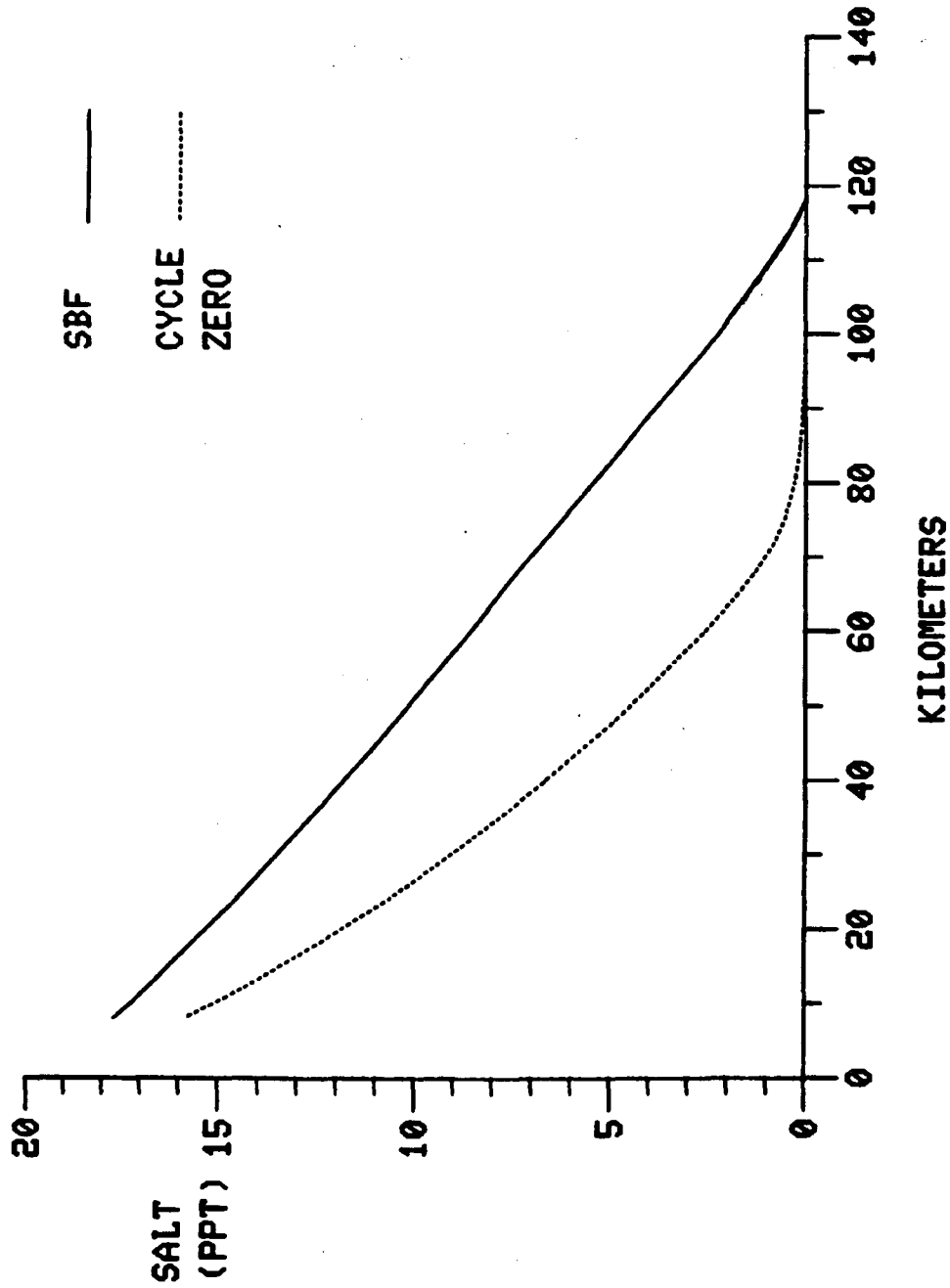


Figure 7-5a. Longitudinal Salinity After Downstream Wind Step Function.

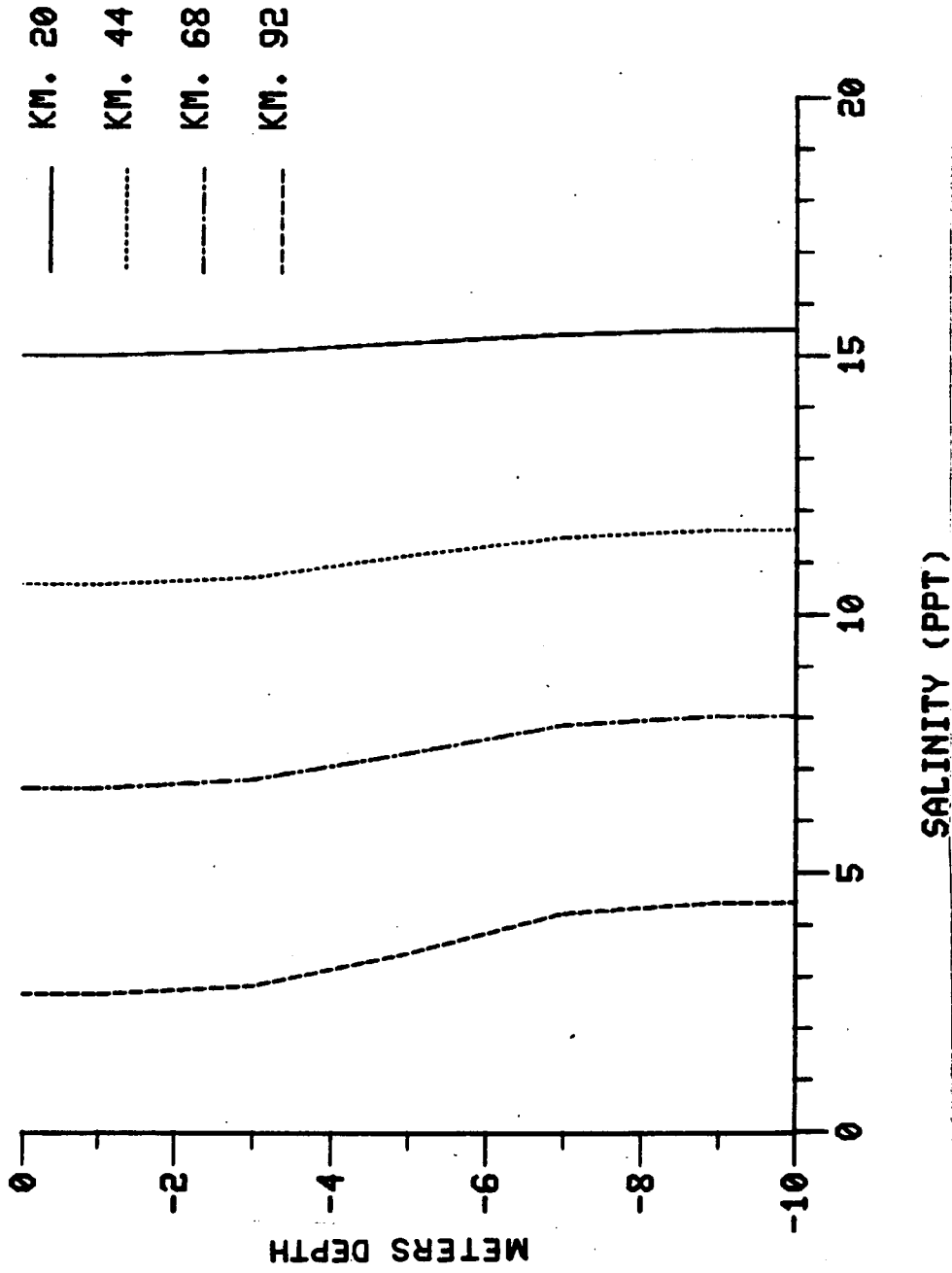
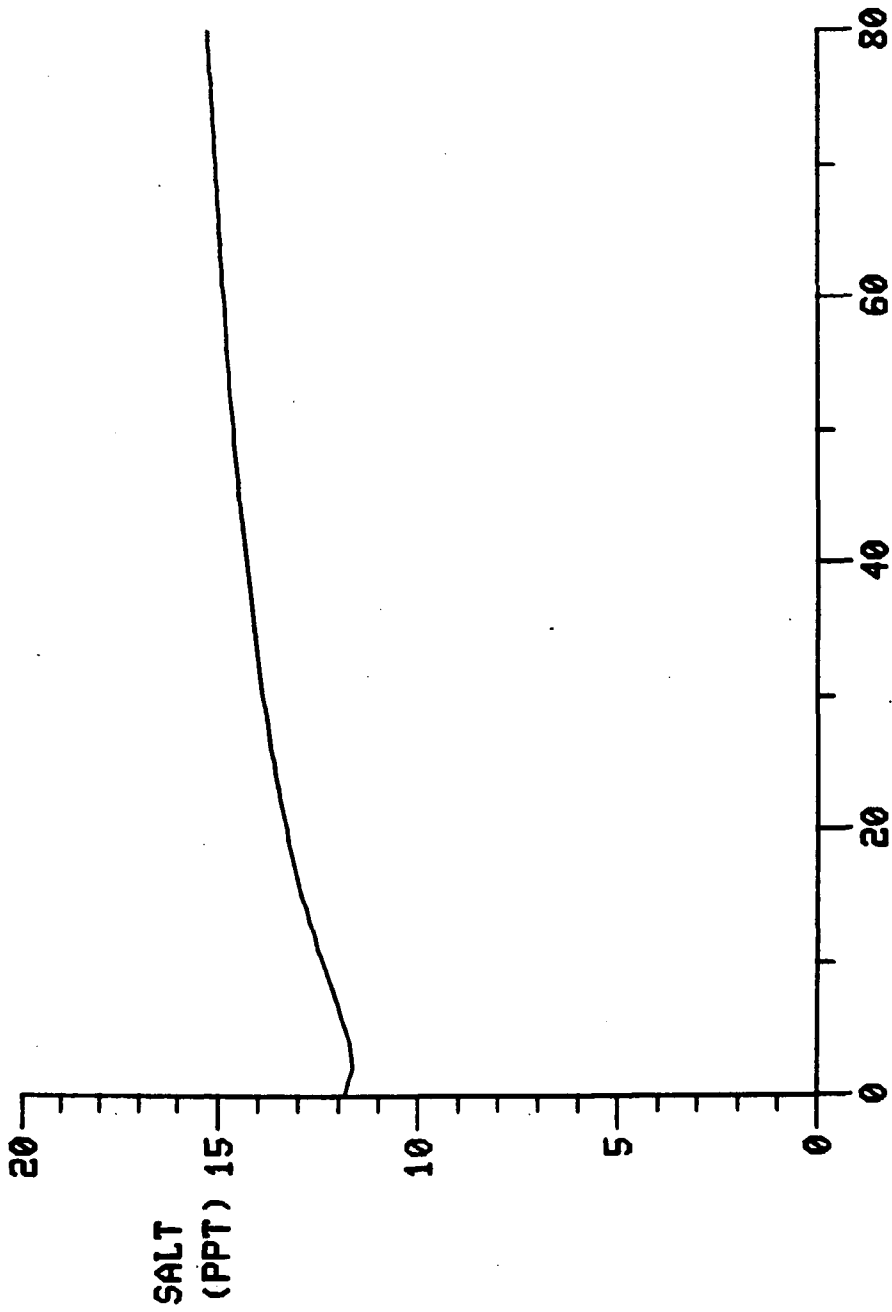
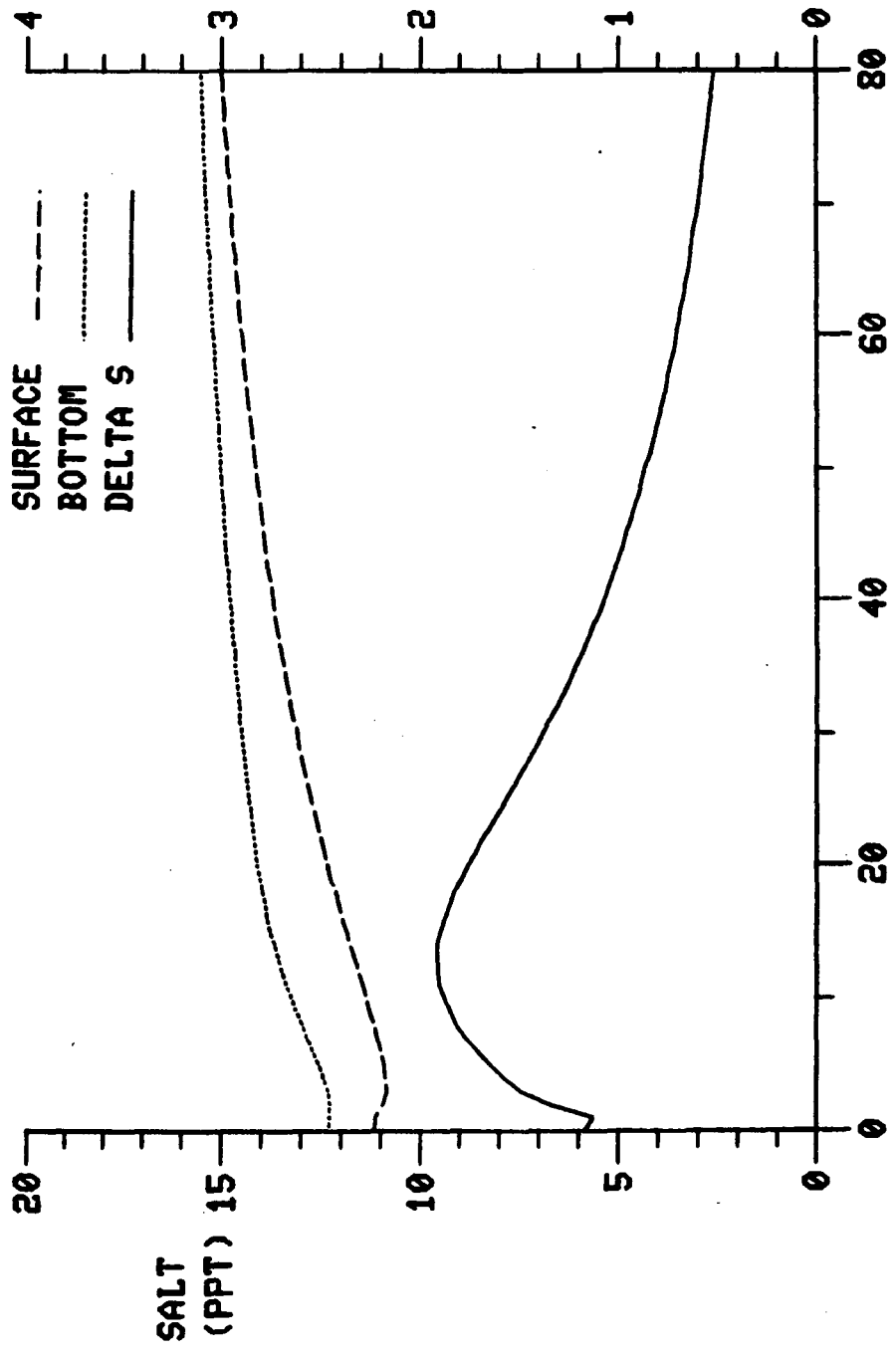


Figure 7-5b. Vertical SBF Salinity After Downstream Wind Step Function.



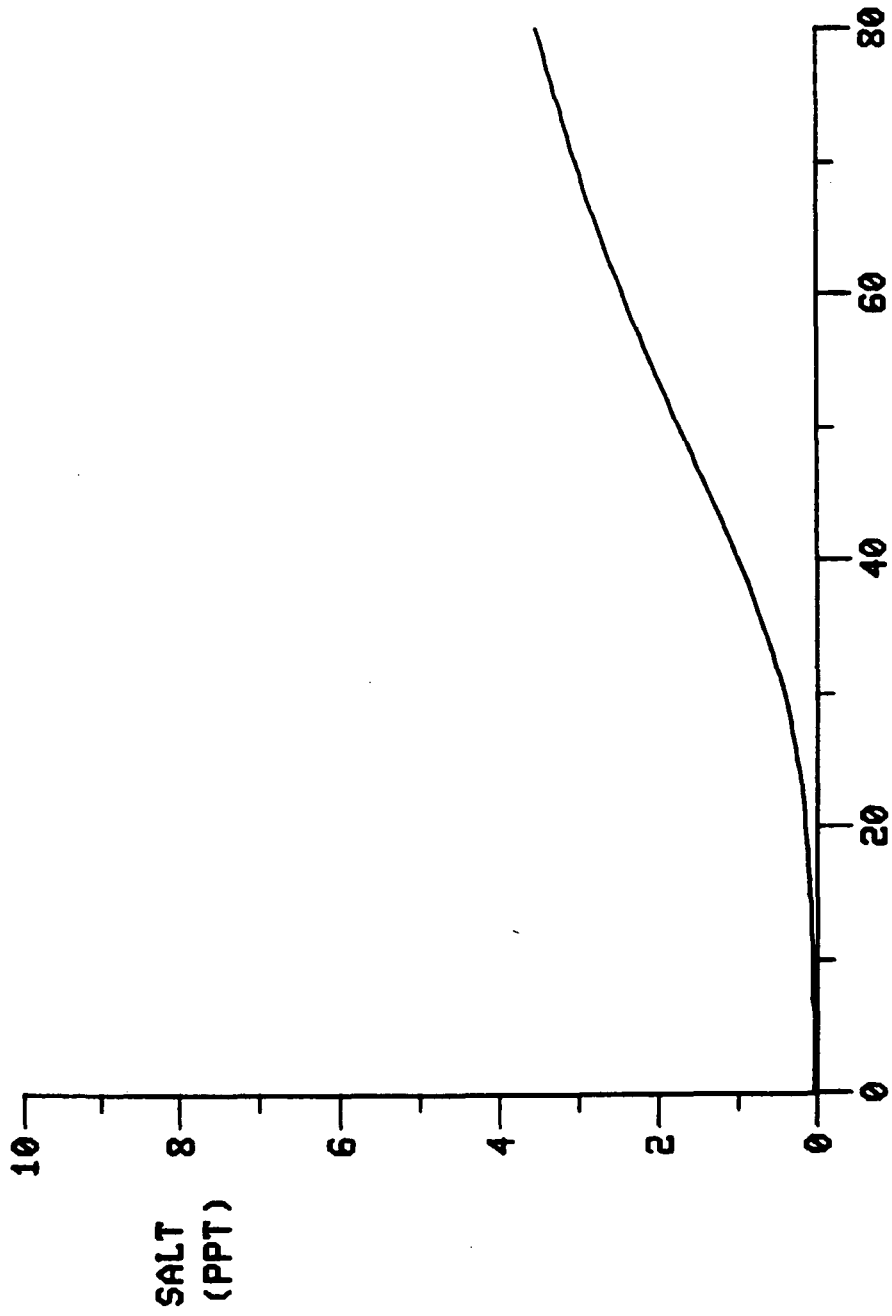
TIDAL CYCLES

Figure 7-5c. Time Series of Depth-Average Salinity at Kilometer 20, Downstream Wind Step Function.



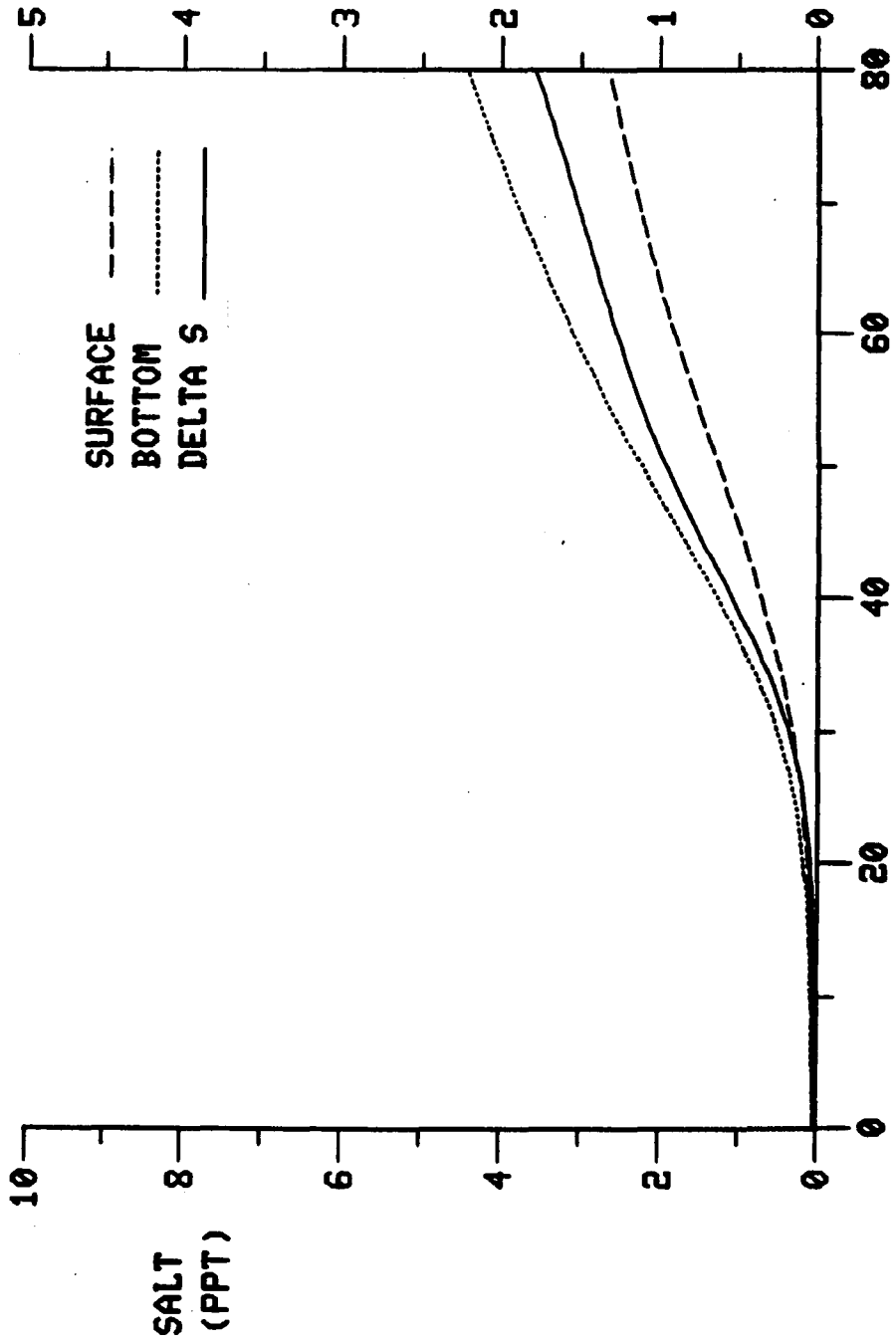
TIDAL CYCLES

Figure 7-5d. Time Series of Stratification at Kilometer 20, Downstream Wind Step Function.

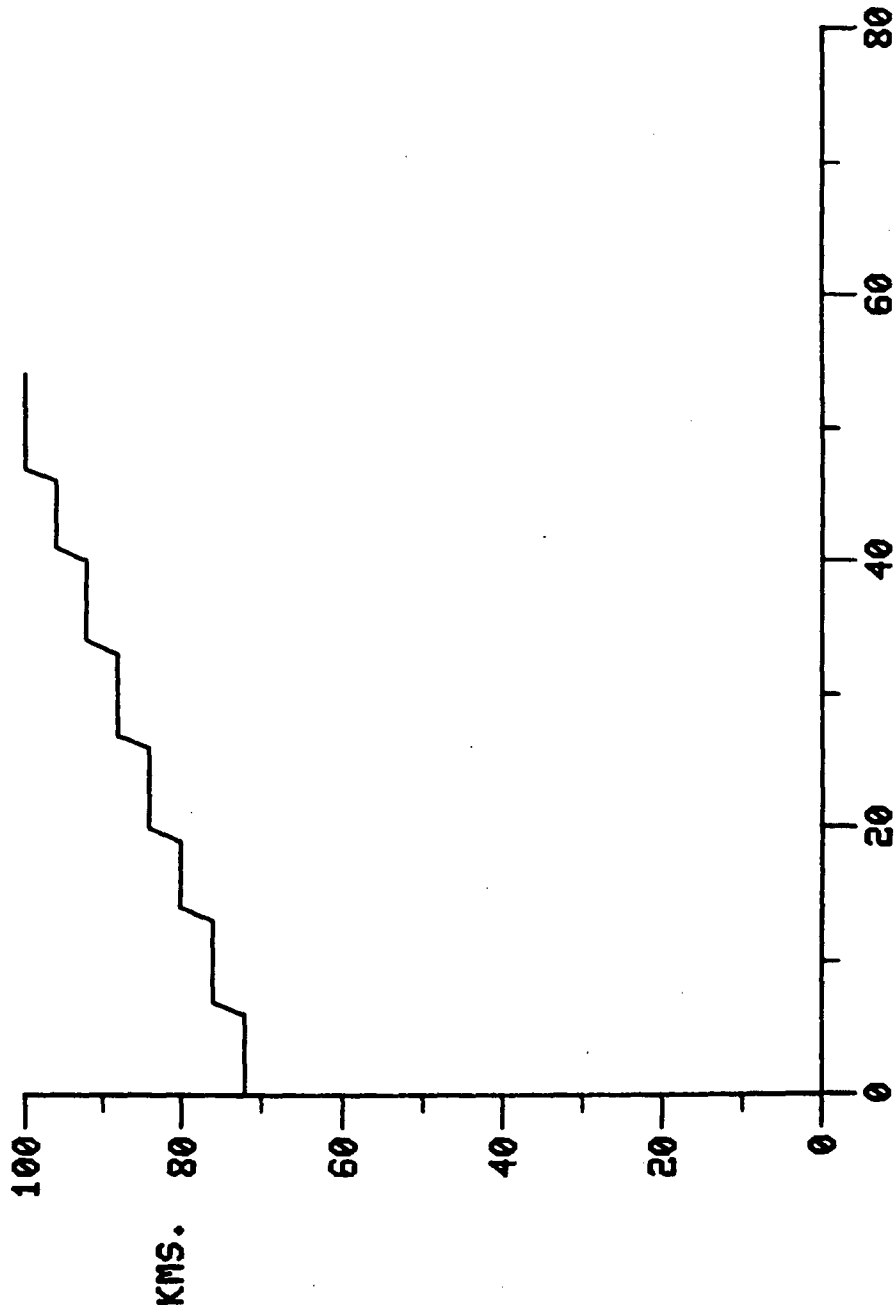


TIDAL CYCLES

Figure 7-5e. Time Series of Depth Average Salinity at Kilometer 92, Downstream Wind Step Function.



TIDAL CYCLES
 Figure 7-5f. Time Series of Stratification at Kilometer 92, Downstream Wind Step Function.



TIDAL CYCLES
 Figure 7-5g. Location of 1 % Isohaline, Downstream Wind Step Function.

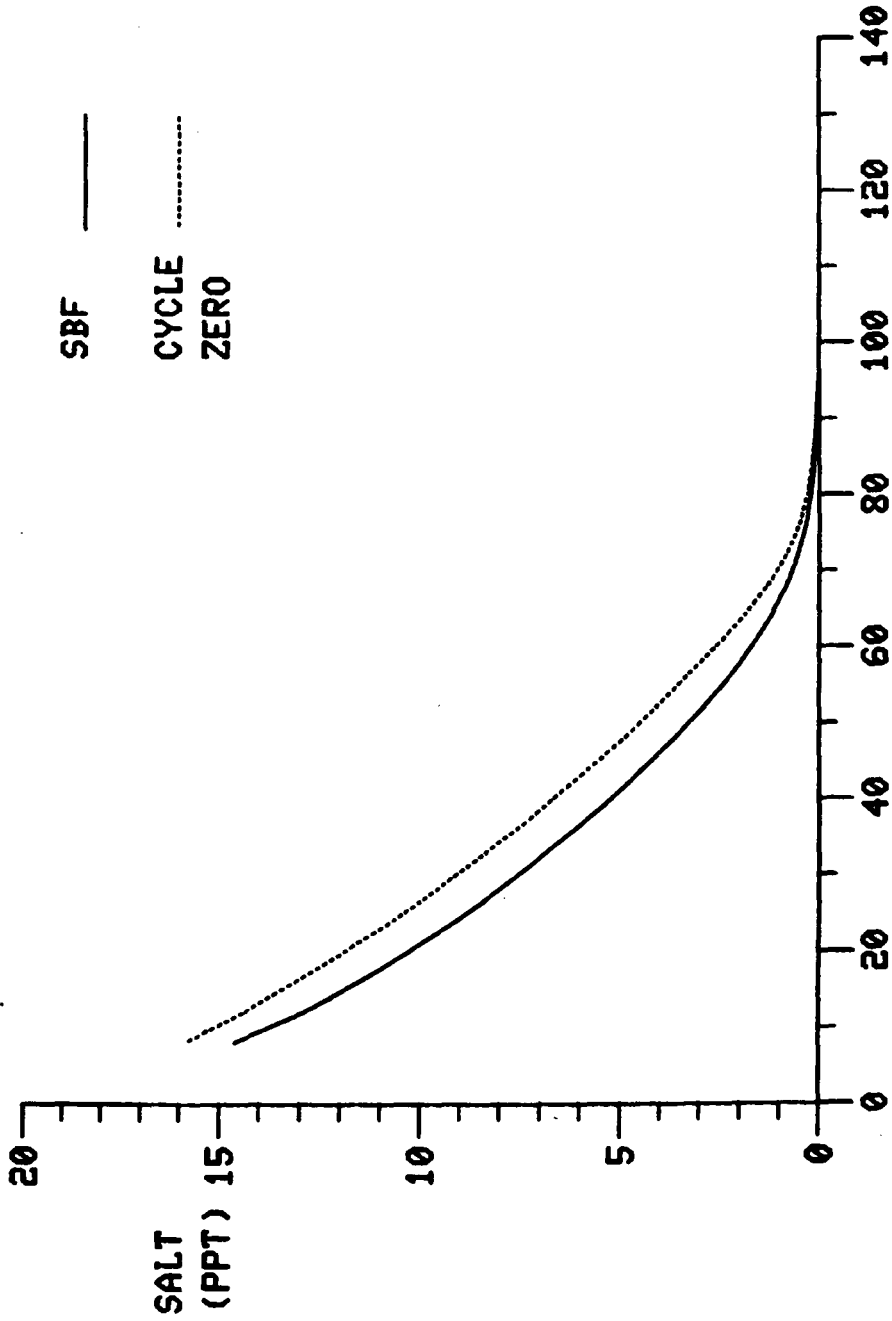
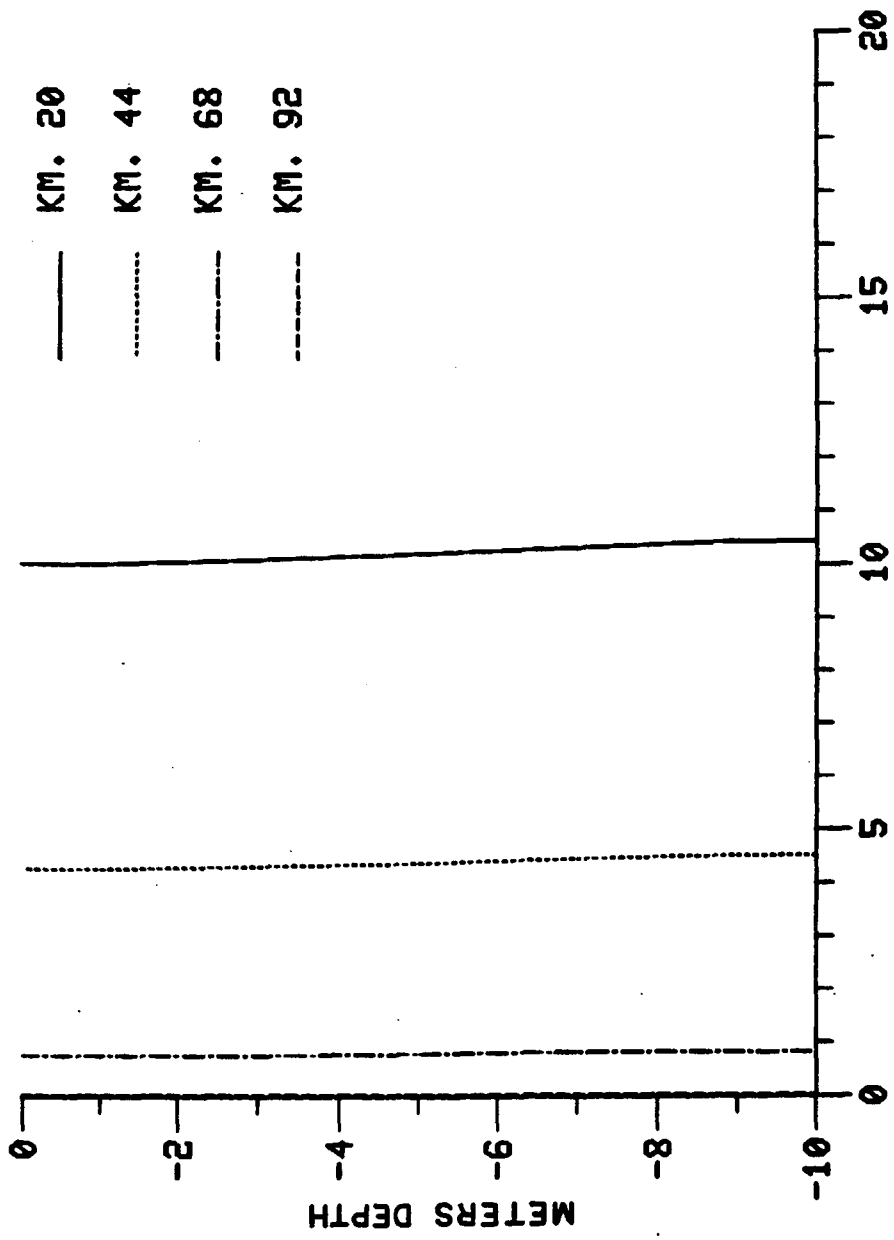
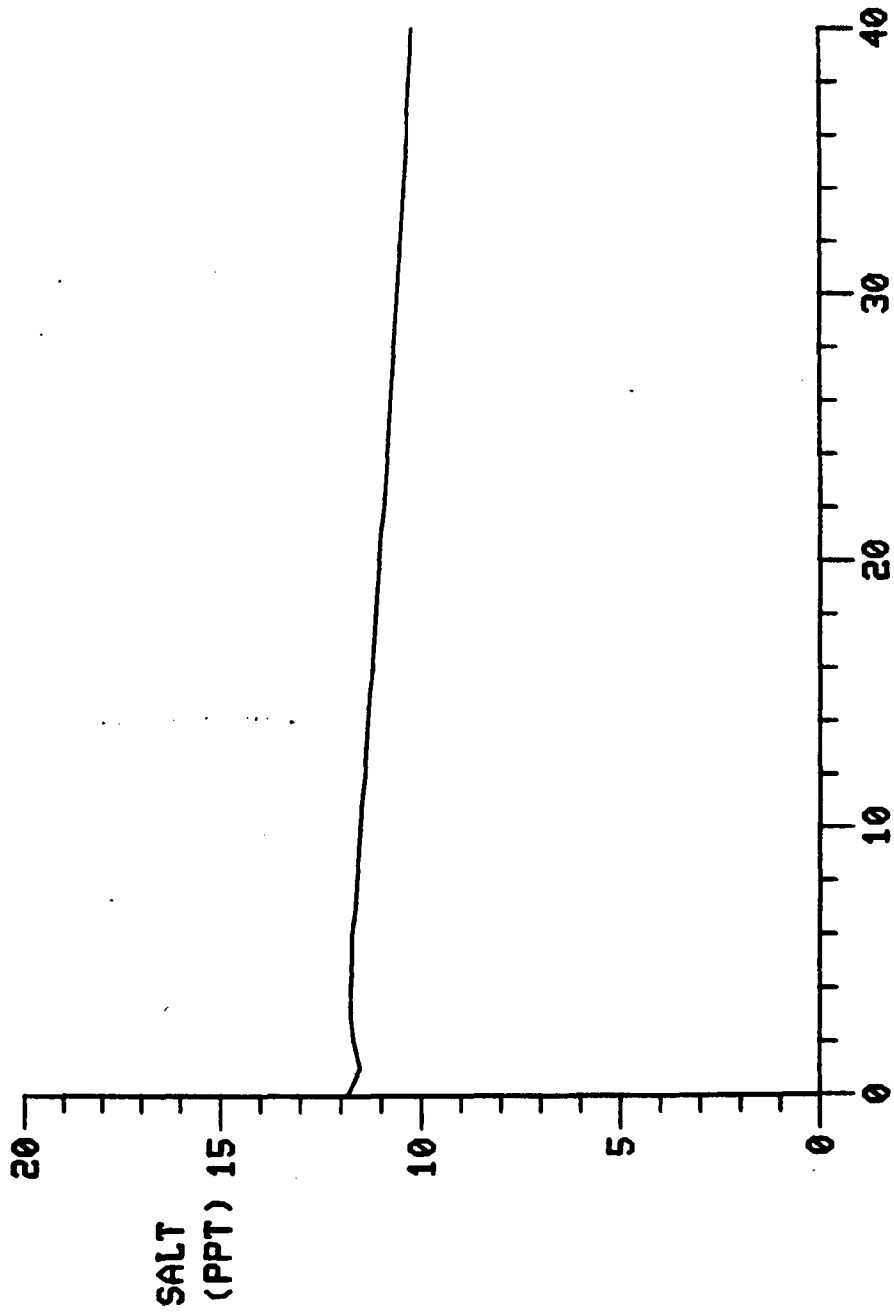


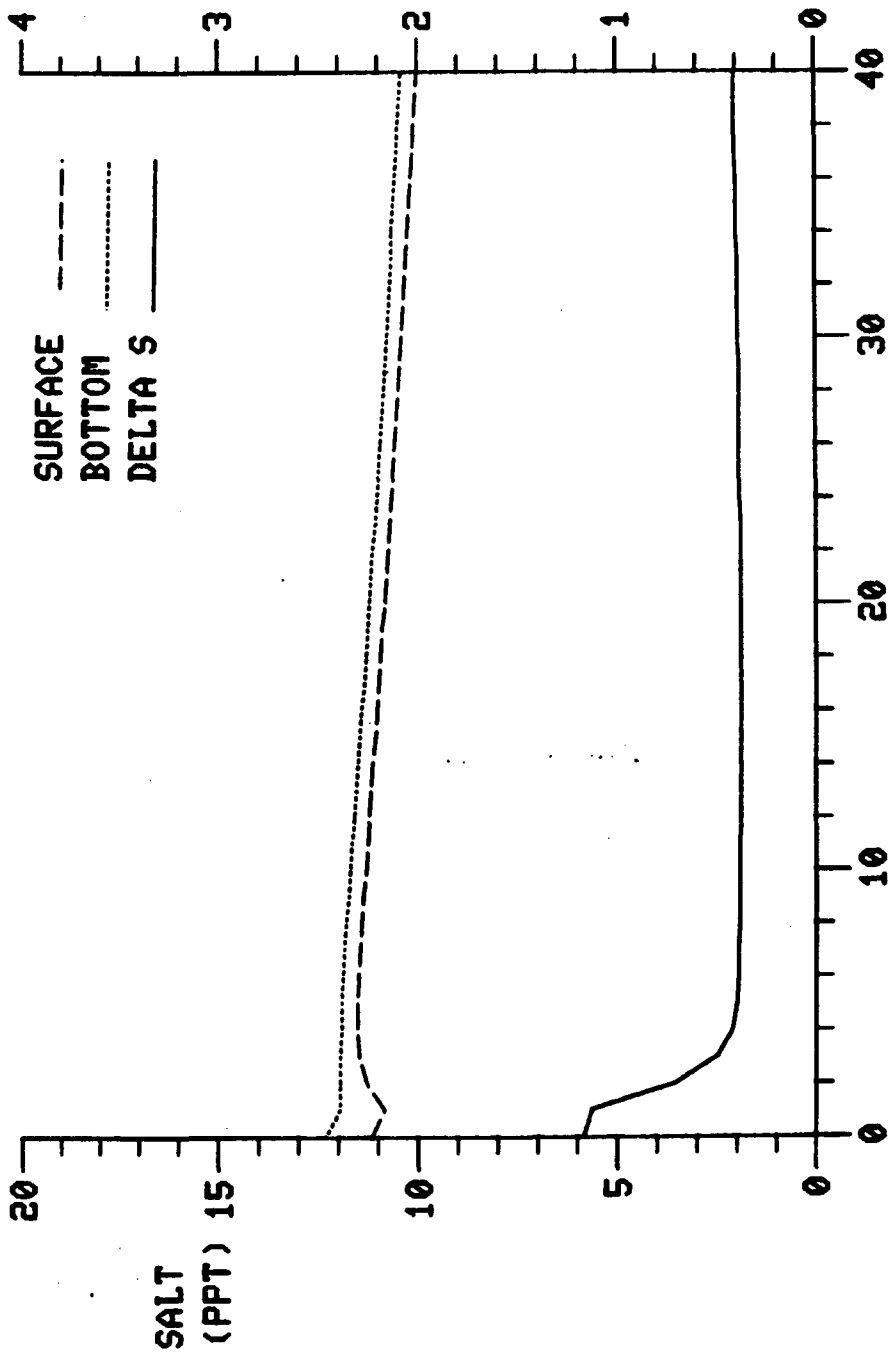
Figure 7-6a. Longitudinal Salinity After Step-Function Increase in Tide Range.



Vertical SBF Salinity (PPT) SALINITY (PPT)
 Figure 7-6b. Vertical SBF Salinity After Step-Function Increase in Tide Range.

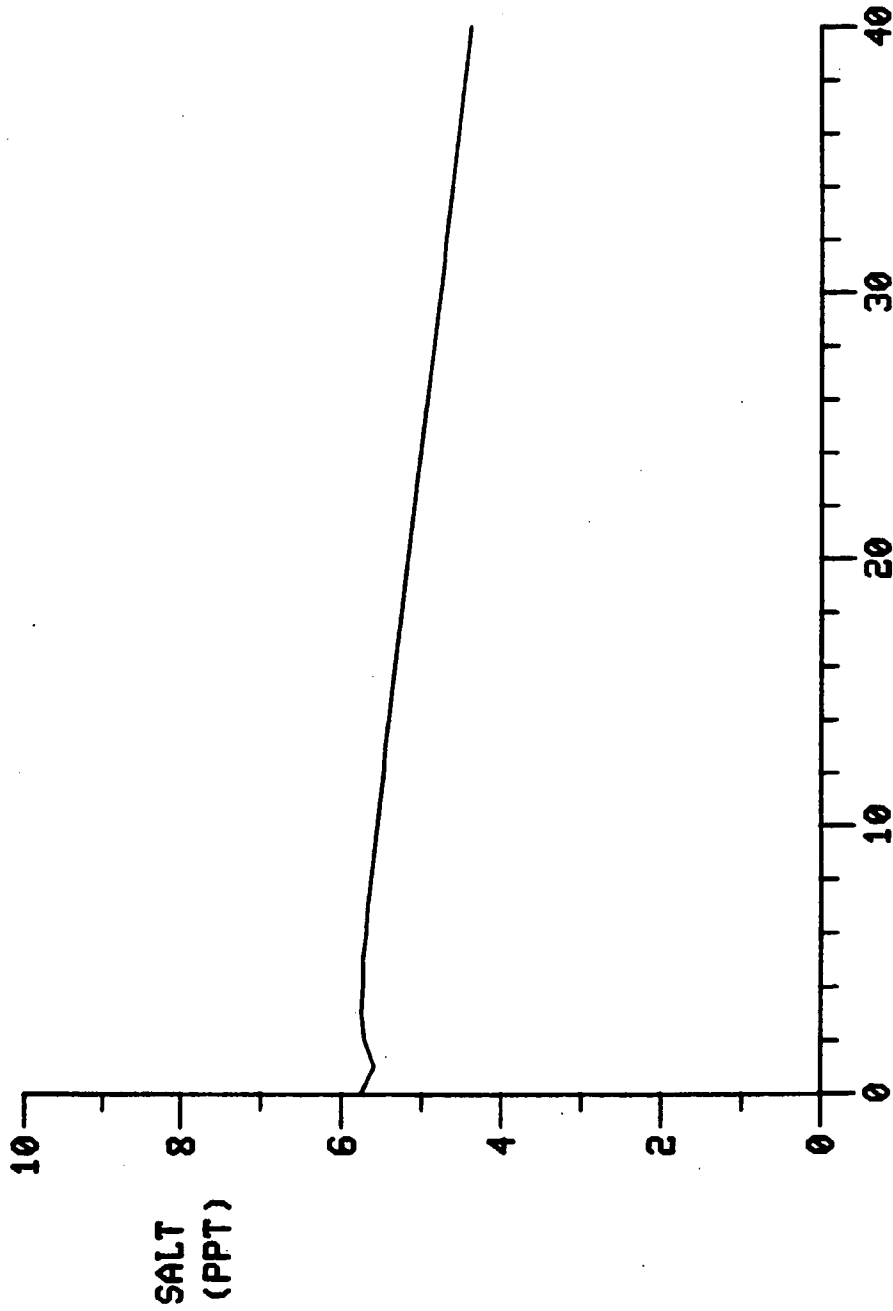


TIDAL CYCLES
 Figure 7-6c. Time Series of Depth-Average Salinity at Kilometer 20, Step-Function Increase in Tide Range.

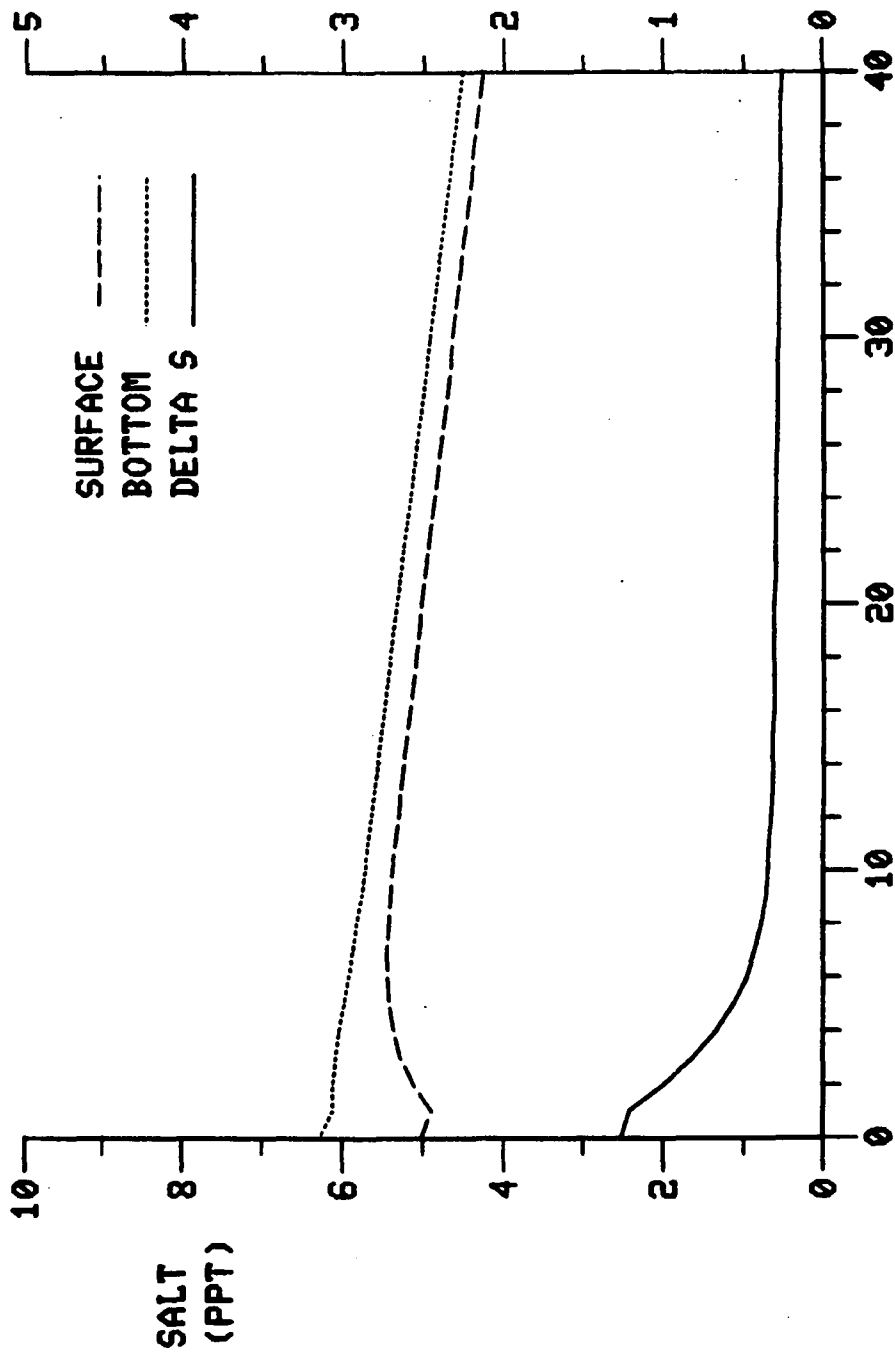


TIDAL CYCLES

Figure 7-6d. Time Series of Stratification at Kilometer 20, Step Function Increase in Tide Range.



TIDAL CYCLES
Figure 7-6e. Time Series of Depth-Average Salinity at Kilometer 44, Step-Function Increase in Tide Range.



TIDAL CYCLES
 Figure 7-6f. Time Series of Stratification at Kilometer 44, Step-Function Increase in Tide Range.

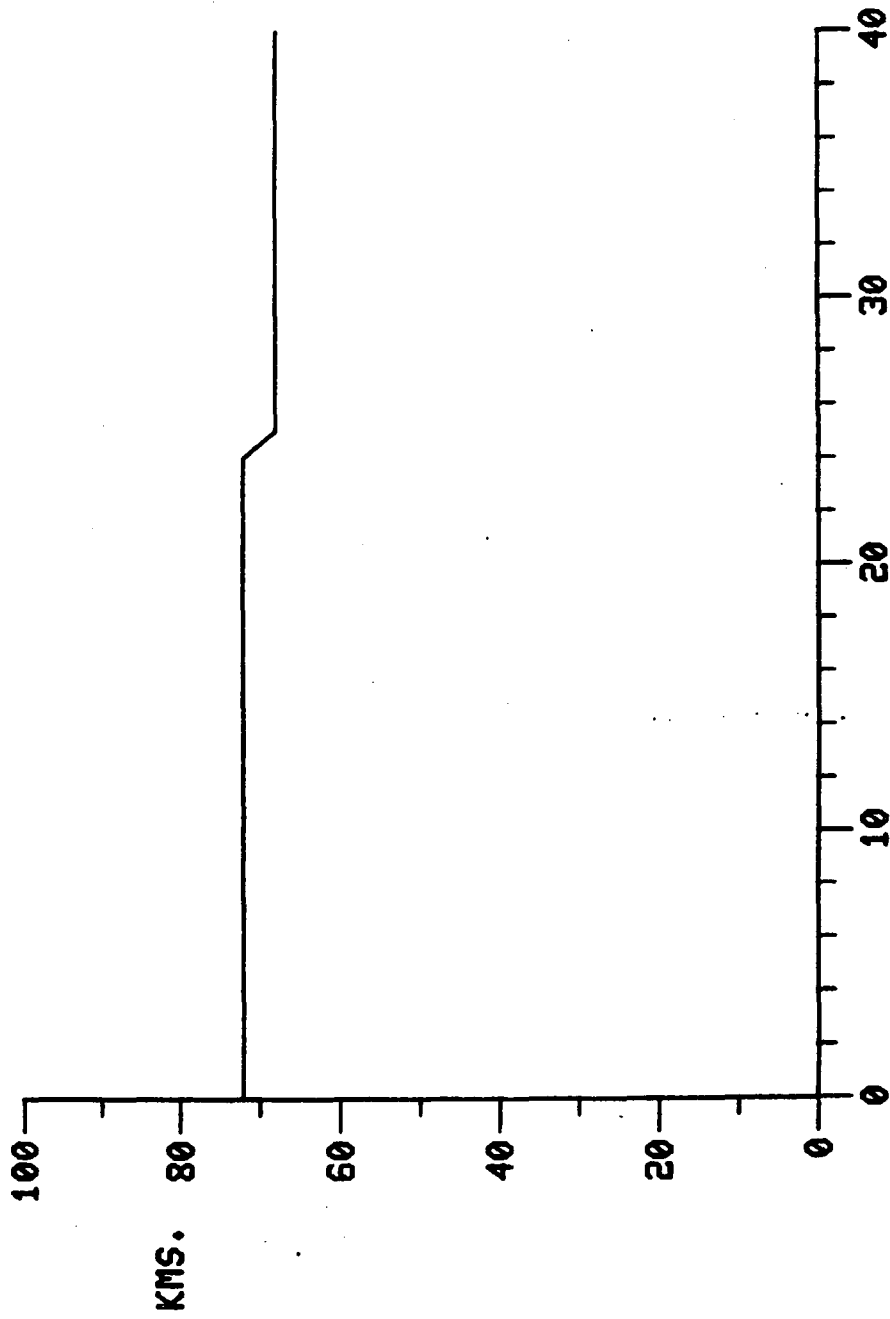


Figure 7-6g. Location of 1 ‰ Isohaline, Step-Function Increase in Tide Range.

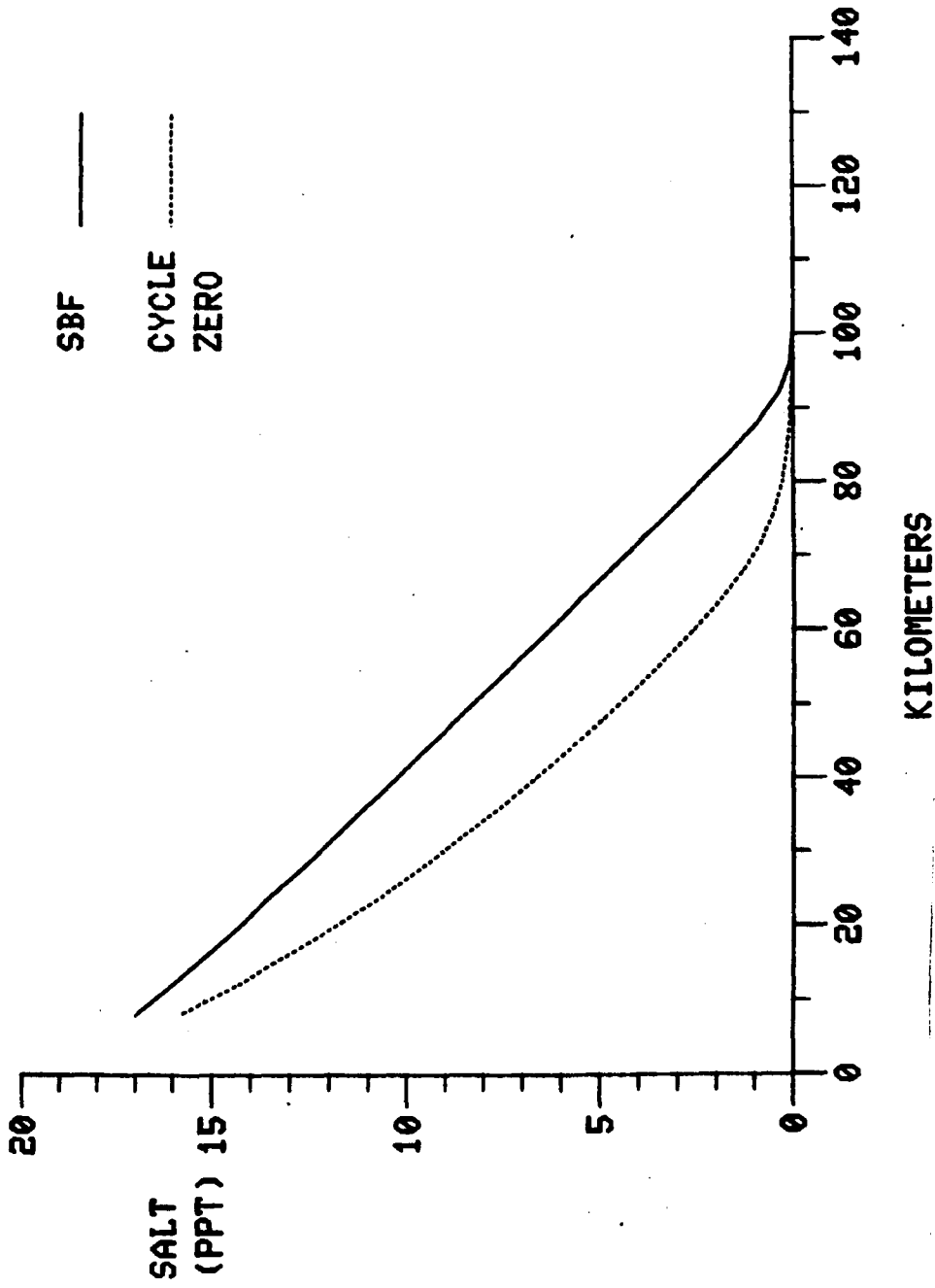


Figure 7-7a. Longitudinal Salinity After Step-Function Decrease in Tide Range.

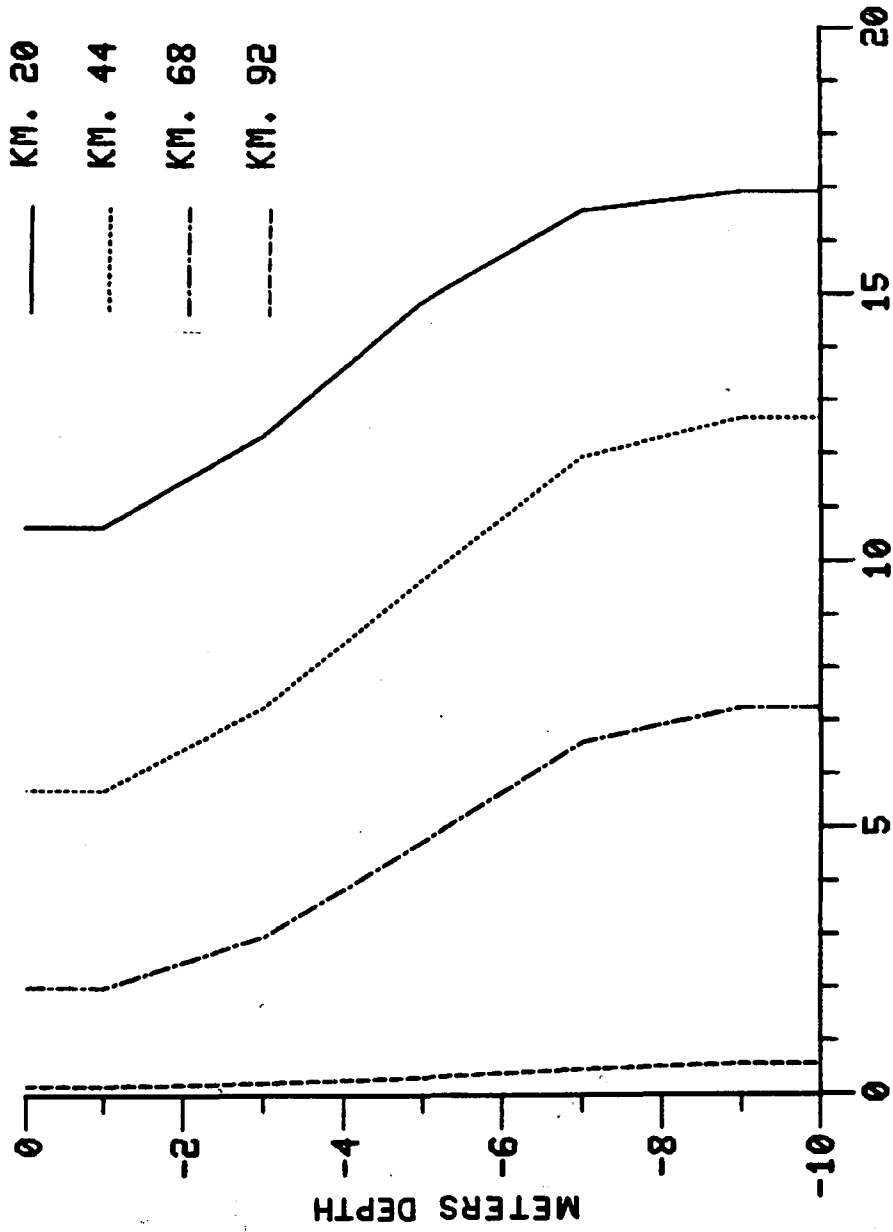
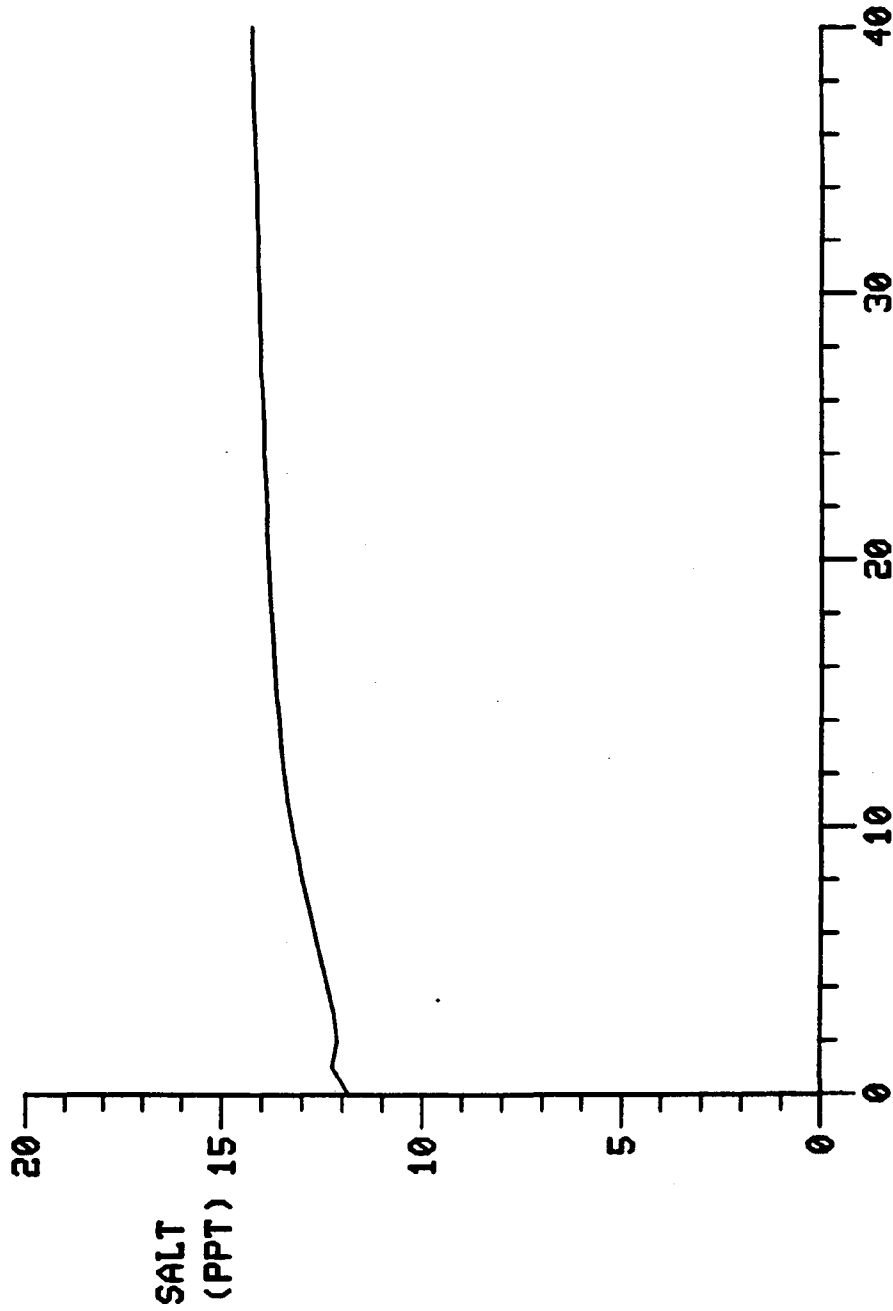
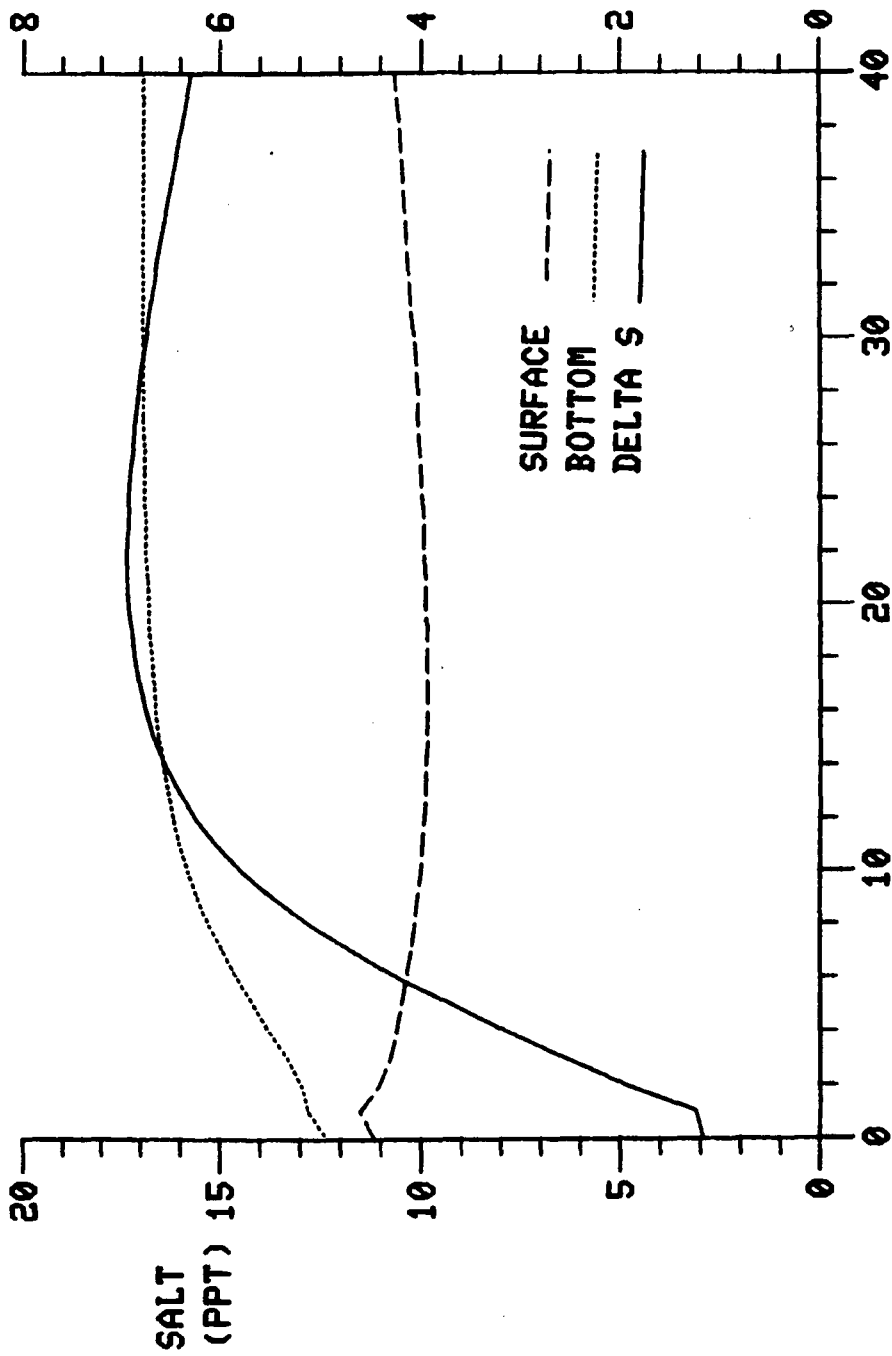


Figure 7-7b. Vertical SBF Salinity After Step-Function Decrease in Tide Range.

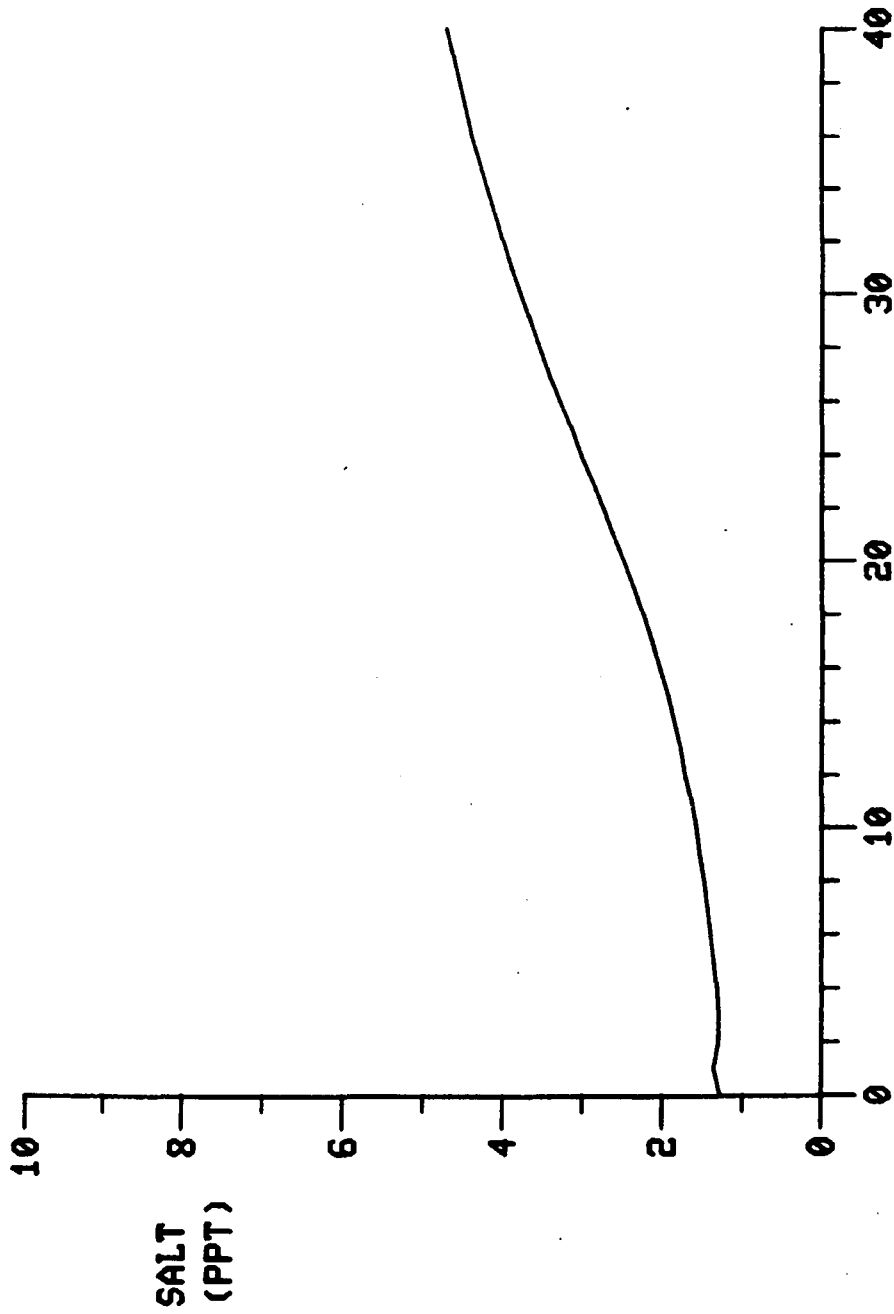


TIDAL CYCLES
Figure 7-7c. Time Series of Depth-Average Salinity at Kilometer 20, Step-Function Decrease in Tide Range.

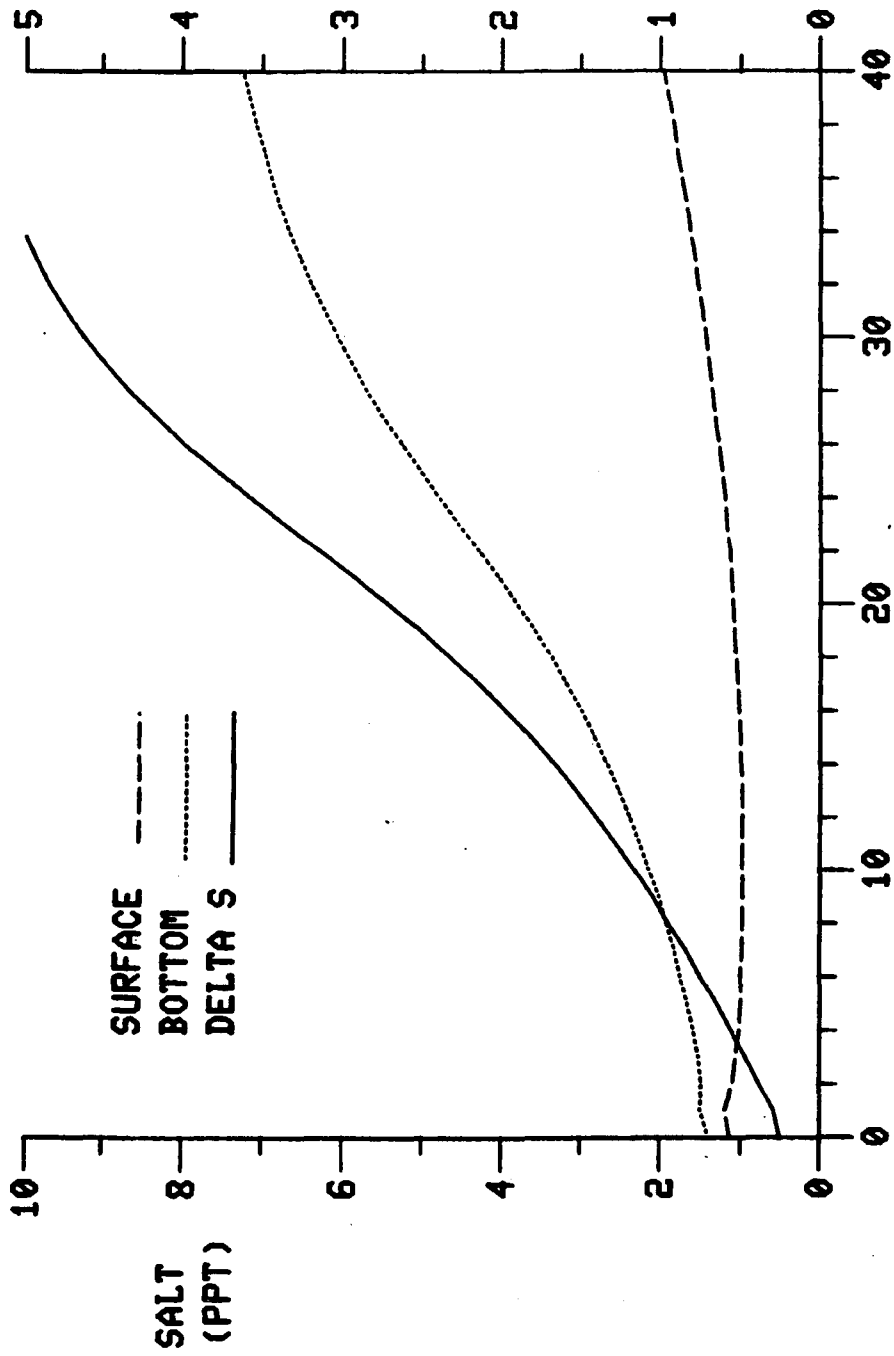


TIDAL CYCLES

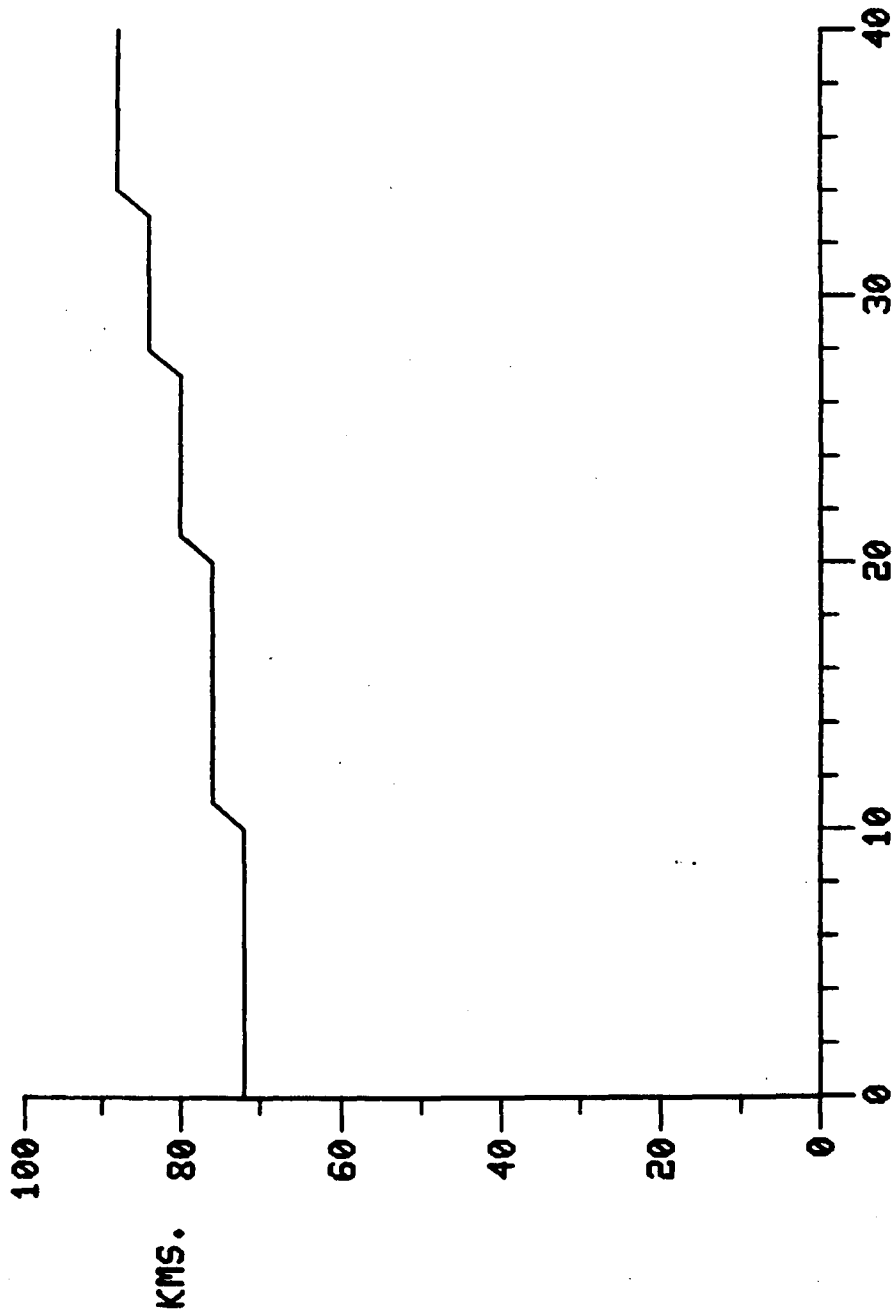
Figure 7-7d. Time Series of Stratification at Kilometer 20, Step-Function Decrease in Tide Range.



TIDAL CYCLES
Figure 7-7e. Time Series of Depth-Average Salinity at Kilometer 68, Step-Function Decrease in Tide Range.



TIDAL CYCLES
 Figure 7-7f. Time Series of Stratification at Kilometer 68, Step-Function Decrease in Tide Range.



TIDAL CYCLES
Figure 7-7g. Location of 1 ‰ Isohaline, Step-Function Decrease in Tide Range.

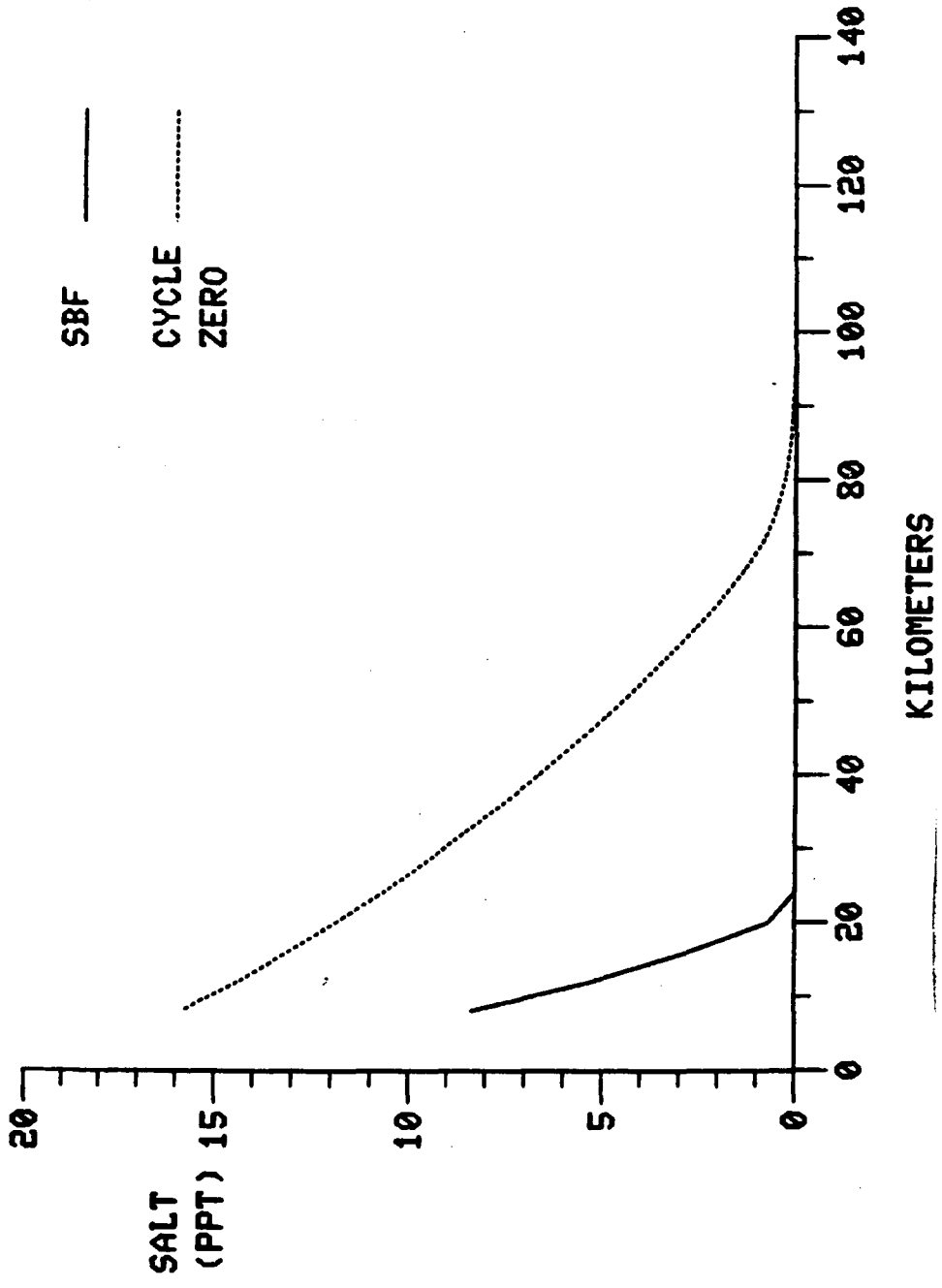
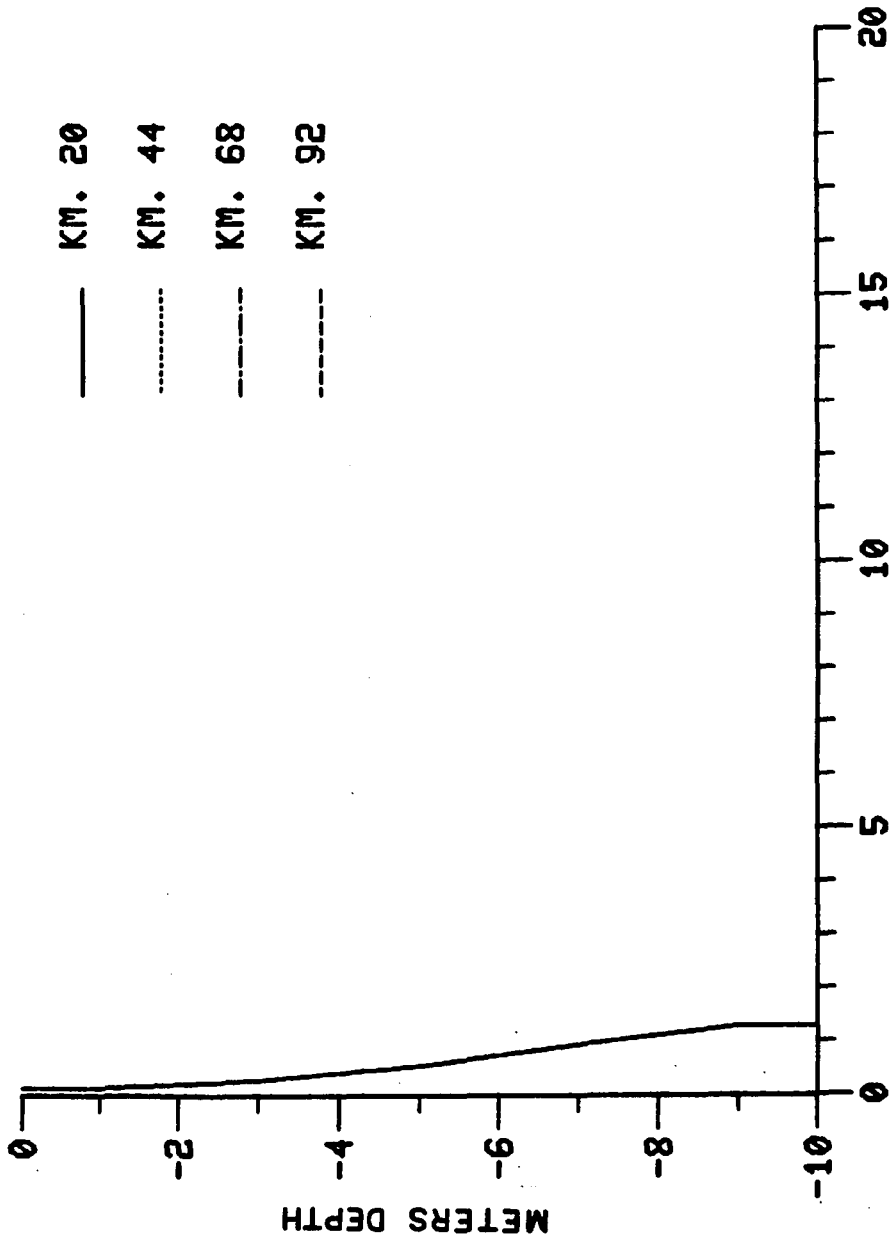


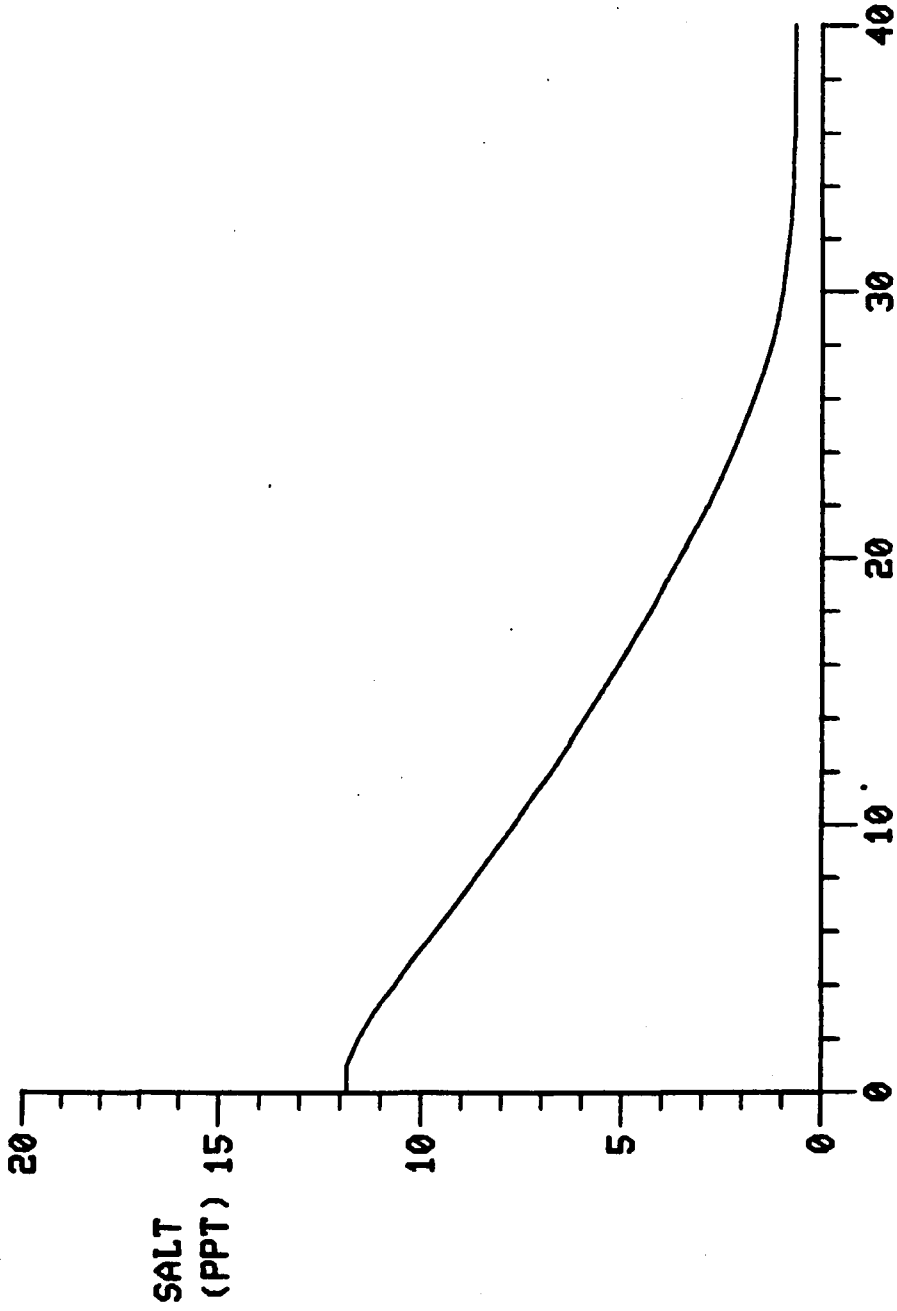
Figure 7-8a. Longitudinal Salinity After Step-Function Increase in Flow.

N

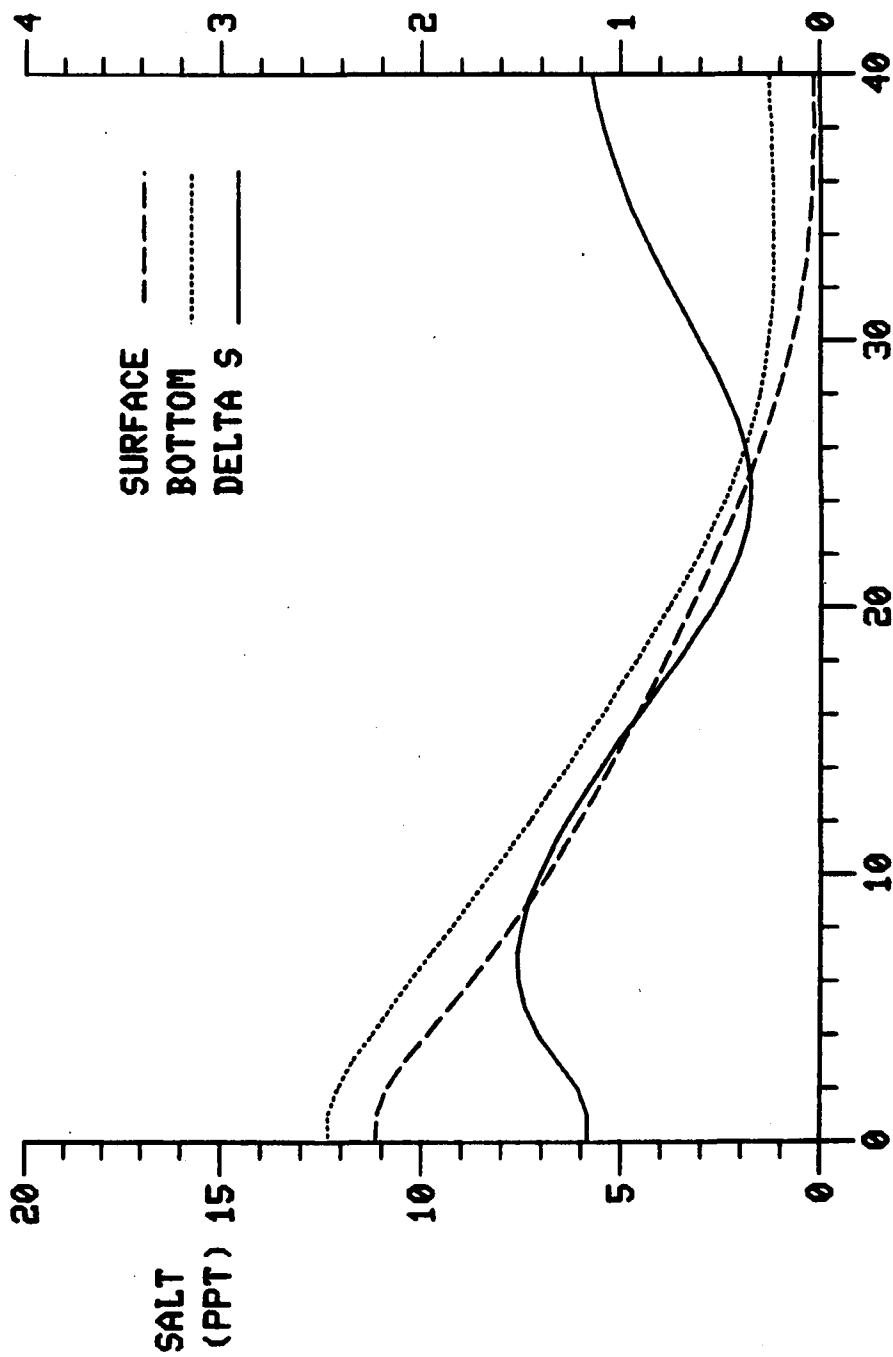


SALINITY (PPT)

Figure 7-8b. Vertical SBF Salinity After Step-Function Increase in Flow.



TIDAL CYCLES
Figure 7-8c. Time Series of Depth-Average Salinity at Kilometer 20, Step-Function Increase in Flow.



TIDAL CYCLES

Figure 7-8d. Time Series of Stratification at Kilometer 20, Step-Function Increase in Flow.

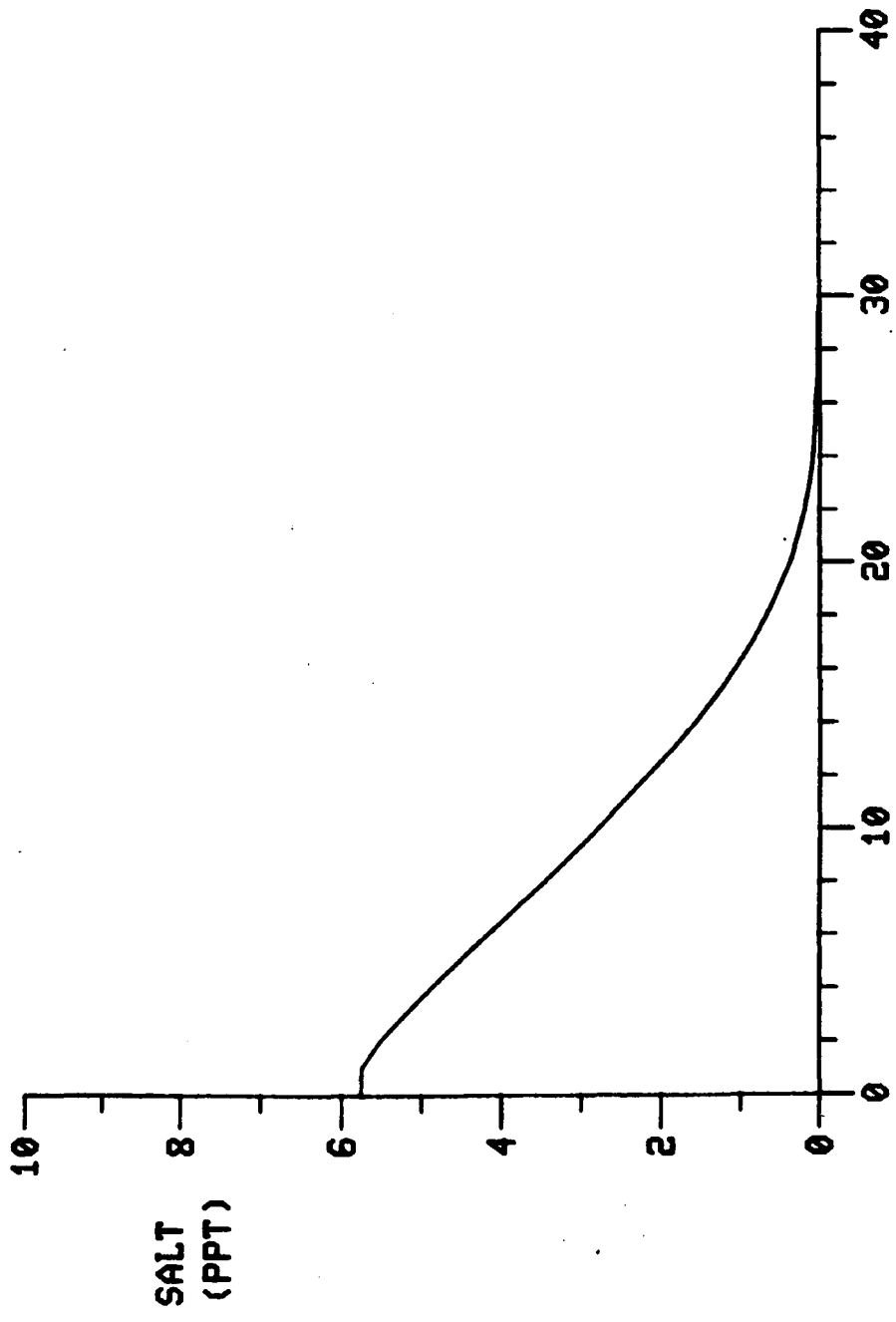
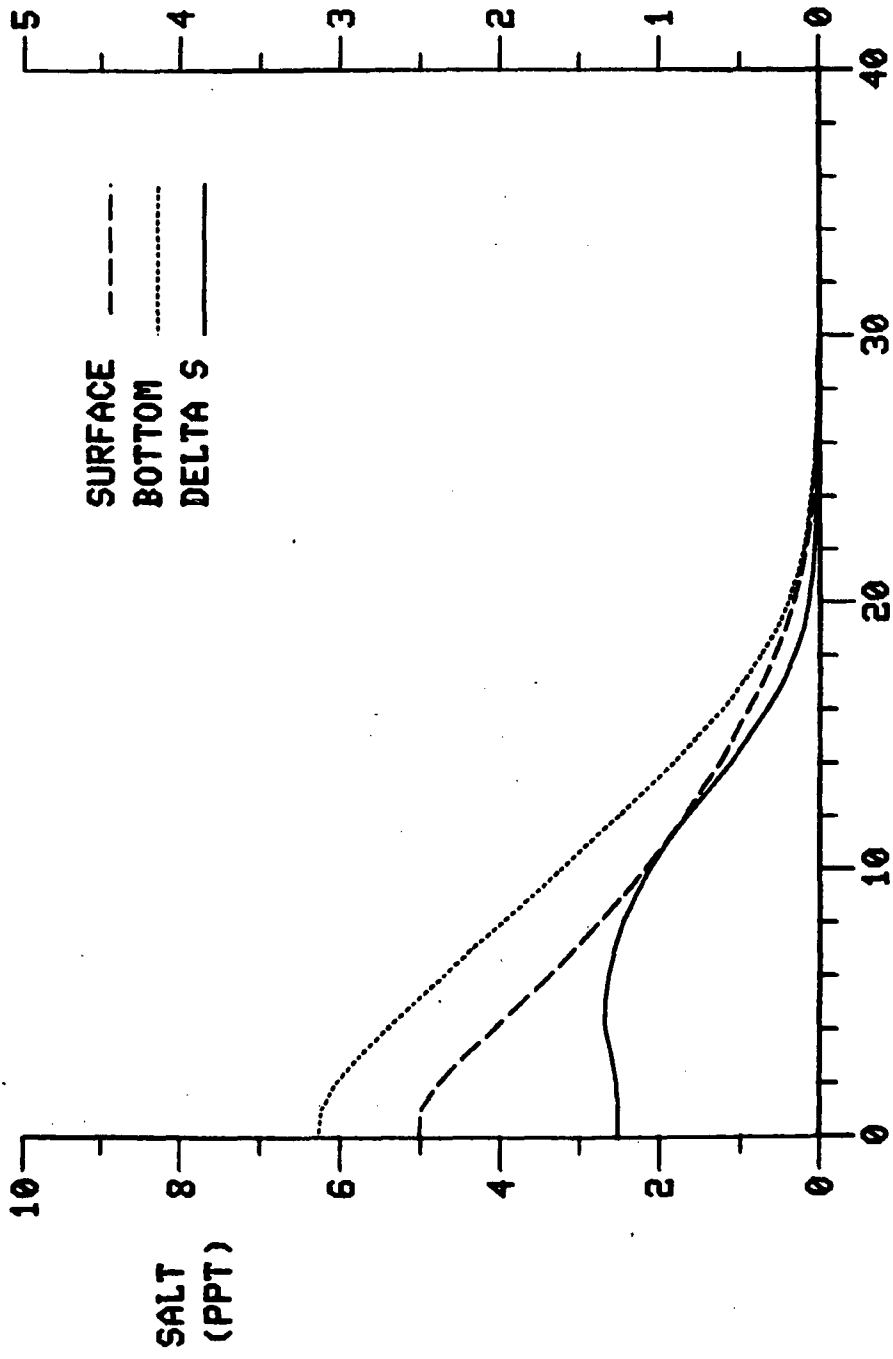
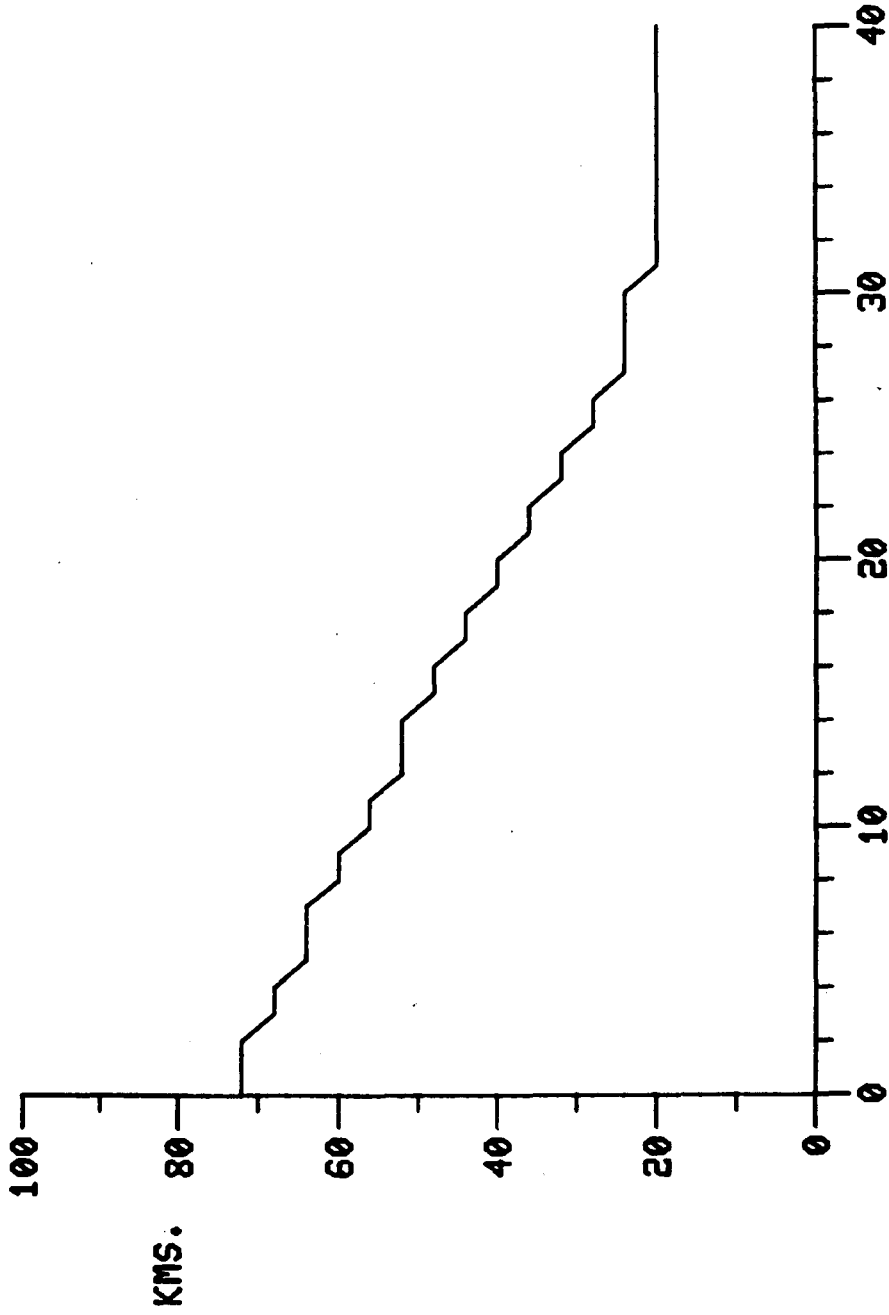


Figure 7-8e. Time Series of Depth-Average Salinity at Kilometer 44, Step-Function Increase in Flow.

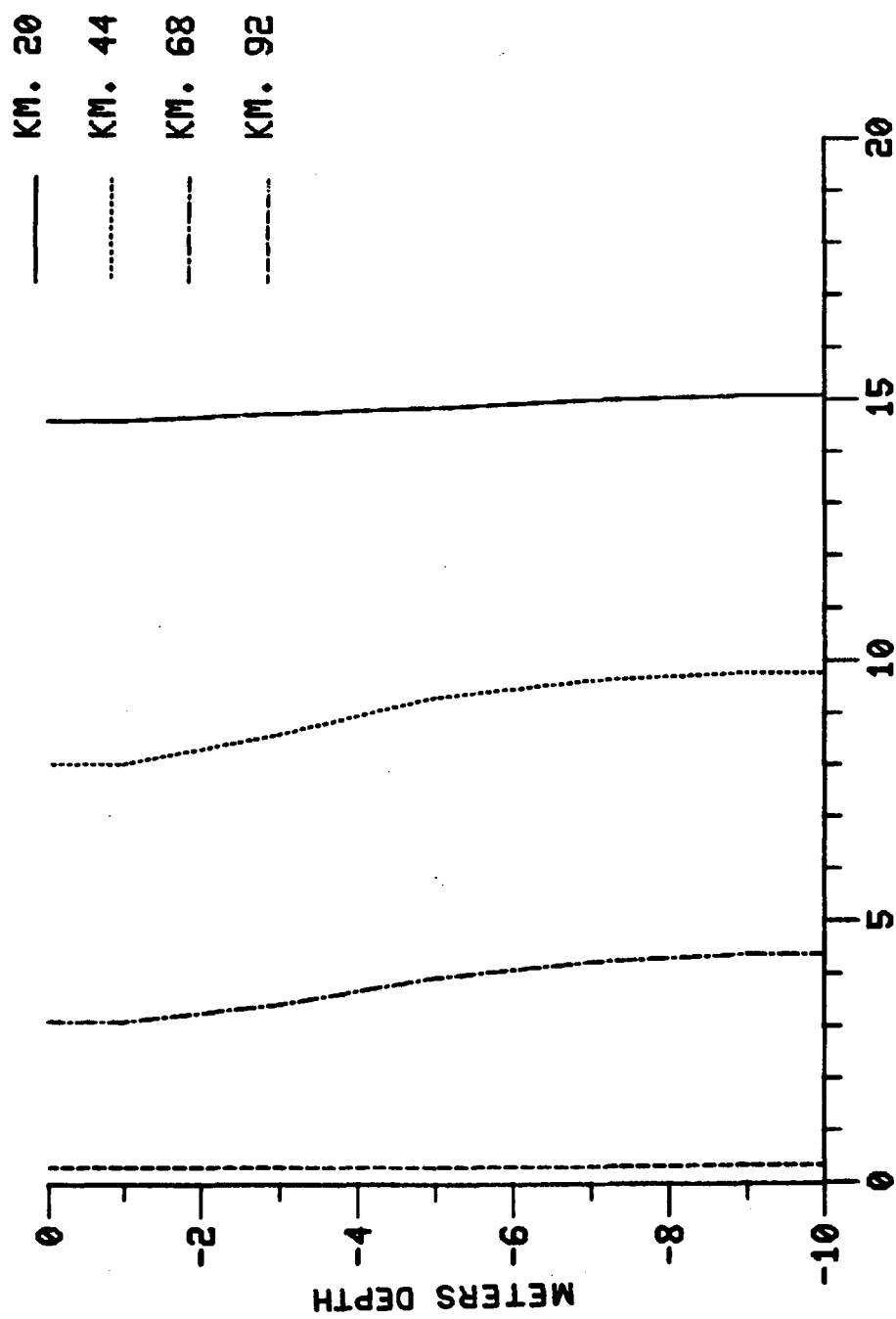


TIDAL CYCLES

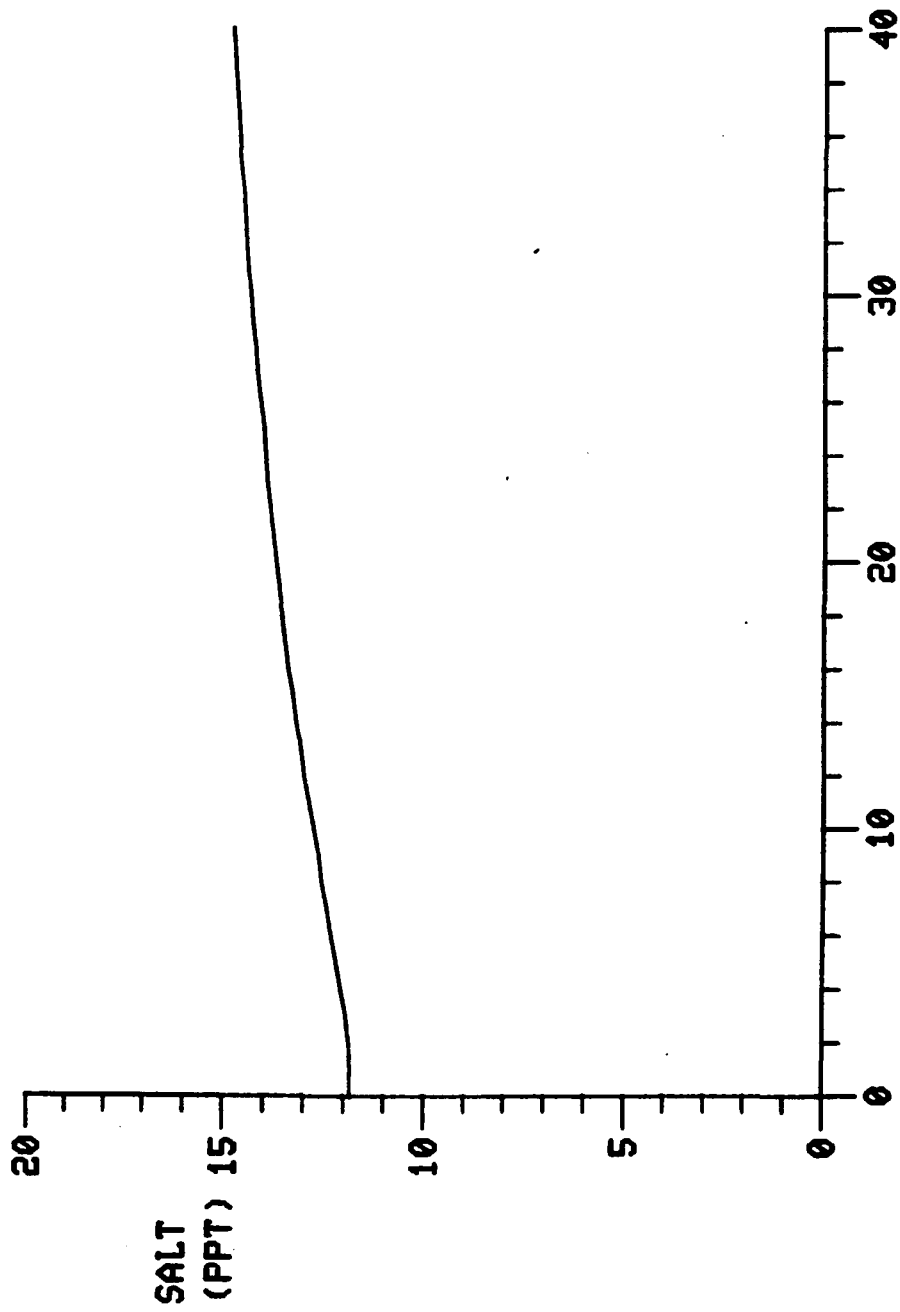
Figure 7-8f. Time Series of Stratification at Kilometer 44, Step-Function Increase in Flow.



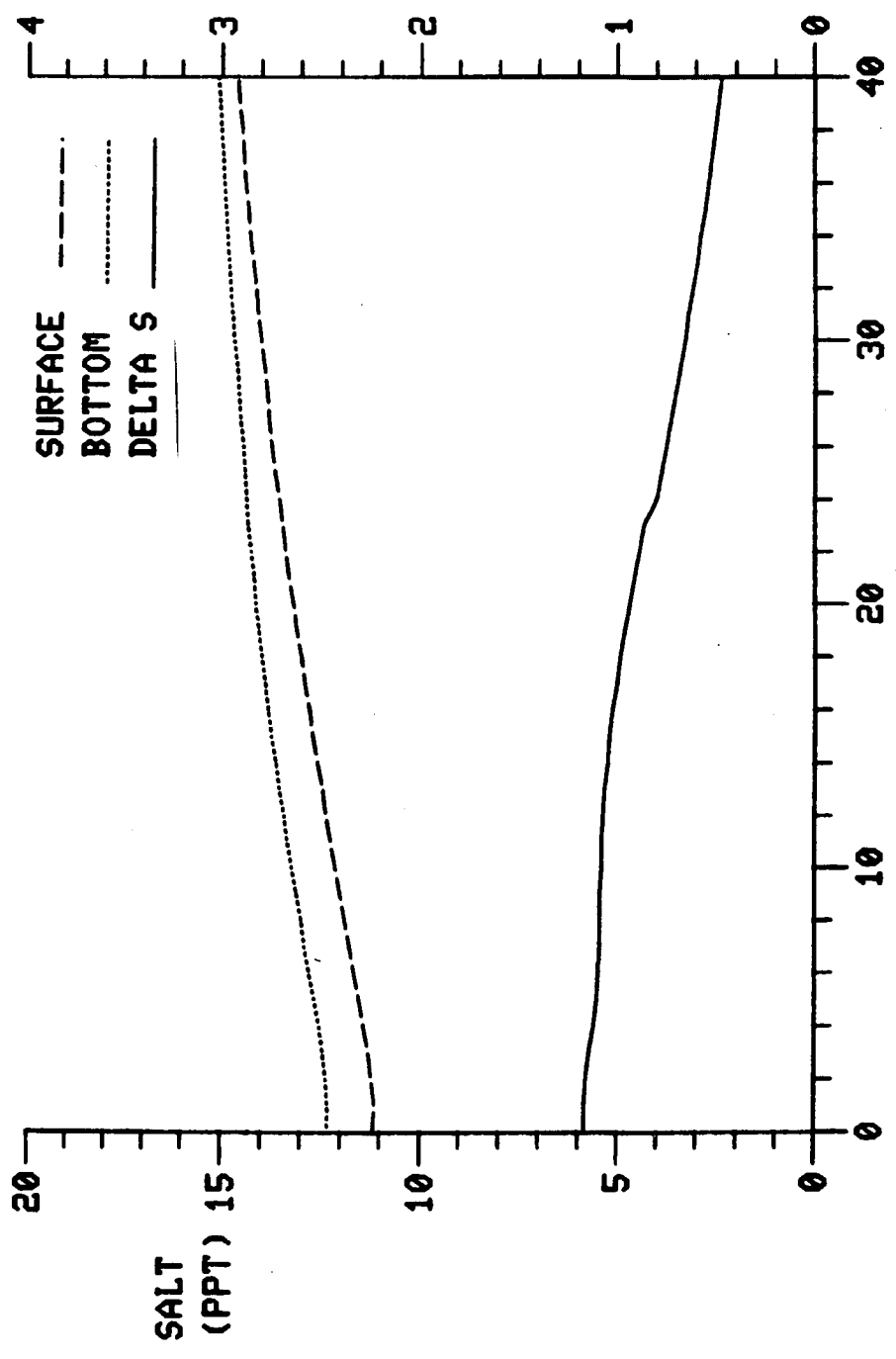
TIDAL CYCLES
Figure 7-8g. Location of 1 ‰ Isohaline, Step-Function Increase in Flow.



SALINITY (PPT)
Figure 7-9b. Vertical SBF Salinity After Step-Function Decrease in Flow.

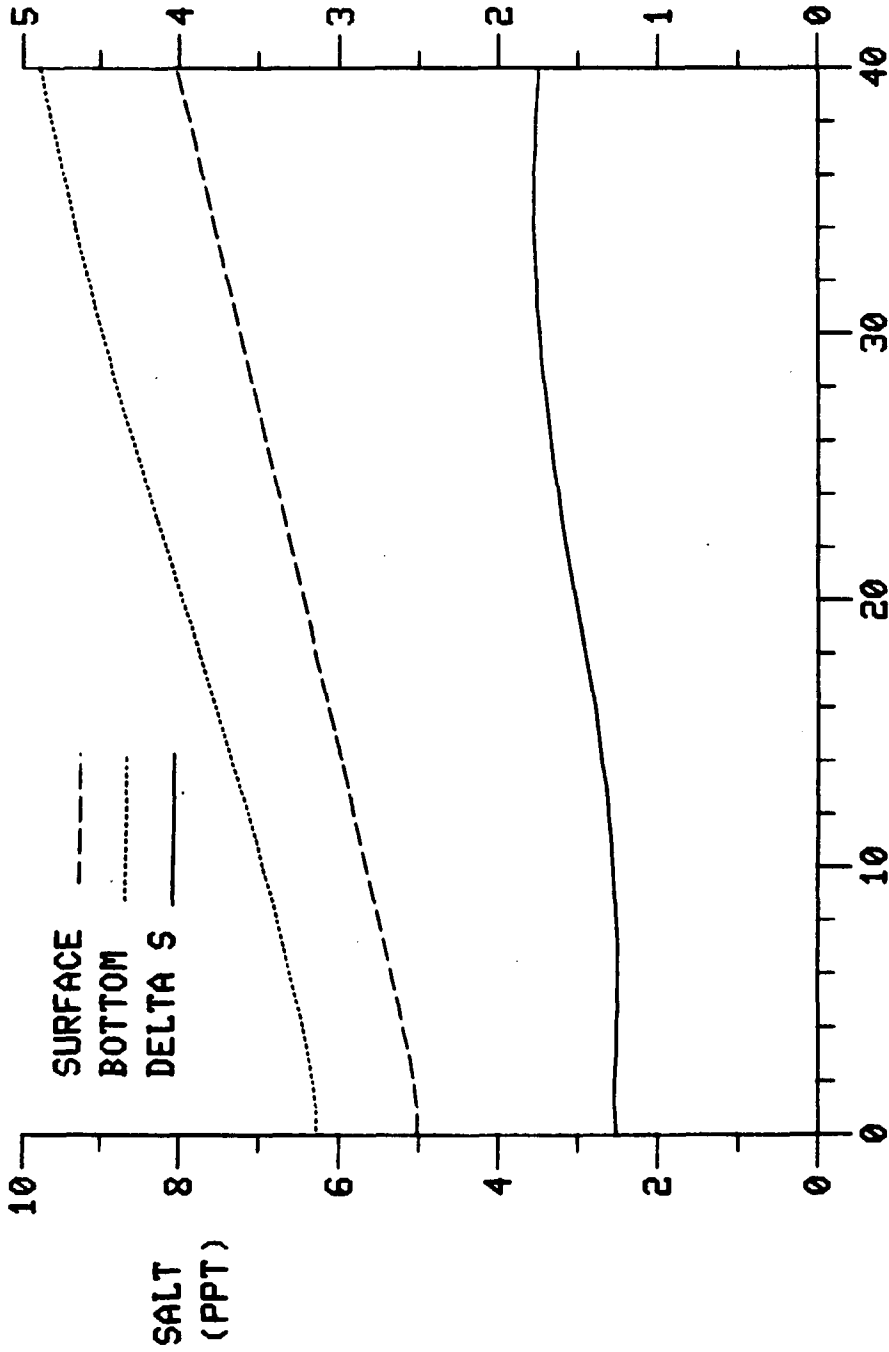


TIDAL CYCLES
Figure 7-9c. Time Series of Depth-Average Salinity at Kilometer 20, Step-Function Decrease in Flow.



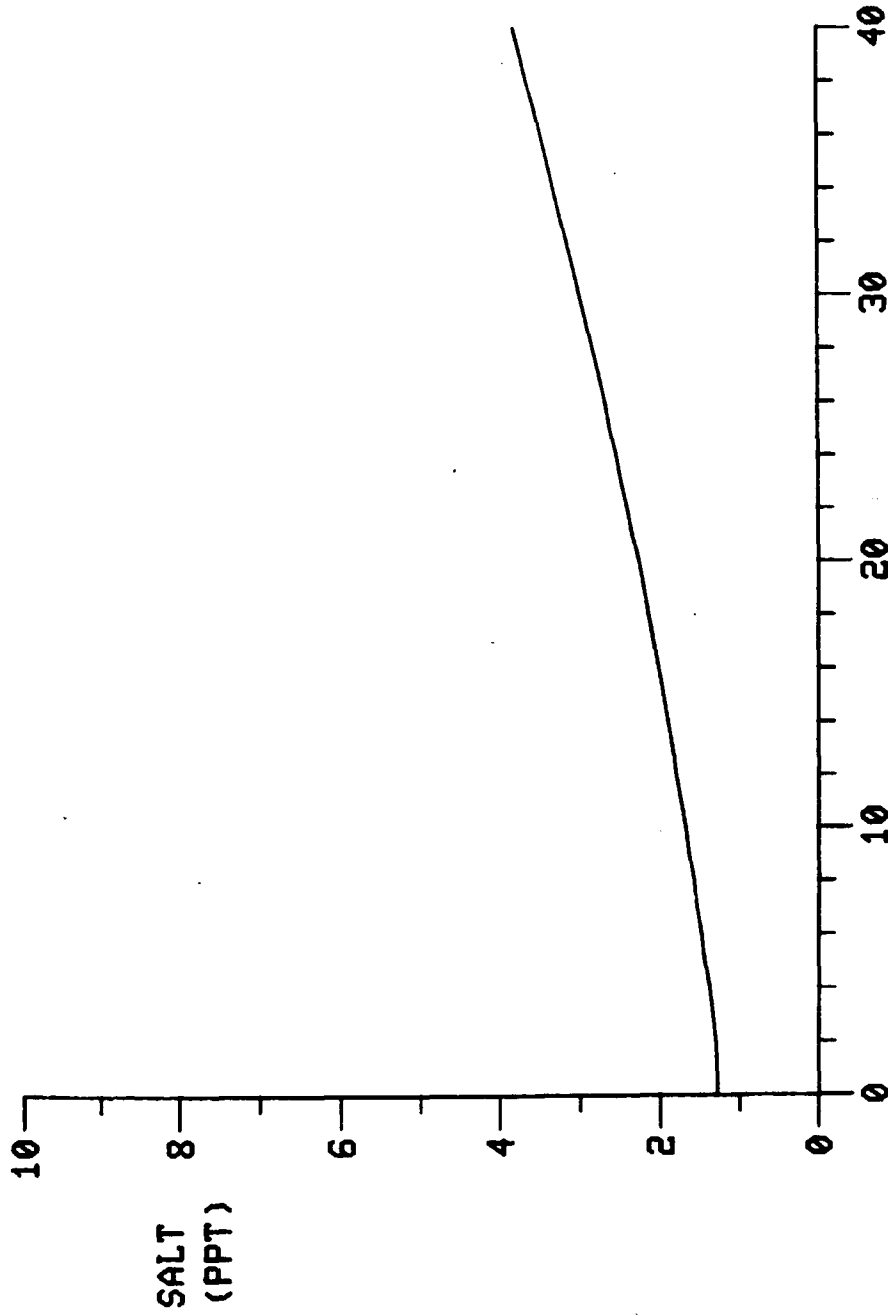
TIDAL CYCLES

Figure 7-9d. Time Series of Stratification at Kilometer 20, Step-Function Decrease in Flow.



TIDAL CYCLES

Figure 7-9f. Time Series of Stratification at Kilometer 44, Step Function Decrease in Flow.



TIDAL CYCLES
Figure 7-9g. Time Series of Depth Average Salinity at Kilometer 68, Step-Function Decrease in Flow.

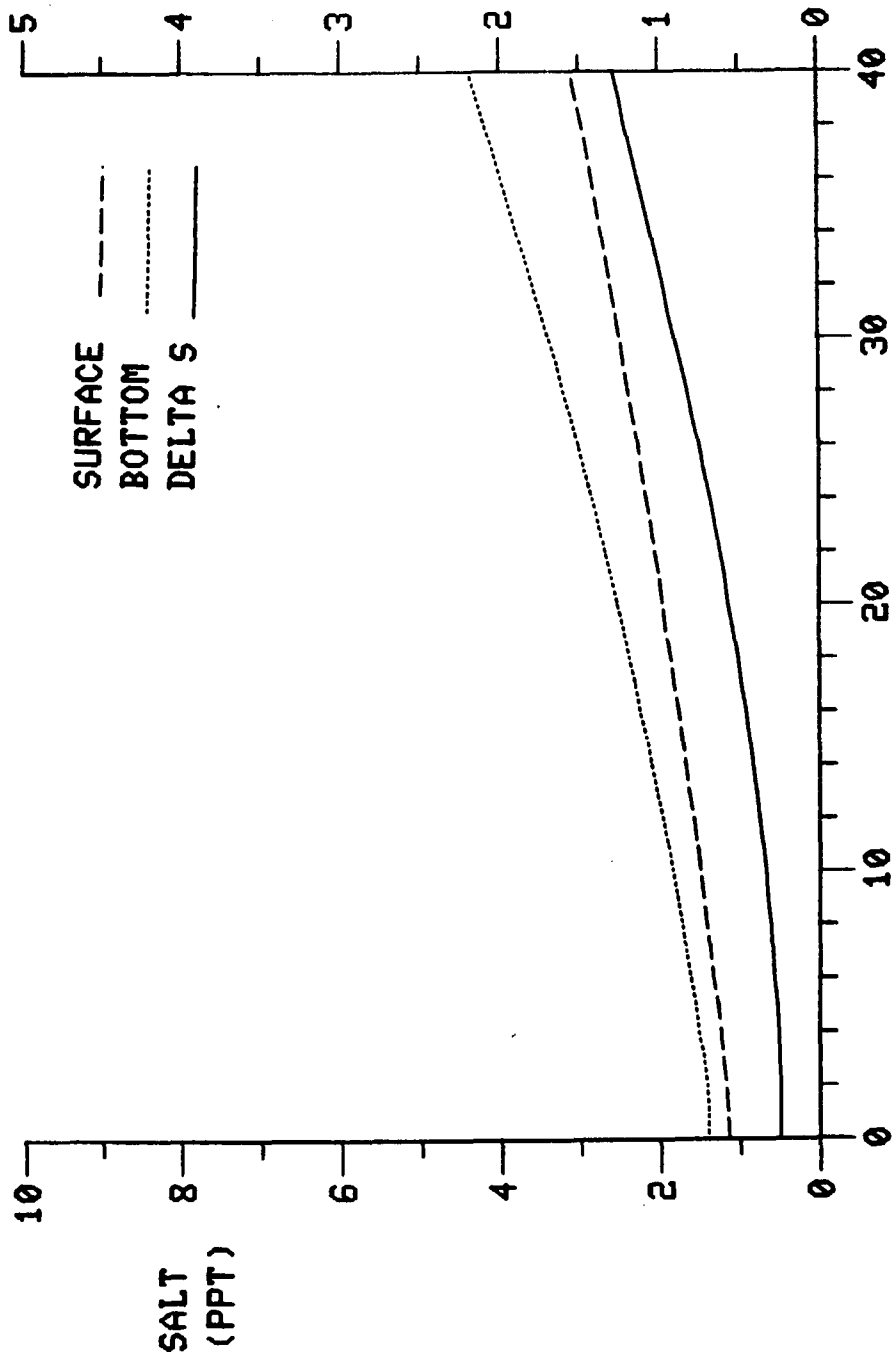
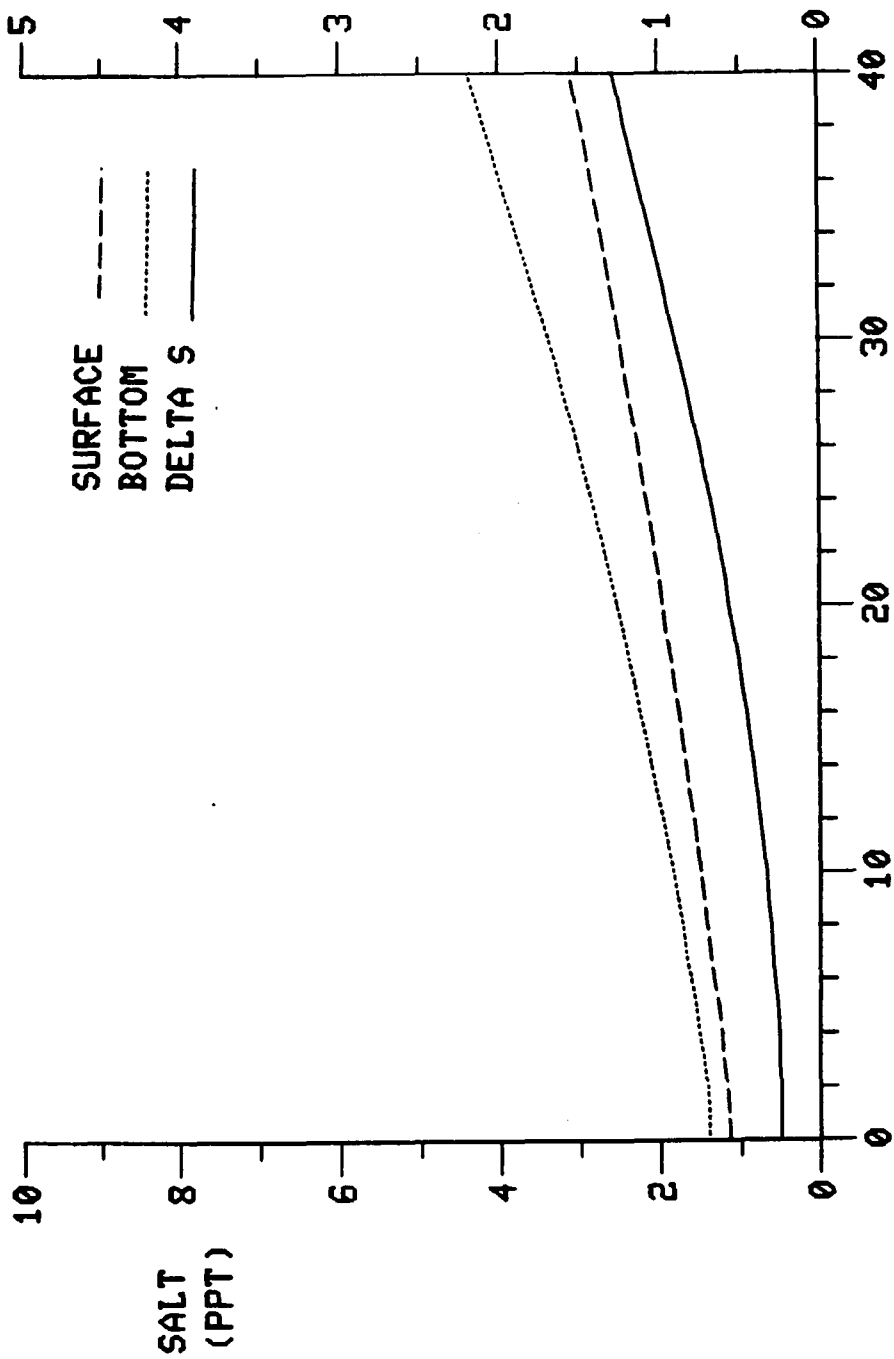
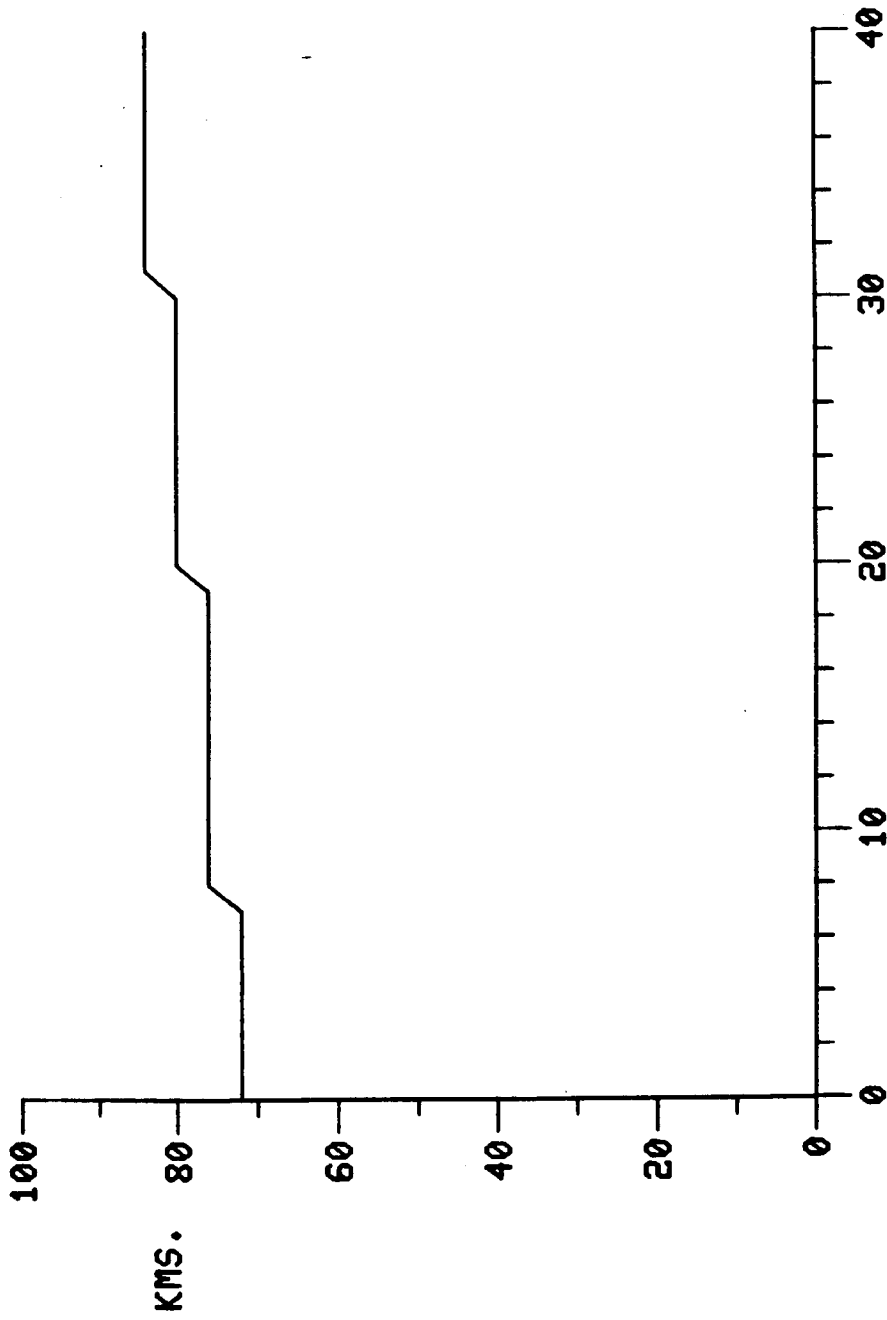


Figure 7-9h. Time Series of Stratification at Kilometer 68, Step-Function Decrease in Flow.



TIDAL CYCLES
 Figure 7-9h. Time Series of Stratification at Kilometer 68, Step-Function Decrease in Flow.



TIDAL CYCLES
Figure 7-91. Location of 1 ‰ Isohaline, Step-Function Decrease in Flow.

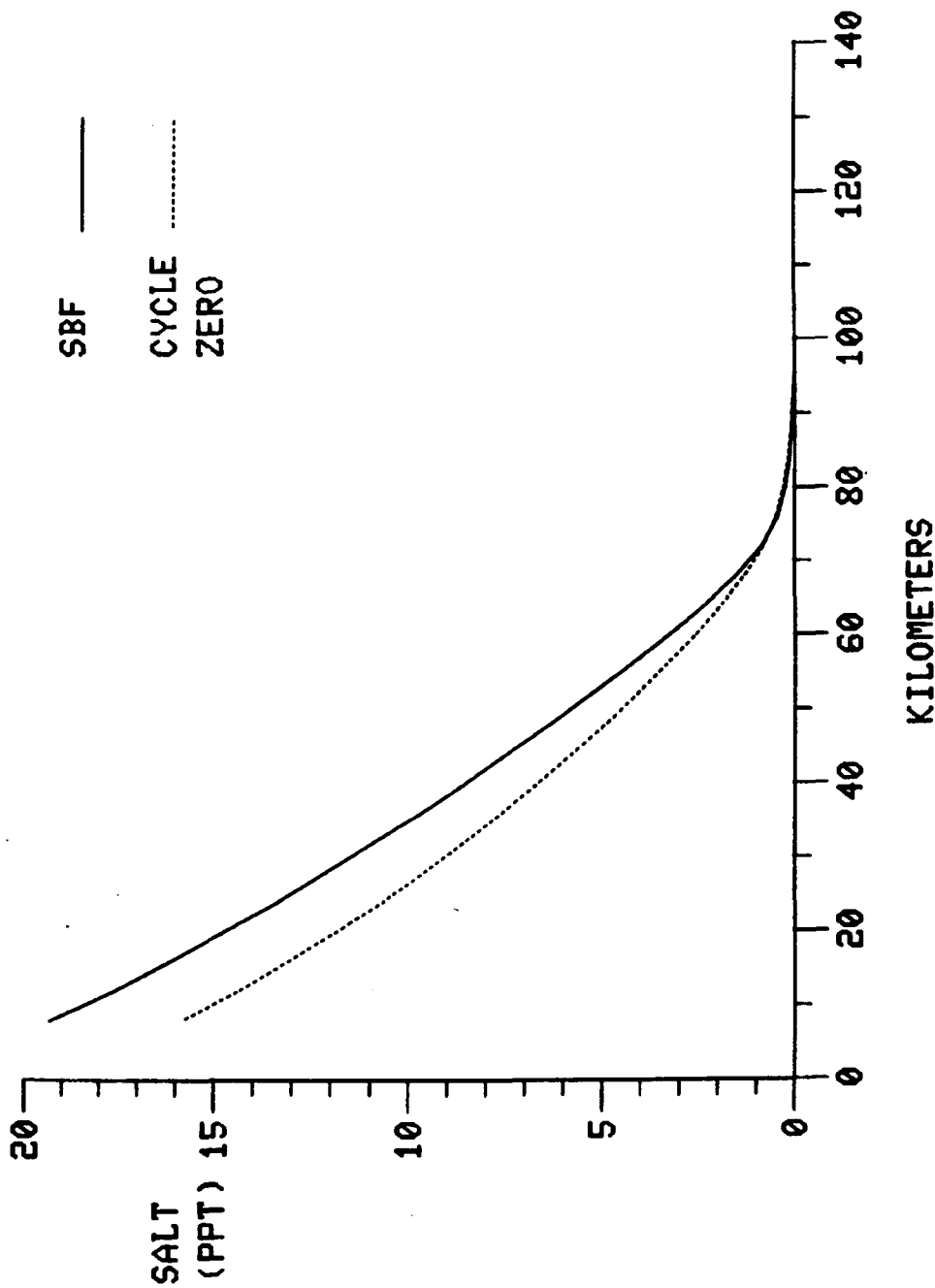


Figure 7-10a. Longitudinal Salinity After Step-Function Increase in Salinity Boundary.

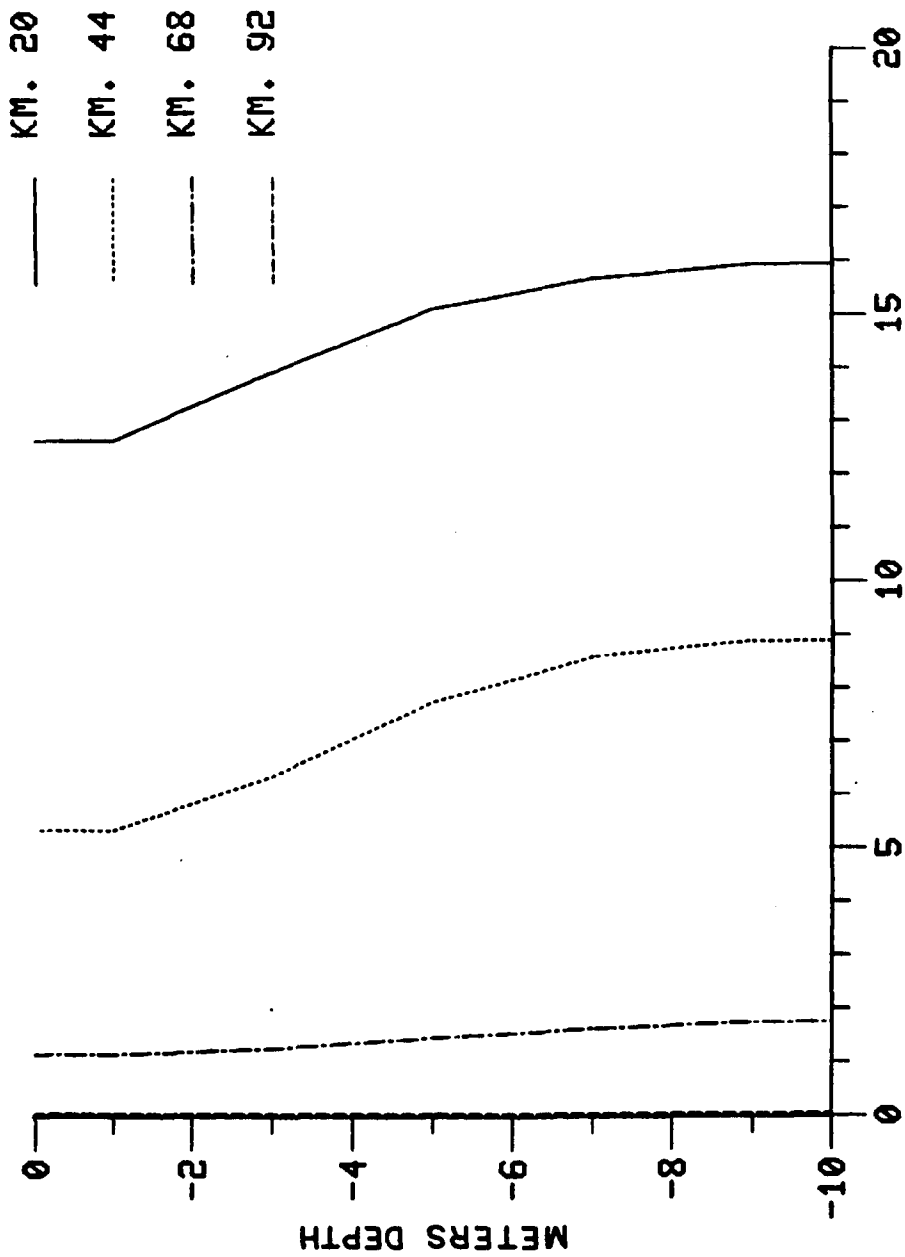


Figure 7-10b. Vertical SBF Salinity After Step-Function Increase in Salinity Boundary.

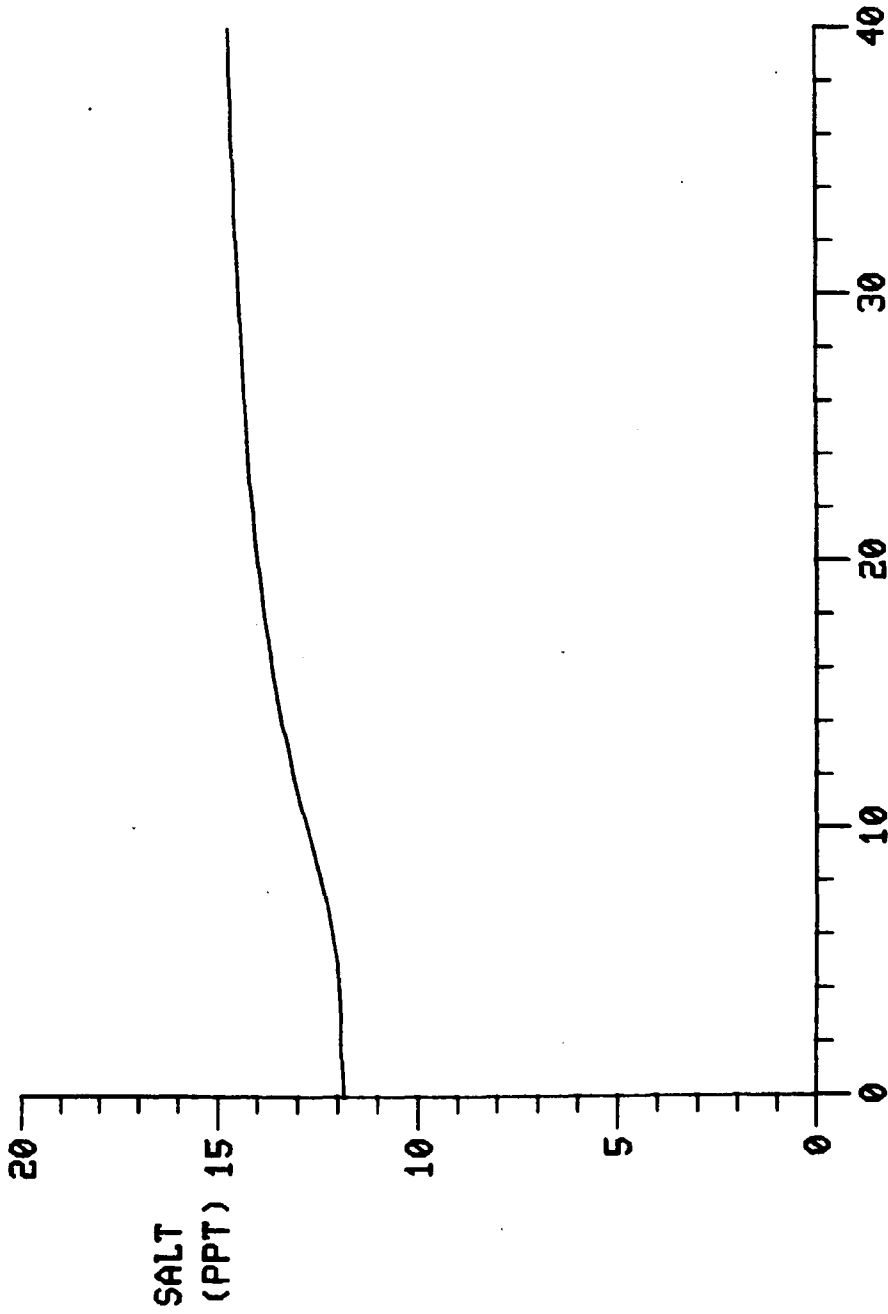
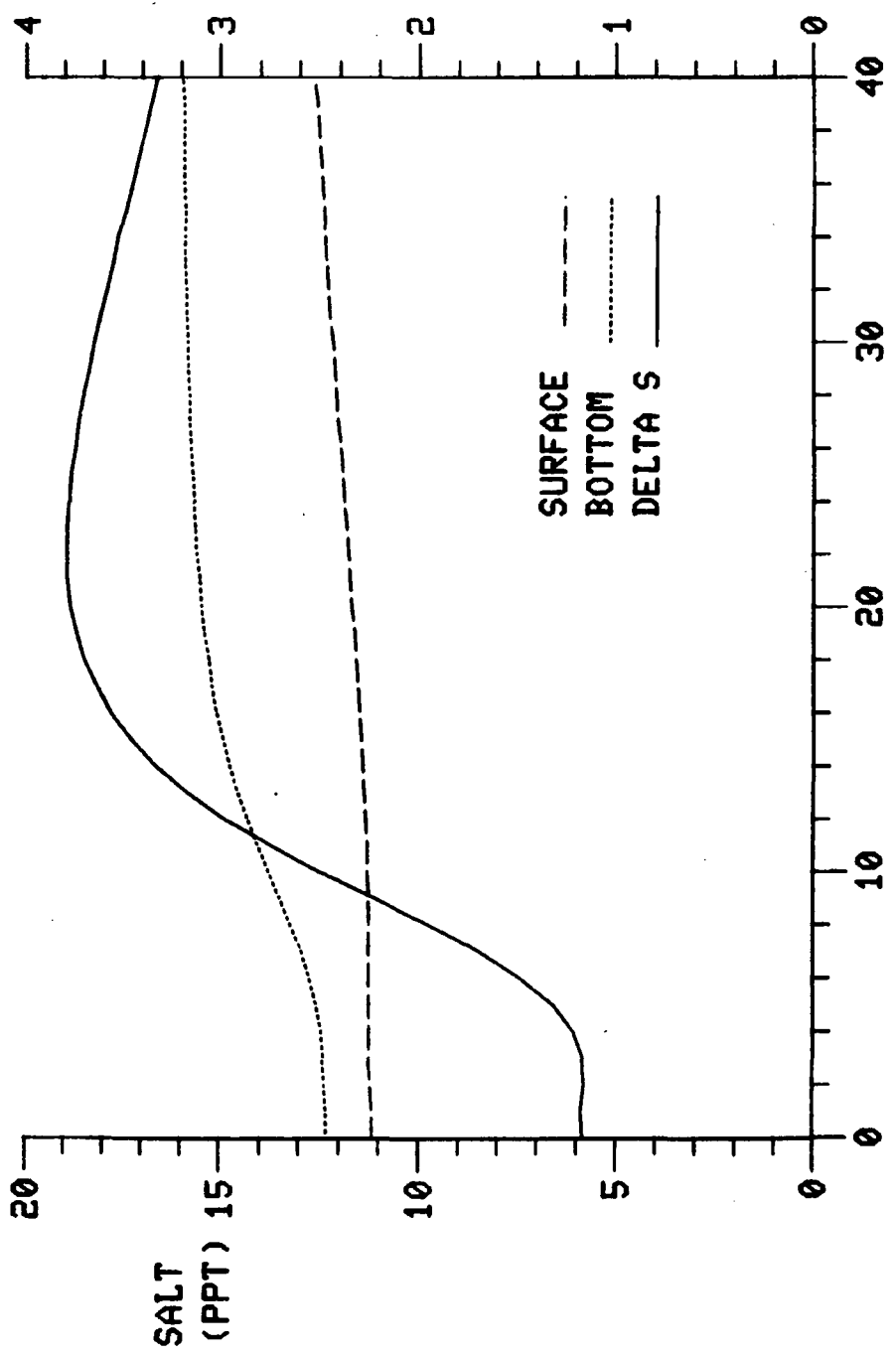
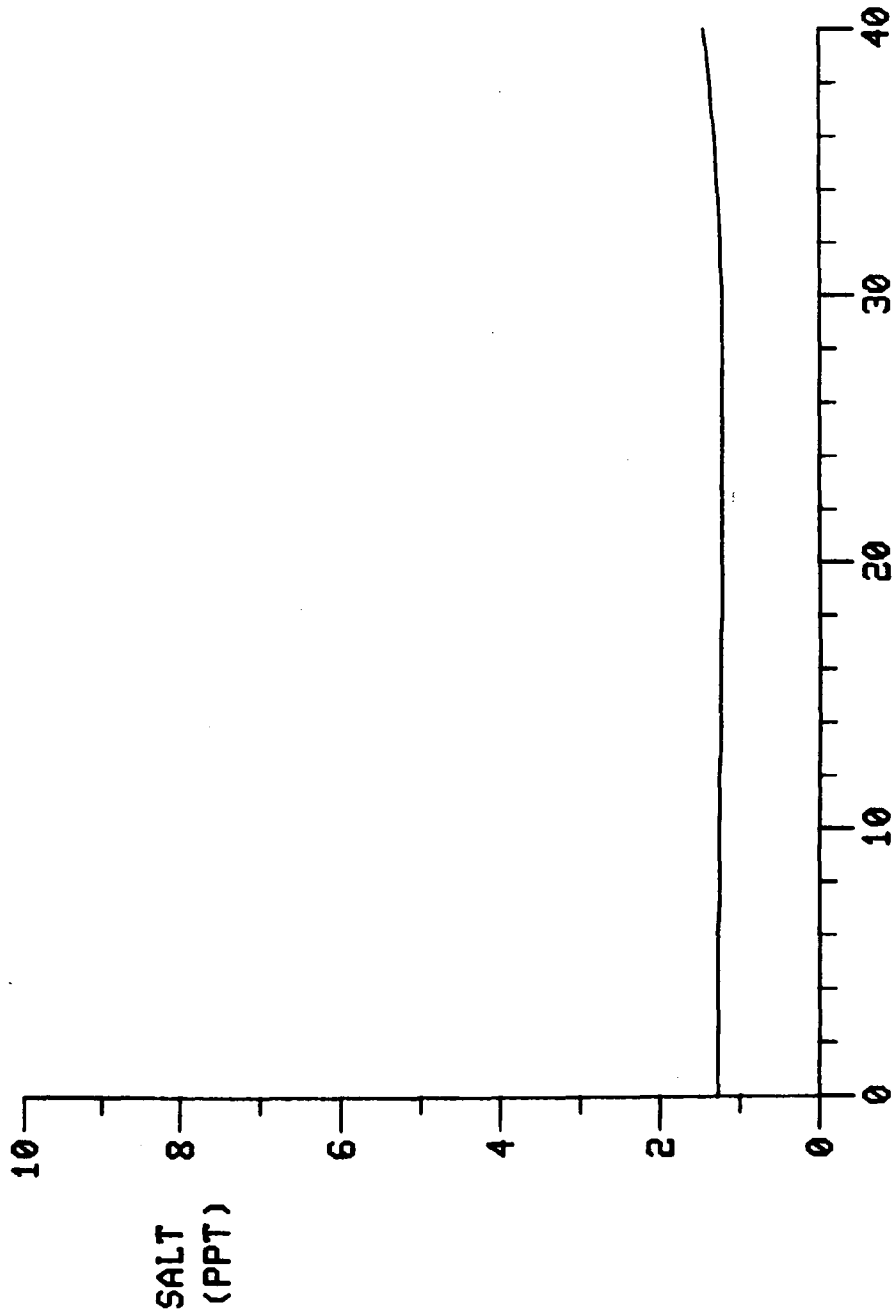


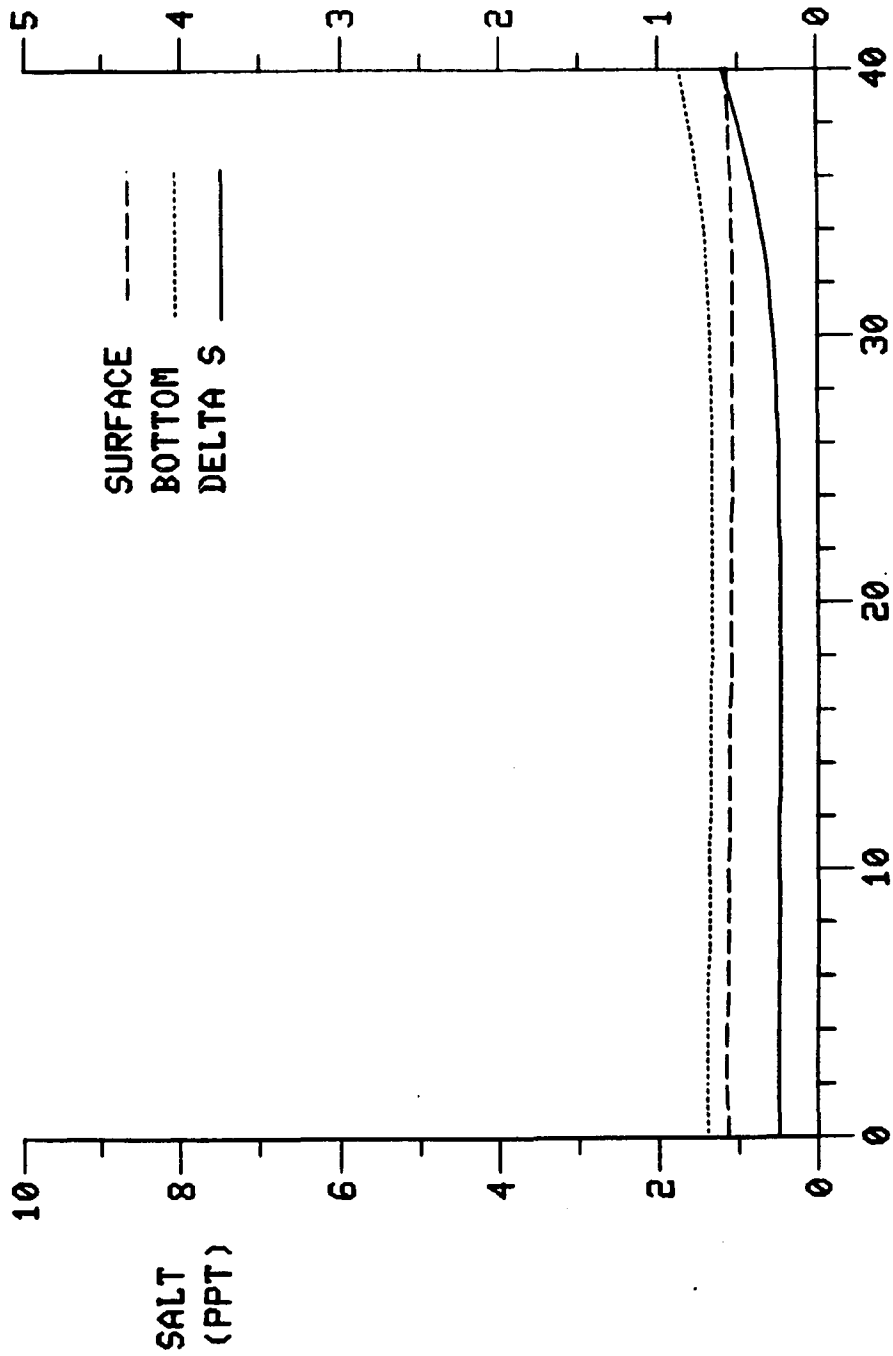
Figure 7-10c. Time Series of Depth-Average Salinity at Kilometer 20, Step-Function Increase in Salinity Boundary.



TIDAL CYCLES
Figure 7-10d. Time Series of Stratification at Kilometer 20, Step-Function Increase in Salinity Boundary.



TIDAL CYCLES
 Figure 7-10e. Time Series of Depth-Average Salinity at Kilometer 68, Step-Function Increase in Salinity Boundary.



TIDAL CYCLES

Figure 7-10f. Time Series of Stratification at Kilometer 68, Step-Function Increase in Salinity Boundary.

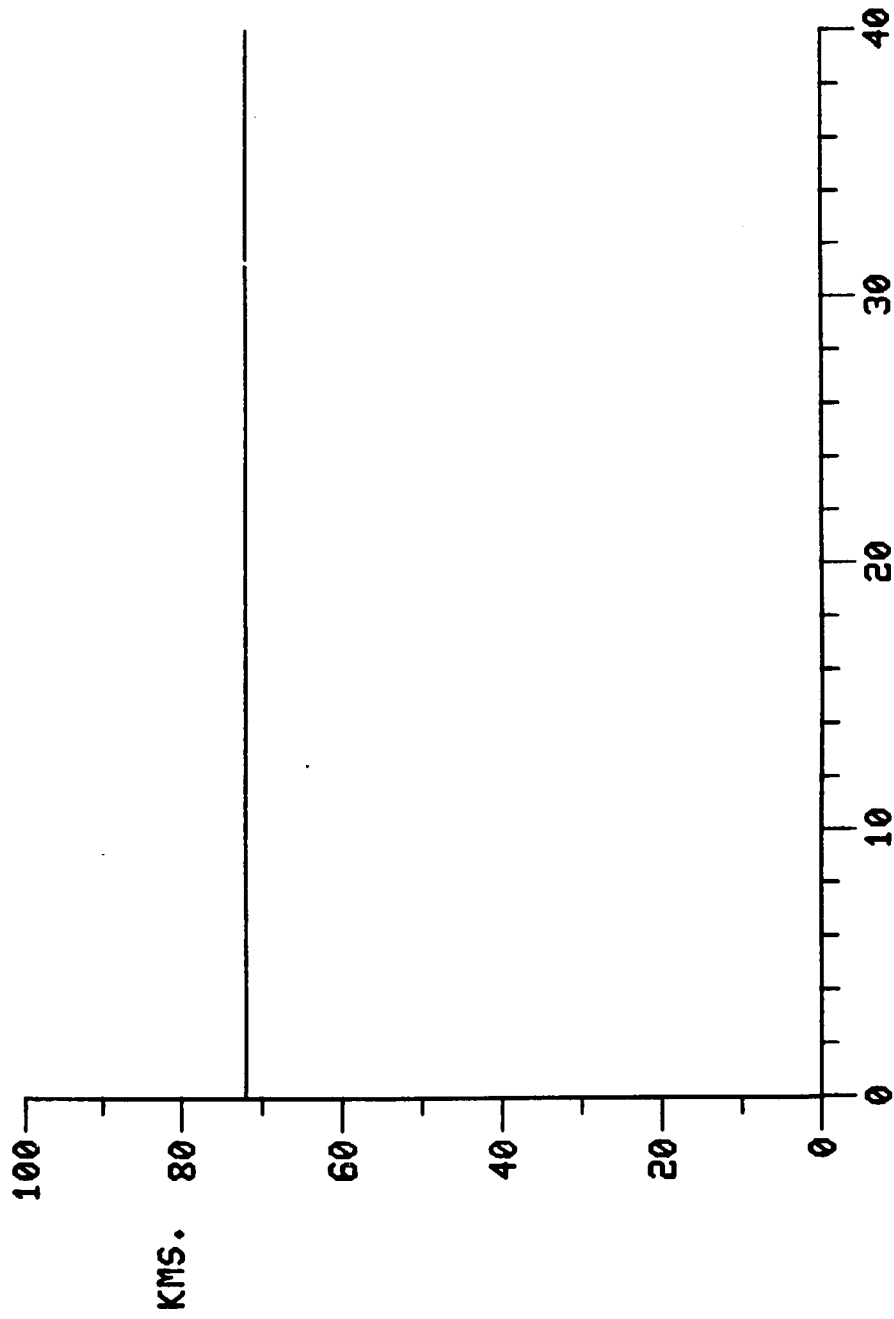


Figure 7-10g. Location of 1 ‰ Isohaline, Step-Function Increase in Salinity Boundary.

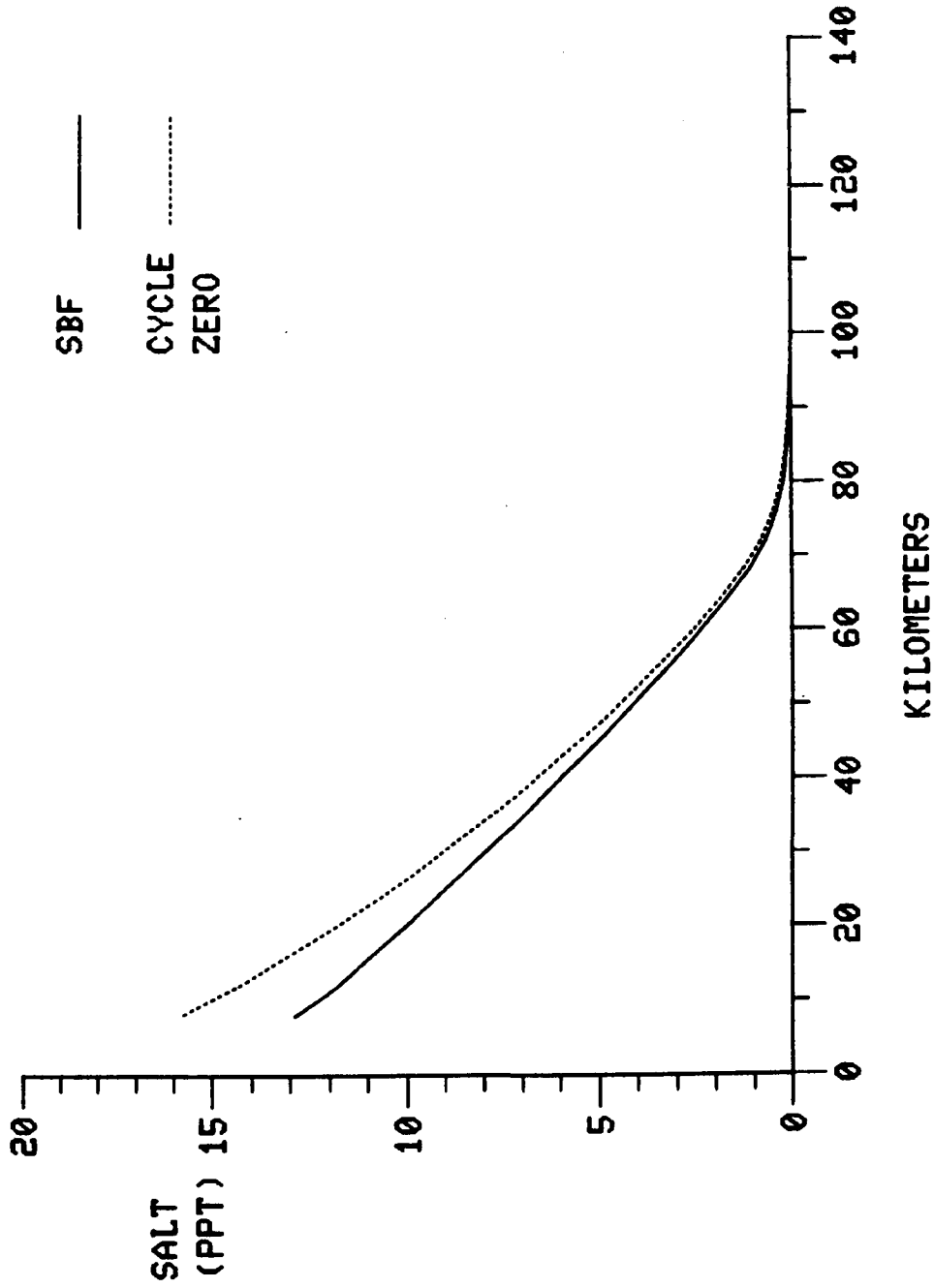


Figure 7-11a. Longitudinal Salinity After Step-Function Decrease in Salinity Boundary.

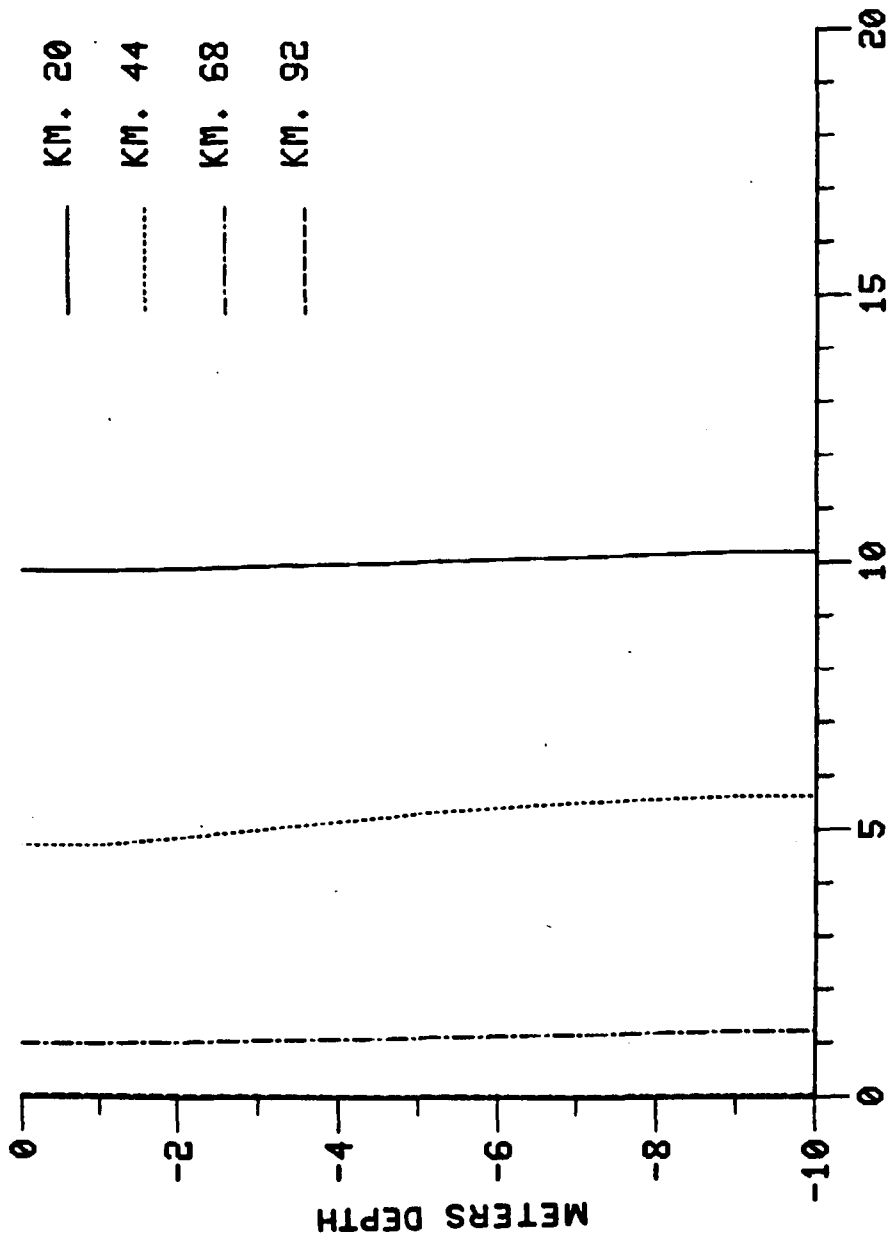
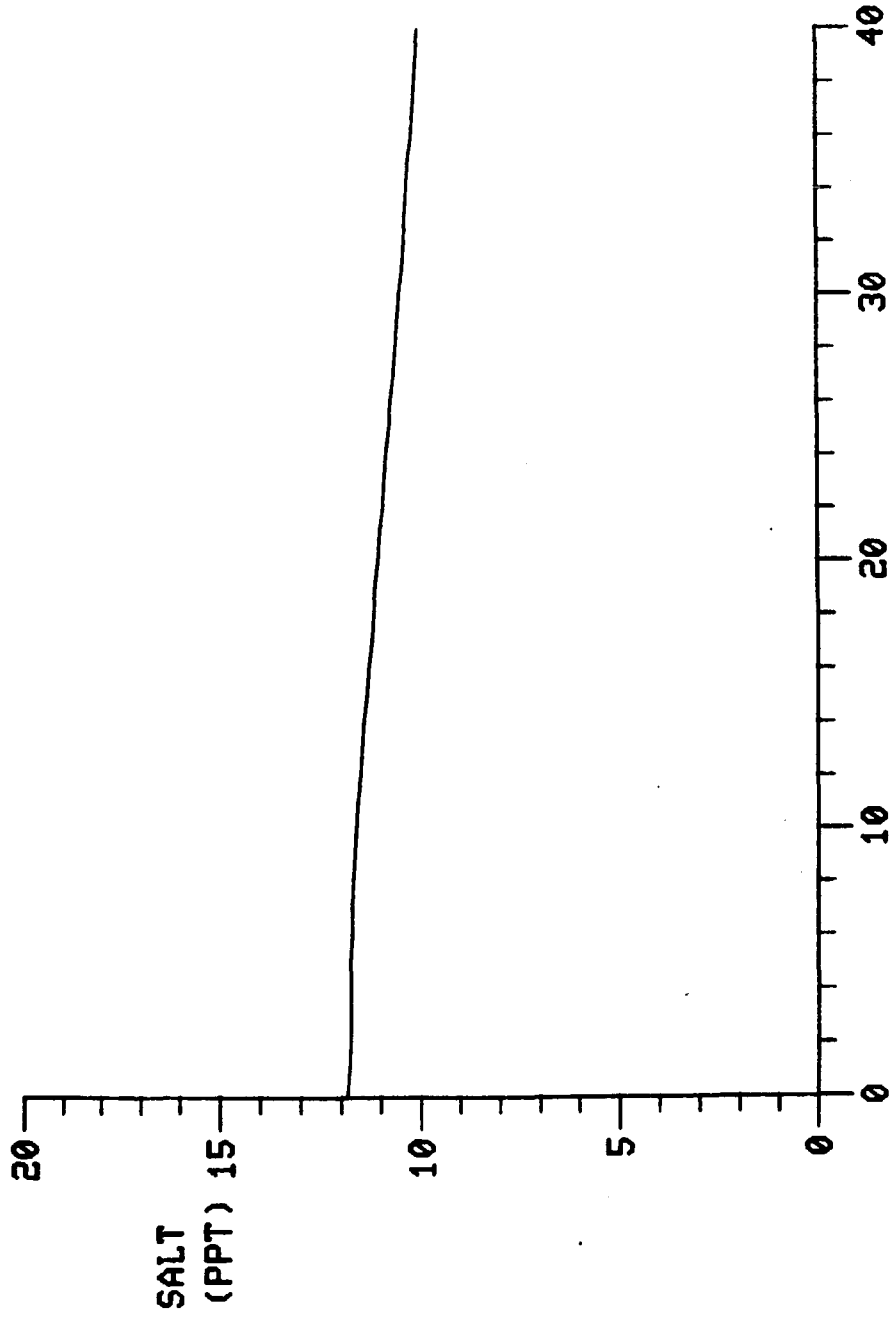
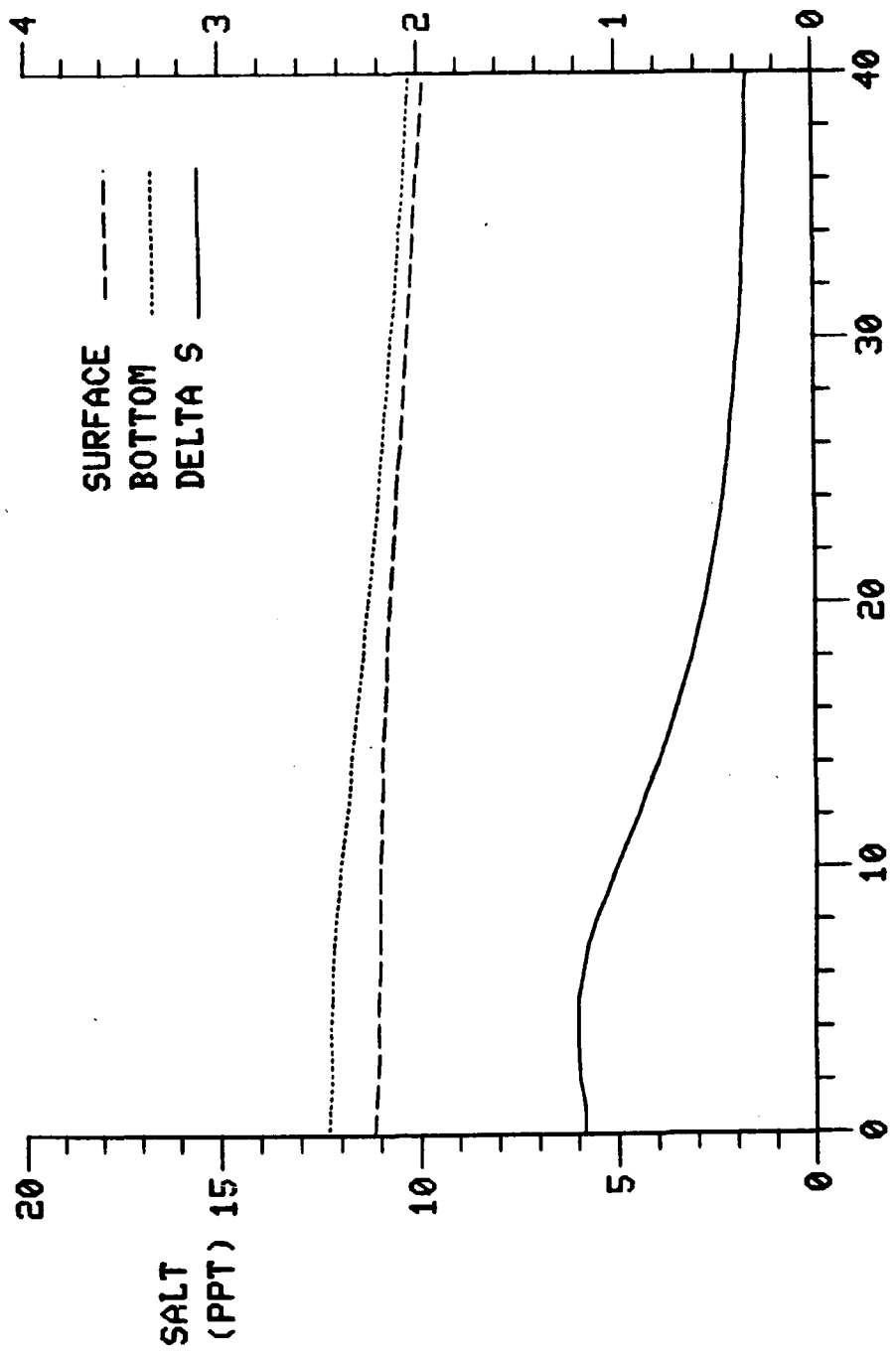


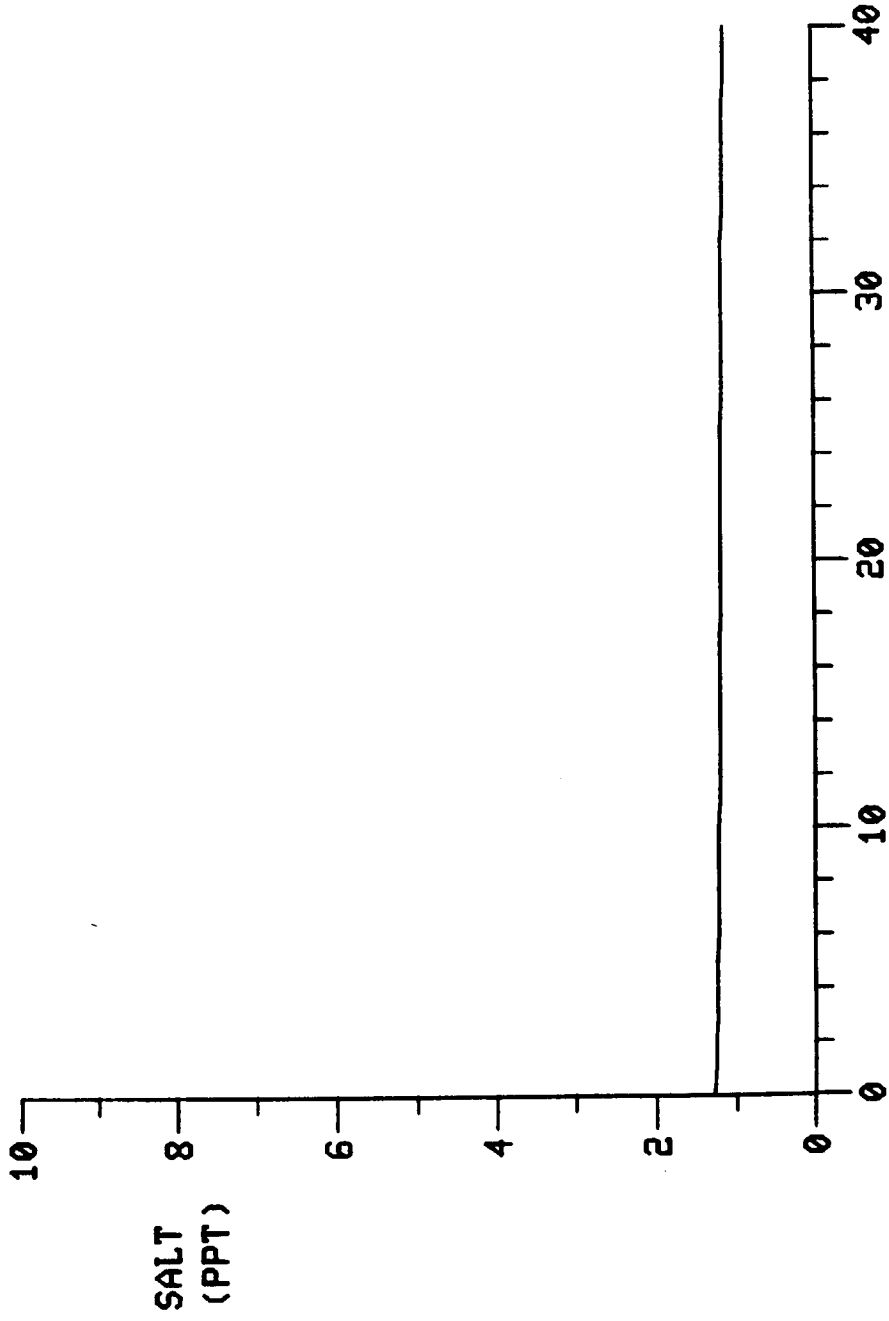
Figure 7-11b. Vertical SBF Salinity After Step-Function Decrease in Salinity Boundary.



TIDAL CYCLES
Figure 7-11c. Time Series of Depth-Average Salinity at Kilometer 20, Step-Function Decrease in Salinity Boundary.

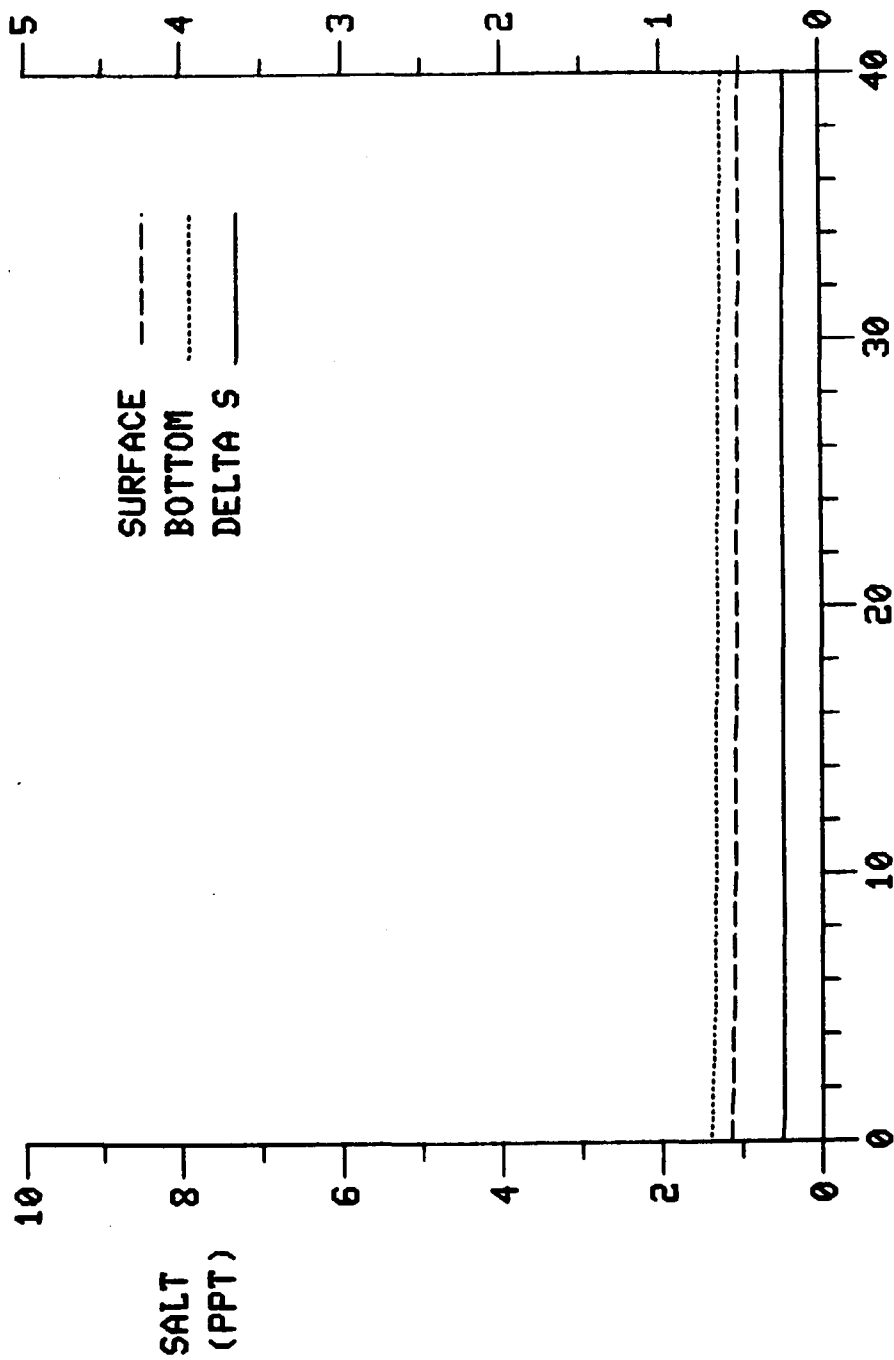


TIDAL CYCLES
 Figure 7-11d. Time Series of Stratification at Kilometer 20, Step-Function Decrease in Salinity Boundary.

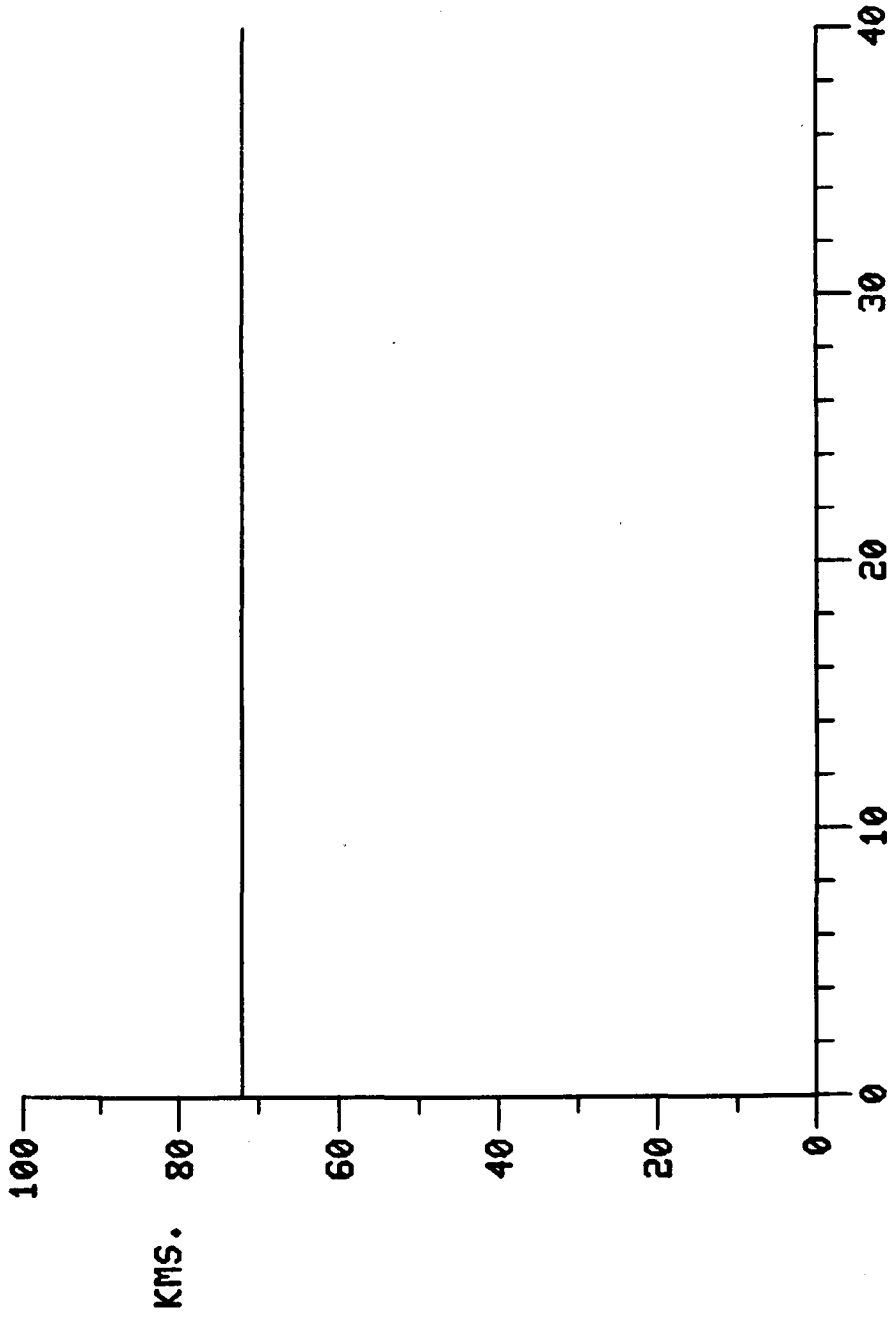


TIDAL CYCLES

Figure 7-11e. Time Series of Depth-Average Salinity at Kilometer 68, Step-Function Decrease in Salinity Boundary.



TIDAL CYCLES
Figure 7-11f. Time Series of Stratification at Kilometer 68, Step-Function Decrease in Salinity Boundary.



TIDAL CYCLES
 Figure 7-11g. Location of 1 ‰ Isohaline, Step-Function Decrease in Salinity Boundary.

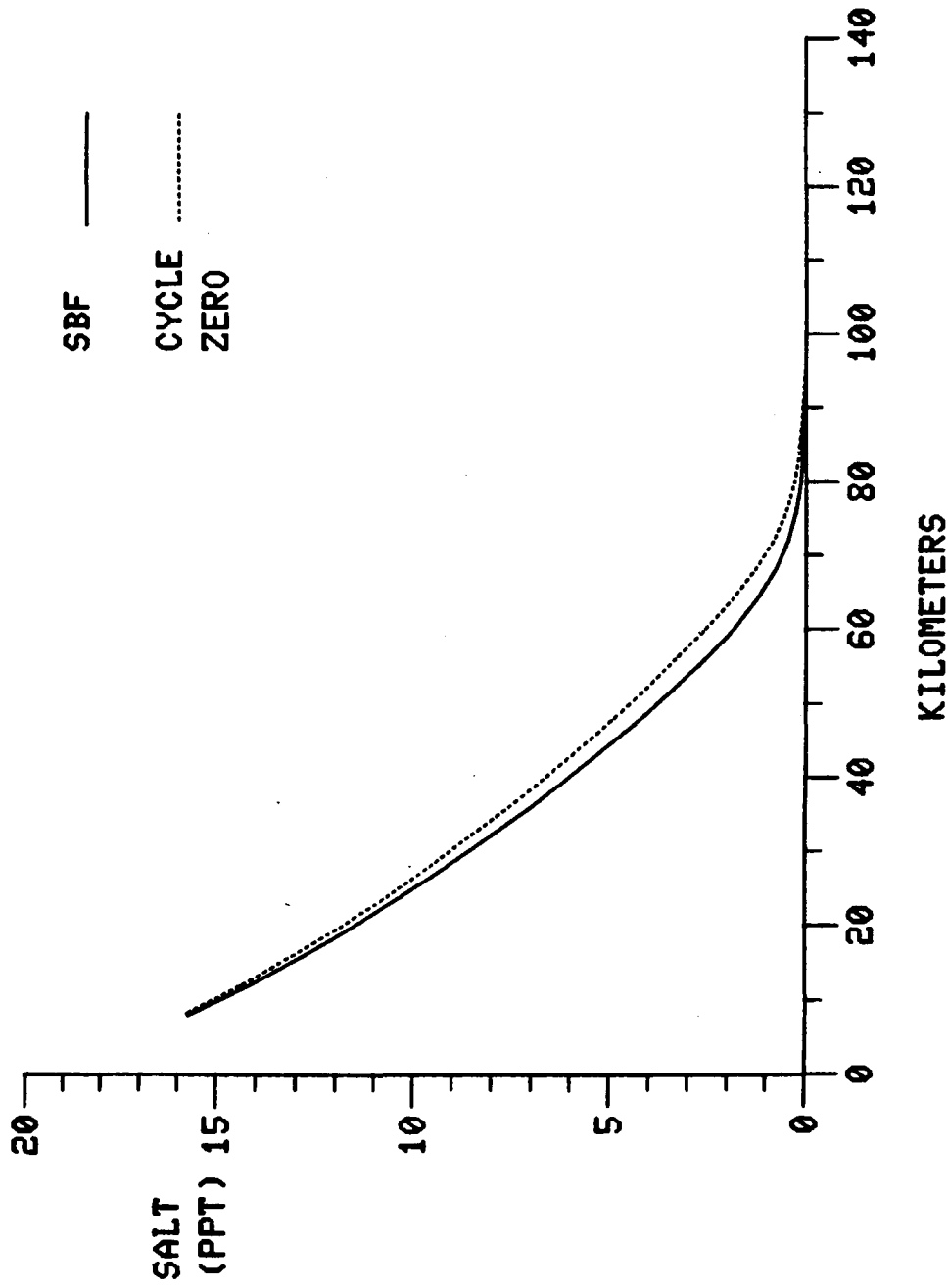


Figure 7-12a. Longitudinal Salinity After Upstream Wind Pulse.

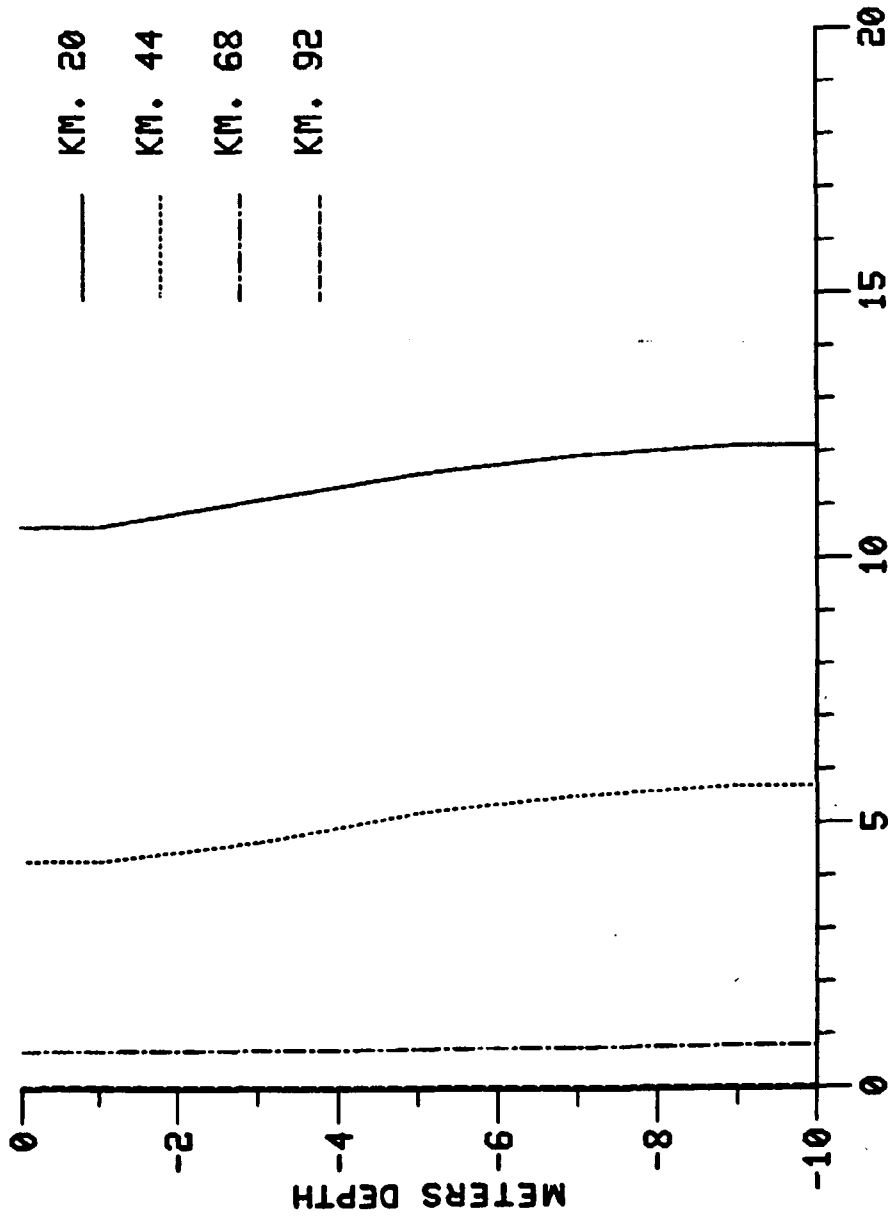


Figure 7-12b. Vertical SBF Salinity After Upstream Wind Pulse.

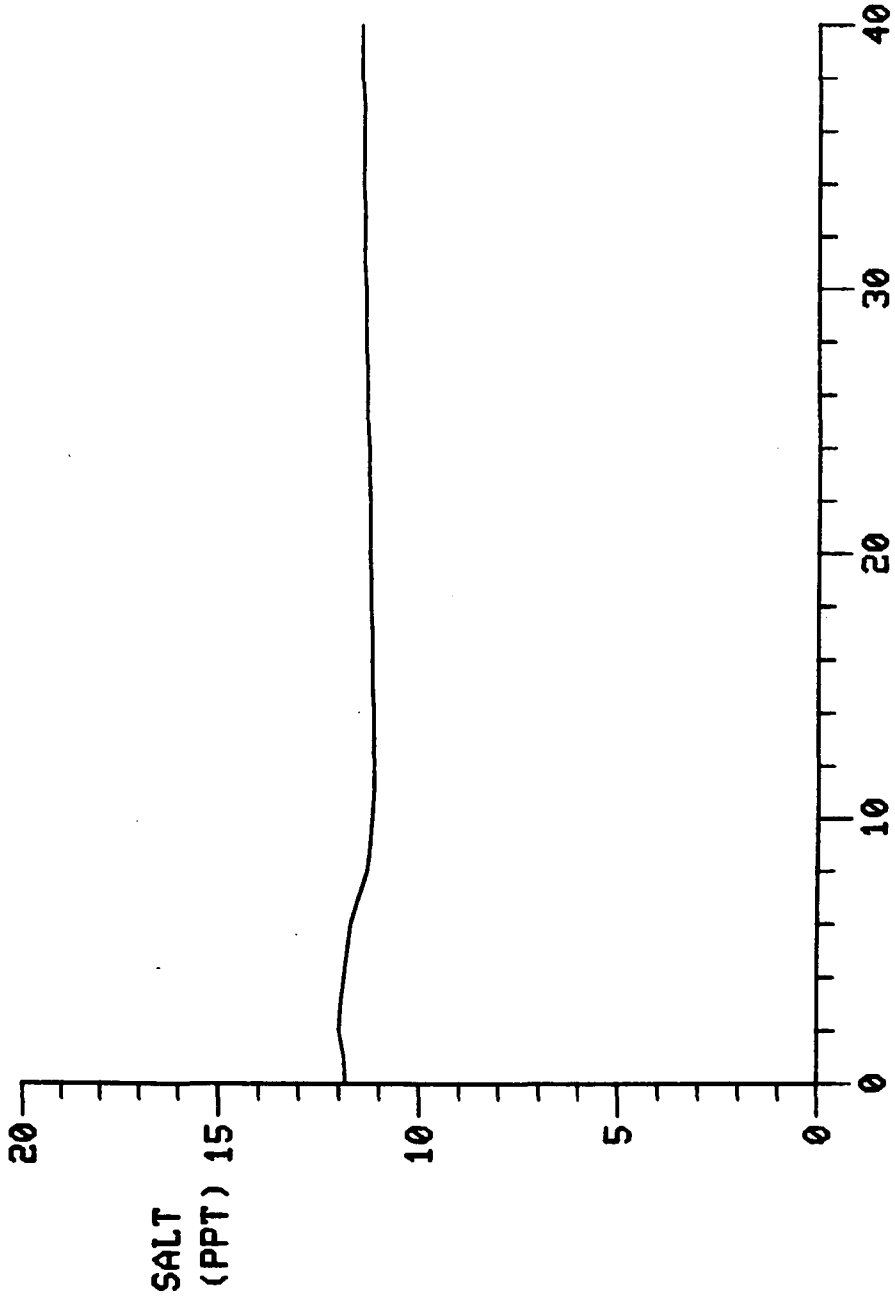
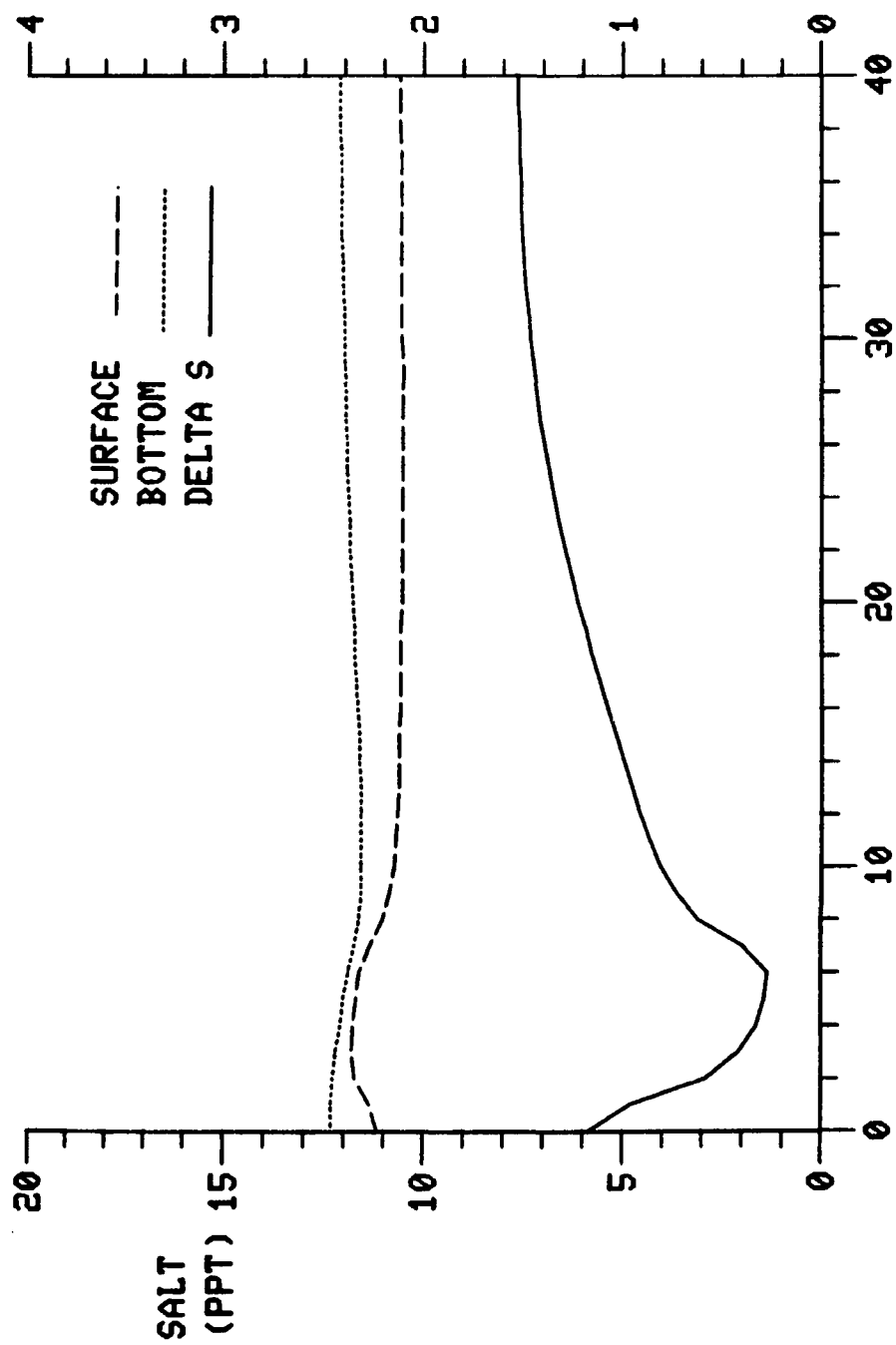


Figure 7-12c. Time Series of Depth-Average Salinity at Kilometer 20, Upstream Wind Pulse.



TIDAL CYCLES

Figure 7-12d. Time Series of Stratification at Kilometer 20, Upstream Wind Pulse.

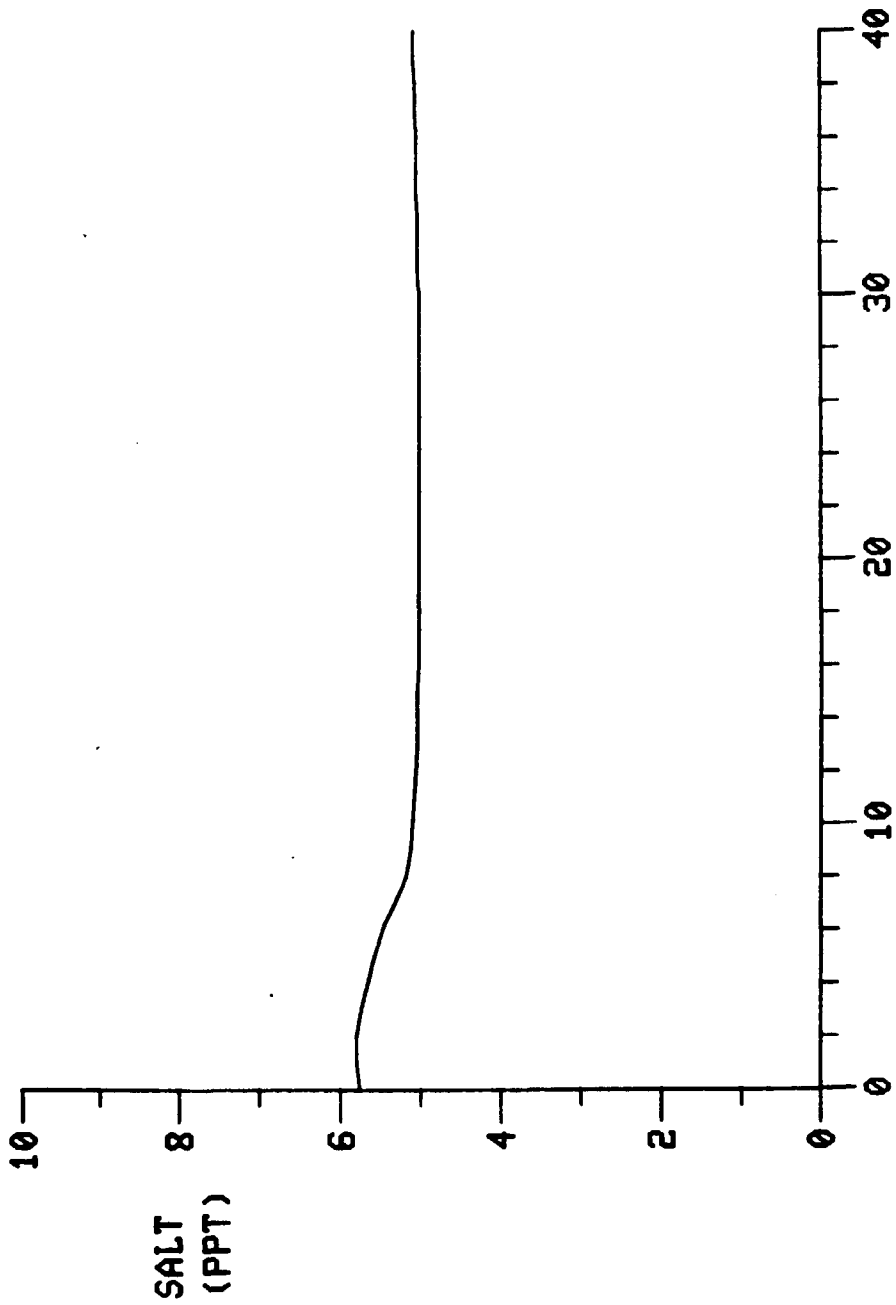
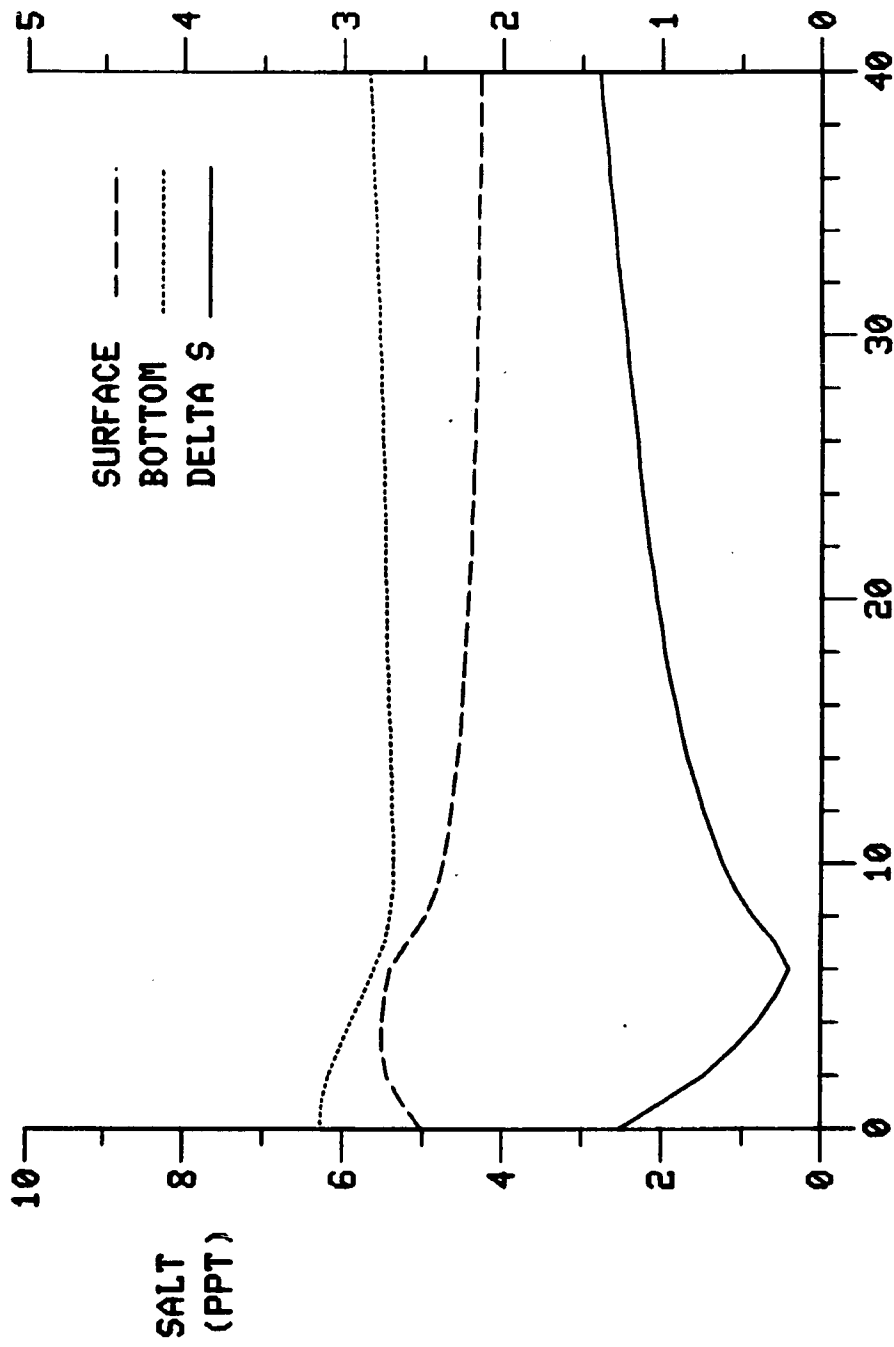
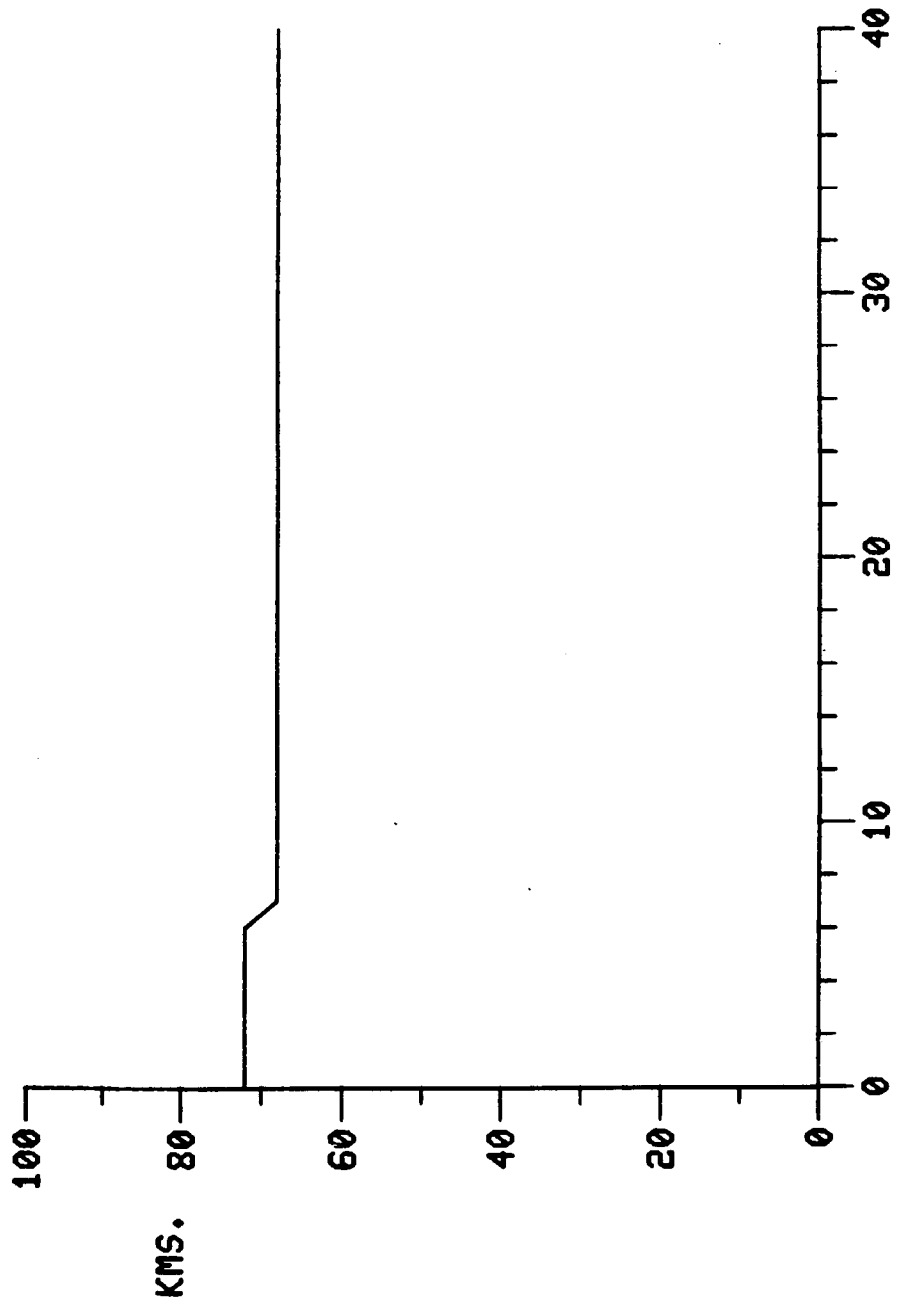


Figure 7-12e. Time Series of Depth-Average Salinity at Kilometer 44, Upstream Wind Pulse.



TIDAL CYCLES
Figure 7-12f. Time Series of Stratification at Kilometer 44, Upstream Wind Pulse.



TIDAL CYCLES
Figure 7-12g. Location of 1 ‰ Isohaline, Upstream Wind Pulse.

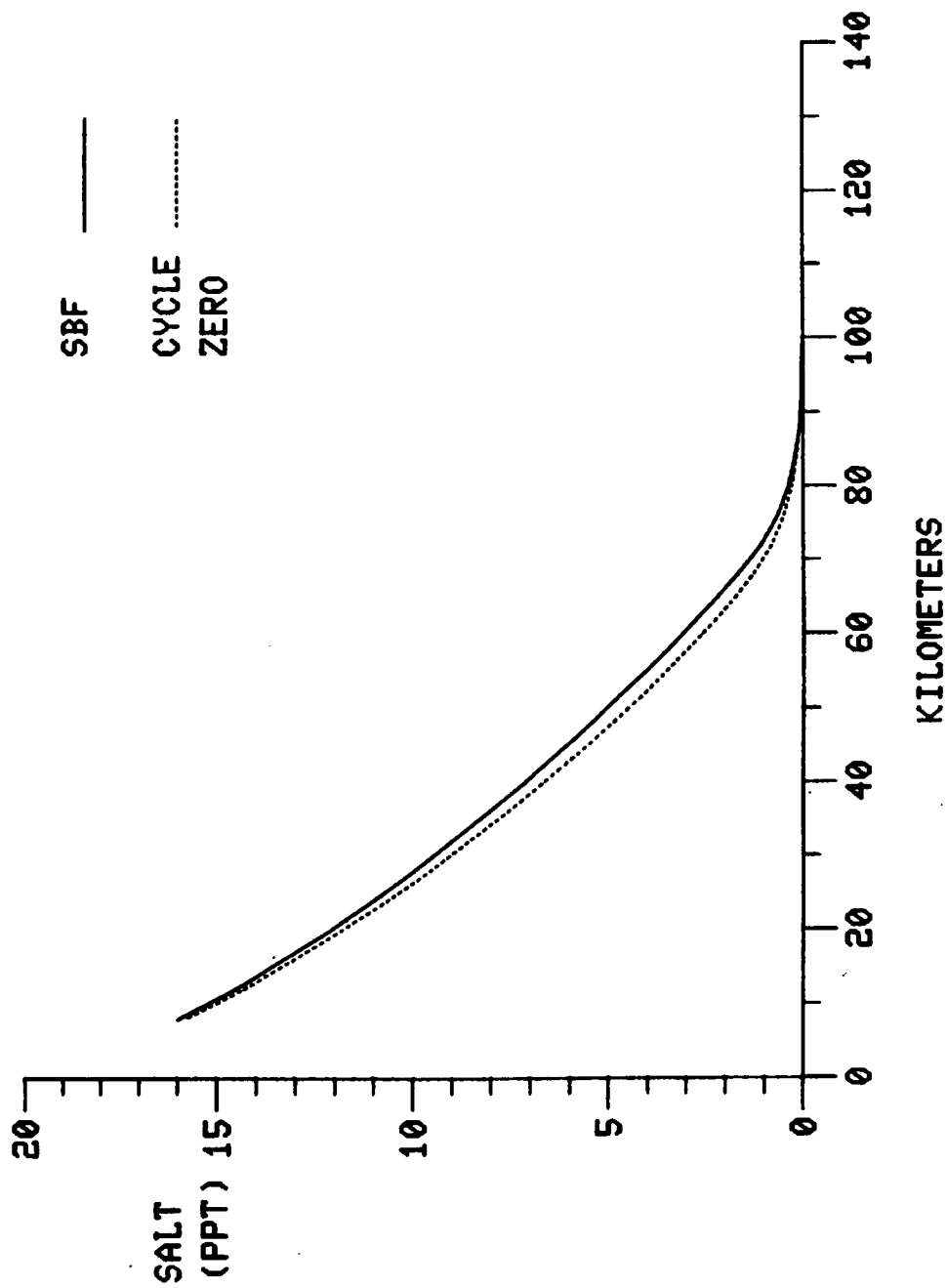
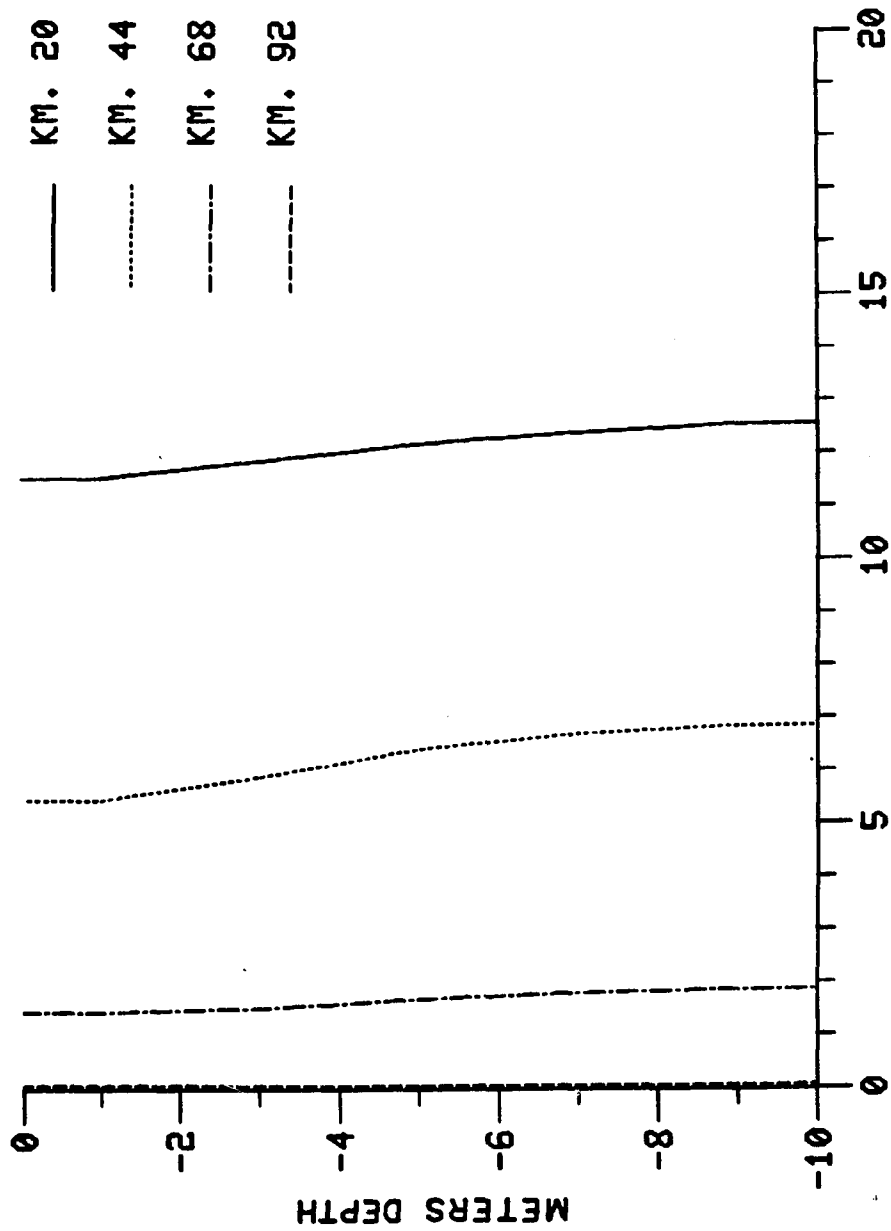
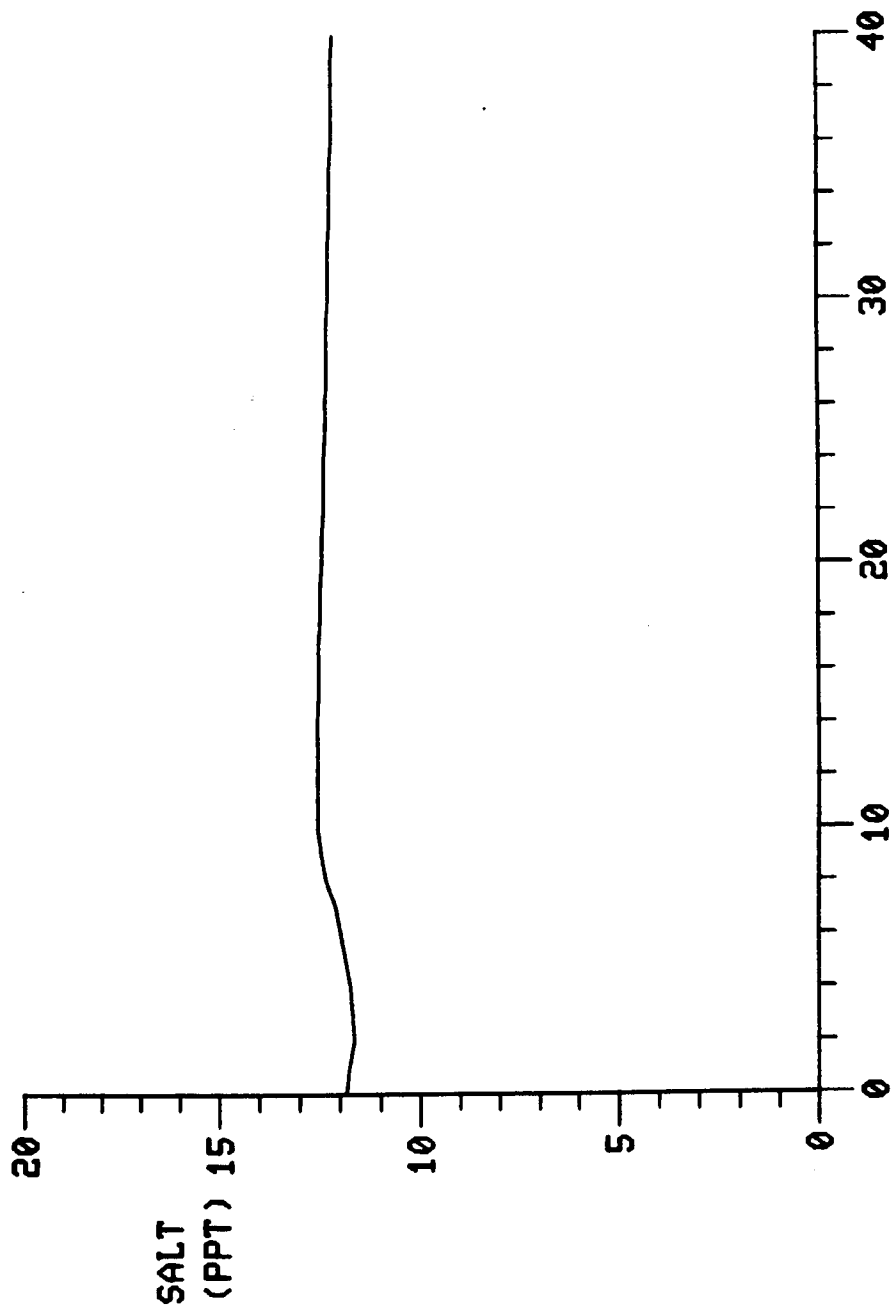


Figure 7-13a. Longitudinal Salinity After Downstream Wind Pulse.

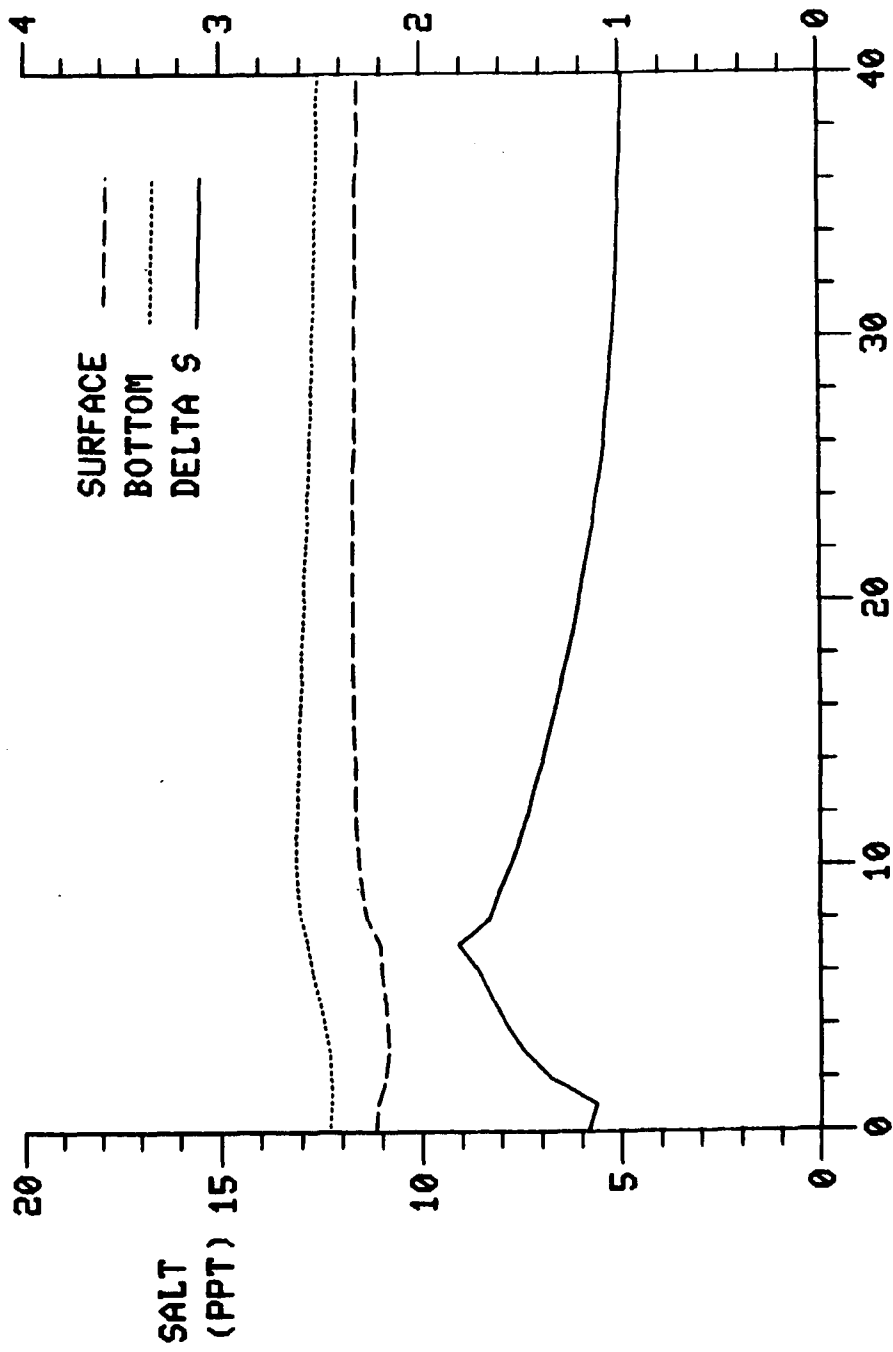


SALINITY (PPT)
Figure 7-13b. Vertical SBF Salinity After Downstream Wind Pulse.



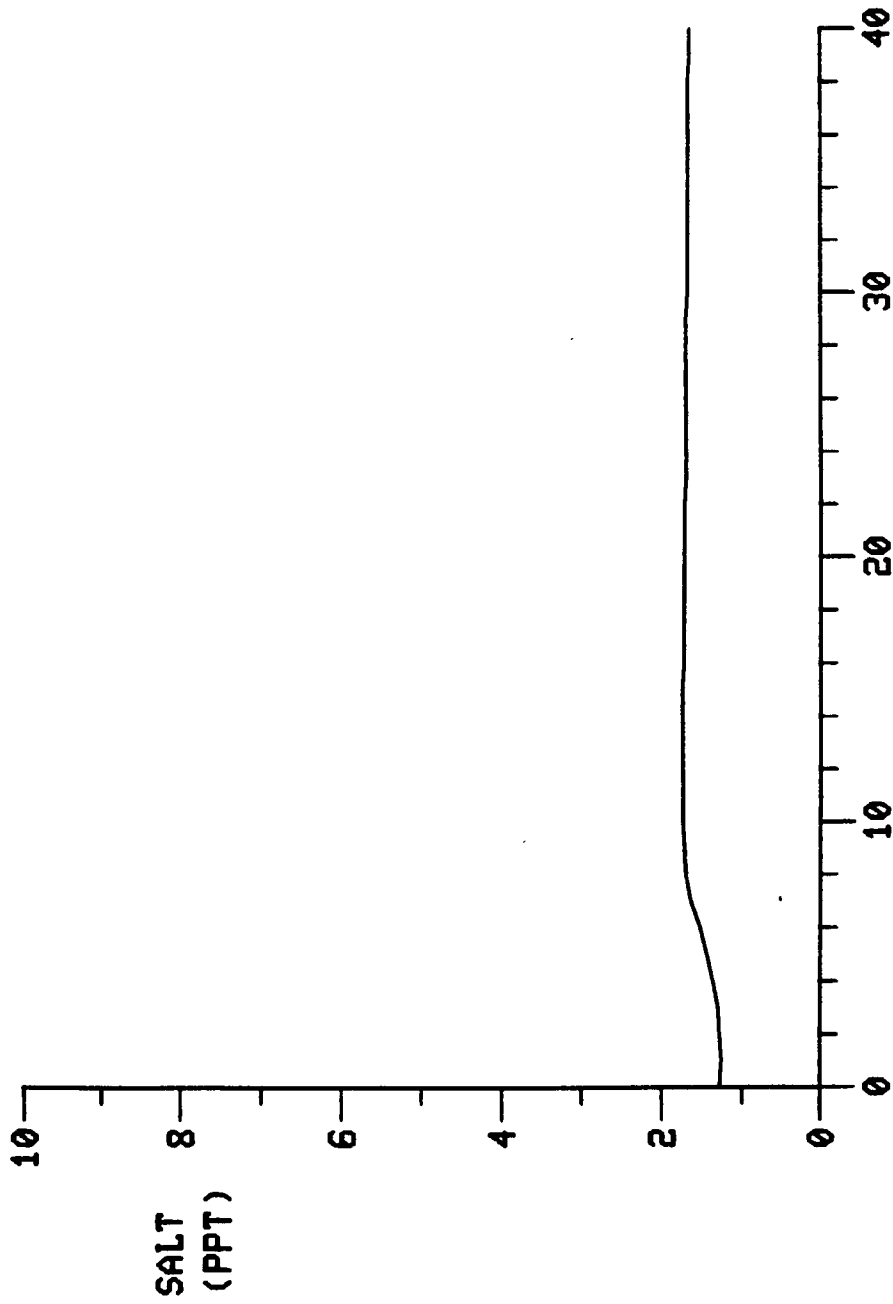
TIDAL CYCLES

Figure 7-13c. Time Series of Depth-Average Salinity at Kilometer 20, Downstream Wind Pulse.



TIDAL CYCLES

Figure 7-13d. Time Series of Stratification at Kilometer 20, Downstream Wind Pulse.



TIDAL CYCLES
Figure 7-13e. Time Series of Depth-Average Salinity at Kilometer 68, Downstream Wind Pulse.

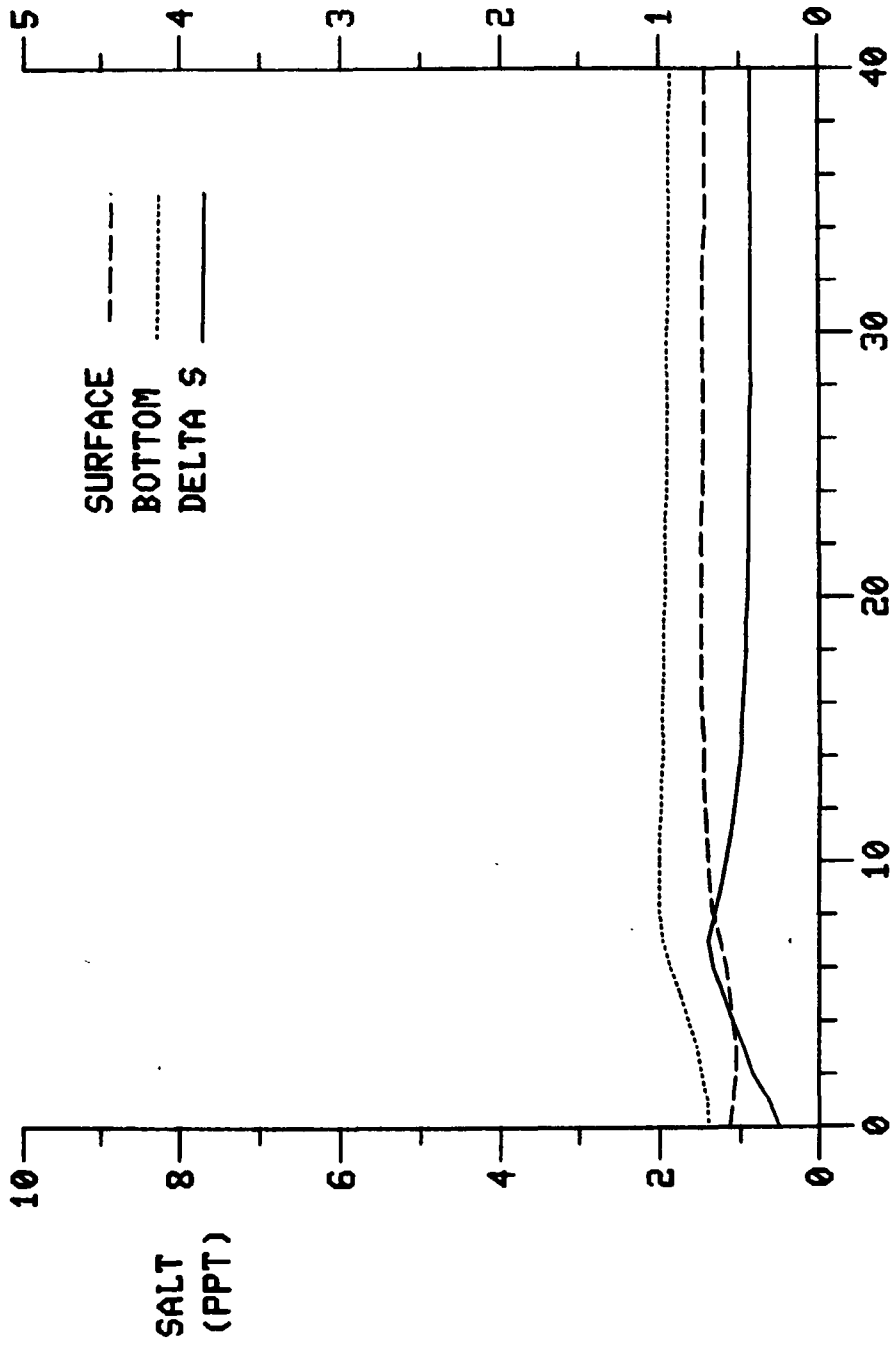
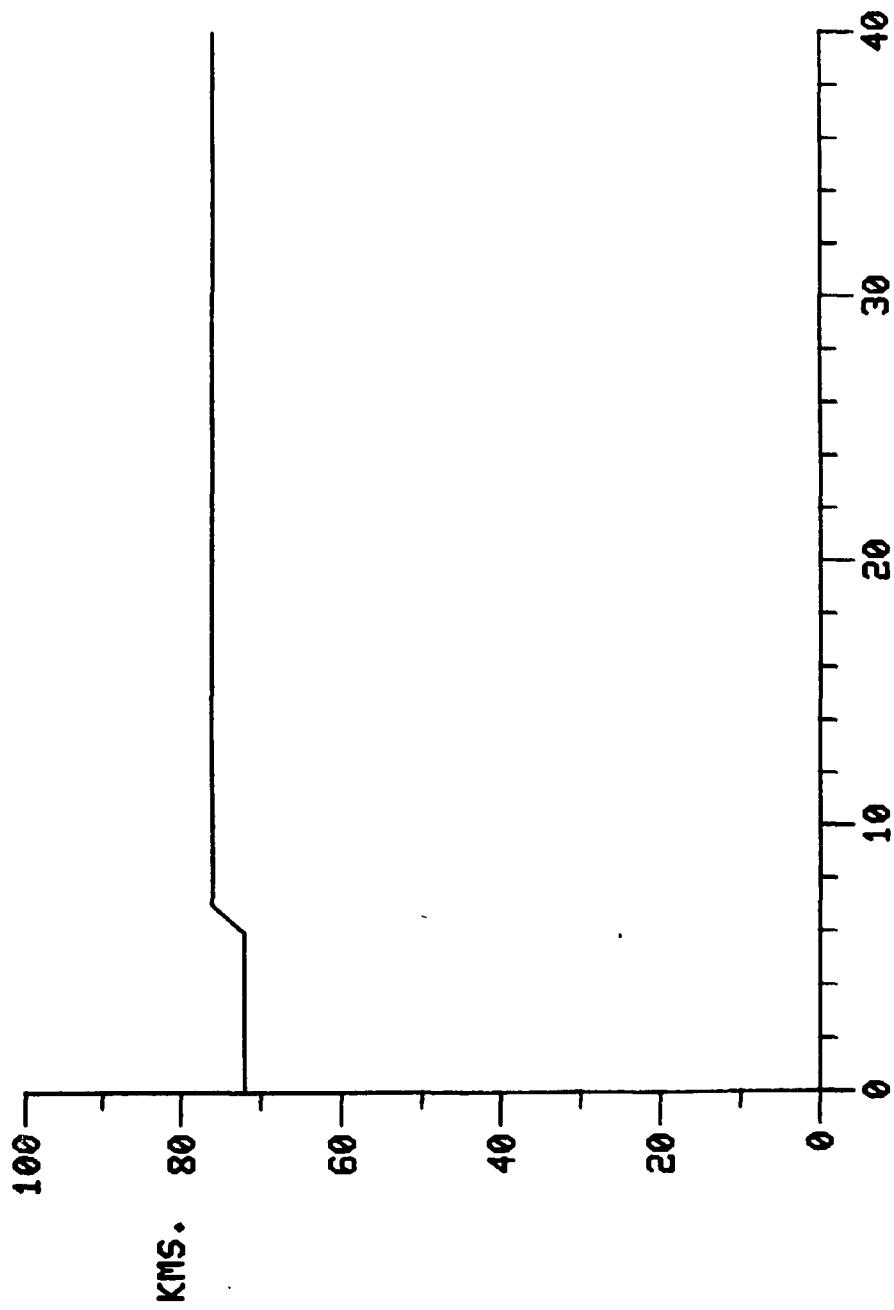
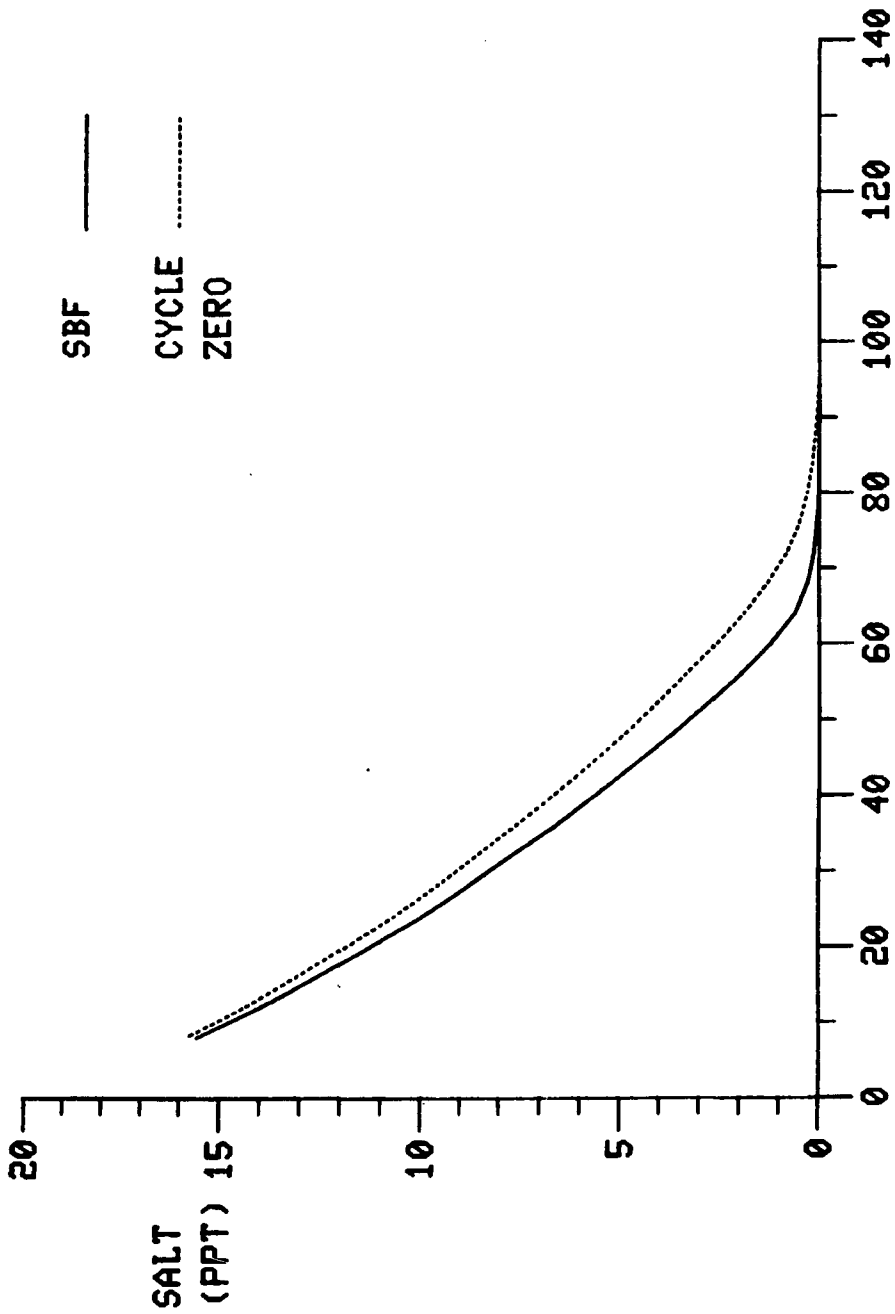


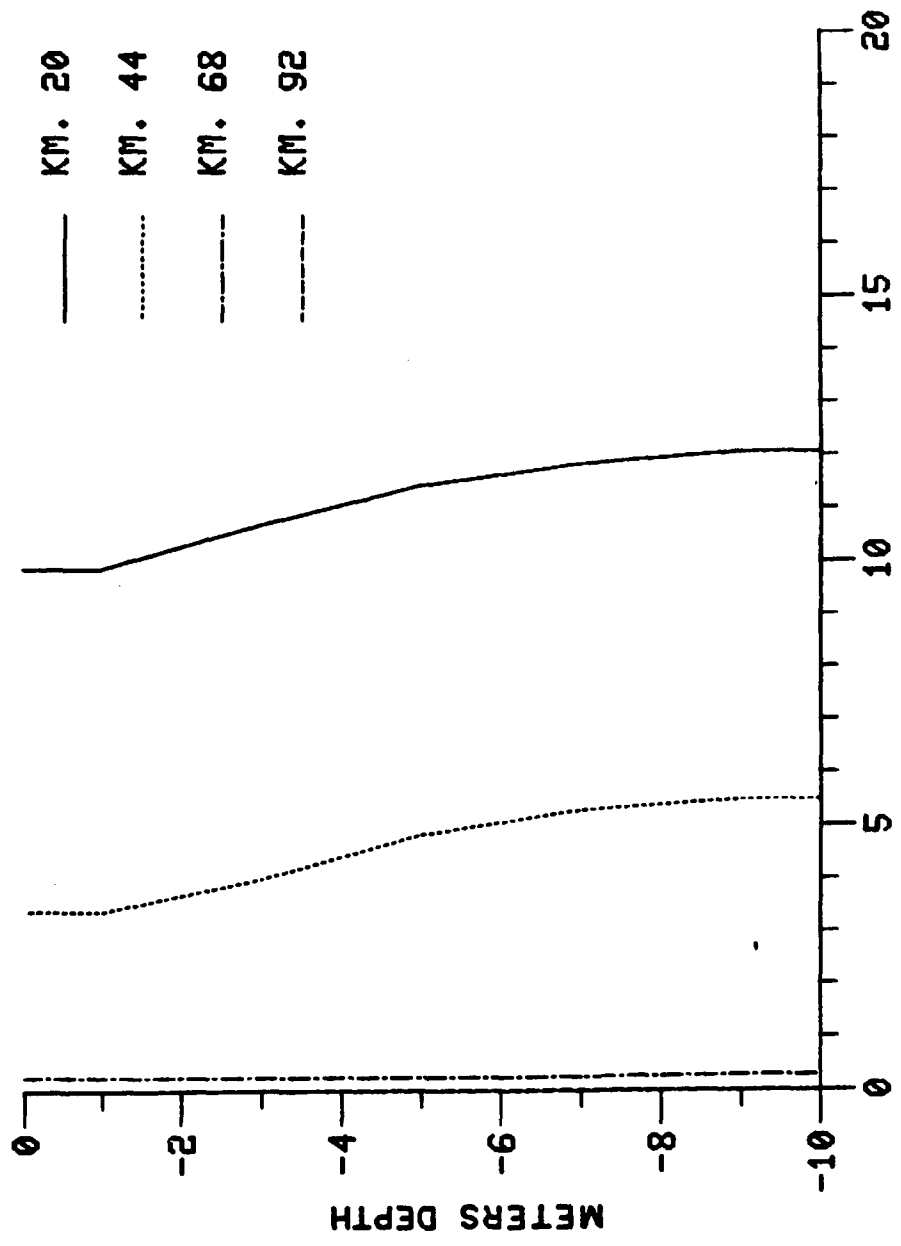
Figure 7-13f. Time Series of Stratification at Kilometer 68, Downstream Wind Pulse.



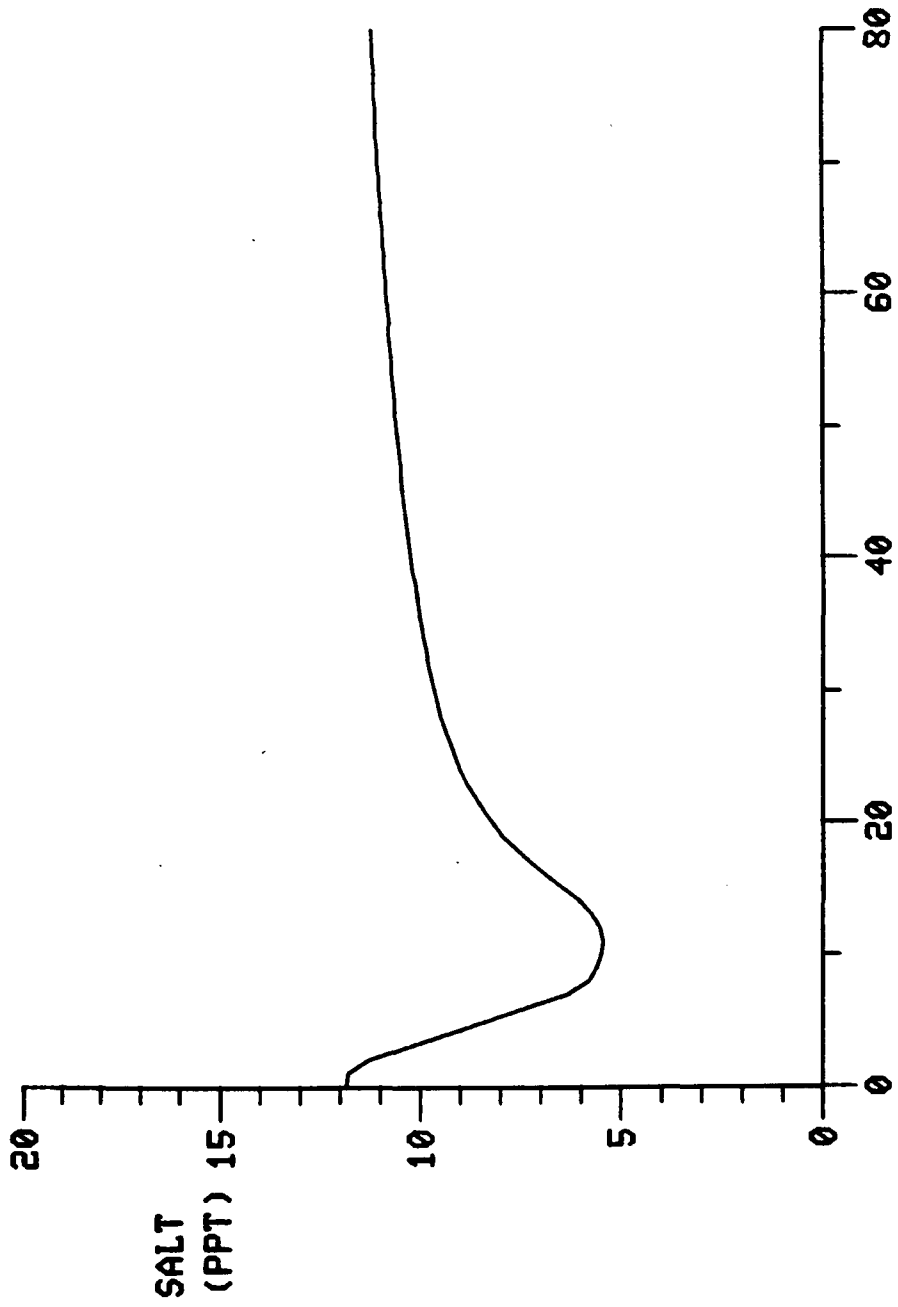
TIDAL CYCLES
Figure 7-13g. Location of 1 ‰ Isohaline, Downstream Wind Pulse.



KILOMETERS
Figure 7-14a. Longitudinal Salinity After Pulse Increase in Flow.

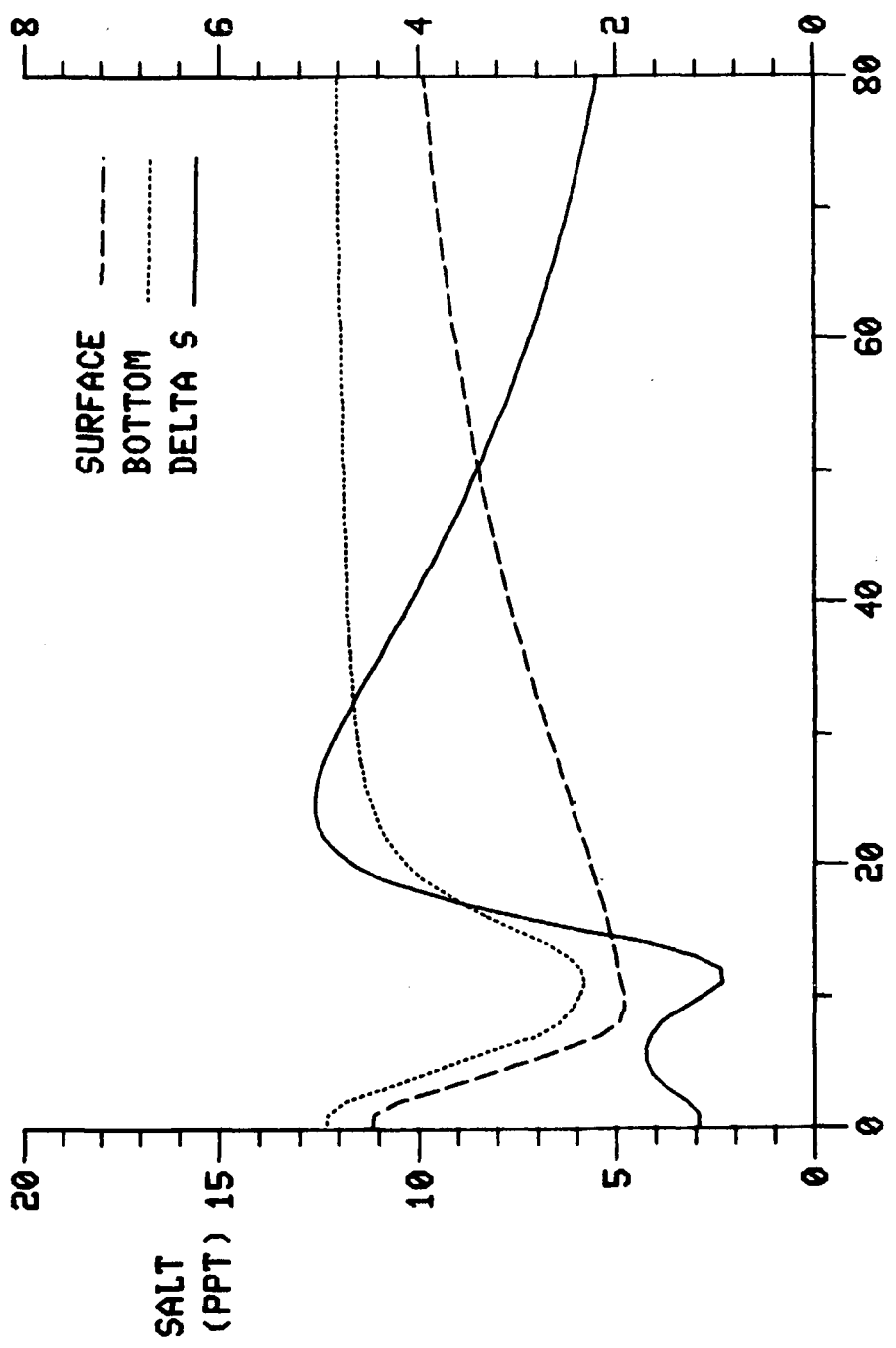


SALINITY (PPT)
Figure 7-14b. Vertical SBF Salinity After Pulse Increase in Flow.



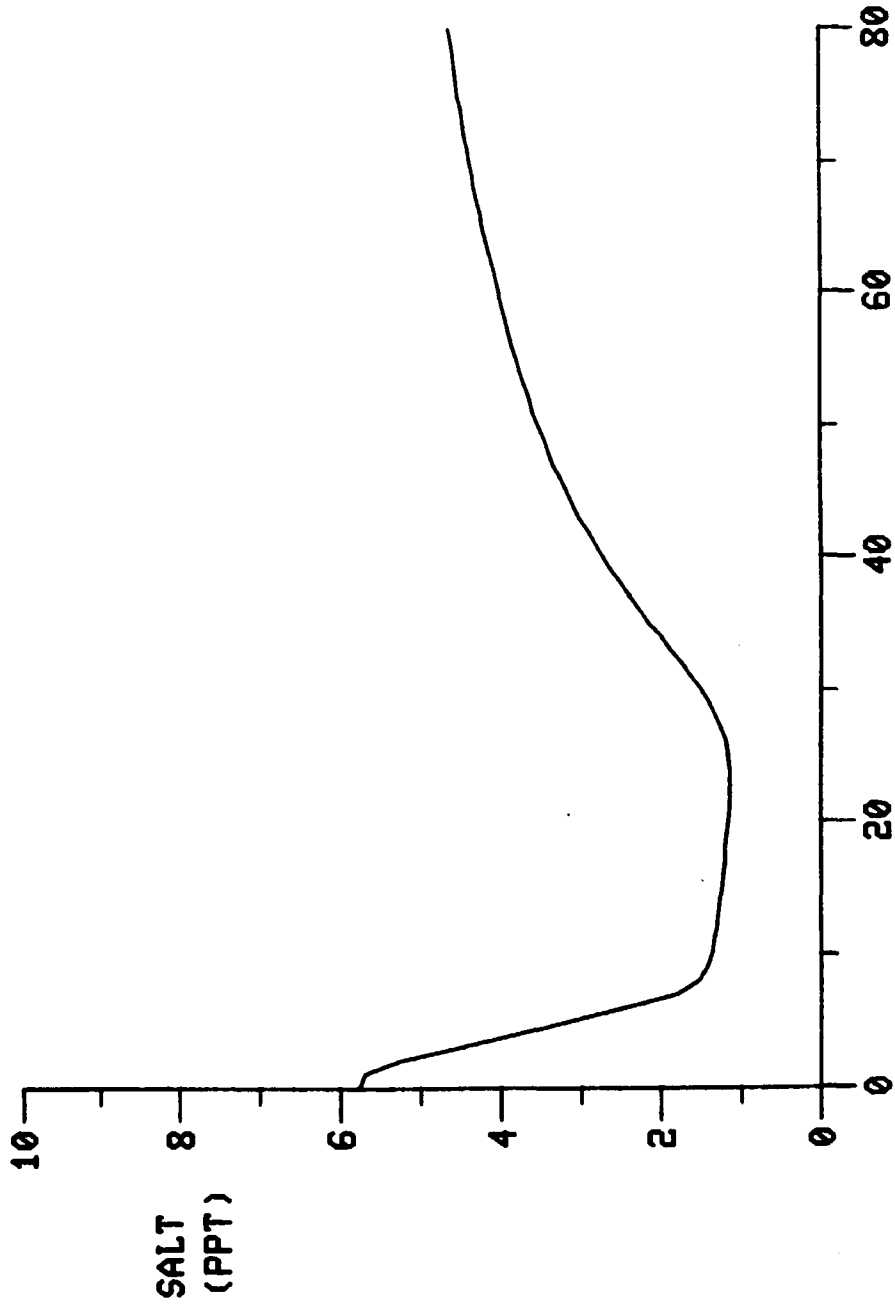
TIDAL CYCLES

Figure 7-14c. Time Series of Depth-Average Salinity at Kilometer 20, Pulse Increase in Flow.

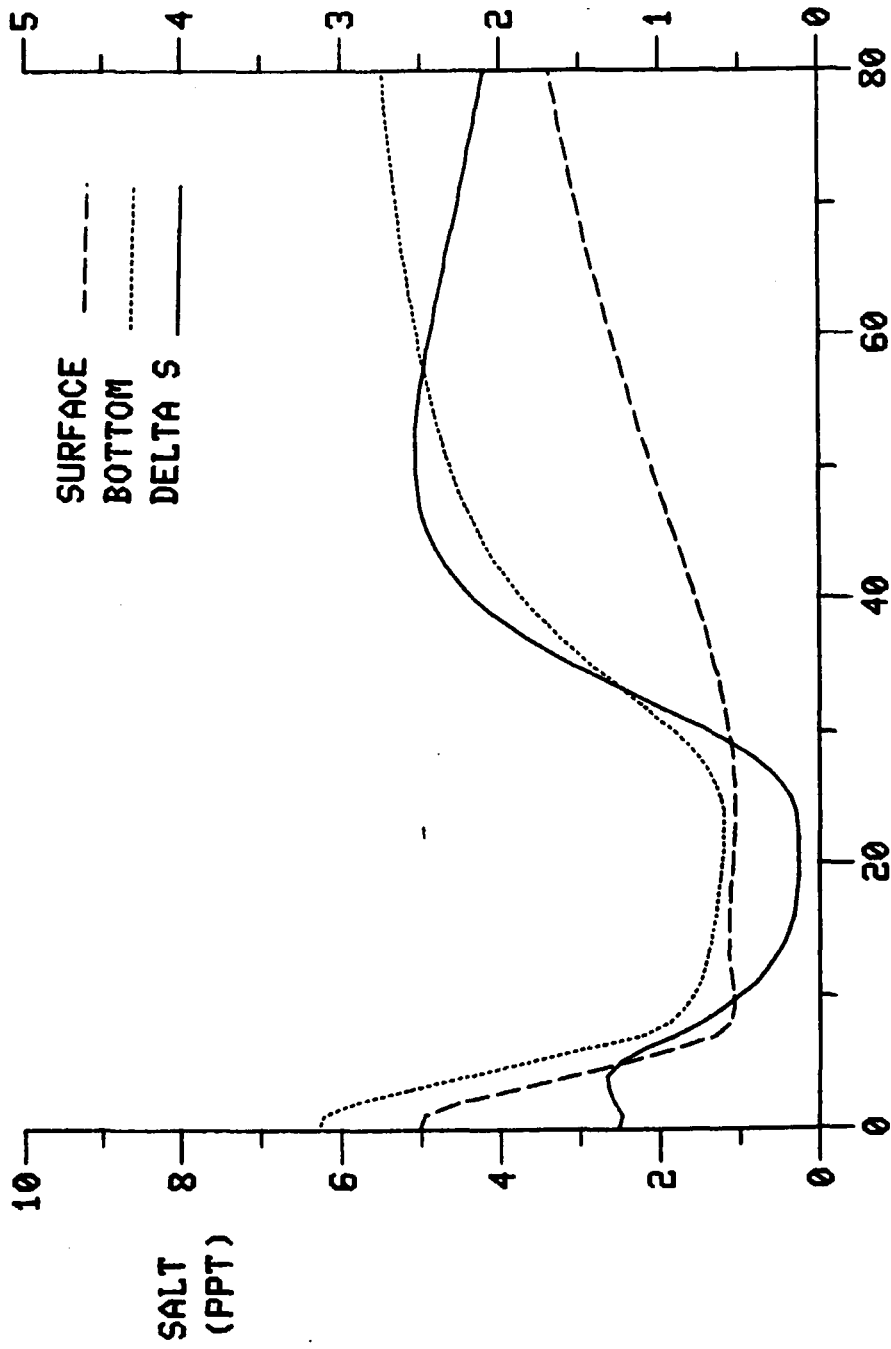


TIDAL CYCLES

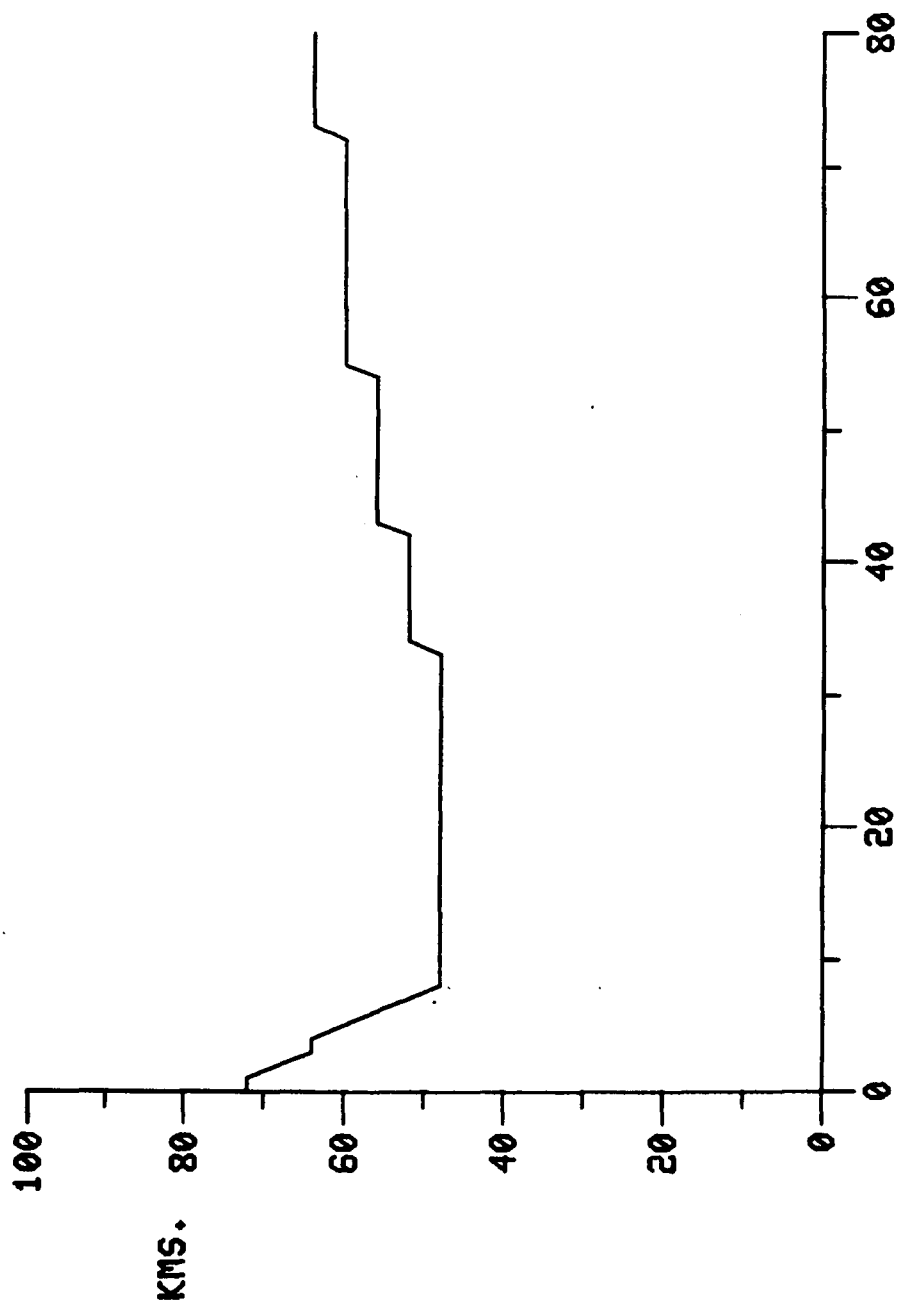
Figure 7-14d. Time Series of Stratification at Kilometer 20, Pulse Increase in Flow.



TIDAL CYCLES
Figure 7-14e. Time Series of Depth-Average Salinity at Kilometer 44, Pulse Increase in Flow.



TIDAL CYCLES
Figure 7-14f. Time Series of Stratification at Kilometer 44, Pulse Increase in Flow.



TIDAL CYCLES

Figure 7-14g. Location of 1 ‰ Isohaline, Pulse Increase in Flow.

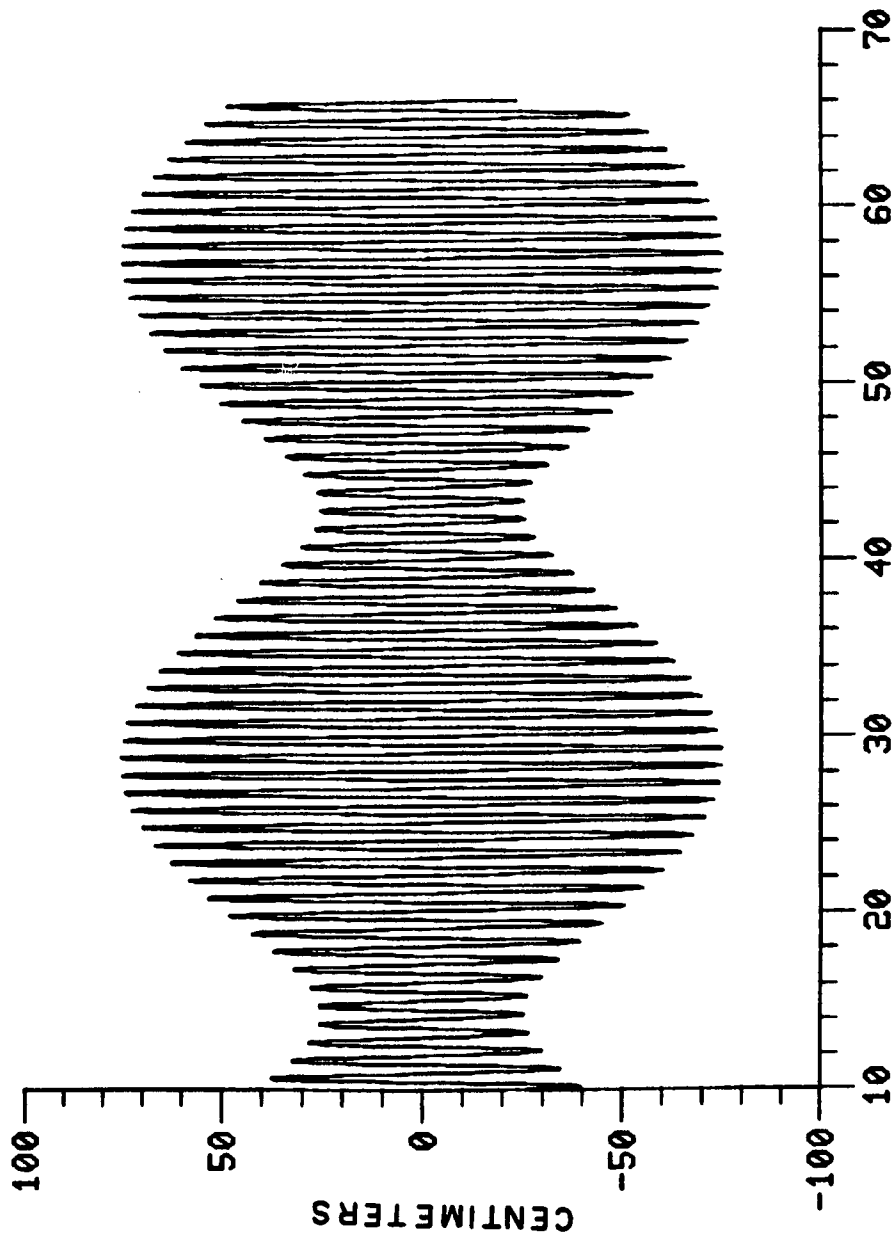
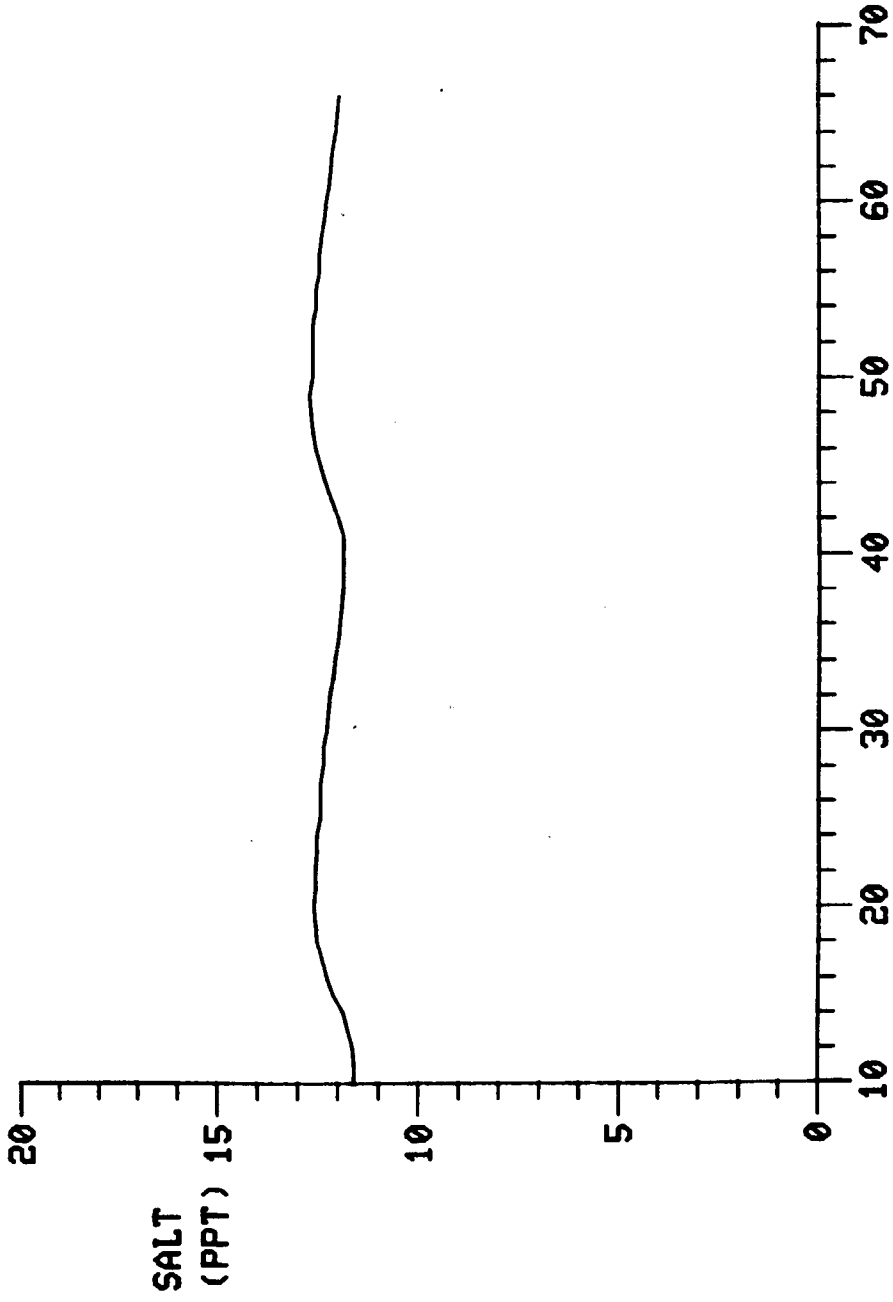
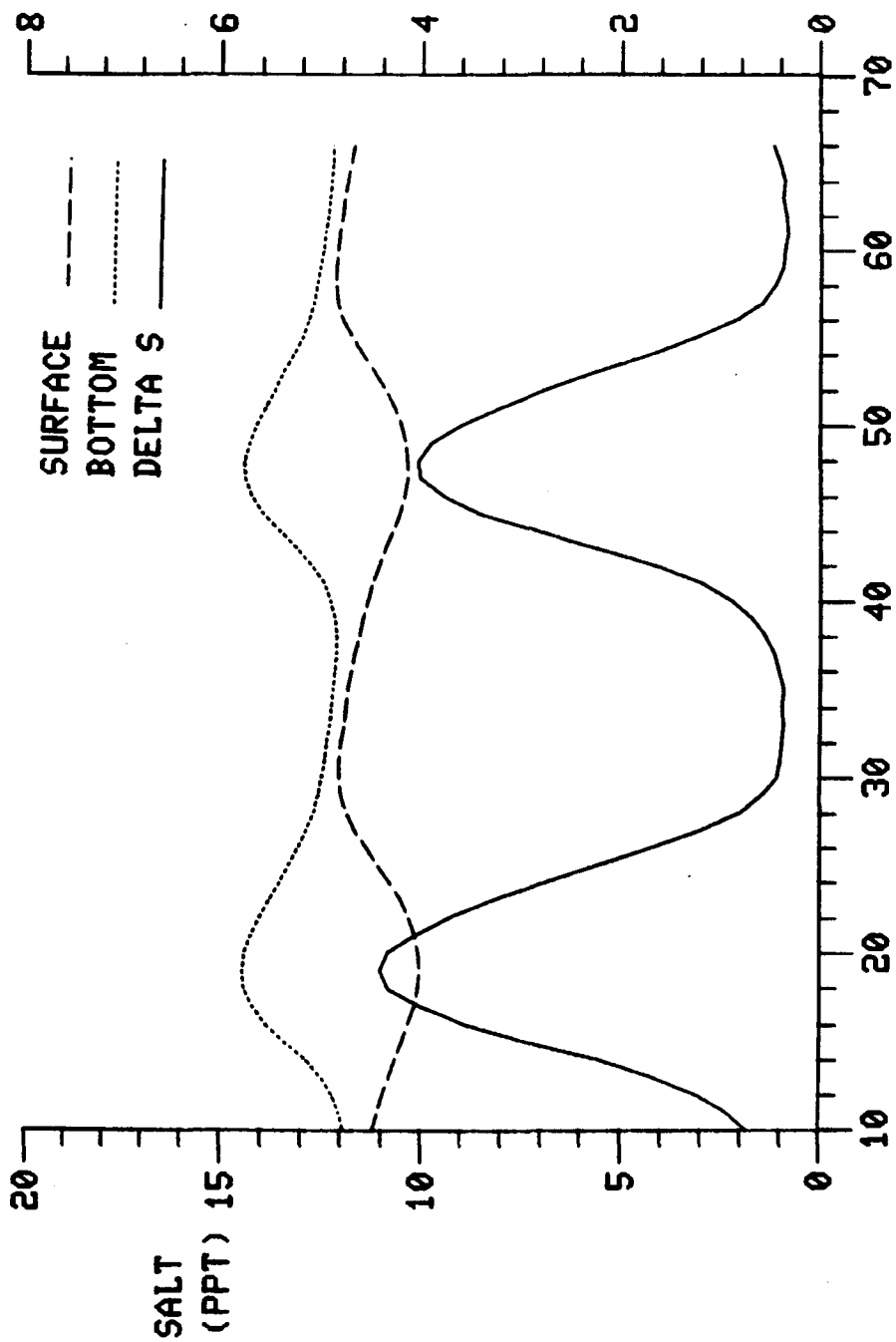


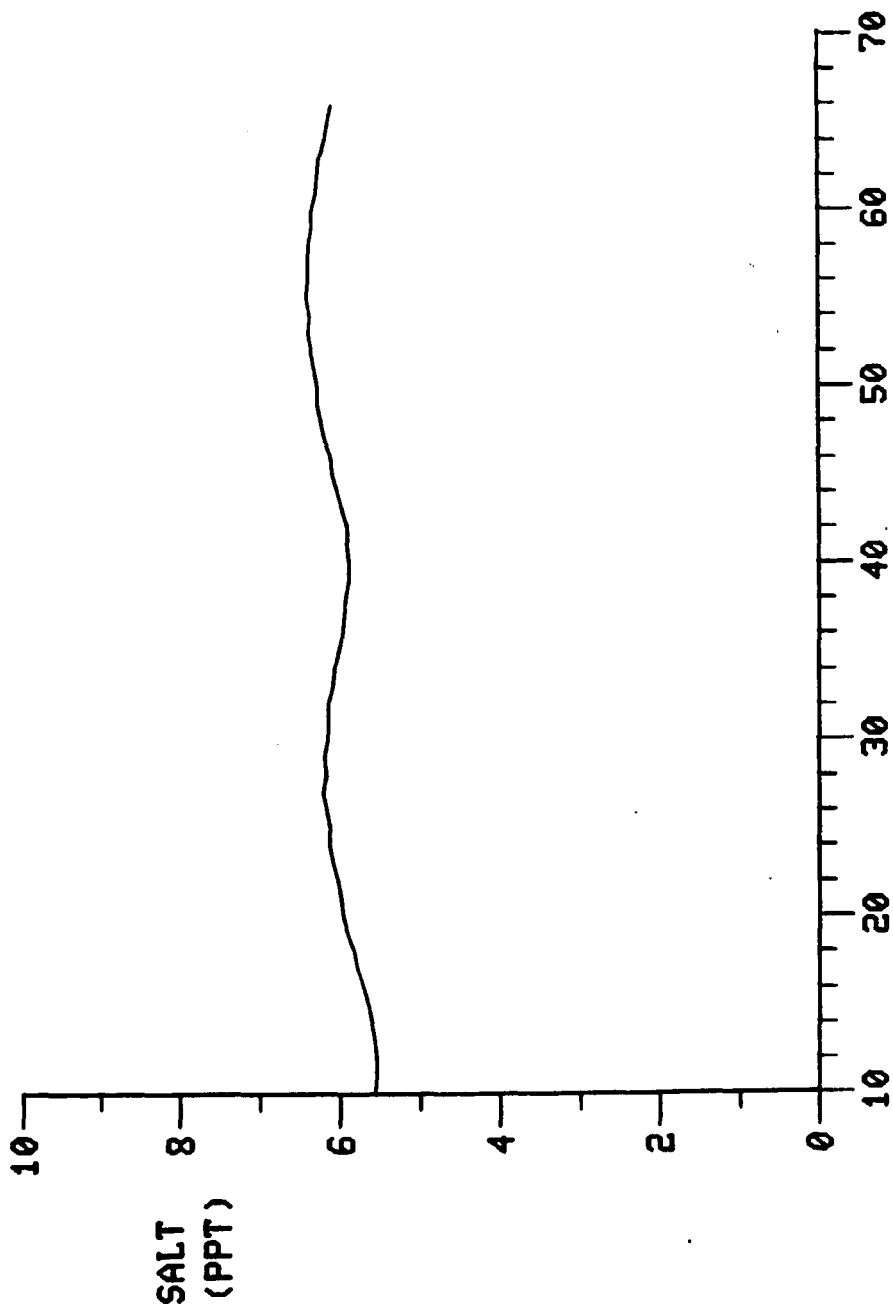
Figure 7-15a. Tide Level at Mouth of Idealized Estuary, Spring-Neap Simulation.



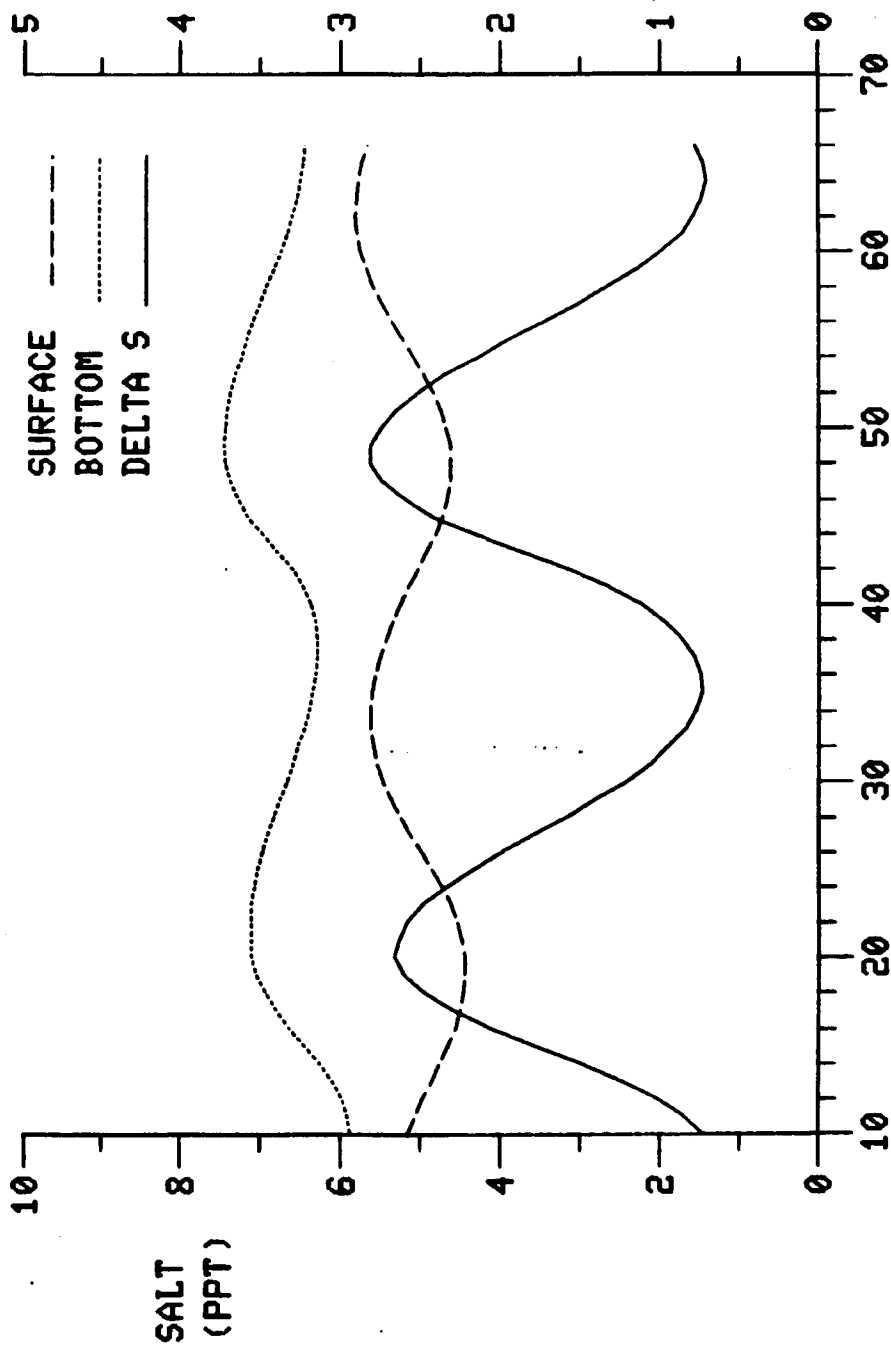
TIDAL CYCLES
 Figure 7-15b. Time Series of Depth-Average Salinity at Kilometer 20, Spring-Neap Simulation.



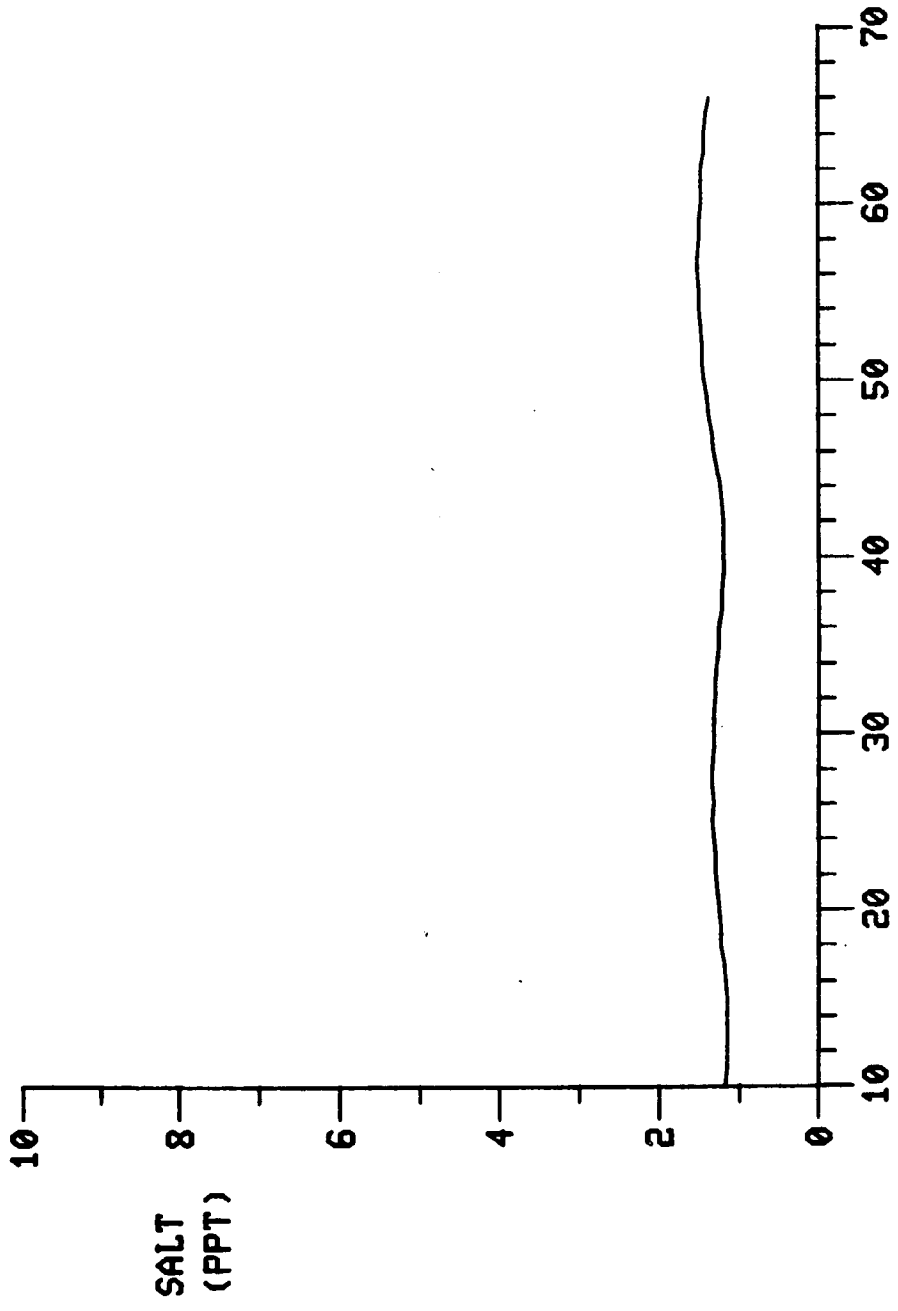
TIDAL CYCLES
 Figure 7-15c. Time Series of Stratification at Kilometer 20, Spring-Neap Simulation.



TIDAL CYCLES
 Figure 7-15d. Time Series of Depth-Average Salinity at Kilometer 44, Spring-Neap Simulation.

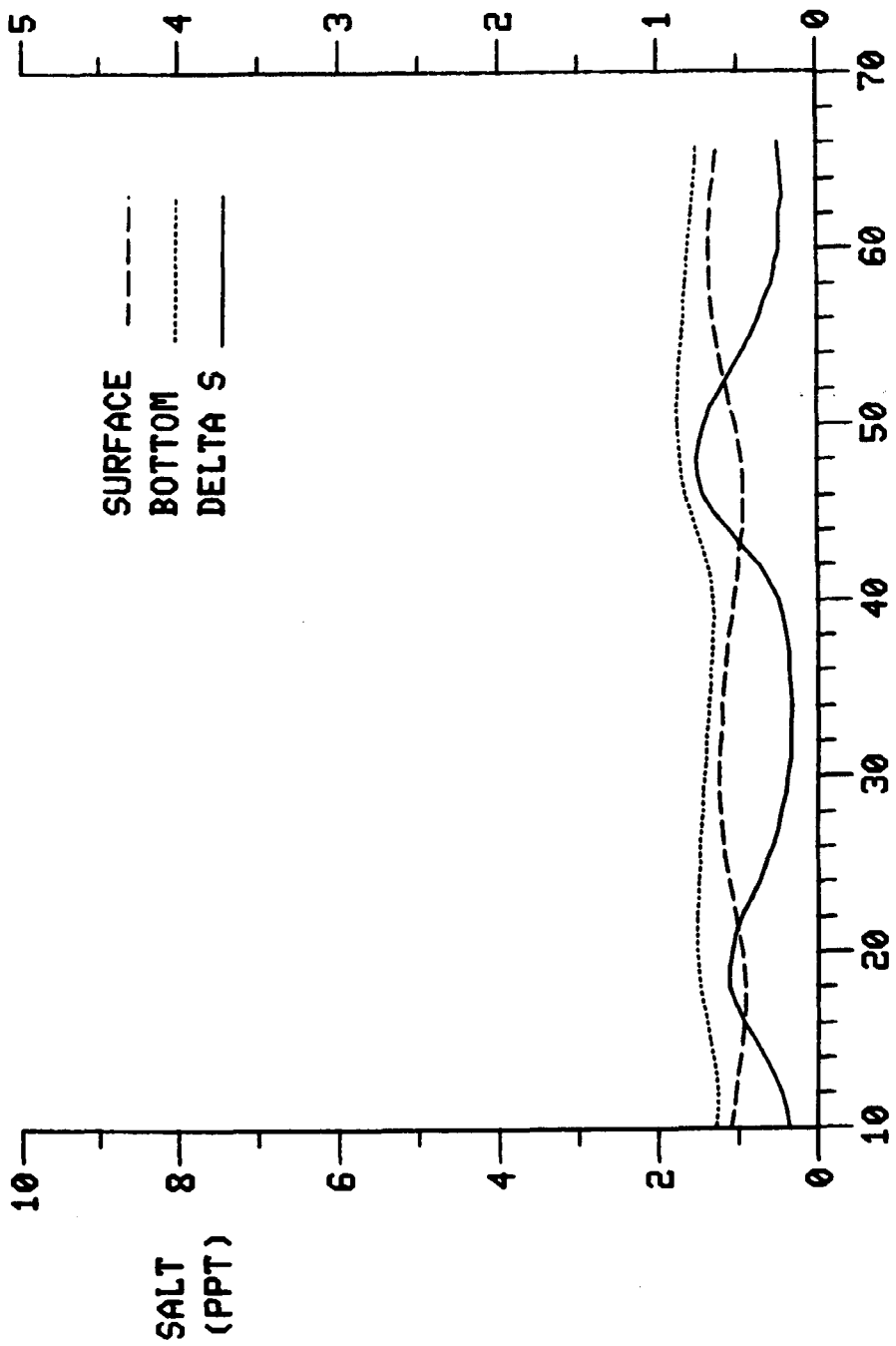


TIDAL CYCLES
 Figure 7-15e. Time Series of Stratification at Kilometer 44, Spring-Neap Simulation.



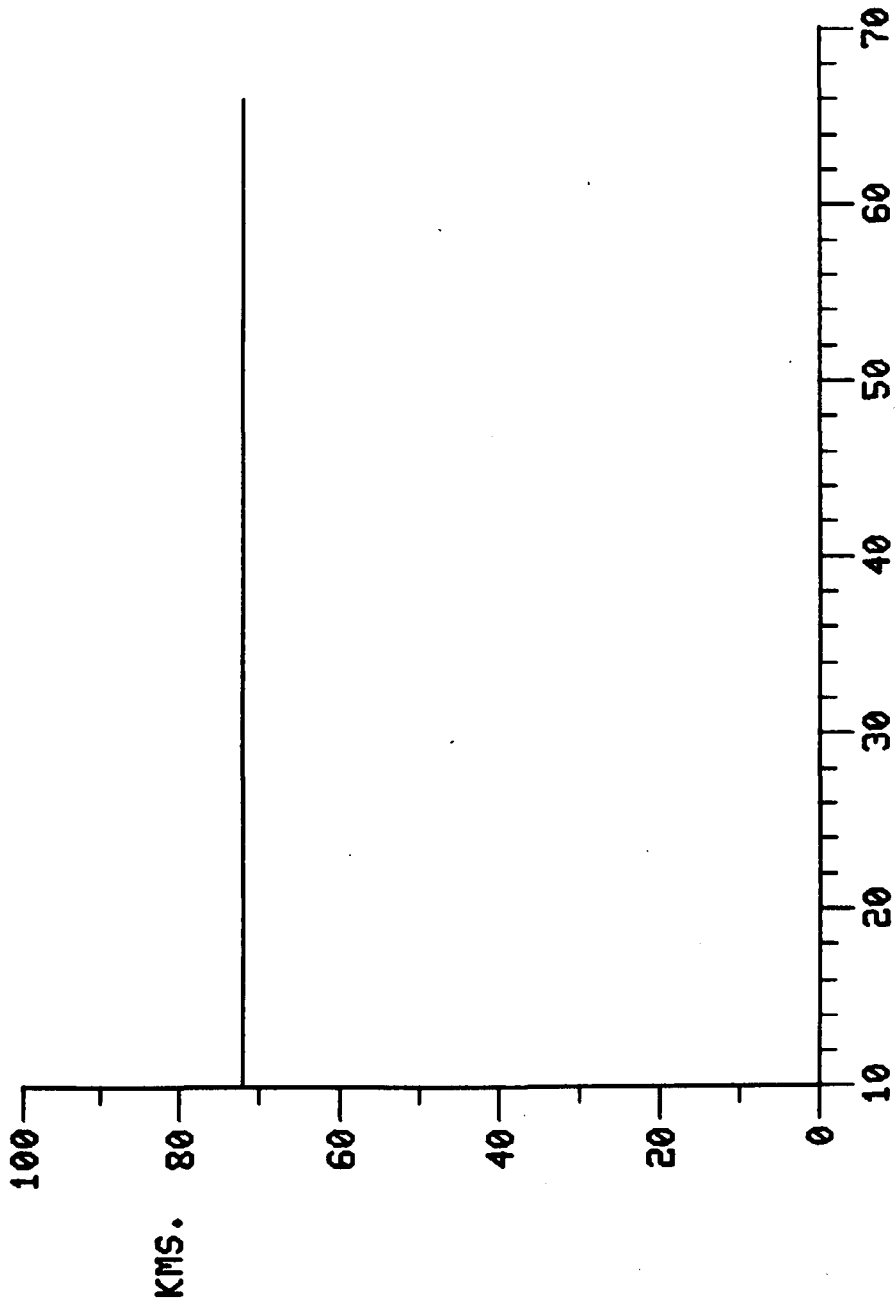
TIDAL CYCLES

Figure 7-15f. Time Series of Depth-Average Salinity at Kilometer 68, Spring-Neap Simulation.



TIDAL CYCLES

Figure 7-15g. Time Series of Stratification at Kilometer 68, Spring-Neap Simulation.



TIDAL CYCLES

Figure 7-15h. Location of 1 ‰ Isohaline, Spring-Neap Simulation.

CHAPTER VIII.

RECOMMENDATIONS FOR FUTURE INVESTIGATORS

The basic objectives of this study, two-dimensional model formulation, verification and utilization, have been fulfilled. In the completion of these objectives, a number of problems arose and were overcome - some with a good deal of success and others less so. The purpose of this chapter is to summarize these problem areas so that future investigators will recognize these difficulties as they occur and also find fruitful topics for additional research.

A. Integration of the Salinity Equation

The salinity equation (3-8) is integrated via an explicit finite-difference scheme. This scheme requires specification of sufficient longitudinal dispersion to maintain convergence (ineq. 3-50). Failure to meet this convergence constraint results in wavelike oscillations in the longitudinal salinity predictions. In this study, these oscillations were especially apparent near the open boundary and were large enough to produce negative salinities which caused subsequent failure of the computer program. (Until this constraint was recognized, initial investigations of the

problem centered on boundary conditions rather than dispersion.) Compliance with ineq. (3-50), for the observed values of u and the selected value of Δx , produced unrealistically large dispersion, however. Thus, a compromise value of dispersion was selected which maintained correct scaling of the terms in the salinity equation and minimized but did not eliminate numerical oscillations. Future investigators may instead wish to select smaller increments of Δx than were employed in this study.

An alternative to explicit integration of the salinity equation would be to use the predictor-corrector method developed by Young and Hirt (1972) and employed by Hamilton (1975). This scheme is effectively implicit and is stable for large time increments but was found to have too much numerical dispersion to be useful for long-term simulations in the James Estuary.

B. Open Boundary Conditions

Specification of conditions at an open boundary is problematical in any model. In this study, both intratidal and long-term salinity boundaries were necessary but detailed measurements were lacking. The expedient of moving the open boundary beyond the region of interest was thus adopted. This means was successful in simulations based on low-to-moderate flows but was less suited to the simulation of the storm pulse. For ideal simulation of

a transient storm flow, the model would have to be extended into Chesapeake Bay or beyond before a constant boundary could be utilized. Otherwise, collection of detailed field data at the mouth of the estuary during and after a storm pulse will be necessary before such an event can be completely modelled.

C. Data Collection

The capability of the model to simulate long-term events was verified through comparison with two sets of prototype data which detailed spring-neap stratification cycling and the response to a transient flow pulse. These data sets consisted of seven and eight salinity surveys, respectively. Much additional data would have been useful, however, both in analyzing prototype behavior and in judging the ability of the model to replicate this behavior. In particular, more closely spaced surveys and more detailed boundary conditions are needed. At present, the art of modelling has advanced so that collection of extensive data for verification is preferable to the development of additionally complex models.

D. Local and Non-Local Meteorological Effects

Local meteorological effects are herein defined as the effects of windstress applied directly to the estuary. In this study, these effects have been explored through analyses of the behavior of an idealized estuary. Determination of wind effects on a prototype is less facile,

however. In the James River (Fig. 2-1), for example, it is possible for a northeast wind to exert an upstream and downstream windstress simultaneously on different portions of the river. The net effect of local geometry combined with windstress is unknown. Neither has the turbulent mixing effect of wind-generated waves been explored. Additional model and prototype studies of the effects of wind are worthwhile fields of endeavor.

Non-local meteorological effects are manifested primarily as periodic changes in sea level in lower Chesapeake Bay. Wang and Elliott (1978) attributed these to an Ekman effect driven by coastal winds. The influence of these sea level changes on the James River is unknown and worth exploring in a model and/or prototype study.

E. Eddy Parameters

In this study, eddy diffusivity and viscosity are proportional to velocity and inversely proportional to the Richardson number (eqs. 4-15 - 4-16). These empirical formulations provide good predictions of stratification under steady conditions but under transient conditions model predictions lag the prototype. Reformulation of the eddy parameters to allow greater variability as a function of velocity is suggested as a means to bring the model predictions into better agreement with the prototype.

F. Estuarine Base Flow

A constant base flow to the James River Estuary of $1 \text{ m}^3/\text{sec}/\text{km}$ has been assumed in this study. This value is consistent with a water balance of the drainage basin and is necessary to prevent salt from intruding too far upstream during low flow periods. (Without this base flow, an unrealistically large eddy viscosity would have to be utilized to prevent upstream salt intrusion.) Summed over the length of the estuary, base flow amounts to $160 \text{ m}^3/\text{sec}$ and is a significant flux compared to the annual average gauged flows of $270 \text{ m}^3/\text{sec}$ and to drought flows of $30 \text{ m}^3/\text{sec}$. Thus, a study to obtain a better estimate of the magnitude of the estuarine base flow and to examine the role of this flux is warranted.

CHAPTER IX.

SUMMARY AND CONCLUSIONS

A two-dimensional, intratidal model of velocity, surface level, and salinity in a partially-mixed estuary has been formulated and verified against analytical solutions, laboratory experiments, and prototype data. Following verification, the model has been used as an experimental tool to analyze the effect on estuarine salinity of several forcing functions. The formulation and application of the model and the experimental results are summarized in this chapter.

A. The Numerical Model

The model is based on the time-variable, laterally-averaged equations of continuity, momentum, and salt balance. Previous applications of similar models have been hampered by computational time requirements and by lack of suitable data bases. Computational time was reduced, in this case, by use of a semi-implicit integration scheme for the momentum equation. By this means, the Courant condition limiting the integration time step was relaxed and the time step was extended from the explicit limit of 360 seconds to 1242 seconds. The model, employing

40 longitudinal segments and 5 to 6 vertical layers, required approximately 10 seconds execution time per tidal cycle on an IBM 370/158 main-frame computer or 20 seconds per tidal cycle on a PRIME 750 mini-computer. Thus, simulation of 80 cycles of prototype behavior were readily conducted.

The semi-implicit integration method is not a panacea which removes all constraints on the time step, however. As the time step is extended, numerical viscosity and phase errors in the prediction of velocity and surface level become large. Of more practical significance are the remaining stability and convergence limitations on the salt equation. Relaxing the Courant condition on the momentum equation does nothing to relax the stability constraint on the explicit solution to the salt equation, $\Delta t \leq K_x / .5u^2$, which limits extension of the time step long before numerical viscosity and phase error become significant.

A convergence constraint for the salinity equation also exists and governs selection of the distance increment: $\Delta x \leq 2K_x / u$. It was noted empirically that this restriction can be relaxed in favor of the more liberal guideline $\Delta x \leq 8K_x / u$ provided that longitudinal salinity gradients are mild.

B. Verification of the Model

Model verification was conducted in three phases. In the first phase, predictions of surface level, based on alternate combinations of time and space increments, were

compared to the analytical solution for a tidal wave traveling in a frictionless, rectangular channel closed at one end. Model predictions of tide range were in good agreement with the analytical solution except in the vicinity of the nodal point where tide range was overpredicted. The discrepancy was noted to increase in proportion to the time step and was attributed to numerical viscosity which is inherent in implicit finite-difference schemes. Varying the space increment, Δx , was observed to have little effect on the predictions of tidal range.

Some phase error was also noted in the predictions of surface level; model predictions tended to lead the analytical solution. This phase error was also proportional to the time step. Selection of the space increment had no effect on the phasing of the solution.

The second step in model verification consisted of comparisons of predictions with longitudinal and vertical salinity and velocity observations in a laboratory flume. Agreement between the tidal-average observations of salinity and the model predictions was excellent. The numerical model reproduced well the characteristic two-dimensional estuarine circulation but under-predicted the strength of the circulation, as observed in the laboratory. This discrepancy was attributed to the nature of the laboratory velocity measurements which were taken in mid-channel and therefore represent over-estimates of the

laterally-averaged velocities predicted by the model. Some discrepancy was also noted between the predictions and observations in the vicinity of the open boundary - a problematic area in both laboratory and numerical models. Of particular interest in this portion of the verification was the agreement of the numerical model with the cell-like circulation observed in the laboratory. Tidal-average vertical velocities were directed downward in the lower portion of the estuary and upward near the head of the salt intrusion.

The third phase in the verification was the comparison of model predictions with prototype data collected in the James River. Model predictions of surface level were compared with NOAA tabulations of tide range and with intratidal data collected at three stations. Model predictions of velocity were compared with intratidal data collected at two depths at the same three stations. Longitudinal salinity, as predicted by the model, was compared with five independent prototype data sets collected under different freshwater flow rates.

Comparisons of model predictions and prototype surface level were generally good. The characteristic behavior of the semi-implicit integration method, observed in the comparisons with the analytical solution, was, however, repeated. That is, the model over-predicted tide range in the vicinity of the nodal point and produced a

phase error in the intratidal predictions of surface level. This phase error showed some tendency to increase with distance from the mouth of the estuary.

Predictions of intratidal velocity showed the same phase error as the predictions of surface level but were otherwise accurate. As in the laboratory verification, the model under-predicted the magnitude of the current but this, again, was attributable to the unavoidable discrepancy between mid-channel velocity observations and laterally-averaged predictions.

Good agreement was noted between model predictions and observations of depth-average salinity. In this portion of the verification, two problems arose: specification of an intratidal salinity boundary condition at the open mouth, and estimation of non-gauged freshwater inflow to the prototype.

Various downstream boundary conditions were attempted. The solution adopted was to extend the model several segments beyond the region of interest and to specify a constant, vertically uniform salinity boundary. Within a few segments of the boundary, the model was noted to establish vertical and intratidal variations in salinity independent of the boundary condition. Thus, maximum predictability and simplicity were obtained simultaneously.

Non-gauged freshwater inflow was incorporated by assuming a constant, distributed base flow of $1 \text{ m}^3/\text{sec}$ per

kilometer of river length. This value was obtained through comparison of model predictions with five independent salinity data sets collected under differing gauged, fresh-water flow rates. No measurements or calculations of base flow to estuarine systems could be located to verify the flow rate obtained herein via model calibration. This topic is an important one and warrants additional investigation.

C. Application of the Model

Aside from computational constraints, modelling of estuaries in the longitudinal and vertical directions has been hampered by lack of sufficient data for verification of long-term model simulations. Two series of surveys detailing the transient behavior of the salinity structure of the James River were available for use in this study, however. The first series consisted of seven surveys conducted during the period Aug. 14 - Sept. 2, 1980. During this interval salinity in the river was observed to undergo a destratification-stratification cycle coincident with the spring-neap tidal cycle. The second series of observations consisted of six surveys conducted during the period April 27 - May 7, 1978. During this interval, the salinity intrusion was displaced 25 km downstream due to a twelve-fold increase in freshwater flow.

Application of the model to the spring-neap stratification cycle was generally successful. Just as in the

prototype, the model was observed to stratify and destratify in response to reductions or increases in the tide range. The exact values of observed stratification were not reproduced in all instances, however. Some discrepancies were attributable to a wind event which was not represented in the model. Stratification and destratification in the model also tended to lag the prototype by four to six tidal cycles. Reformulation of the eddy viscosity and diffusivity parameters (eqs. 4-15 and 4-16) to allow greater variability as a function of instantaneous velocity is suggested as a means by which this lag may be reduced.

Application of the model to the simulation of longitudinal motion of the salinity intrusion was also successful. The model accurately represented both the downstream displacement of depth-average salinity and the increase in relative stratification due to increased flow.

In this simulation, specification of a constant downstream salinity was no longer satisfactory. Instead, an alternate boundary condition which eliminated dependence on the downstream salinity during ebb flows and imposed a constant longitudinal gradient during flood flows was adopted. Although this boundary was sufficient for this application, simulation of a longer interval encompassing the post-storm recovery of salinity would have been impossible without detailed prototype observations of the downstream salinity. An alternate approach to the lack

of downstream boundary conditions would be to extend the model into Chesapeake Bay to a point where salinity is little-affected by pulses in tributary flow.

Some difficulty with convergence of the salinity equation was encountered as salt moved downstream in response to the flood flow. Due to the sharp longitudinal salinity gradients which were produced, the relaxed convergence criterion $K_x \geq u\Delta x/8$ was no longer sufficient to guarantee damping of numerical oscillations. Neither could dispersion be increased without overwhelming advective transport. Since the numerical oscillations which resulted occurred only at the end of the simulation and were confined to the downstream portion of the estuary, the effects were minor. Extension of the simulation would have required conformation to the guideline expressed by eq. (3-50), however, achieved through resegmentation of the model based on a smaller distance increment.

D. Experiments on a Model Estuary

Once verification of the model in the simulation of prototype behavior was complete, the model was employed to examine the response of salinity in an idealized estuary to variations in wind, tide range, flow, and salinity boundary conditions. Based on the results of the experiments, the perturbations were divided into two classes: those which affect primarily stratification (wind and tide) and those which affect both stratification and the

longitudinal salinity distribution (flow and boundary salinity). The classes are not exclusive, however, since the factors which altered stratification were capable of altering longitudinal salinity over lengthy time periods.

Reaction to alterations in the forcing functions was rapid, generally within two tidal cycles of the perturbation. Only in the instances of changes in the boundary conditions was the response delayed. The complete responses were prolonged, however. Thirty or more tidal cycles were required for the estuary to achieve a steady state in response to step-changes in the forcing functions. Twenty or more cycles were required for the estuary to recover its initial steady state following the cessation of pulse-like forcing functions. These long response periods and relaxation times confirm that under prototype conditions in which forcing functions are periodic and superimposed, an estuary is never truly at steady state.

BIBLIOGRAPHY

- Blumberg, A. F. (1975). A Numerical Investigation into the Dynamics of Estuarine Circulation. Chesapeake Bay Institute, The Johns Hopkins University. Technical Report 91.
- Boon, J. D., and Kiley K. P. (1978). Harmonic Analysis and Tidal Prediction by the Method of Least Squares. Va. Inst. of Marine Science, Gloucester Pt., Va. Special Report 186.
- Bowden, K. F., and Hamilton, P. (1975). "Some Experiments with a Numerical Model of Circulation and Mixing in a Tidal Estuary". Estuarine and Coastal Marine Science, Vol. 3, pp. 281-301.
- Cederstrom, D. J. (1945). Geology and Groundwater Resources of the Coastal Plain in Southeastern Virginia. Virginia Geological Survey, University of Virginia. Bulletin 63.
- Davis, J., ed. (1974). The Effects of Tropical Storm Agnes on the Chesapeake Bay Estuarine System. Va. Inst. of Marine Science, Gloucester Pt., Va. SRAMSOE 57.
- Elliott, A. J. (1976). A Study of the Effect of Meteorological Forcing on the Circulation in the Potomac Estuary. Chesapeake Bay Institute, The Johns Hopkins University. Special Report 56.
- Elliott, A. J. (1976). A Numerical Model of the Internal Circulation in a Branching Tidal Estuary. Chesapeake Bay Institute, The Johns Hopkins University. Special Report 54.
- Festa, J. F., and Hansen, D. V. (1976). "A Two-Dimensional Numerical Model of Estuarine Circulation: The Effects of Altering Depth and River Discharge". Estuarine and Coastal Marine Science, Vol. 4, pp. 309-323.

- Fisher, J. S., Ditmars, J. D., and Ippen, A. T. (1972). Mathematical Simulation of Tidal Time-Averages of Salinity and Velocity Profiles in Estuaries. Ralph M. Parsons Laboratory, Mass. Inst. of Tech., Cambridge, Mass. Report 151.
- Haas, L. W. (1977). "The Effect of the Spring-Neap Tidal Cycle on the Vertical Salinity Structure of the James, York, and Rappahannock Rivers, Virginia, U.S.A.". Estuarine and Coastal Marine Science, Vol. 5, pp. 485-496.
- Hamilton, P. (1975). "A Numerical Model of the Vertical Circulation of Tidal Estuaries and its Application to the Rotterdam Waterway". Geophys. J. R. Astr. Soc., Vol. 40, pp. 1-21.
- Hamilton, P. (1977). "On the Numerical Formulation of a Time-Dependent Multi-Level Model of an Estuary, With Particular Reference to Boundary Conditions" in Estuarine Processes, Vol. II. Academic Press, Inc., New York.
- Hansen, D. V., and Rattray, M. R. (1965). "Gravitational Circulation in Straits and Estuaries". J. of Marine Res., Vol. 23, pp. 104-122.
- Harleman, D. R. F. and Ippen, A. T. (1967). Two-Dimensional Aspects of Salinity Intrusion in Estuaries: Analysis of Salinity and Velocity Distributions. Committee on Tidal Hydraulics, Corps of Engineers, U. S. Army. Tech. Bull. 13.
- Harlow, F. H. and Amsden, A. A. (1970). Fluid Dynamics: An Introductory Text. Los Alamos Scientific Laboratory of the University of California, Los Alamos, N. M.
- Hunter, J. R. (1975). A Method of Velocity Field Interpolation Applicable to Stratified Estuaries. Chesapeake Bay Institute, The Johns Hopkins University. Special Report 45.
- Hyer, P. V., and Ruzecki, E. P. (1974). "Changes in the Salinity Structure of the James, York, and Rappahannock Estuaries Resulting from the Effects of Tropical Storm Agnes" in The Effects of Tropical Storm Agnes on the Chesapeake Bay Estuarine System, Davis ed. Va. Inst. of Marine Science, Gloucester Pt., Va. SRMSOE 57.

- Ippen, A. T. and Harleman, D. R. F. (1961). One-Dimensional Analysis of Salinity Intrusion In Estuaries, Committee on Tidal Hydraulics, Corps of Engineers, U. S. Army. Tech. Bull. 5.
- Ippen, A. T., and Harleman, D. R. F. (1966). "Tidal Dynamics in Estuaries" in Estuary and Coastline Hydrodynamics, A. T. Ippen, ed. Engineering Societies Monographs, McGraw Hill Book Co., Inc., New York.
- Kuo, A., Nichols, M., and Lewis, J. (1978). Modelling Sediment Movement in the Turbidity Maximum of an Estuary. Virginia Water Resources Research Center, Blacksburg, Va. Bulletin 111.
- Kwizak, M., and Robert, A. J. (1971). "A Semi-Implicit Scheme for Grid-Point Atmospheric Models of the Primitive Equations". Monthly Weather Review, Vol. 99, pp. 32-36.
- Leendertse, J. J. (1970). A Water-Quality Simulation Model for Well-Mixed Estuaries and Coastal Seas. The Rand Corporation, Santa Monica, Calif.
- Linsley, R. K., Kohler, M. A., and Paulhus, J. L. (1975). Hydrology for Engineers. McGraw-Hill, Inc., New York.
- Officer, C. B. (1976). Physical Oceanography of Estuaries (and Associated Coastal Waters). John Wiley and Sons, New York.
- Pritchard, D. W. (1967). "Observations of Circulation in Coastal Plain Estuaries" in Estuaries, G. H. Lauff ed. American Association for the Advancement of Science, Washington, D. C.
- Roache, P. J. (1972). Computational Fluid Dynamics. Hermosa Publishers, Albuquerque, N. M.
- Seitz, R. C. (1971). Drainage Area Statistics for the Chesapeake Bay Freshwater Drainage Basin. Chesapeake Bay Institute, The Johns Hopkins University. Special Report 119.
- Wang, D. P. and Elliott, A. J. (1978). "Non-Tidal Variability in the Chesapeake Bay and Potomac River: Evidence for Non-Local Forcing". J. of Physical Oceanography, Vol. 8, pp. 225-232.

Wang, D. P., and Kravitz, D. W. (1980). "A Semi-Implicit Two-Dimensional Model of Estuarine Circulation". J. of Physical Oceanography, Vol. 10, pp. 441-454.

Young, J. A., and Hirt, C. W. (1972). "Numerical Calculation of Internal Wave Motion". J. of Fluid Mechanics, Vol. 56, pp. 256-276.

VITA

Carl Francis Cerco

Born in Jersey City, N. J., January 29, 1951. Attended Public School No. 20 (1956-1964) and St. Henry-on-the-Hill High School (1964-1968) in that city. Obtained a Bachelor of Science in Mechanical Engineering from Newark College of Engineering, Newark, N. J. (1972). Obtained a Master of Science from the Department of Environmental Sciences and Engineering, University of North Carolina at Chapel Hill (1974). Obtained a Master of Science in Civil Engineering from the Massachusetts Institute of Technology, Cambridge, Mass. (1977). Entered the doctoral program at the School of Marine Science, College of William and Mary in 1978. Has finally had his fill of schooling (1982).